



HAL
open science

Estimation algorithms for thermoacoustic instabilities with distributed and nonlinear dynamics

Nils Christian Aars Wilhelmsen

► **To cite this version:**

Nils Christian Aars Wilhelmsen. Estimation algorithms for thermoacoustic instabilities with distributed and nonlinear dynamics. Automatic Control Engineering. Université Paris sciences et lettres, 2021. English. NNT: 2021UPSLM055 . tel-03621302

HAL Id: tel-03621302

<https://pastel.hal.science/tel-03621302>

Submitted on 28 Mar 2022

HAL is a multi-disciplinary open access archive for the deposit and dissemination of scientific research documents, whether they are published or not. The documents may come from teaching and research institutions in France or abroad, or from public or private research centers.

L'archive ouverte pluridisciplinaire **HAL**, est destinée au dépôt et à la diffusion de documents scientifiques de niveau recherche, publiés ou non, émanant des établissements d'enseignement et de recherche français ou étrangers, des laboratoires publics ou privés.

THÈSE DE DOCTORAT

DE L'UNIVERSITÉ PSL

Préparée à MINES ParisTech

Algorithmes d'estimation pour les instabilités thermoacoustiques avec dynamique distribuée et non-linéaire

Estimation algorithms for thermoacoustic instabilities with distributed and nonlinear dynamics

Soutenue par

**Nils Christian Aars
WILHELMSSEN**

Le 14 Décembre 2021

Ecole doctorale n°621

**Ingénierie des Systèmes,
Matériaux, Mécanique,
Énergétique (ISMME)**

Spécialité

**Mathématique et
Automatique**

Composition du jury :

Emmanuel WITRANT Professeur, GIPSA-lab Grenoble	<i>Président</i>
Gustavo Artur DE ANDRADE Professeur, UF de Santa Catarina	<i>Rapporteur</i>
Maximillian ZAHN Ingénieur en chef, GE Aviation Munich	<i>Examineur</i>
Lucie BAUDOUIN Chargée de recherche, LAAS-CNRS	<i>Examineur</i>
Florent DI MEGLIO Maître-assistant, MINES ParisTech	<i>Co-directeur de thèse</i>
Pierre ROUCHON Professeur, MINES ParisTech	<i>Directeur de thèse</i>

UNIVERSITÉ PARIS SCIENCES & LETTRES
DOCTORAL SCHOOL ISMME
INGÉNIERIE DES SYSTÈMES, MATÉRIAUX,
MÉCANIQUE, ÉNERGÉTIQUE

DOCTORAL THESIS

Specialty : MATHEMATICS AND CONTROL

Nils Christian Aars WILHELMSSEN

Estimation Algorithms for Thermoacoustic Instabilities with Distributed and Nonlinear Dynamics

Thesis Advisor: Pierre ROUCHON

Co-advisor: Florent DI MEGLIO

prepared at Centre Automatique et Systèmes, MINES ParisTech

This thesis is submitted in partial fulfilment of the requirements for the degree of Philosophiae Doctor in Mathematics and Control. The research has been carried out within the European Union's Horizon 2020 project MAGISTER¹ under grant agreement N° 766264. The consortium partner Armines has been involved with this work directly, and industrial partners GE Aviation and Ansys through collaboration.



¹Machine learning for Advanced Gas turbine Injection Systems To Enhance combustor performance

Résumé

Les instabilités thermoacoustiques sont néfastes pour les systèmes de combustion dans lesquels elles apparaissent, tels que les chambres de combustion de turbines à gaz. Des systèmes de surveillance avancés sont nécessaires pour estimer et prévoir ce phénomène afin de le prévenir, et possiblement de le supprimer grâce à des méthodes de contrôle. Dans cette thèse, nous proposons d'utiliser une description sous forme de systèmes à paramètres distribués des phénomènes acoustiques couplés à des modèles de dégagement de chaleur. Les non-linéarités sont prises en compte chaque fois que possible, pour décrire les instabilités. Des algorithmes d'estimation d'état et de paramètres prenant en compte ces effets dynamiques sont proposés. Deux niveaux de complexité différents sont considérés. D'une part, on s'intéresse à une configuration de laboratoire et un modèle de modes thermoacoustiques longitudinaux dans une chambre de combustion. Pour ce système, un estimateur de l'état d'un tube de Rijke chauffé électriquement est synthétisé. Puis, un observateur globalement convergent, prenant en compte les non-linéarités du réchauffeur électrique et la dynamique distribuée, est proposé et analysé. Celui-ci est associé à un algorithme d'identification de paramètres pour estimer les impédances acoustiques aux frontières du domaine spatial. L'observateur d'état et l'identification de paramètres sont testés à la fois dans des simulations et expérimentalement. Ensuite, nous proposons un algorithme pour estimer les deux paramètres aux limites de systèmes hyperboliques linéaires 2×2 avec une seule mesure aux limites. En outre, un modèle dynamique de l'acoustique dans un conduit avec une section transversale variable dans l'espace est dérivé. En utilisant ces deux résultats ensemble, le schéma d'estimation des paramètres aux limites pour le tube de Rijke est étendu à des conduits plus généraux. Un bouclage de sortie, combinant une loi de commande par retour d'état et un observateur frontière colocalisé, pour les instabilités thermoacoustiques longitudinales dans un modèle d'une chambre de combustion avec acoustique distribuée et un modèle de flamme linéaire est ensuite proposé. Enfin, nous proposons un estimateur d'état pour un modèle de chambre de combustion avec une flamme non linéaire. Une méthode basée sur l'utilisation de réseaux de neurones est utilisée pour concevoir un observateur pour le sous-système de flamme, qui est ensuite vérifié sur les données CFD.

Abstract

Unwanted thermoacoustic instabilities are harmful to combustion systems that suffer from them such as gas turbine combustors operating under lean premixed conditions. Advanced monitoring systems are needed to estimate and forecast the phenomenon to assist in decision making and automatic stabilization. In this thesis we propose using a distributed description of acoustics interfaced to heat release models, with nonlinearities whenever possible, to describe the instabilities. State and parameter estimation algorithms taking these dynamic effects into account are explored. Two different levels of complexity are considered: we start with a laboratory setup and move towards a model of longitudinal thermoacoustic modes in a can combustor. First, state estimation for the electrically heated Rijke tube is considered. A globally convergent observer, taking into account nonlinearities from the electrical heater and distributed dynamics, is proposed and analysed. This is paired with a parameter identifier for estimating boundary acoustic impedances. The state observer and parameter identifier are tested both in simulations and experimentally. Next, a parameter identifier to estimate both boundary parameters of 2×2 linear hyperbolic systems with a single boundary measurement is proposed. Also, a transient model of acoustics in a duct with spatially varying cross-sectional area is derived. Using these two results together the boundary parameter estimation scheme for the Rijke tube is extended to more general ducts. An output feedback controller, combining a full-state feedback control law and collocated boundary observer, for longitudinal thermoacoustic instabilities in a model of a can combustor with distributed acoustics and a linear flame model is proposed next. Convergence is proven and it is tested in simulations. Lastly, the state estimation problem for a can combustor model with a nonlinear flame is considered. Neural networks are used to design an observer for the flame subsystem, which is subsequently verified on CFD data.

Acknowledgments

This thesis would not have been possible were it not for the input, collaboration and support from a large number of individuals. First and foremost I would like to thank my advisor Florent Di Meglio for his guidance and support all the way from project conception to writing of the thesis. His quick wit and availability to help in a very hands-on way with short notice has been invaluable for the completion of this research, with simple questions sometimes turning into spontaneous, hours-long discussions and explanations where you always left wiser and more knowledgeable than you came. His encyclopedic knowledge and deep understanding of systems and control theory have added theoretical weight to the work, and his cunning mind has generated excellent suggestions and perspectives that have been of great help. I would also like to thank Pierre Rouchon for having taken the role and responsibility of being the administrative director of the thesis.

Next I would like to thank Emmanuel Witrant and Gustavo Artur de Andrade from the defence committee for taking the time to read and review the manuscript, with Emmanuel also serving as president of the committee. Their reviews came with many good suggestions for improvement, and led to interesting discussions during the defence, especially with Gustavo who has worked on similar topics to those presented in this manuscript. Also I would like to thank Lucie Baudouin and Maximilian Zahn for featuring as examiners during the thesis defence, asking thought-provoking questions and offering additional perspective.

Throughout my three years as a member of the Centre Automatique et Systèmes (CAS) at MINES ParisTech I have met many gifted people with whom I have had the privilege of working and discussing a vast array of topics with. Firstly I would like to thank Laurent Praly and Pauline Bernard for sharing their vast knowledge and understanding of nonlinear observers, and also Laurent for his sharp insights and pointed comments on parameter identification. Also, I would like to thank Nicolas Petit for facilitating a stimulating working environment at CAS through his role as the lab director, and also Delphine Bresch-Pietri and Philippe Martin for their good stories. Thanks to Jean Levine for his excellent flatness-based nonlinear control course. A large number of other PhD students, PostDocs and visitors have passed through the lab at various points during my time there, and it has been a pleasure taking innumerable coffee breaks with and working alongside Ulf Jakob Flø Aarsnes, Loris Amabile, Pierre-Cyril Aubin-Frankowski, Jean Auriol, Lukas Bahr, Arthur Bizzi, Maxime Brunet, Mona Buisson-Fenet, Leobardo Camacho-Solorio, Xi Chen, Charles-Henri Clerget, Aurélien Fiot, Haavard Holta, Sijia Kong, Pierre-Olivier Lamare, Hubert Ménou, Aradhana Nayak, Hoai-Minh Nguyen, Pierre Six, Dilshad Surroop, Gia Quoc Bao Tran, Naveen Velmurugan, Matthieu Vigne, Hana Yahia and Feng Yang.

The other axis of involvement this thesis work has brought me into is that of the MAGISTER project, and here I would first and foremost like to thank Jim Kok from the University of Twente for conceptualizing and organizing the entire project. Additionally, the project coordinators Jorien van Loon and Bridgette Con-

nell deserve a huge thank you for keeping all the pieces together. Also, I would like to thank Thomas Ripplinger and Luis Fernando Figueira da Silva for hosting the secondments. A special thanks to Matthew Juniper and Valéry Morgenthaler for interesting discussions. Throughout the MAGISTER project we had a range of workshops organized where a number of interesting and useful lectures were given. I would like to thank Carl Edward Rasmussen for his probabilistic machine learning workshop, Tim Lieuwen, Wolfgang Polifke and Aimee Morgans for the summer school on combustion, Thierry Poinsot and colleagues for the course on numerical methods for large eddy simulation and Björn Stelzner for the lecture series on experimental techniques for spray flames. Before the COVID-19 pandemic these were hosted in various locations around Europe, and here I had the pleasure of getting to know and work with many talented PhD students spread across the consortium partners. For this I would like to thank Ushnish Sengupta and Francesco Garita from the University of Cambridge, Michael McCartney and Nilam Tathawadkar from GE Aviation, Sagar Kulkarni and Alireza Javarehshkian from TU Munich, Louise da Costa Ramos from Ansys, Varun Shastry from Cerfacs, Alireza Ghasemi, Edmond Shehadi and Sara Navarro Arredondo from the University of Twente, Thomas Lafarge and Walter Agostinelli from Safran, and Thomas Christou from Karlsruhe Institute of Technology, in addition to the PhD students from the ANNULIGHT project with whom we had some shared training, for all the good times.

Last but not least I would like to thank all my friends and family for their love and support.

Nils Christian Aars Wilhelmsen

Contents

List of Acronyms	xi
I Background	1
1 Introduction	3
1.1 Background	3
1.2 Approach	6
1.3 Contributions	8
1.4 Thesis structure	9
2 Mathematical Modelling	11
2.1 Modelling principles	12
2.2 Heat release	13
2.2.1 Electrical heater	13
2.2.2 Flames	15
2.3 Acoustics	22
2.3.1 Duct with spatially varying cross section	22
2.3.2 Special cases	25
2.4 Boundary conditions	26
2.4.1 Acoustic impedance	26
2.4.2 Heat release–acoustics coupling	28
2.5 Summary of models	31
2.5.1 Rijke tube – Chapter 3	31
2.5.2 Acoustic duct for boundary parameter identification – Chapters 4–5	31
2.5.3 Can combustor – Chapters 6–7	32
II Lab Setup : The Rijke Tube	33
3 The Rijke Tube – State Observer	47
3.1 Literature review	48
3.2 Observer design	48
3.2.1 Model in Riemann coordinates	48
3.2.2 Observer design	51
3.2.3 Convergence analysis	53
3.2.4 Robustness to modelling error in boundary condition	54
3.3 Simulations	56
3.3.1 First simulation - Smaller impedances	56

3.3.2	Second simulation - Larger impedances	60
3.4	Experiment	68
3.5	Discussion	71
4	The Rijke Tube – Parameter Identifier	73
4.1	Literature review	74
4.2	Parameter identifier	75
4.2.1	Model in Riemann coordinates	76
4.2.2	Regressor form	77
4.2.3	Identification scheme	78
4.3	Simulations	79
4.3.1	Parameter identification simulations	79
4.3.2	State observer simulations - Correct boundary coefficients . .	81
4.4	Experiments	87
4.4.1	Parameter identification experiment	87
4.4.2	State observer experiment - Estimated boundary coefficients .	89
4.5	Discussion	90
III	Towards Combustors	93
5	Boundary Parameter Estimation	97
5.1	Background	98
5.1.1	Problem statement	98
5.1.2	Literature review	98
5.2	Boundary parameter estimation 2×2 hyperbolic systems	100
5.2.1	Mapping to target system	100
5.2.2	Regressor form	102
5.2.3	Adaptive law	104
5.3	Simulations	106
5.3.1	Simulation example	106
5.3.2	Robustness to noise	109
5.4	Application to estimation of acoustic impedance in duct with spatially varying cross section	110
5.4.1	Model in Riemann coordinates	110
5.4.2	Regressor form	112
5.5	Discussion	114
6	Linear Combustor	117
6.1	Background	118
6.1.1	Literature review	118
6.1.2	Model in Riemann coordinates	119
6.1.3	Problem statement	122
6.2	Control Design	123
6.2.1	Mapping into simpler cascade	124

6.2.2	Analysis of kernels	126
6.2.3	Full control law	128
6.3	Observer Design	130
6.3.1	Mapping into stable cascade	130
6.3.2	Analysis of kernels	132
6.3.3	Observer	133
6.4	Output Feedback Controller	134
6.5	Simulations	135
6.5.1	Simulation parameters	135
6.5.2	Simulation results	137
6.6	Discussion	139
7	Nonlinear Flame	149
7.1	Background	150
7.1.1	Problem statement	150
7.1.2	Observer for nonlinear ODE coupled to hyperbolic PDE system	151
7.1.3	KKL observers	153
7.2	Numerical design of observer for Kornilov’s flame	155
7.2.1	Methodology	155
7.2.2	Generation of training data	159
7.2.3	Training of neural networks	162
7.2.4	Resultant transformation	166
7.3	Simulation and verification	167
7.3.1	Direct observer tests	167
7.3.2	Verification on Kornilov’s flame data	170
7.4	Discussion	173
IV	Backmatter	175
8	Conclusion and Perspectives	177
8.1	Summary	177
8.2	Discussion	178
	Appendices	181
	A Trained Neural Network Coefficients	183
	Bibliography	189

List of Acronyms

ADC Analog-to-Digital Converter	41
BNC Bayonet Neill-Concelman	41
CFD Computational Fluid Dynamics	8
DAE Differential-Algebraic Equation	139
FDF Flame Describing Function	19
FTF Flame Transfer Function	19
GAS Globally Asymptotically Stable	52
I/O Input and Output	12
ISS Input-to-State Stable	54
IV Instrumental Variables	110
IVP Initial Value Problem	24
KKL Kazantzis-Kravaris-Luenberger	151
LS Least Squares	74
LTI Linear Time Invariant	153
MOC Method Of Characteristics	74
ODE Ordinary Differential Equation	7
PDE Partial Differential Equation	7
PE Persistently Exciting	78
ROM Reduced Order Model	151
SPL Sound Pressure Level	139
SWR Standing-Wave-Ratio	74
UGD Uniformly Gridded Discretization	106

Part I

Background

Introduction

Contents

1.1	Background	3
1.2	Approach	6
1.3	Contributions	8
1.4	Thesis structure	9

Dans ce chapitre introductif, le sujet de la thèse est motivé et une revue de la littérature des travaux antérieurs sur le sujet est présentée. Par la suite, notre approche est introduite et comparée aux approches précédentes, assurant sa nouveauté et l'intérêt d'appliquer une telle approche. Une liste de contributions et de publications qui sont un résultat direct du travail présenté ici est énoncée, avant que la structure de la thèse ne soit expliquée.

In this introductory chapter, the thesis topic is motivated and a literature review of previous work on the topic is presented. Thereafter our approach is introduced and compared to previous approaches, ensuring its novelty and the interest of applying such an approach. A list of contributions and publications which are a direct result of the work presented here are stated, before the thesis structure is explained.

1.1 Background

The ever increasing demand of energy and transport in society since the industrial revolution has gone hand in hand with an increase in emissions into the atmosphere, which in turn contribute to undesirable effects such as global warming and more extreme weather patterns [Masson-Delmotte *et al.* 2021]. One particular technology which has, since the first useful one in the sense of providing net power output was built in 1903 by Ægidius Elling [Bakken *et al.* 2004], been especially ubiquitous in both power generation applications and for use as a propulsion system for vehicles such as ships and aircraft [Nasir *et al.* 2018] is the gas turbine (see Figure 1.1). Since then numerous improvements to the technology have been developed, with more efficient power outputs and cleaner emissions in each generation. One direction of improvement which is especially promising with respect to decreasing emissions into the atmosphere, especially in the form of NO_x formation, and hence contributing to an overall cleaner technology is the operation of gas turbines under so-called

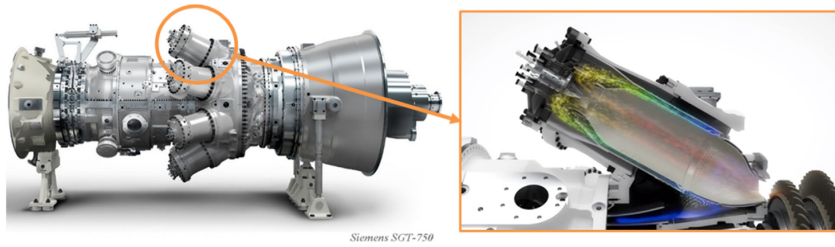


Figure 1.1: Siemens SGT-750 gas turbine (left) and cross section of combustion chamber (right). From [Rashwan *et al.* 2020].

lean premixed conditions [Seo 2003]. The main challenge faced in implementing this technique in practice is the increased likelihood of detrimental *thermoacoustic instabilities* [Lieuwen *et al.* 2001] in the combustion chamber, the part of the gas turbine shown on the right of Figure 1.1, under this operating regime. Due to the widespread use of and reliance on gas turbines by society, overcoming this issue would be a significant contribution towards solving the current climate crisis.

Within the context of their spontaneous occurrence in combustion chambers, thermoacoustic instabilities are an undesirable phenomenon, with consequences ranging from wear and tear in the less severe cases up to the combustor exploding in the more extreme cases [Poinsot 2017], possibly in a matter of seconds. An



Figure 1.2: Burner assembly that has been damaged by thermoacoustic instabilities. From [Goy *et al.* 2005].

example from [Goy *et al.* 2005] of a burner assembly that has undergone a beating from these instabilities is shown in Figure 1.2. As noted in [McManus *et al.* 1993],

answering the question of whether or not a combustor will suffer from such instabilities is notoriously difficult to answer in the design and even production stages, with thermoacoustic oscillations usually first being observed in latter stages of the development cycle.

Thermoacoustic instabilities were initially studied as a physical curiosity before they became an issue in practical technologies, with the first published study based on work by [Higgins 1802]. This was followed by work in [Rijke 1859], which standardized the experimental setup now known as the *Rijke tube* by generating thermoacoustic instabilities via a heated gauze placed in the lower half of an open-ended tube. A physical mechanism for the instability is qualitatively suggested in [Rayleigh 1878], later to be quantified more precisely in [Putnam & Dennis 1954]. In practice and with thermoacoustic instabilities possibly occurring in a wide range of combustion technologies, such as solid [Price 1969] and liquid [Crocco 1965] propellant rocket motors, ramjets [Rogers & Marble 1956], turbojet thrust augmenters [Bonnell *et al.* 1971], boilers [Putnam 1971] and furnaces [Lieuwen & Yang 2005] to give a non-exhaustive list, a high number of different factors play in and hence the precise classification of thermoacoustic instabilities is a difficult task. In [Williams 2018] thermoacoustic instabilities due to combustion are classified in three different categories:

1. Intrinsic instabilities.
2. Chamber instabilities.
3. System instabilities.

The first of these, intrinsic instabilities, occur when there is some unstable feedback mechanism of a combustion process interacting with itself and is often characterized by being of lower frequency than the other types. A well-known mathematical model that gives an example of this type of instability mechanism on laminar flame fronts is the Kuramoto-Sivashinsky equation [Kuramoto 1978, Sivashinsky 1977], and has been studied recently by multiple authors from a system dynamics perspective due to its interesting instability properties (see e.g. [Liu & Krstić 2001, Baudouin *et al.* 2013, Coron & Lü 2015]). Such instabilities are however outside the scope of this work, and instead the focus is directed towards the second type, namely chamber instabilities. In practice these occur when combustion occurs inside a confined volume, which is the case one has inside gas turbine combustion chambers. Compared to intrinsic instabilities, these instabilities tend to be characterized by much higher frequencies, typically dominated by the acoustic properties of the combustor. The main mechanism driving the instability here is the acoustics in the chamber being in phase with the heat release process, causing a self-sustaining oscillation that grows exponentially until being saturated by nonlinear effects [Sujith *et al.* 2016]. The third type of instability, system instabilities, occur due to the interaction of the combustion system with other parts of the system, such as the feed or exhaust system. These are however also outside the scope of this work.

1.2 Approach

To deal with the thermoacoustic instability issue, one must disrupt the constructive coupling between heat release and acoustic waves in some sense. Much of the early work on tackling this problem has been based on applying what one can consider “traditional engineering” approaches of physically augmenting the system, known as *passive control methods* (see e.g. [Culick 1988]). Passive methodologies are still an active field of development and some of the strategies employed include but are not limited to Helmholtz resonators [Gysling *et al.* 2000], acoustic liners for internal damping inside the combustor [Eldredge & Dowling 2003] and quarter wave tubes [Zahn *et al.* 2016]. Analysing the frequency domain properties [Zahn *et al.* 2015] of combustors fits naturally well with passive stabilization methods because they allow investigations, such as sensitivity analyses [Magri & Juniper 2013] and determinations of stability margins [Betz *et al.* 2017], into how the ad-hoc system augmentation influences the overall system eigenvalues to be readily performed.

As noted in [Morgans & Dowling 2007], a drawback of passive methodologies is that they are potentially expensive and time consuming to implement due to their bespoke nature, and often times they only work under specific operating conditions. A possibly more flexible approach is active stabilization methods, which were already investigated in a theoretical setting for instabilities in rocket engines in the 1950s [Tsien 1952]. The first experimental studies on empirically based control strategies of feeding back a phase-shifted and amplified sensor signal, tuned via a trial-and-error approach, started being performed for the Rijke tube around three decades later in [Dines 1984]. Since then a multitude of different approaches have been studied, with an overview of contributions up to the mid-2000s given in [Dowling & Morgans 2005]. Gradually more and more model-based control strategies started appearing, with some notable contributions from around the turn of the millennium being [Krstić *et al.* 1999, Annaswamy *et al.* 2000].

In this thesis the main focus is the design of model-based algorithms for estimating unmeasured states and unknown parameters of transient models reproducing thermoacoustic instabilities. The literature on model-based estimation methods for thermoacoustic instabilities is highly sparse in comparison to its control counterpart, but some notable contributions are [Hong & Lin 2007, de Andrade *et al.* 2020] and a review of typical sensors used are given in [Docquier & Candel 2002]. The intended application of these algorithms would be to run in real time with the physical process, where use cases could be general monitoring and in early-warning systems, but also in conjunction with control algorithms that need access to unmeasured state and parameter data. A trade-off one faces in the modelling stage for such algorithm design is model complexity, where one wants a model that is simple enough that it can be run online, but complex enough to capture the most important features of the dynamics. Two important aspects of thermoacoustic instabilities (of the chamber instability type) is the distributed nature of the acoustics but also strong nonlinearities in the heat release model, which has an effect of saturating the thermoacoustic

instability into a limit cycle oscillation [Han *et al.* 2015].

Many of the previous model-based control and estimation algorithms from the literature base themselves on an approach of first lumping the mathematical model into a finite dimensional model (see e.g. [Bonciolini *et al.* 2021]), basing the algorithm design on this reduced model. This approach is often referred to as *early-lumping*. A well-known issue from vibration control that can come up with early-lumping is the so-called *spillover phenomenon* [Safi *et al.* 2018], where higher order modes that have been neglected in the modelling are inadvertently destabilized. The spillover phenomenon has been observed in experiments involving control of thermoacoustic instabilities with early-lumped model-based controllers, see e.g. [Bloxsidge *et al.* 1987, Gulati & Mani 1992]. A way of overcoming this issue is to take a so-called *late-lumping* approach, where the full distributed nature of the dynamics is taken into account in the algorithm design, only discretizing the model in the implementation stages.

In this thesis a late lumping approach is taken for the model-based estimation algorithm design, aiming to preserve the distributed nature of the phenomenon as much as possible, yet basing the algorithm design on a model that is feasible to implement in real time. Little work of this type has been addressed previously in the literature for application towards thermoacoustic instabilities. In the past decade some work has been done taking a similar approach for the Rijke tube [Olgac *et al.* 2014, Epperlein *et al.* 2015, de Andrade *et al.* 2018a], but the heat release models are in this case always linearized, thus losing the important nonlinear nature of the phenomenon. Hence, the aim of this thesis is to explore the design of model-based estimation algorithms for thermoacoustic instabilities that take into account both the distributed and nonlinear aspects, whenever possible. The general model structure that will be used to describe the chamber instabilities is that of coupled Partial Differential Equation (PDE)–Ordinary Differential Equation (ODE) models [Barreau *et al.* 2018, Ghousein & Witrant 2020], where roughly speaking the PDE represents the chamber acoustics and the ODE represents the heat release model. Also, as discussed extensively in [Poinsot 2017], the literature heavily focuses on studies investigating laboratory setups but which are not directly useful for understanding and tackling the problem of thermoacoustic instabilities in practical engines. Although the work in this thesis uses the Rijke tube as a starting point, the aim is to leverage this as a stepping stone towards estimation design for more complicated mathematical models that can better describe a combustion chamber towards the second half of the work. This can then serve as a general framework for further investigations of the same nature, where the algorithms can be extended to larger scale system instabilities, or be modified to take into account the smaller scale effects of intrinsic instabilities. Also, the framework could be extended to design estimation algorithms for more complicated chamber instabilities such as those found in annular combustors.

For the algorithm designs, we assume limited instrumentation is available. Precisely, all the algorithms considered assume a single pressure measurement is available, only. Arguably the most important states to estimate when regarding chamber

instabilities is the distributed pressure and velocity together with heat release rate. A parameter of high significance in the stability properties of chamber instabilities, but which is typically difficult to know a priori, are the boundary acoustic impedances. Hence focus will be placed on estimation of these parameters. Overall, the objectives of the thesis can be summarized as follows:

1. Design observers estimating distributed states and heat release under perfect model assumptions.
2. Design parameter identification algorithms relying on parsimonious measurements.
3. When possible, take into account the nonlinearity of the heat release process.

Next, in Section 1.3 the contributions of the thesis are stated, before the thesis structure is summarized in Section 1.4.

1.3 Contributions

Following on from the statement of objectives in Section 1.2, we state here the main contributions which have come about as a result of this thesis work. They can be summarized as follows:

1. A globally convergent state observer for the Rijke tube, using a distributed model of the acoustics and a nonlinear model of the heat release rate, has been designed and analysed. It has also been tested in simulations and experimentally.
2. A distributed transient model of the acoustics, suitable for control and estimation algorithm design, in a duct with spatially varying cross-sectional area is derived. This model generalizes the model of acoustics in a duct with constant cross-sectional area. Also, the coupling with a flame at a boundary with sudden area expansion has been treated.
3. A parameter identification scheme for estimating both boundary acoustic impedances of the Rijke tube, relying on a single pressure measurement is derived. It is tested in simulations and experimentally. Also, using the model from Contribution 2, how this scheme generalizes to the case of a duct with spatially varying cross-sectional area has been considered.
4. A state observer and full-state feedback controller for a linearized model of a can combustor, assuming actuation is collocated to the pressure sensor, has been designed. These can be combined into an output feedback controller. The designs have been tested in simulations.
5. An observer for a nonlinear flame model has been designed numerically using neural networks. The observer has been verified using Computational Fluid Dynamics (CFD) data.

Part of the work presented in this thesis has resulted in the following first-author publications:

- **Conference publications:**

- **N.C.A. Wilhelmsen**, F. Di Meglio. *An Observer for the Electrically Heated Vertical Rijke Tube with Nonlinear Heat Release*. IFAC-PapersOnLine, vol. 53, no. 2, pages 4181–4188, 2020.
- **N.C.A. Wilhelmsen**, F. Di Meglio. *Estimating Both Reflection Coefficients of 2×2 Linear Hyperbolic Systems with Single Boundary Measurement*. In 2020 59th IEEE Conference on Decision and Control (CDC), pages 658–665. IEEE, 2020.

- **Journal publication:**

- **N.C.A. Wilhelmsen**, F. Di Meglio. *Acoustic Boundary Output Feedback Stabilization of Dynamic $n - \tau$ Flame Model via Duct with Spatially Varying Cross Section*. IEEE Transactions on Automatic Control, 2021. Submitted.

It should also be noted that some of the work presented in this thesis is as of yet unpublished, and may warrant future publication.

1.4 Thesis structure

Part I This part presents the problem considered and states underlying assumptions. It lays the groundwork for the remainder of the thesis.

Chapter 1 In this chapter, which is the current one, background literature on the problem has been introduced. The approach taken and contributions are stated.

Chapter 2 This chapter is responsible for presenting the mathematical models the algorithm designs appearing in Part II & III are based on. Part of the content in this chapter appears in [Wilhelmsen & Di Meglio 2021].

Part II For this part of the thesis the Rijke tube, a laboratory setup, is considered. The state observation and boundary parameter identification problems are solved.

Chapter 3 In this chapter, a state observer for the Rijke tube is derived and analysed, before being tested in simulations and experimentally. Part of this chapter appears in [Wilhelmsen & Di Meglio 2020b].

Chapter 4 Here the acoustic boundary parameter identification problem is considered. A simple scheme for estimating both boundary parameters with a single pressure sensor is proposed, and afterwards tested in simulations and experimentally. Part of the material presented in this chapter appears in [Wilhelmsen & Di Meglio 2020a].

Part III The aim of this part is to move the study of estimation algorithms from a laboratory setup towards more complicated combustor dynamics.

Chapter 5 In this chapter, the boundary parameter identification scheme problem for general 2×2 linear hyperbolic PDEs is studied. A generalization of the estimation scheme from Chapter 4 to more complicated combustor acoustics is suggested. The main contribution from [Wilhelmsen & Di Meglio 2020a] is presented in this chapter, along with a minor unpublished result.

Chapter 6 This chapter derives an output feedback controller for a linearized model of a combustor with distributed acoustics. All of this chapter is based on content from from [Wilhelmsen & Di Meglio 2021].

Chapter 7 Here the state observer design for a combustor model with distributed acoustics but nonlinear flame model is considered. Using results from the literature, the state estimation problem is reduced to the problem of static function approximation, for which neural networks are employed. The nonlinear observer is verified on CFD data. All the novel material in this chapter is as of yet unpublished.

Part IV This last part suggests some conclusions, and houses the appendix and bibliography.

Chapter 8 In this chapter the progress made is summarized, and reflections are made. Some directions for further research are proposed.

Mathematical Modelling

Contents

2.1	Modelling principles	12
2.2	Heat release	13
2.2.1	Electrical heater	13
2.2.2	Flames	15
2.3	Acoustics	22
2.3.1	Duct with spatially varying cross section	22
2.3.2	Special cases	25
2.4	Boundary conditions	26
2.4.1	Acoustic impedance	26
2.4.2	Heat release–acoustics coupling	28
2.5	Summary of models	31
2.5.1	Rijke tube – Chapter 3	31
2.5.2	Acoustic duct for boundary parameter identification – Chapters 4–5	31
2.5.3	Can combustor – Chapters 6–7	32

Les modèles mathématiques qui constituent la base du reste de la thèse sont développés dans ce chapitre. Nous présentons d’abord l’approche générale de modélisation adoptée, sous forme d’interconnexions de modèles dans le domaine temporel. Cette approche considère le système thermoacoustique comme étant composé de multiples sous-systèmes avec des interfaces bien définies. Les modèles de dégagement de chaleur sont le premier type de sous-système à être couvert. Deux types sont considérés, à savoir le dégagement de chaleur d’un appareil de chauffage électrique et le dégagement de chaleur dû à la présence d’une flamme. Nous dérivons ensuite un modèle des phénomènes acoustiques. Nous proposons un modèle adapté à l’estimation et à la conception d’algorithmes de contrôle, décrivant les oscillations longitudinales dans un conduit à géométrie variable dans l’espace. Il est simplifié à deux cas particuliers, le premier étant pour un écoulement moyen nul et le second étant le modèle pour l’acoustique dans un conduit avec une section transversale constante. Le troisième type de sous-système, les impédances acoustiques, est ensuite considéré. Nous terminons ce chapitre par la

description du couplage entre le dégagement de chaleur et l'acoustique, avant de résumer les modèles de réseaux complets qui seront considérés tout au long de la thèse.

The mathematical models which form the basis for the rest of the thesis are developed in this chapter. It starts with introducing the general approach to modelling taken, which is a time domain network model approach. This approach considers the thermoacoustic system as consisting of multiple subsystems with well-defined interfaces. Heat release models are the first type of subsystem to be covered. Two types are considered, namely heat release from an electrical heater and heat release due to flames. We then derive a model of the acoustic phenomenon. We propose a model suitable for estimation and control algorithm design, describing longitudinal oscillations in a duct with spatially varying geometry. It is simplified to two special cases, the first one being for zero mean flow and the second special case being the model for acoustics in a duct with constant cross-sectional area. The third type of subsystem, acoustic impedances, are considered next. This is followed by the description of coupling between the heat release and acoustics, before the complete network models that will be considered throughout the thesis are summarized.

2.1 Modelling principles

In this thesis we are concerned with longitudinal thermoacoustic oscillations, using $1-D$ distributed models to describe the acoustics. Here, the acoustic modes along a privileged coordinate is described, with flow field fluctuations along the other spatial coordinates assumed constant or negligible for the analysis of modes along the axis of interest. Although this assumption is too simplistic to describe highly complex cases such as azimuthal modes mixing with longitudinal modes as one can in practice find in annular combustors [Pankiewicz & Sattelmayer 2003, Lieuwen & Yang 2005], studying the simpler cases is essential to understanding the more complex cases. To describe the heat release, $0-D$ models based on the assumption that the spatial extent of the heat source is negligible compared to the length scale of the acoustics inside the combustor are employed. This allows the heating element/flame to be considered an acoustically compact source [Lieuwen 2021], and its internal structure can be disregarded and instead an Input and Output (I/O) description used. With interfaces defined between the heat source and the acoustics, the complete system can be described as an interconnected model of acoustic elements. Such a modelling approach is referred to in the literature as *thermoacoustic network modelling* [Polifke & Gentemann 2004, Stow & Dowling 2009, Moeck 2010], and is the approach taken here. A schematic of the structure of a typical thermoacoustic network model is shown in Figure 2.1.

As described in [Emmert 2016], there are two main paradigms within network modelling of thermoacoustics. The more classical approach is to consider the frequency domain properties of the thermoacoustic instabilities, such as wave number and complex frequency of the oscillations. This approach lends itself well to com-

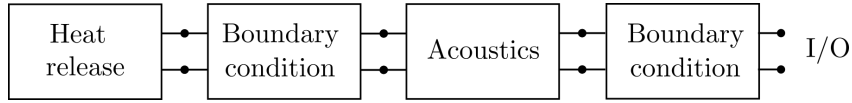


Figure 2.1: Example schematic of thermoacoustic network model.

putation of the eigenmodes of a given combustor setup to determine its intrinsic stability properties, and hence useful for passive stabilization approaches of thermoacoustic instabilities. Some contributions in the literature that apply this approach are [Dowling 1995, Schuermans *et al.* 2000]. On the other hand, rather than basing the analysis around specific wave numbers and frequencies of oscillation, a different approach is to simply describe the thermoacoustic instabilities by a set of mathematical models (typically state space representations) of the subsystems interconnected by well-defined interfaces, that physically represent the averaged acoustic quantity at the point of the interface. This approach lends itself well to time domain analysis, and is the approach taken here. Some other examples from the literature that employ this approach are [Schuermans *et al.* 2003, Bothien *et al.* 2007].

In the following sections, we introduce the mathematical models of the various subsystems that will be employed in the network models used in this thesis. First, in Section 2.2 heat release models that are considered are described. The first heat release model considered is that of an electrical heater, which is used in the work on the Rijke tube in Part II of this thesis. Flame models are instead considered in Part III of the thesis, and these are subsequently described. Next, in Section 2.3, the acoustics is modelled. These models are used throughout the thesis, and this section contains a generalization of $1 - D$ infinite dimensional acoustics models for the case when one has a duct with spatially varying geometry and non-zero mean flow. Then in Section 2.4 the model boundary conditions and interfaces are described, including descriptions of acoustic impedance and coupling between the acoustics and heat release. The final network models that are used throughout the thesis are summarized in Section 2.5.

2.2 Heat release

2.2.1 Electrical heater

Modelling of the electrical heater used in the Rijke tube considered in this thesis is based on work done originally by [King 1914] and [Lighthill 1954]. A description of the modelling process is given in [Epperlein *et al.* 2015], but it is included here for completeness and convenience for the reader. Consider an electrical heater made of a wire of length l_w and diameter d_w , in a laminar flow field, as depicted in Figure 2.2. We are interested in quantifying the power of heat release Q from the electrical heater into the flow field, which occurs due to convection and conduction processes. There are two main quantities affecting these processes, namely the local velocity V

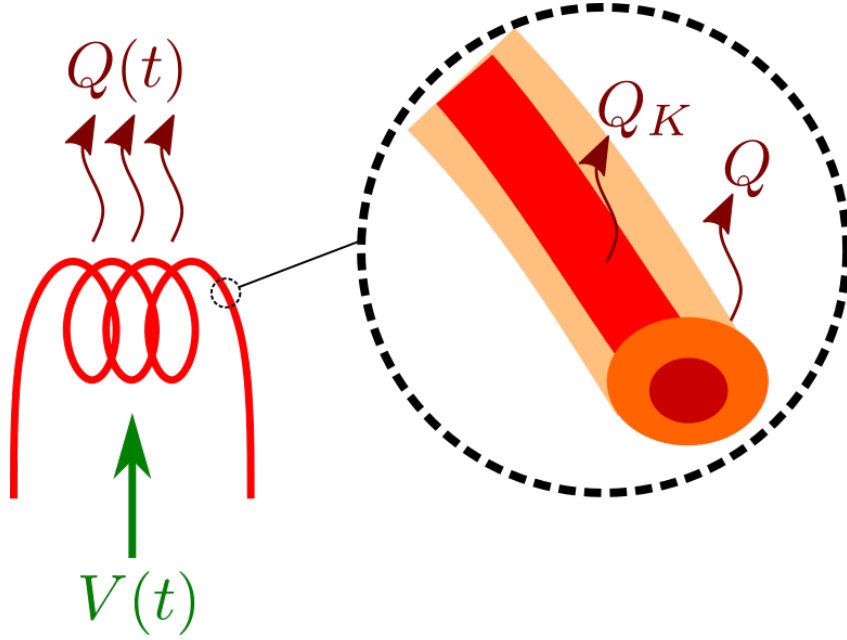


Figure 2.2: Heat release Q from electrical heater in laminar flow field of velocity V . Global view (left) and boundary layer around wire due to fluctuating velocity field (right).

of the flow field around the heater and the difference between the wire temperature T_w and the surrounding gas temperature T_g . We make the following assumptions:

Assumption 1. *The flow is laminar and equal throughout the cross section perpendicular to the direction of the flow.*

Assumption 2. *The steady-state flow states density $\bar{\rho}$, pressure \bar{P} , and velocity \bar{V} are constant in time.*

Assumption 3. *The wire temperature T_w and gas temperature T_g are described by constant scalars.*

King's law developed by [King 1914] gives an approximate algebraic relationship between heat release Q_K ¹ and the aforementioned quantities which reads

$$Q_K = l_w \left(\kappa + \kappa_v \sqrt{|\bar{V}|} \right) (T_w - T_g) \quad (2.1)$$

where κ represents thermal conductivity of the surrounding fluid, and κ_v is a proportionality constant that must be empirically determined.

The algebraic relationship (2.1) works well in describing the heat release when the flow field around the electrical heater is constant, but in thermoacoustic systems

¹Subscript K used here to denote heat release as predicted by King's law.

such as the Rijke tube the local velocity is changing rapidly, and hence additional dynamic effects must be taken into consideration. When the flow around the heater is fluctuating, a boundary layer is formed around the wire, as illustrated in Figure 2.2. Hence, the heat release from the wire predicted by (2.1) is not released directly into the flow field, but must pass through the boundary layer first. In [Lighthill 1954] it was found that these dynamics can be approximated by a first-order transfer function, relating the heat release Q_K directly from the wire as input and the resultant heat release Q released into the flow as output, given by

$$\frac{Q}{Q_K}(s) = \frac{1}{\tau s + 1} \quad (2.2)$$

where τ is a time constant computed as

$$\tau = \frac{d_w}{5\bar{V}},$$

the quantity \bar{V} appearing in the denominator denoting mean flow velocity. Combining then (2.1)–(2.2) and writing in the time domain, we have a scalar ODE describing the heat release rate Q from the electrical heater given by

$$\dot{Q}(t) = -\frac{1}{\tau}Q(t) + \frac{1}{\tau}l_w \left(\kappa + \kappa_v \sqrt{|V(t)|} \right) (T_w - T_g). \quad (2.3)$$

This model can be used as a subsystem in a thermoacoustic network model by considering the averaged (in space over the cross section perpendicular to the direction of flow) local velocity V as the input variable and heat release rate Q as output variable. It is used in Chapter 3 where we derive a state observer for a thermoacoustic model of the Rijke tube. Next in Section 2.2.2 we describe flame models which rely on the same I/O variables and can hence be easily integrated into thermoacoustic network models.

2.2.2 Flames

Mathematical modelling of flames and combustion processes is a rich and complex field, and going deep into this topic is outside the scope of this thesis. For the interested reader, in-depth sources covering the topic such as [Lieberman 2010, Lieuwen 2021, Poinsot & Veynante 2005, De Goey *et al.* 2011] can be consulted. Rather, we are interested in obtaining an external description of the flame and its interaction with the flow field.

Flames are the result of combustion, which in essence is an exothermic chemical reaction between a fuel and an oxidizer. The flames we consider are assumed to have sufficiently low speeds to be so-called *deflagrations*, rather than *detonations* which occur at much higher speeds [Poinsot & Veynante 2005, Oran & Boris 2005]. Within the scope of this work we are mainly interested in flames that can be considered *premixed* and *laminar*. That is to say the fuel and oxidizer are mixed before arriving at the flame, rather than introduced separately which is the case for

diffusion flames, and the flow field around the flame is laminar rather than *turbulent*. This assumption is not as restrictive as it might seem from first glance, for two main reasons. Firstly, in practice the issue of thermoacoustic instabilities often occurs within lean premixed combustors [Seo 2003], and hence using premixed flame models makes sense from a practical perspective. Secondly, as noted in [Poinsot & Veynante 2005], many models of turbulent flames, such as flamelet theory [Williams 1975], use smaller laminar flame models as their building blocks.

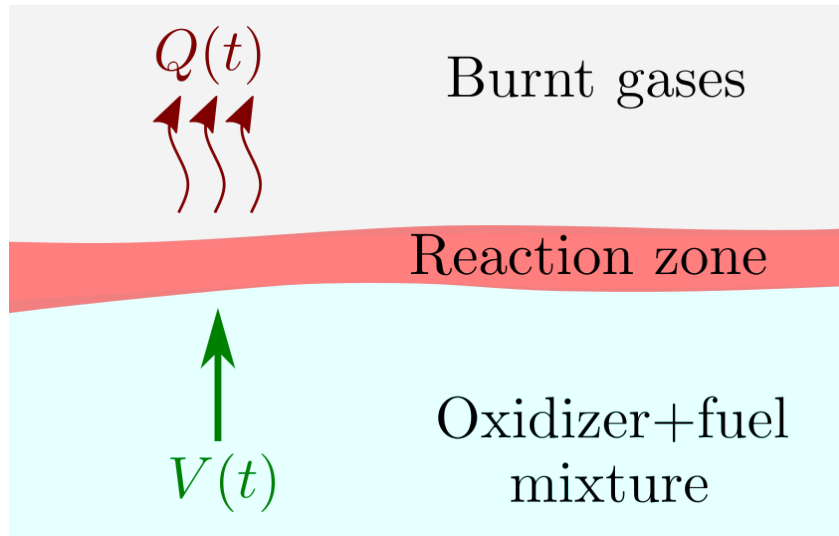


Figure 2.3: Heat release Q from exothermic reduction-oxidation reaction in laminar flow field of velocity V .

Consider the scenario depicted in Figure 2.3. We have a laminar flow of unburned gas consisting of a mix of fuel and oxidizer flowing into a reaction zone (flame). Within the flame, a series of exothermic reduction-oxidation reactions occur, releasing heat into the flow and a mix of burned gases at the downstream boundary of the reaction zone. Note that the flame is travelling into the unburned gases with laminar burning velocity V_l , being stabilized by the flow field moving in the opposite direction with similar velocity.

Depending on the particular fuel and oxidizer used and the conditions under which the reaction occurs, in practice a high number of different chemical reactions with varying rates of reaction, possibly involving multiple reaction steps, can occur. However, for the purpose of this work we consider the chemistry to occur in a single-step irreversible reaction, represented by the general chemical formula



where F , O and P are placeholders for chemical formulas of the fuel, oxidizer and product respectively, and n_F , n_O denote the relative quantities of fuel and oxidizer in the reaction. Some examples of combustion reactions represented by the gen-

n_F	F	n_O	O	P
2	C_3H_8	7	O_2	$6CO_2 + 8H_2O$
2	CH_3OH	3	O_2	$2CO_2 + 4H_2O$
1	H_2	1	Cl_2	$2HCl$

Table 2.1: Examples of combustion reaction species fitting together in the formula (2.4).

eral formula (2.4) are listed in Table 2.1. An important metric to characterize the combustion process is the *equivalence ratio* ϕ , defined by

$$\phi := \varpi \frac{\dot{m}_F}{\dot{m}_O} \quad (2.5)$$

where \dot{m}_F and \dot{m}_O are respectively the mass flow rates of fuel and oxidizer, and the mass stoichiometric ratio ϖ is defined by

$$\varpi := \frac{n_O W_O}{n_F W_F} \quad (2.6)$$

with W_F , W_O being the molar masses of fuel and oxidizer, respectively. The combustion process is said to be *lean* if $\phi < 1$, *rich* if $\phi > 1$ and *at stoichiometry* if $\phi = 1$. As mentioned previously, the main focus within this work is on lean combustion, where there is an excess of oxidizer in the flow. It is in this case reasonable to assume that the gas upstream and downstream of the reaction zone have similar physical properties, such as density and adiabatic constant.

The thickness of the reaction zone separating the unburned and burned gas regions in Figure 2.3 is assumed to be small in relation to the wavelength of the acoustics considered. One can hence apply the so-called thin flame limit and consider the flame to be an infinitesimally thin sheet separating the two regions of the flow [Lieuwen & Yang 2005] via a jump condition in the flow field. The location of this infinitesimally thin region, referred to as the *flame front*, in the flow as a function of radial position from the centre of a burner is depicted in Figure 2.4 for the case of a conical flame. Based on the velocity V the dynamics of the flame front can be described by the G-equation [Williams 1985]

$$\frac{\partial G}{\partial t} + V(t) \frac{\partial G}{\partial z} = -V_l \sqrt{\left(\frac{\partial G}{\partial z}\right)^2 + \left(\frac{\partial G}{\partial r}\right)^2} \quad (2.7)$$

where the level set $G(z, r, t) = 0$ represents the flame front and the flame speed V_l is assumed constant. The flame height h_F and tip angle α_F are calculated from the steady-state solution to (2.7), by setting $V(t) \equiv \bar{V}$ and $\frac{\partial G}{\partial t} = 0$. As can be seen, perturbations in the local velocity vector V affects the local displacement of the flame front, something which can be observed experimentally as shown by the Schlieren images in Figure 2.5. This in turn impacts the total area A_F of the flame

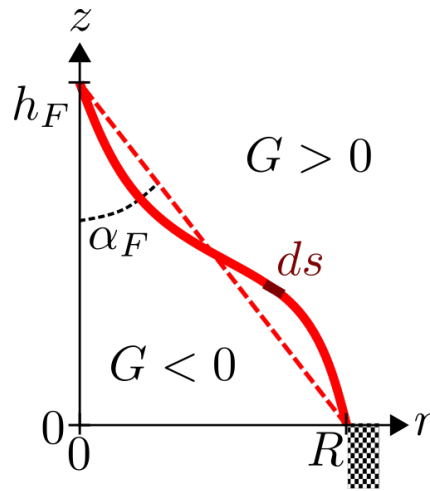


Figure 2.4: Location of conical flame front along vertical z direction as function of radius r , stabilized to edge of burner of radius R . Steady state position (dashed red line) and perturbed position (solid red line).

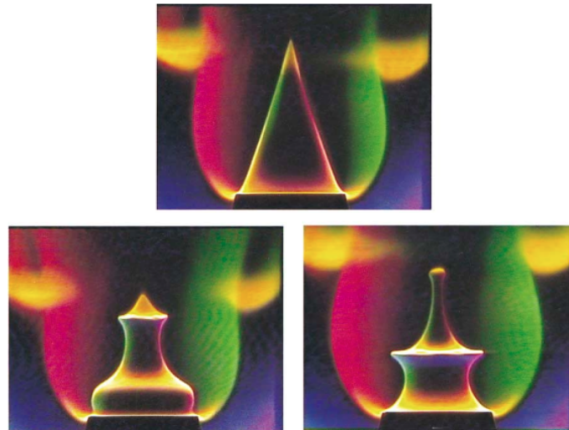


Figure 2.5: Schlieren images from [Ducruix *et al.* 2000] of a premixed conical flame under steady state conditions (top image) and velocity perturbations (bottom images).

front at any given point in time, given by

$$A_F = \int_0^R 2\pi r \frac{ds}{dr} dr, \quad (2.8)$$

where ds is an infinitesimal displacement along the flame surface (see Figure 2.4). Assuming a homogenous equivalence ratio throughout the incoming premixed gas, the heat release rate fluctuations \check{Q} are related to the displacements in flame surface area $\check{A}_F = A_F - \bar{A}_F$, \bar{A}_F being the steady-state flame area, given by [Ducruix *et al.* 2000]

$$\check{Q} = \rho V_l \Delta q \check{A}_F. \quad (2.9)$$

where ρ is the density of the gas and Δq is the heat release per unit mass (caloric value) of the premixed gas. So far, in addition to Assumptions 1, 2, we have introduced the following Assumptions in the preceding discussion:

Assumption 4. *The fuel and oxidizer enter the reaction zone premixed.*

Assumption 5. *The combustion is lean so the equivalence ratio, assumed to be constant, satisfies $\phi < 1$. Hence the physical properties of the gas are similar before and after the reaction zone.*

Assumption 6. *The combustion reaction can be approximated by a single-step chemical reaction of the form (2.4).*

Assumption 7. *The spatial extent of the reaction zone is considered small compared to the acoustic wavelength, so it can be considered an infinitesimally thin discontinuity.*

Assumption 8. *The flame sheet is a deflagration and hence moves into the unburned gases at a constant velocity V_l of comparable magnitude to the local steady-state flow velocity \bar{V} .*

Although the formulation (2.7)–(2.9) of variation of the heat release rate due to fluctuations in the incoming flow velocity paints an intuitive picture of the process, it is rather complex and nontrivial to apply it directly for analysis of thermoacoustics from a global perspective. Indeed, computing the heat release involves integrating a path (2.8) along a level set of the solution to a nonlinear PDE (2.7), which may be both computationally expensive and inconvenient for analysis. A more practical alternative is to heuristically describe the I/O characteristics of the flame, which under Assumptions 1, 2, 4–8 can be achieved via the Flame Transfer Function (FTF) [Schuller *et al.* 2003] (or for nonlinear frequency domain analysis the Flame Describing Function (FDF) [Noiray *et al.* 2008]) formulation. Conventionally, the FTF \mathcal{F} is defined as the ratio of the normalized heat release rate fluctuations \check{Q}/\bar{Q} to the normalized velocity fluctuations \check{V}/\bar{V} at each frequency $\omega > 0$, i.e.

$$\mathcal{F}(j\omega) := \frac{\check{Q}(\omega)\bar{V}}{\check{V}(\omega)\bar{Q}}. \quad (2.10)$$

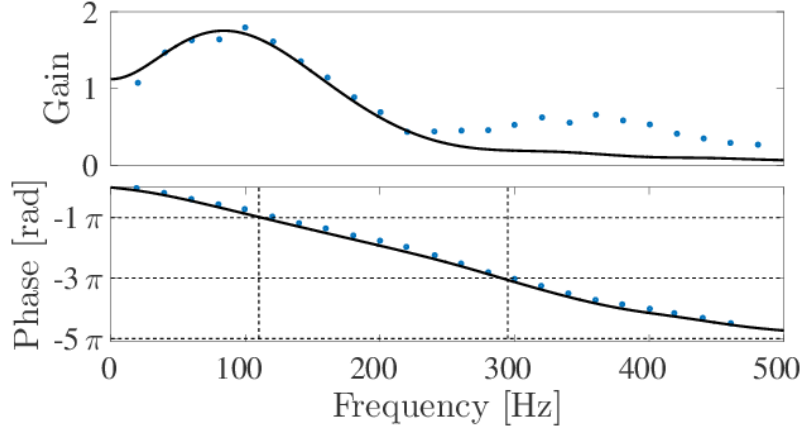


Figure 2.6: Gain and phase data of FTF from [Silva *et al.* 2017]. Prediction from simulations (solid line) and data collected from experiments (individual points).

Being complex functions, FTFs are typically represented by their gain and phase data, an example from [Silva *et al.* 2017] shown in Figure 2.6.

One of the earliest and simplest FTFs to be established and used in practice is the $n - \tau$ model [Crocco & Cheng 1956], a phenomenological model initially developed from research on combustion instabilities in liquid fuel rockets, and later shown to be useful in modelling thermoacoustic instabilities in other combustion systems [Lieuwen & Yang 2005], such as lean premixed combustors. It describes the flame based on two parameters, the interaction index n and a time delay τ . Using the Laplace variable $s := \sigma + j\omega$ we have

$$\mathcal{F}(s) = ne^{-\tau s}. \quad (2.11)$$

Assigning the output $Y := \check{Q}/\bar{Q}$ and input $U := \check{V}/\bar{V}$, in the time-domain the $n - \tau$ model (2.11) gives the algebraic relation

$$Y(t) = nU(t - \tau). \quad (2.12)$$

In practice it has been shown that in addition to the time delay, lean premixed flames exhibit low-pass filter behaviour [Blackshear 1952, Merk 1957, Ducruix *et al.* 2000]. It is well known from linear systems theory that low pass filters can be described by strictly proper rational transfer functions [Zumbahlen 2007], and only taking into account this aspect of the flame behaviour one has a flame transfer function of the form

$$\mathcal{F}(s) = \frac{N(s)}{D(s)} \quad (2.13)$$

where N, D are polynomials in s , where $\deg(N) < \deg(D)$.

Similar to what is done in [Freitag 2009, Cuquel 2013], we consider an FTF that combines the effects of an input time delay as described by (2.11) and low-pass filter

behaviour as described by (2.13). We propose a flame transfer function of the form

$$\mathcal{F}(s) = \frac{N_1(s) + N_2(s)e^{-\tau s}}{D(s)} \quad (2.14)$$

which is obtained by multiplying a transfer function of the form (2.13) with a transfer function of the form (2.11), and adding a polynomial term $N_1(s)$ to the numerator to account for possible instantaneous low-pass filtering effects. An example from the literature of an FTF, also for a conical flame, fitting the form (2.14) is found in [Sugimoto & Matsui 1982] by measuring fluctuations in CH^* radicals. It is reproduced here as

$$\mathcal{F}(s) = 2 \frac{-1 + (s - \beta)\tau + e^{-(s-\beta)\tau}}{(s - \beta)^2 \tau^2}$$

where expressions for the parameters β and τ are given by

$$\beta = \alpha V_i, \quad \tau = \frac{h_F}{V_i}$$

where V_i is the (assumed constant) propagation velocity of CH^* radicals, α is a constant describing the distribution of CH^* radicals emitted along the flame front, and h_F is the flame height.

Recall that for strictly proper rational transfer functions $\frac{N_1(s)}{D(s)}$, $\frac{N_2(s)}{D(s)}$ there exists $(A_1, b_1, C_1) \in \mathbb{R}^{n_1 \times n_1} \times \mathbb{R}^{n_1 \times 1} \times \mathbb{R}^{1 \times n_1}$, $(A_2, b_2, C_2) \in \mathbb{R}^{n_2 \times n_2} \times \mathbb{R}^{n_2 \times 1} \times \mathbb{R}^{1 \times n_2}$, respectively, such that

$$\frac{N_1(s)}{D(s)} = C_1(sI - A_1)^{-1}b_1, \quad \frac{N_2(s)}{D(s)} = C_2(sI - A_2)^{-1}b_2. \quad (2.15)$$

We then obtain a state-space realization of (2.14) with state $X \in \mathbb{R}^n$, $n := n_1 + n_2$, as

$$\dot{X}(t) = AX(t) + \bar{B}_0 \check{V}(t) + \bar{B}_1 \check{V}(t - \tau) \quad (2.16a)$$

$$Y(t) = \frac{1}{V} \bar{C} X(t) \quad (2.16b)$$

where

$$A := \begin{bmatrix} A_1 & 0_{n_1 \times n_2} \\ 0_{n_2 \times n_1} & A_2 \end{bmatrix}$$

$$\bar{B}_0 := \begin{bmatrix} b_1 \\ 0_{n_2 \times 1} \end{bmatrix}, \quad \bar{B}_1 := \begin{bmatrix} 0_{n_1 \times 1} \\ b_2 \end{bmatrix}$$

$$\bar{C} := [C_1 \quad C_2].$$

The formulation (2.14) and its equivalent time-domain representation (2.16) can both be used as *linear* representations of premixed flame dynamics, as we do in Chapter 6. In reality flames can have strong nonlinearities that can be important to take into account for thermoacoustic analysis. As noted in [Lieuwen 2005], nonlinearities are more pronounced at conditions such as higher perturbation frequencies

and shorter flame lengths. Using an FDF, which describes the response not only as a function of the velocity perturbation frequency but also the forcing amplitude, is one method of capturing nonlinearities in the frequency domain. In Chapter 7, we take an alternative approach and propose to use a nonlinear time domain generalization of (2.16) in the form of an input-affine nonlinear state space model to capture the nonlinearity of the flame response. This gives a generic model of the form

$$\dot{X}(t) = f(X(t)) + \bar{g}_0(X(t))\check{V}(t) + \bar{g}_1(X(t))\check{V}(t - \tau) \quad (2.17a)$$

$$Y(t) = \frac{1}{\bar{V}}\bar{h}(X(t)) \quad (2.17b)$$

where the functions $f(\cdot)$, $\bar{g}_0(\cdot)$, $\bar{g}_1(\cdot)$, $\bar{h}(\cdot)$ can e.g. be fitted using nonlinear regression software, based on I/O data of flame response from simulations or experiments.

This concludes the heat release and flame modelling. Next in Section 2.3, modelling of the acoustics is covered, before they are coupled with the heat release models in Section 2.4.

2.3 Acoustics

We first derive the model of acoustic fluctuations in a duct with spatially varying cross-sectional area and a non-zero steady-state velocity with low Mach number. This is subsequently simplified to the special cases of zero velocity in a duct with spatially varying cross section, and duct with constant cross-sectional area and arbitrary low Mach number steady-state velocity

2.3.1 Duct with spatially varying cross section

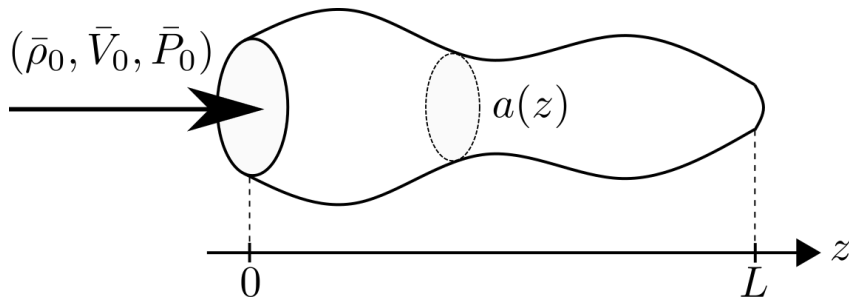


Figure 2.7: Duct of length L with spatially varying cross-sectional area $a(z)$ for $z \in [0, L]$.

Consider the setup shown in Figure 2.7. It consists of a duct of length L , with spatially varying cross-sectional area $a(z)$ for $z \in [0, L]$, through which a gas is flowing with mean inlet density $\bar{\rho}_0$, velocity \bar{V}_0 and pressure \bar{P}_0 . In addition to Assumptions 1, 2, we assume the following:

Assumption 9. *The steady state velocity $\bar{V} \ll c$, with c being the speed of sound, for $z \in [0, L]$ so that the Mach number $Ma \ll 1$.*

Assumption 10. *The duct geometry can be approximated by a solid of revolution around the z -axis for $z \in [0, L]$.*

Assumption 11. *Internal damping contributions from the duct wall material can be neglected.*

To obtain a mathematical model for the acoustics, we start with the mass, momentum and energy equations of gas dynamics. They can respectively be written [Bale 2002] in 1 – D for the scenario shown in Figure 2.7 as the system

$$\partial_t (a(z)\rho(z, t)) = -\partial_z (a(z)\rho(z, t)V(z, t)) \quad (2.18a)$$

$$\partial_t (a(z)\rho(z, t)V(z, t)) = -\partial_z (a(z) (P(z, t) + \rho(z, t)V^2(z, t))) + a'(z)P(z, t) \quad (2.18b)$$

$$\partial_t (a(z)e(z, t)) = -\partial_z (a(z) (e(z, t) + P(z, t))V(z, t)) + Q(z, t) \quad (2.18c)$$

giving a description of the density ρ , velocity V , pressure P and pointwise energy e at each spatial coordinate $z \in [0, L]$ and point in time $t \geq 0$. It is initialized from

$$\rho(z, 0) = \rho_0(z), \quad V(z, 0) = V_0(z), \quad P(z, 0) = P_0(z), \quad e(z, 0) = e_0(z)$$

where $\rho_0, V_0, P_0, e_0 \in L^2(0, L)$, with possible distributed heat release rate Q as a source term in (2.18c). We assume the total energy e is composed of potential and kinetic energy, so that

$$\underbrace{e(z, t)}_{\text{Total energy}} = \underbrace{\rho(z, t)U(z, t)}_{\text{Potential energy}} + \underbrace{\frac{1}{2}\rho(z, t)V^2(z, t)}_{\text{Kinetic energy}} \quad (2.19)$$

with U being specific internal energy. Assuming that the air satisfies the ideal gas law, the specific internal energy U can be related to pressure P and density ρ via [Epperlein *et al.* 2015]

$$U(z, t) = \frac{C_v}{R} \frac{P(z, t)}{\rho(z, t)} \quad (2.20)$$

where C_v is the specific heat capacity of the gas at constant volume, and R the universal gas constant. Substituting (2.19)–(2.20) into (2.18), after some algebraic manipulation, we have the nonlinear PDE system in (ρ, V, P) written as

$$\rho_t(z, t) = -V(z, t)\rho_z(z, t) - \rho(z, t)V_z(z, t) - \frac{a'(z)}{a(z)}\rho(z, t)V(z, t) \quad (2.21a)$$

$$V_t(z, t) = -\frac{1}{\rho(z, t)}P_z(z, t) - V(z, t)V_z(z, t) \quad (2.21b)$$

$$P_t(z, t) = -\gamma P(z, t)V_z(z, t) - V(z, t)P_z(z, t) - \gamma \frac{a'(z)}{a(z)}P(z, t)V(z, t) + \frac{\bar{\gamma}}{a(z)}Q(z, t) \quad (2.21c)$$

where γ is the adiabatic constant, defined in terms of R and C_v as

$$\gamma := 1 + \frac{R}{C_v} \quad (2.22)$$

and $\bar{\gamma} := \gamma - 1$.

With constant inlet conditions in Figure 2.7 thanks to Assumption 2, the acoustics are considered “small” perturbations around an equilibrium flow profile of (2.21). This requires to assume the following:

Assumption 12. *Temporal variations in the density, velocity and pressure can be approximated sufficiently well by first-order perturbations around the mean flow.*

As will be discussed further down in Section 2.4, we consider only pointwise interaction of the heat release rate with acoustic field, and hence the heat release rate is disregarded for the equilibrium profile calculation. Setting the temporal derivative on the left-hand side of (2.21) equal to zero and rearranging, the steady state is found to satisfy the Initial Value Problem (IVP)

$$\frac{d}{dz} \begin{bmatrix} \bar{\rho}(z) \\ \bar{V}(z) \\ \bar{P}(z) \end{bmatrix} = \frac{a'(z)}{a(z)} \frac{1}{\bar{\rho}(z)\bar{V}^2(z) - \gamma\bar{P}(z)} \begin{bmatrix} -\bar{\rho}^2(z)\bar{V}^2(z) \\ \gamma\bar{P}(z)\bar{V}(z) \\ -\gamma\bar{P}(z)\bar{\rho}(z)\bar{V}^2(z) \end{bmatrix} \quad (2.23a)$$

$$\begin{bmatrix} \bar{\rho}(0) \\ \bar{V}(0) \\ \bar{P}(0) \end{bmatrix} = \begin{bmatrix} \bar{\rho}_0 \\ \bar{V}_0 \\ \bar{P}_0 \end{bmatrix} \quad (2.23b)$$

for $z \in (0, L)$.

Using Assumption 12, we introduce now perturbations $\check{\rho}$, \check{V} , \check{P} around the mean values solved from the IVP (2.23), so we decompose

$$\rho(z, t) = \bar{\rho}(z) + \check{\rho}(z, t), \quad (2.24a)$$

$$V(z, t) = \bar{V}(z) + \check{V}(z, t), \quad (2.24b)$$

$$P(z, t) = \bar{P}(z) + \check{P}(z, t). \quad (2.24c)$$

Substituting (2.24) into (2.21) and neglecting higher order and affine terms, we end up with

$$\begin{aligned} \begin{bmatrix} \check{\rho}_t(z, t) \\ \check{V}_t(z, t) \\ \check{P}_t(z, t) \end{bmatrix} &= \begin{bmatrix} -\bar{V}(z) & \bar{\rho}(z) & 0 \\ 0 & -\bar{V}(z) & -\frac{1}{\bar{\rho}(z)} \\ 0 & -\gamma\bar{P}(z) & \bar{V}(z) \end{bmatrix} \begin{bmatrix} \check{\rho}_z(z, t) \\ \check{V}_z(z, t) \\ \check{P}_z(z, t) \end{bmatrix} + \begin{bmatrix} 0 \\ 0 \\ \frac{\bar{\gamma}}{a(z)} \end{bmatrix} \check{Q}(z, t) \\ &+ \begin{bmatrix} -l_1(\bar{V}(z)) & -l_1(\bar{\rho}(z)) & 0 \\ 0 & -\bar{V}'(z) & 0 \\ 0 & -l_\gamma(\bar{P}(z)) & -\gamma l_1(\bar{V}(z)) \end{bmatrix} \begin{bmatrix} \check{\rho}(z, t) \\ \check{V}(z, t) \\ \check{P}(z, t) \end{bmatrix} \end{aligned} \quad (2.25)$$

where possible heat release rate fluctuations $\check{Q} = Q - \bar{Q}$ appear as an external source term. The term $l_\kappa(f)$ is defined

$$l_\kappa(f(\cdot)) := f'(\cdot) + \kappa \frac{a'(\cdot)}{a(\cdot)} f(\cdot) \quad (2.26)$$

for constant $\kappa \in \mathbb{R}$ and function $f \in C^1(0, L)$. Next, similar to what is done for acoustics in a duct with constant cross-sectional area considered in e.g. [Epperlein *et al.* 2015], dimensional analysis shows that for low Mach number flow (Assumption 9) we can approximate $\bar{V} \approx 0$ in relation to the other steady state quantities and decouple the expressions for \check{V} , \check{P} from the expression for $\check{\rho}$. This gives a simplified linear acoustic PDE system in (\check{V}, \check{P}) which reads

$$\check{V}_t(z, t) = -\frac{1}{\bar{\rho}(z)} \check{P}_z(z, t) - \bar{V}'(z) \check{V}(z, t) \quad (2.27a)$$

$$\begin{aligned} \check{P}_t(z, t) = & -\gamma \bar{P}(z) \check{V}_z(z, t) - \left(\bar{P}'(z) + \gamma \frac{a'(z)}{a(z)} \bar{P}(z) \right) \check{V}(z, t) \\ & - \gamma \bar{V}'(z) \check{P}(z, t) + \frac{\bar{\gamma}}{a(z)} \check{Q}(z, t). \end{aligned} \quad (2.27b)$$

2.3.2 Special cases

We present here two scenarios for which the acoustic equations (2.27) can be written in a simpler form. First in Section 2.3.2.1 we consider the case when there is zero mean flow at the inlet of the duct. Secondly, we show how (2.27) simplifies to the constant cross-sectional area case in Section 2.3.2.2.

2.3.2.1 Special case I : Duct with zero mean flow

We let here $\bar{V}_0 = 0$ in the IVP (2.23). It can in this case be shown by direct substitution that the solution satisfies

$$\bar{\rho}(z) \equiv \bar{\rho}_0, \quad \bar{V}(z) \equiv 0, \quad \bar{P}(z) \equiv \bar{P}_0.$$

Substituting these steady-state solutions into (2.27) gives us the simplified acoustics equations

$$\check{V}_t(z, t) = -\frac{1}{\bar{\rho}} \check{P}_z(z, t) \quad (2.28a)$$

$$\check{P}_t(z, t) = -\gamma \bar{P} \check{V}_z(z, t) - \gamma \frac{a'(z)}{a(z)} \bar{P} \check{V}(z, t) + \frac{\bar{\gamma}}{a(z)} \check{Q}(z, t) \quad (2.28b)$$

This model is used in Chapter 5.

2.3.2.2 Special case II : Duct with constant cross-sectional area

We let here the cross-sectional area $a(z) \equiv a_0$ be constant. Firstly, this implies $a'(z) \equiv 0$, and substituting into (2.23) we obtain the constant solution

$$\bar{\rho}(z) \equiv \bar{\rho}_0, \quad \bar{V}(z) \equiv \bar{V}_0, \quad \bar{P}(z) \equiv \bar{P}_0$$

for the equilibrium profile. We then have that the acoustics are described by

$$\check{V}_t(z, t) = -\frac{1}{\check{\rho}} \check{P}_z(z, t) \quad (2.29a)$$

$$\check{P}_t(z, t) = -\gamma \bar{P} \check{V}_z(z, t) + \frac{\bar{\gamma}}{a} \check{Q}(z, t) \quad (2.29b)$$

This model is used in Chapters 3–4.

We consider next in Section 2.4 boundary conditions for the acoustics (2.27)–(2.29) and coupling between the heat release and acoustic field.

2.4 Boundary conditions

Boundary conditions for the thermoacoustic models considered in this thesis are discussed here. First, the modelling of acoustic impedance is presented in Section 2.4.1. This is followed by coupling between flame and acoustics, which is considered in Section 2.4.2.

2.4.1 Acoustic impedance

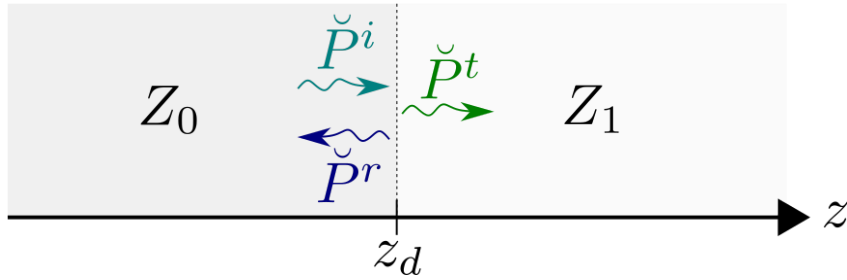


Figure 2.8: Incident pressure wave \check{P}^i being decomposed into reflected \check{P}^r and transmitted \check{P}^t waves at surface at surface of discontinuity between region of characteristic impedance Z_0 (left) and Z_1 (right).

To introduce the concept of acoustic impedance, consider the scenario presented in Figure 2.8. It shows an incident acoustic wave \check{P}^i propagating perpendicularly towards a surface of discontinuity separating two different media at $z = z_d$, with respectively constant density ρ_0, ρ_1 and speed of sound c_0, c_1 . Due to the surface of discontinuity, the incident wave is split into two components - a transmitted wave \check{P}^t , which continues in the same direction of travel as \check{P}^i , and a reflected

wave \check{P}^r which propagates in the opposite direction. As shown in [Kim 2010], the magnitude of the reflected and transmitted waves are computed via the reflection d_r and transmission d_t coefficients respectively, defined as

$$d_r := \frac{Z_1 - Z_0}{Z_1 + Z_0} \quad (2.30a)$$

$$d_t := \frac{2Z_1}{Z_1 + Z_0} \quad (2.30b)$$

where Z_i denotes the characteristic impedance of medium $i \in \{0, 1\}$, computed as the product of density and speed of sound

$$Z_i = \rho_i c_i. \quad (2.31)$$

At any point z in an acoustic field the local pressure and velocity are related via the impedance Z through the relation

$$\check{P}(z, t) = Z\check{V}(z, t) \quad (2.32)$$

This gives a basis for modelling the boundary conditions of the acoustics equations described in Section 2.3. When modelling the duct termination via a scalar

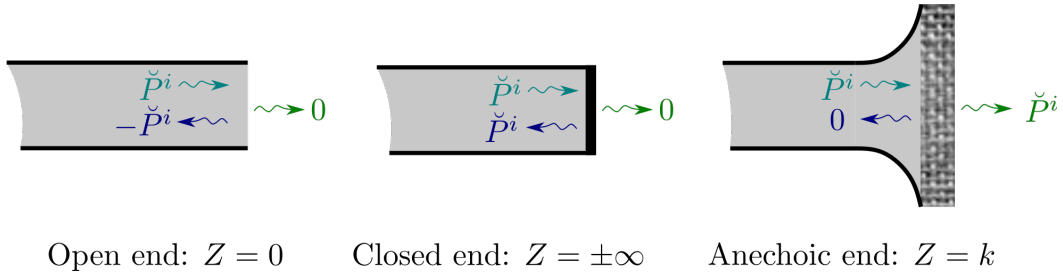


Figure 2.9: Theoretical ideal cases for duct termination impedance. Open end (left), closed end (middle) and anechoic end (right).

impedance as (2.32), there are three important theoretical edge cases to consider as shown in Figure 2.9. The first is an ideal open end, where the impedance $Z = 0$. Applying (2.30a) with $Z_1 = Z$ and $Z_0 = k$, k being the characteristic impedance of the gas inside the duct, one obtains a reflection coefficient $d_r = -1$ for the case of an ideal open end. The second edge case is that of an ideal closed end, where the impedance $Z = \pm\infty$, and thus the reflection coefficient $d_r = 1$. Finally, we have the case of an ideal anechoic end, which has an impedance of $Z = k$ and hence reflection coefficient $d_r = 0$.

In practice the impedance typically falls somewhere between these edge cases, as there will always be a certain amount of damping present causing acoustic waves to neither perfectly transmit nor perfectly reflect. Knowing the exact value of the acoustic impedance at the terminations of a given duct is often difficult to know a

priori or compute analytically in practice. As a representation of the duct terminations, we use the boundary conditions

$$\check{P}(L, t) = Z_L \check{V}(L, t) + W_L(t) \quad (2.33a)$$

$$\check{P}(0, t) = Z_0 \check{V}(0, t) + W_0(t). \quad (2.33b)$$

One should note that in the general case acoustic impedance is simply the ratio between velocity and pressure at any given position z and time t , so that

$$Z(z, t) := \frac{\check{P}(z, t)}{\check{V}(z, t)}, \quad (2.34)$$

and hence it depends on both the media of propagation and the acoustic field. The special case of *locally reacting* linear surfaces [Rienstra & Hirschberg 2004] models the acoustic impedance as a general linear system, with input being velocity perturbations and output being pressure perturbations. This description is common to use in frequency domain analysis of acoustics as the impedance can be modelled as a complex function of frequency $Z = Z(\omega)$, where the real component is the *resistive* part and the imaginary component the *reactive* part. In the time domain, the relation between pressure and velocity within this description would hence be a convolution

$$\check{P}(t) = \int_0^t Z(t - \tau) \check{V}(\tau) d\tau, \quad (2.35)$$

which can be inconvenient to use directly in time domain analysis if no further assumptions about the structure of Z are taken. Hence the boundary conditions (2.33), although being a simplification that models the impedance as only having a constant, resistive component, is convenient to use for algorithm design and serves as a sufficiently good approximation in many practical scenarios. Hence, using boundary conditions of the form (2.33) relies on the following Assumption:

Assumption 13. *The boundary acoustic impedances can be approximated by scalar constants.*

2.4.2 Heat release–acoustics coupling

2.4.2.1 Electrical heater

As done in e.g. [Epperlein *et al.* 2015, de Andrade *et al.* 2018b], we assume the electrical heater is considered a point source inside the acoustic domain at fixed position $z_0 \in (0, L)$. This yields the following Assumption, analogous to Assumption 7 for the flame models:

Assumption 14. *The spatial extent of the electrical heater is small compared to the acoustic wavelength, and can hence be modelled by a point source in the flow.*

To model this, the Dirac delta function δ is used giving rise to the representation

$$\check{Q}(z, t) = \delta(z - z_0)\check{Q}(t) \quad (2.36)$$

that will be used for the heat release source term in (2.29b) when modelling the Rijke tube, with the heat release rate fluctuations $\check{Q} = Q - \bar{Q}$ coming from (2.3).

2.4.2.2 Flame models

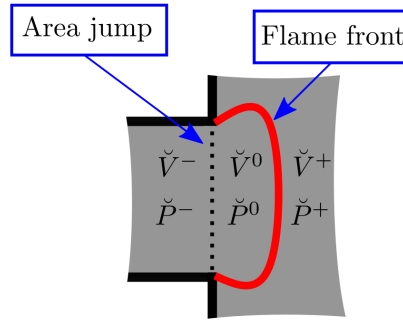


Figure 2.10: Jump condition around flame.

For the combustor models considered, we assume the flame is located at the base of the combustion chamber, namely at $z = 0$. We make the following assumption for the boundary condition upstream ($z < 0$) of the flame:

Assumption 15. *There is a non-reflective boundary condition upstream of the flame.*

The jump condition around the flame can be considered to be composed of three regions (see Figure 2.10): the region directly upstream of the area expansion where the premixed fuel-air mixture is entering, the region of unburned gases directly downstream of the area expansion but upstream of the flame front, and the region of burnt gases directly downstream of the flame front. We denote respectively the pressure and velocity in these three regions around $z = 0$ as $(\check{P}^-, \check{V}^-)$, $(\check{P}^0, \check{V}^0)$ and $(\check{P}^+, \check{V}^+)$.

As suggested in [Gentemann *et al.* 2003], the pressure and velocity fluctuations \check{P}^0, \check{V}^0 are assumed to be in the linear regime related to their respective upstream counterparts \check{P}^-, \check{V}^- via the relation

$$\check{P}^0(0, t) = \check{P}^-(0, t) + \left(1 - \zeta - \left(\frac{A_u}{A_d}\right)^2\right) M_u \bar{k} \check{V}^-(0, t) \quad (2.37a)$$

$$\bar{k} \check{V}^0(0, t) = -M_d \check{P}^-(0, t) + \frac{A_u}{A_d} \bar{k} \check{V}^-(0, t) \quad (2.37b)$$

where ζ is the pressure loss coefficient across the area expansion, A_u, A_d are respectively the area directly upstream and downstream of the area expansion, M_u, M_d are the flow Mach numbers directly upstream and downstream of the area expansion and \bar{k} is the mean characteristic impedance of the unburned gas.

With Assumption 9 we have $M_u, M_d \ll 1$, so we set $M_u \approx 0, M_d \approx 0$ and the terms involving these are neglected, yielding

$$\check{P}^0(0, t) \approx \check{P}^-(0, t) \quad (2.38a)$$

$$\check{V}^0(0, t) \approx \frac{A_u}{A_d} \check{V}^-(0, t). \quad (2.38b)$$

After the jump condition involving the area expansion, there is another jump condition as the flow passes through the flame. This condition is in [Polifke 2015] derived from the Rankine-Hugoniot equations, and in the linear regime can be written as

$$\check{P}^+(0, t) = \check{P}^0(0, t) - \theta M_d \bar{k} \check{V}^0(0, t) - \bar{k} \bar{V}(0) \theta M_d \frac{\check{Q}(t)}{Q} \quad (2.39a)$$

$$\bar{k} \check{V}^+(0, t) = \bar{k} \check{V}^0(0, t) + \bar{k} \bar{V}_0 \theta \frac{\check{Q}(t)}{Q} - \theta M_d \gamma \check{P}^0(0, t) \quad (2.39b)$$

where θ is defined as

$$\theta := \frac{T_h}{T_c} - 1 \quad (2.40)$$

with T_c, T_h being respectively the absolute temperatures at the cold (upstream) and hot (downstream) sides of the flame, and \bar{V}_0 is the mean velocity at $z = 0$. Neglecting again the terms involving the Mach number $M_d \ll 1$ in their product, yields the approximate relations

$$\check{P}^+(0, t) \approx \check{P}^0(0, t) \quad (2.41a)$$

$$\check{V}^+(0, t) \approx \check{V}^0(0, t) + \bar{V}_0 \theta \frac{\check{Q}(t)}{Q}. \quad (2.41b)$$

Substituting then (2.38) into (2.41), we obtain the boundary conditions

$$\check{P}^+(0, t) = \check{P}^-(0, t) \quad (2.42a)$$

$$\check{V}^+(0, t) = \alpha \check{V}^-(0, t) + \varsigma \frac{\check{Q}(t)}{Q} \quad (2.42b)$$

where we have denoted

$$\alpha := \frac{A_u}{A_d}, \quad \varsigma := \bar{V}_0 \theta.$$

The flame models (2.16) or (2.17) are in turn coupled with the average local velocity fluctuation $\check{V}(\cdot) := \frac{1}{2}(\check{V}^-(0, \cdot) + \check{V}^+(0, \cdot))$.

2.5 Summary of models

With the different model components described in Section 2.2–2.4, we put together the subsystems and present the complete network models in this section. The Rijke tube model in Section 2.5.1 and can combustor model in Section 2.5.3 both assume the following:

Assumption 16. *Heat transfer between the duct walls and internal gas is neglected.*

2.5.1 Rijke tube – Chapter 3

The first model we consider is the electrically heated Rijke tube. It consists of a cylindrical tube with constant cross-sectional area, and an electrical heater inside the tube. The complete model consists hence of the mathematical model of the electrical heater (2.3), the acoustics within a duct with constant cross-sectional area (2.29) with heat release coupled via (2.36) and general acoustic boundary conditions (2.33). We only consider state estimation of the Rijke tube, and let the boundary actuation signals $W_0 \equiv 0$, $W_L \equiv 0$. This gives rise to the complete model

$$\dot{Q}(t) = -\frac{1}{\tau}Q(t) + \frac{1}{\tau}l_w(\kappa + \kappa_v\sqrt{|\check{V}(z_0, t) + \bar{V}|})(T_w - T_g) \quad (2.43a)$$

$$\check{V}_t(z, t) = -\frac{1}{\rho}\check{P}_z(z, t) \quad (2.43b)$$

$$\check{P}_t(z, t) = -\gamma\bar{P}\check{V}_z(z, t) + \frac{\bar{\gamma}}{a}\delta(z - z_0)(Q(t) - \bar{Q}) \quad (2.43c)$$

$$\check{P}(L, t) = Z_L\check{V}(L, t) \quad (2.43d)$$

$$\check{P}(0, t) = Z_0\check{V}(0, t) \quad (2.43e)$$

$$\check{P}(x, 0) = \check{P}_0(x) \quad (2.43f)$$

$$\check{V}(x, 0) = \check{V}_0(x) \quad (2.43g)$$

$$Q(0) = Q_0 \quad (2.43h)$$

initialized from $\check{P}_0, \check{V}_0 \in L^2(0, L)$ and $Q_0 \in \mathbb{R}$.

2.5.2 Acoustic duct for boundary parameter identification – Chapters 4–5

For the purpose of boundary parameter identification, we consider a model of an acoustic duct with zero mean flow as given by (2.28), but with no heat release fluctuations, so that $\check{Q} \equiv 0$. This is coupled to the boundary conditions (2.33), with W_0 or W_L used as identification signals. The mathematical model is then

$$\check{V}_t(z, t) = -\frac{1}{\rho}\check{P}_z(z, t) \quad (2.44a)$$

$$\check{P}_t(z, t) = -\gamma\bar{P}\check{V}_z(z, t) - \gamma\frac{a'(z)}{a(z)}\bar{P}\check{V}(z, t) \quad (2.44b)$$

$$\check{P}(L, t) = Z_L \check{V}(L, t) + W_L(t) \quad (2.44c)$$

$$\check{P}(0, t) = Z_0 \check{V}(0, t) + W_0(t) \quad (2.44d)$$

$$\check{P}(x, 0) = \check{P}_0(x) \quad (2.44e)$$

$$\check{V}(x, 0) = \check{V}_0(x) \quad (2.44f)$$

initialized from $\check{P}_0, \check{V}_0 \in L^2(0, L)$.

2.5.3 Can combustor – Chapters 6–7

Lastly, we consider a mathematical model representing longitudinal oscillations in a can combustor. The acoustics are described by (2.27), and a flame modelled by (2.16) or (2.17) is located at $z = 0$, coupling to the acoustics via (2.42). The other end of the combustor is assumed to be modelled by a generic constant resistive impedance (2.33a), where the input signal W_L can be used for stabilization of thermoacoustic instabilities. The model is then given by

$$\dot{X}(t) = f(X(t)) + \bar{g}_0(X(t))\check{V}(0, t) + \bar{g}_1(X(t))\check{V}(0, t - \tau) \quad (2.45a)$$

$$\check{Q}(t) = \frac{\bar{Q}}{\bar{V}_0} \bar{h}(X(t)) \quad (2.45b)$$

$$\check{V}_t(z, t) = -\frac{1}{\bar{\rho}(z)} \check{P}_z(z, t) - \bar{V}'(z) \check{V}(z, t) \quad (2.45c)$$

$$\check{P}_t(z, t) = -\gamma \bar{P}(z) \check{V}_z(z, t) - \left(\bar{P}'(z) + \gamma \frac{a'(z)}{a(z)} \bar{P}(z) \right) \check{V}(z, t) - \gamma \bar{V}'(z) \check{P}(z, t) \quad (2.45d)$$

$$\check{P}(L, t) = Z \check{V}(L, t) + W(t) \quad (2.45e)$$

$$\check{P}^+(0, t) = \check{P}^-(0, t) \quad (2.45f)$$

$$\check{V}^+(0, t) = \alpha \check{V}^-(0, t) + \varsigma \frac{\check{Q}(t)}{\bar{Q}} \quad (2.45g)$$

$$\check{P}(x, 0) = \check{P}_0(x) \quad (2.45h)$$

$$\check{V}(x, 0) = \check{V}_0(x) \quad (2.45i)$$

$$X(0) = X_0 \quad (2.45j)$$

where the more general ODE (2.17) has been used for the flame model. The model is initialized from $\check{P}_0, \check{V}_0 \in L^2(0, L)$ and $X_0 \in \mathbb{R}^n$.

Part II

Lab Setup : The Rijke Tube

Introduction to Part II

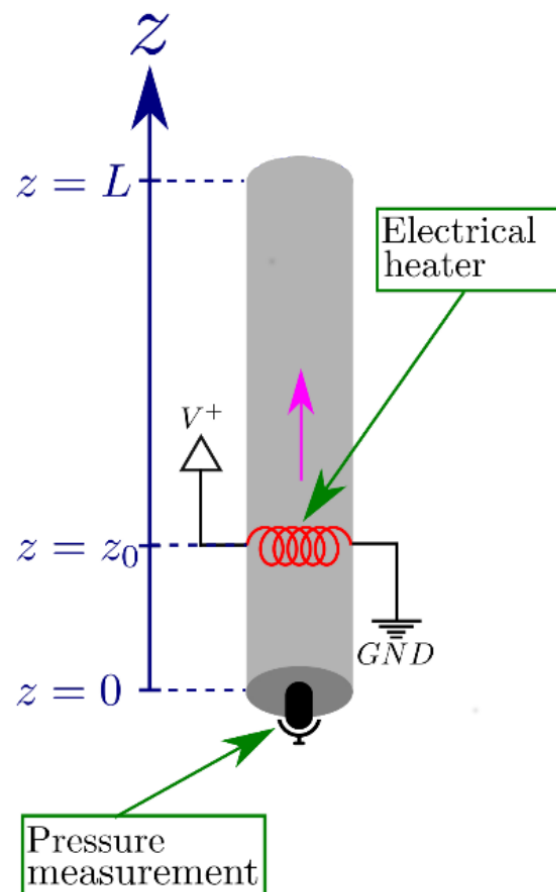


Figure ii.1: Diagram of Rijke tube setup to be considered for observer design in Chapter 3. The Rijke tube is set up vertically and an electrical heater is located in the lower half of the tube.

As stated in Chapter 1, Part II is focused on the Rijke tube, which is schematically depicted in Figure ii.1 for the case when there is a microphone sensing the lower boundary. The model (2.43) of the Rijke tube can be written in the form of a network model as discussed in Section 2.1, and this will be the basis for algorithm design.

The Rijke tube, being a common experimental setup for studying thermoacoustic instabilities, is one of the simplest arrangements capable of exhibiting the phe-

nomenon. The electrically heated version has the advantage of being simple to model due to the absence of complex combustion dynamics. The version of the Rijke tube with a heated gauze was first introduced in [Rijke 1859], and due to its simplicity has since been the subject of numerous studies to gain understanding of and develop methods to mitigate thermoacoustic instabilities, see [Raun *et al.* 1993] for a review.

We describe here the simulation and experimental setup considered in testing the algorithms to be designed in Chapters 3–4.

Simulation setup

Simulations are performed using MATLAB. The PDEs are solved using a first-order upwind scheme, and the heat release model is solved using a fourth-order Runge-Kutta scheme. A spatial discretization of $\mathbf{dx} = 1.00 \times 10^{-2}$ and a constant time step of $\mathbf{dt} = 9.74 \times 10^{-6}$ is used. The parameter update scheme is discretized in time using a first-order Euler scheme with a time-step of $\mathbf{dt} = 1.17 \times 10^{-5}$ s. The

Parameter	Symbol	Value	Unit
Acoustic parameters			
Adiabatic constant	γ	1.40	–
Mean pressure	\bar{P}	1.00×10^5	Pa
Mean density	$\bar{\rho}$	1.20	$kg \cdot m^{-3}$
Mean velocity	\bar{V}	0.350	$m \cdot s^{-1}$
Length of tube	L	1.40	m
Cross-sectional radius of tube	r	3.57×10^{-2}	m
Top acoustic impedance	Z_L	20.0	$Pa \cdot s \cdot m^{-1}$
Bottom acoustic impedance	Z_0	–15.0	$Pa \cdot s \cdot m^{-1}$
Electrical heater parameters			
Mean heat release rate	\bar{Q}	7.20×10^2	W
Wire time constant	τ	2.00×10^{-3}	s
Temperature of wire	T_w	9.33×10^2	K
Temperature of gas	T_g	3.00×10^2	K
Empirical constant for King’s law	κ_v	1.50	$W \cdot s^{0.5} \cdot m^{-1.5} \cdot K^{-1}$
Thermal conductivity of air	κ	2.638×10^{-2}	$W \cdot m^{-1} \cdot K^{-1}$
Length of wire	l_w	1.067	m
Position of heater	z_0	0.350	m

Table ii.1: Physical parameters used in Rijke tube simulations.

physical parameters considered in the simulations are summarized in Table ii.1. The simulation is initialized from

$$\check{P}_0(x) = 0, \quad \check{V}_0(x) = 0, \quad \check{Q}_0 = 0.$$

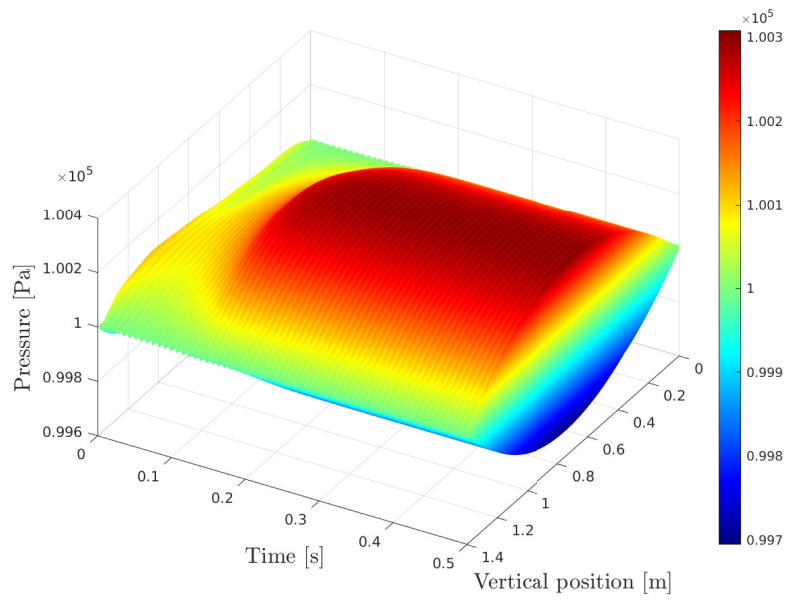


Figure ii.2: Open-loop pressure response of Rijke tube in simulations.

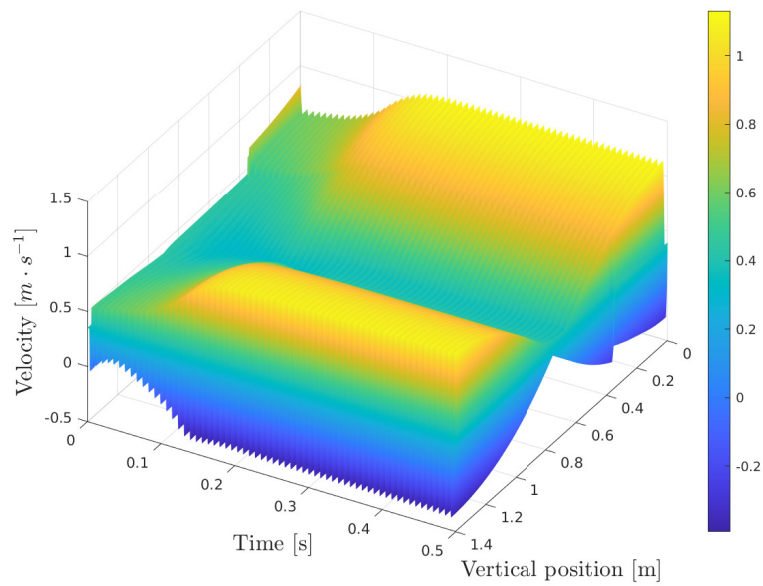


Figure ii.3: Open-loop velocity response of Rijke tube in simulations.

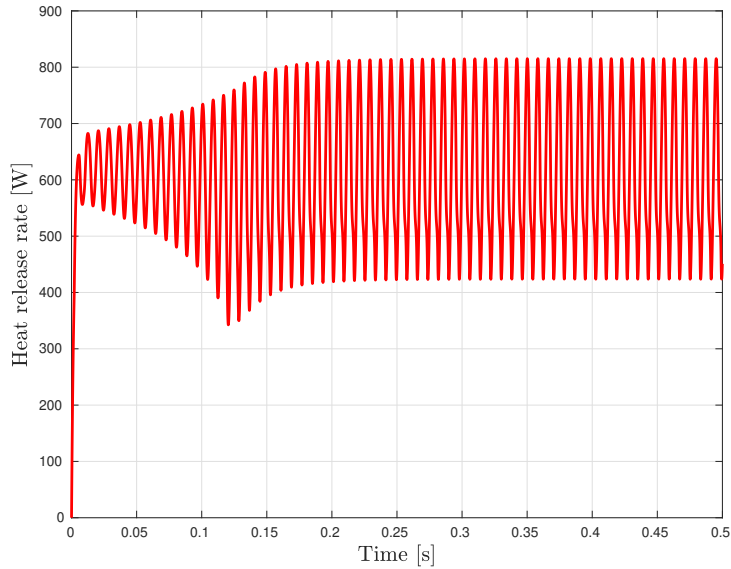


Figure ii.4: Open-loop heat release rate response of Rijke tube in simulations.

To visualize the plant dynamics with the choice of parameters presented in Table ii.1, the open loop response of the plant simulated for $t_s = 0.5$ s is plotted. In Figure ii.2, the pressure for $(z, t) \in [0, L] \times [0, t_s]$ is shown, and likewise in Figure ii.3 the velocity is plotted for $(z, t) \in [0, L] \times [0, t_s]$. Lastly, in Figure ii.4 the simulated heat release rate from the electrical heater is shown.

Since the simulation is initialized from zero initial conditions, the thermoacoustic instabilities which can be seen in Figures ii.2–ii.4 arise naturally as a consequence of the model (2.43) and the parameters summarized in the Table ii.1. As expected, the oscillations have an initial period of exponential growth before they saturate into a limit cycle, which is typical of thermoacoustic instabilities. Additionally, the open-loop pressure response can be seen to have nodes by the tube boundaries, whereas the open-loop velocity response has anti-nodes by the tube boundaries, being representative of the open ends of the Rijke tube.

Experimental setup

The Rijke tube used for the experiments conducted is shown in Figure ii.5. It consists of a cylindrical steel tube of length $L = 1.00$ m and radius $r = 35.7$ mm, which is propped up by a wooden frame via plastic strips. A heating element is positioned into the bottom of the tube via a steel rod, as can be seen under the tube in Figure ii.5.

On top of the steel rod, the heating element, which consists of a nickel-chromium alloy coil [Ome], is supported via a Mica support. The heating coil is shown in

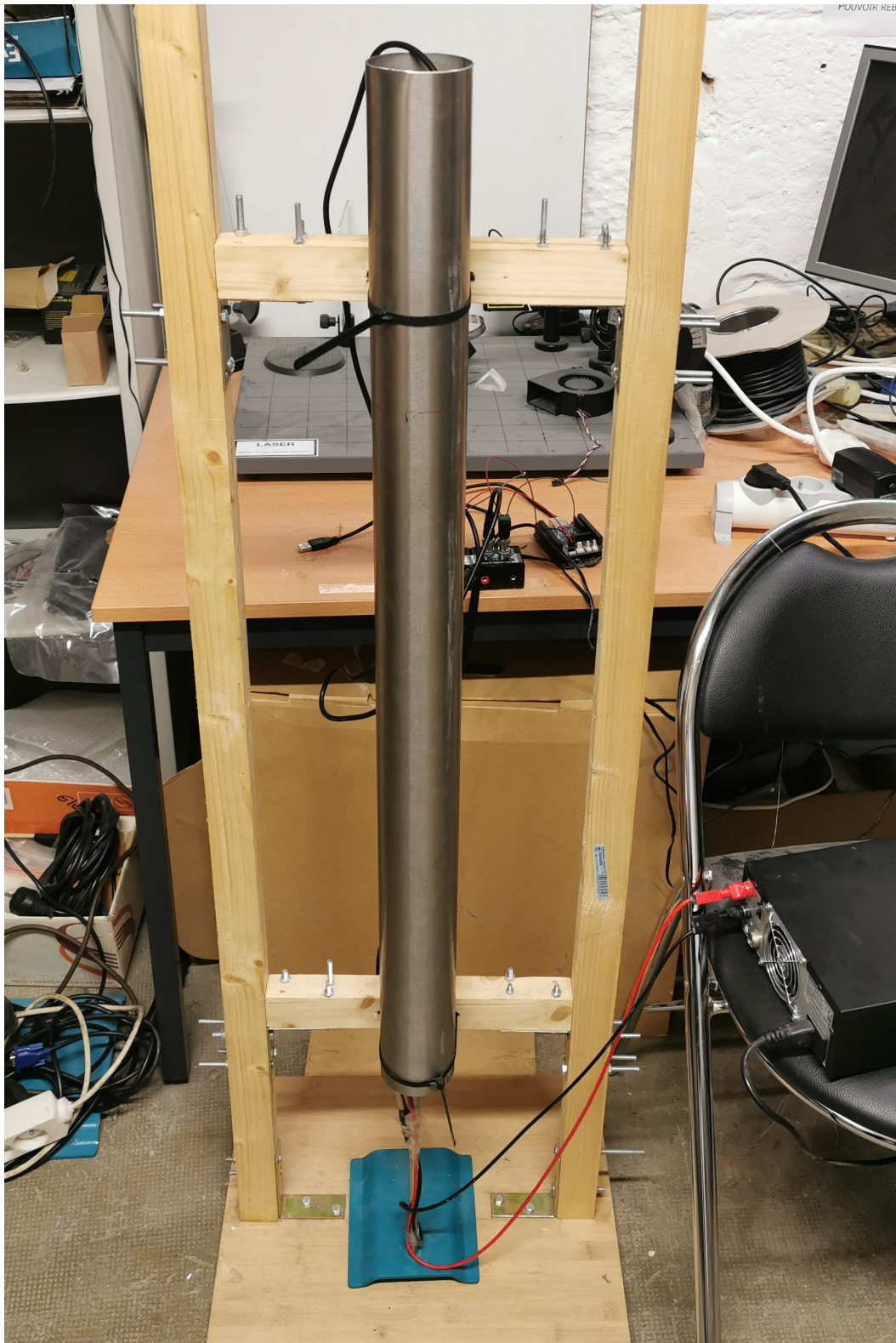


Figure ii.5: Rijke tube.



Figure ii.6: Coil turned off



Figure ii.7: Coil turned on



Figure ii.8: Power supply.



Figure ii.9: Microphone.

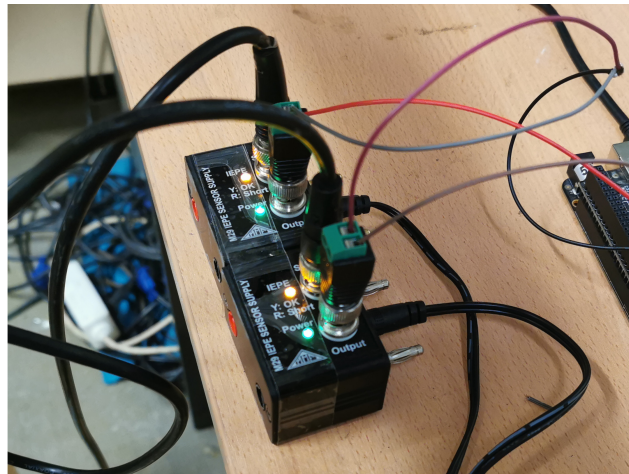


Figure ii.10: Pressure sensor supply.

Figure ii.6, for the case when the power supply is turned off, and in Figure ii.7 with the power supply turned on. The power supply used is a VOLTCRAFT DPS-32-15 [Con 2016], pictured in Figure ii.8. During the experiment, the heating coil is positioned at $z_0 = 0.25 \text{ m}$ from the base of the tube, and fed a current of $I = 16.5 \text{ A}$ through a voltage of $E = 24.0 \text{ V}$, giving an estimated power dissipated from the coil of $\bar{Q} = 396 \text{ W}$.

For the pressure sensor readings, two ROGA RG-50 microphones [ROG], one of which is pictured in Figure ii.9, are used. They are each powered by an MMF M29 IEPE Sensor Supply [Met 2017] as pictured in Figure ii.10, interfaced via Bayonet Neill-Concelman (BNC) connectors. From the IEPE Sensor Supply, the analog pressure signal is passed into a Bela Board [McPherson 2017], pictured in Figure ii.11, which is used for data acquisition. The Bela Board has an onboard Analog-to-Digital Converter (ADC) and C compiler, and the sensor reading is sampled at $f_s = 44.1 \text{ KHz}$.

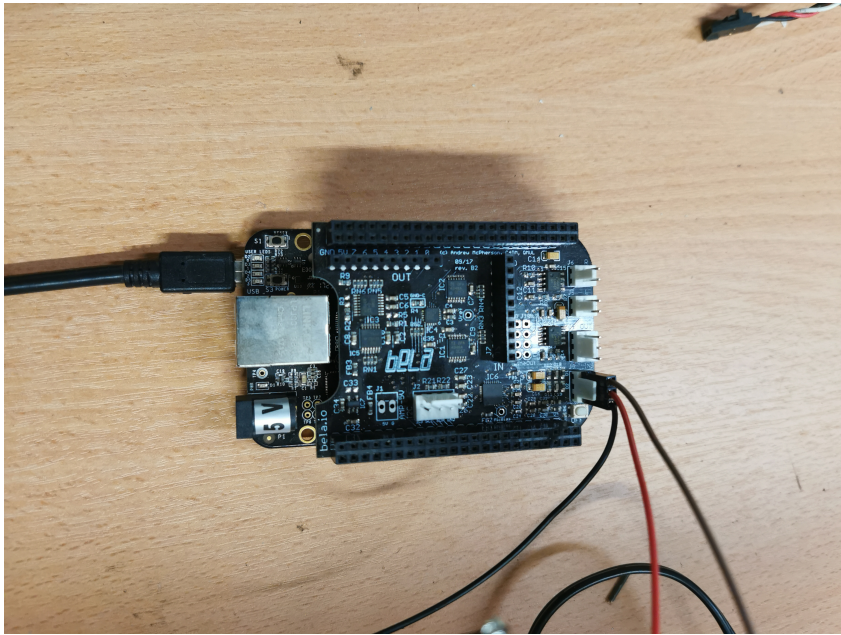


Figure ii.11: Bela board used for data acquisition.

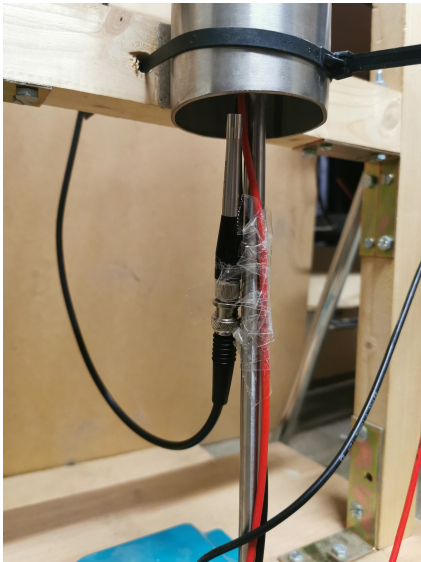


Figure ii.12: Boundary pressure measurement. For observer.



Figure ii.13: In-domain pressure measurement. For validation.



Figure ii.14: Loudspeaker.



Figure ii.15: Acoustic parameter identification setup.

To test the state observer developed in Chapter 3 with experimental data, two pressure measurements are taken. The first pressure measurement is taken at the bottom boundary of the tube, as shown in Figure ii.12. This signal is used as the input to the observer. The second pressure measurement is taken upstream of the heater at $z_v = 0.85 \text{ m}$ within the tube, as shown in Figure ii.13, and is used for validation.

To test the parameter identifier to be presented in Chapter 4 in estimating the boundary impedances Z_0 , Z_L , the experimental setup is slightly different. The electrical heater is not used for this experiment, but instead a Sony SRS-XB01 loudspeaker [Son 2018], as shown in Figure ii.14, is used to excite the cylindrical tube. One pressure sensor is placed in order to capture the output of the loudspeaker, while the other sensor is placed to record the response of the tube, as shown in Figure ii.15. This setup is used instead of passing the desired loudspeaker signal

directly into the parameter identifier to prevent possible loudspeaker distortions from negatively affecting the parameter identification.

Parameter	Symbol	Value	Unit
Acoustic parameters			
Adiabatic constant	γ	1.40	–
Mean pressure	\bar{P}	1.00×10^5	Pa
Mean density	$\bar{\rho}$	1.20	$kg \cdot m^{-3}$
Length of tube	L	1.00	m
Cross-sectional radius of tube	r	3.57×10^{-2}	m
Electrical heater parameters			
Voltage over coil	E	24.0	V
Current through coil	I	16.5	A
Diameter of coil wire	d_w	1.00×10^{-3}	m
Temperature of gas	T_g	3.00×10^2	K
Empirical constant for King's law	κ_v	1.50	$W \cdot s^{0.5} \cdot m^{-1.5} \cdot K^{-1}$
Thermal conductivity of air	κ	2.638×10^{-2}	$W \cdot m^{-1} \cdot K^{-1}$
Position of heater	z_0	0.250	m
Derived parameters			
Mean heat release rate	\bar{Q}	3.96×10^2	W
Temperature of wire	T_w	1.11×10^3	K
Length of wire	l_w	0.918	m
Mean velocity	\bar{V}	0.163	$m \cdot s^{-1}$
Wire time constant	τ	5.71×10^{-4}	s

Table ii.2: Physical parameters used in data post-processing for Rijke tube experiments.

After the data is collected with the experimental setups described above, it is tested with the observer and parameter identifier in MATLAB. The parameters used for this data post-processing is summarized in Table ii.2. Compared to Table ii.1, the acoustic impedances are omitted as these are considered unknown, and will be estimated using the method to be presented in Chapter 4.

The first three parameters listed under *Acoustic parameters*, namely γ , \bar{P} and $\bar{\rho}$ are taken to correspond to standard atmospheric conditions. Next, the length L and radius r are measured directly from the tube shown in Figure ii.5.

Under *Electrical heater parameters*, the measured voltage E and current I is documented. Also, the diameter of the coil wire d_w is taken from the manufacturer documentation [Ome]. The temperature of the gas T_g is set to standard room temperature, and the parameters κ_v and κ are the same in Tables ii.1 and ii.2, being estimates based on standard conditions of air in room temperature and estimates from the literature (see e.g [Epperlein *et al.* 2015], [de Andrade *et al.* 2016], [de Andrade *et al.* 2017]). The position of the heater z_0 is measured relative to the

positioning of the tube.

The mean heat release \bar{Q} is under *Derived parameters*, as this is computed from the voltage E and current I supplied. Additionally the wire temperature T_w is estimated according to the manufacturer documentation [Ome] based on the supplied current I , and in turn from this the wire length l_w is estimated, also based on the manufacturer documentation [Ome]. From the calculated wire temperature T_w together with gas temperature T_g , gravitational constant g and wire diameter d_w , as shown in [Epperlein 2014] the mean velocity $\bar{V} = \sqrt{g \frac{T_w - T_g}{T_g} d_w}$. Also, based on the formula given in [Epperlein et al. 2015], the wire time constant τ is estimated based on the wire diameter d_w and mean velocity \bar{V} as $\tau = \frac{d_w}{5\bar{V}}$.

The Rijke Tube – State Observer

Contents

3.1	Literature review	48
3.2	Observer design	48
3.2.1	Model in Riemann coordinates	48
3.2.2	Observer design	51
3.2.3	Convergence analysis	53
3.2.4	Robustness to modelling error in boundary condition	54
3.3	Simulations	56
3.3.1	First simulation - Smaller impedances	56
3.3.2	Second simulation - Larger impedances	60
3.4	Experiment	68
3.5	Discussion	71

Dans ce chapitre, nous proposons un observateur d'état pour le modèle de tube de Rijke (2.43). Il est basé sur l'hypothèse qu'une mesure de pression à la frontière inférieure du domaine spatial est disponible. Après avoir réécrit le modèle en coordonnées de Riemann et replié le domaine spatial autour du modèle de dégagement de chaleur, l'observateur est proposé en copiant la dynamique du modèle et en reconstruisant la frontière non mesurée. Il est démontré que l'estimation de l'état de la frontière non mesurée converge vers la valeur réelle de manière exponentielle. Ceci permet ensuite d'établir des propriétés de convergence globale pour tous les états du modèle. Par la suite, un résultat mineur affirmant que les estimations d'état restent bornées en cas d'incertitude sur la connaissance des paramètres de la frontière est donné. Les résultats théoriques sont suivis d'une validation, d'abord en simulations, puis en expériences. La sensibilité des estimations aux différentes valeurs des paramètres limites suggère que des estimations de ceux-ci devraient être obtenues, motivant le sujet du chapitre 4.

In this chapter, we propose a state observer for the Rijke tube model (2.43). It is based on the assumption that the lower boundary is measured. After rewriting the model in Riemann coordinates and folding the spatial domain around the heat release model, thus moving it to the rewritten model boundary, the observer is proposed by copying the model dynamics and reconstructing the unmeasured boundary. It is shown that the estimate of the unmeasured boundary state converges to the

true value exponentially. This in turn allows establishment of global convergence properties for all states in the model. Subsequently, a minor result asserting that the state estimates remain bounded under uncertainty in knowledge of the boundary parameters is given. The theoretical results are followed by validation, first in simulations and then in experiments. The sensitivity to the estimates to different values of the boundary parameters suggests estimates of these should be obtained, motivating the topic of Chapter 4.

3.1 Literature review

Much of the previous work on the Rijke tube has consisted in characterizing its stability limits, with [Carrier 1955] pioneering linear stability analysis of the system and later [Bayly 1986] taking into account nonlinear features. In addition to experimental studies of the stability limits of the Rijke tube, studies on active control strategies applied to attenuate the thermoacoustic oscillations in the Rijke tube have been performed. A control law consisting in measuring the pressure signal upstream of the heater and subsequently sending this signal phase-shifted and amplified to a loudspeaker has been applied to a Rijke tube in [Heckl 1988], being one of the first studies investigating active control of the Rijke tube. More recently, a more sophisticated full-state feedback boundary control law designed via infinite-dimensional backstepping on a linearised PDE-ODE model of the electrically heated Rijke tube has been derived in [de Andrade *et al.* 2018b]. To pair with this full-state feedback control law, a corresponding boundary observer for the linearized PDE-ODE model is derived in [de Andrade *et al.* 2018a]. This work was continued in [de Andrade *et al.* 2020], where experimental verification of the observer was obtained. Also, in [Auriol *et al.* 2020b], [de Andrade & Vazquez 2020] observer designs for the Rijke tube using in-domain measurements rather than just a boundary measurement are considered.

As explained in Chapter 2, the heat release model (2.3) captures the nonlinear effects of the electrically heated Rijke tube. For the observer design in [de Andrade *et al.* 2018a] (2.3) is linearized, which makes the mathematical analysis tractable - however this linear ODE model does not reflect the full nonlinear dynamics one typically obtains in practice. A nonlinear heat release model is needed to model the saturated response one sees for large amplitudes and resultant limit cycle behaviour [Agostino *et al.* 2002]. To maintain this behaviour in the design, we propose in Section 3.2 an observer taking into account the nonlinear features of King's law.

3.2 Observer design

3.2.1 Model in Riemann coordinates

Consider the setup shown in Figure ii.1. It consists of an unflanged, cylindrical tube of length L and constant cross-sectional area a , with an electrical heater located

in the interior of the tube at vertical position $z_0 \in (0, \frac{L}{2}]$. With real-time gauge pressure data from a microphone located at $z = 0$, the aim of the state observer is to infer the unmeasured pressure and velocity perturbations along the vertical axis of the tube, together with the heat release rate from the electrical heater.

In Chapter 2, a mathematical model to describe the distributed pressure \check{P} and velocity perturbations \check{V} coupled with the heat release rate Q from the electrically heated coil is introduced, and given by (2.43). We assume the boundary pressure measurement

$$Y(t) := \check{P}(0, t) \quad (3.1)$$

is known.

Remark 1. *In an ideal theoretical setting, since the Rijke tube is open at both ends, a pressure node is located at both $z = 0$ and $z = L$. However, in practice the nodes are located slightly outside the tube ends ([Levine & Schwinger 1948],[Epperlein et al. 2015]) making boundary pressure sensing feasible. This fact is modelled by the non-zero impedances Z_0, Z_L in (2.43d)–(2.43e).*

In order to use the model for observer design, it is convenient to rewrite the linearised acoustics from (2.43) in Riemann invariant coordinates and fold the spatial domain around z_0 to move the heat release to the system boundary. To facilitate this, we introduce the invertible affine spatial coordinate transforms $z_i : x \mapsto z$,

$$z_1(x) := z_0(1 - x) \quad (3.2a)$$

$$z_2(x) := z_0 + x(L - z_0) \quad (3.2b)$$

with $x \in [0, 1]$ and $i \in \{1, 2\}$ to rewrite the linearised acoustics from (2.43) in Riemann invariant coordinates. The subscript i denotes which part of the Rijke tube x is mapped to, with z_1 mapping x to points below the electrical heater and z_2 mapping x to points above the electrical heater. Next, define the Riemann coordinates

$$u_i(x, t) := \check{P}(z_i(x), t) + k\check{V}(z_i(x), t) \quad (3.3a)$$

$$v_i(x, t) := \check{P}(z_i(x), t) - k\check{V}(z_i(x), t) \quad (3.3b)$$

where k is the characteristic impedance of the gas, defined as

$$k := \sqrt{\gamma \bar{P} \bar{\rho}}. \quad (3.4)$$

This allows us to rewrite the parts of the linearised acoustics (2.43b)–(2.43c) for $z \neq z_0$, over $(x, t) \in (0, 1) \times [0, \infty)$ as

$$u_{1,t}(x, t) = \lambda_1 u_{1,x}(x, t) \quad (3.5a)$$

$$v_{1,t}(x, t) = -\lambda_1 v_{1,x}(x, t) \quad (3.5b)$$

$$u_{2,t}(x, t) = -\lambda_2 u_{2,x}(x, t) \quad (3.5c)$$

$$v_{2,t}(x, t) = \lambda_2 v_{2,x}(x, t) \quad (3.5d)$$

where

$$\lambda_1 := \frac{c}{z_0} \quad (3.6a)$$

$$\lambda_2 := \frac{c}{L - z_0}, \quad (3.6b)$$

with c being the speed of sound inside the tube, given by

$$c := \sqrt{\frac{\gamma \bar{P}}{\bar{\rho}}}. \quad (3.7)$$

Remark 2. Since $z_0 \leq \frac{L}{2}$ we have that $\lambda_1 \geq \lambda_2$. This fact is useful later on in the observer design.

Next, the acoustic boundary conditions (2.43d)–(2.43e) are rewritten as

$$u_1(1, t) = d_0 v_1(1, t) \quad (3.8a)$$

$$v_2(1, t) = d_1 u_2(1, t) \quad (3.8b)$$

where the reflection coefficients d_0, d_1 are defined as

$$d_0 := \frac{Z_0 + k}{Z_0 - k} \quad (3.9a)$$

$$d_1 := \frac{Z_L - k}{Z_L + k}. \quad (3.9b)$$

Since the spatial domain is folded around z_0 , the electrical heater is moved to the boundary of the model. To deal with this, we consider the Laplace transform of the PDE dynamics in Riemann coordinates around the electrical heater. These can be rewritten as ODEs in the spatial coordinate z as

$$\frac{d}{dz} u(z, s) = -\frac{s}{c} u(z, s) + \frac{\bar{\gamma}}{ac} \delta(z - z_0) \check{Q}(s) \quad (3.10a)$$

$$\frac{d}{dz} v(z, s) = \frac{s}{c} v(z, s) - \frac{\bar{\gamma}}{ac} \delta(z - z_0) \check{Q}(s) \quad (3.10b)$$

As shown in e.g. [Epperlein *et al.* 2015], we can then write

$$u(z_0^+, s) = u(z_0^-, s) + \frac{\bar{\gamma}}{ac} \check{Q}(s)$$

$$v(z_0^+, s) = v(z_0^-, s) - \frac{\bar{\gamma}}{ac} \check{Q}(s)$$

where z_0^- is the position directly under the heater and z_0^+ is the position directly above the heater. Using the spatial change of variables (3.2) and writing in the time domain, this gives rise to the boundary conditions

$$v_1(0, t) = v_2(0, t) + \mu \check{X}(t) \quad (3.12a)$$

$$u_2(0, t) = u_1(0, t) + \mu \check{X}(t) \quad (3.12b)$$

where we have denoted $\check{X} := \check{Q}$, and the ODE boundary coefficient μ is defined

$$\mu := \frac{\bar{\gamma}}{ac}. \quad (3.13)$$

Denoting $X := Q$, the heat release model (2.43a) is rewritten as

$$\dot{X}(t) = -aX(t) + b_1 \sqrt{|b_2 + b_3(u_1(0, t) - v_2(0, t))|} + b_4 \quad (3.14)$$

with

$$\begin{aligned} a &:= \frac{1}{\tau} \\ b_1 &:= \frac{l_w(T_w - T_g)\kappa_v}{\tau} \\ b_2 &:= \bar{V} \\ b_3 &:= \frac{1}{2k} \\ b_4 &:= \frac{l_w(T_w - T_g)\kappa}{\tau}. \end{aligned}$$

The gauge pressure measurement (3.1) is in the Riemann invariant coordinates, defined via (3.3), written as $Y(\cdot) = \frac{1}{2}(u_1(1, \cdot) + v_1(1, \cdot))$. Applying the boundary condition for u_1 we see by defining the boundary measurement signal

$$y(t) := v_1(1, t) \quad (3.15)$$

the gauge pressure measurement is reconstructed as

$$Y(t) = \frac{1 + d_0}{2} y(t). \quad (3.16)$$

These dynamics are schematically depicted in Figure 3.1. Notice that several feedback loops make the dynamics potentially unstable.

3.2.2 Observer design

With the measurement signal y defined in (3.15), we propose the observer

$$\dot{\hat{X}}(t) = -a\hat{X}(t) + b_1 \sqrt{|b_2 + b_3(\hat{u}_1(0, t) - \hat{v}_2(0, t))|} + b_4 \quad (3.17a)$$

$$\hat{u}_{1,t}(x, t) = \lambda_1 \hat{u}_{1,x}(x, t) \quad (3.17b)$$

$$\hat{u}_{2,t}(x, t) = -\lambda_2 \hat{u}_{2,x}(x, t) \quad (3.17c)$$

$$\hat{v}_{1,t}(x, t) = -\lambda_1 \hat{v}_{1,x}(x, t) \quad (3.17d)$$

$$\hat{v}_{2,t}(x, t) = \lambda_2 \hat{v}_{2,x}(x, t) \quad (3.17e)$$

$$\hat{u}_2(0, t) = \hat{u}_1(0, t) + \mu(\hat{X}(t) - \bar{X}) \quad (3.17f)$$

$$\hat{v}_1(0, t) = \hat{v}_2(0, t) + \mu(\hat{X}(t) - \bar{X}) \quad (3.17g)$$

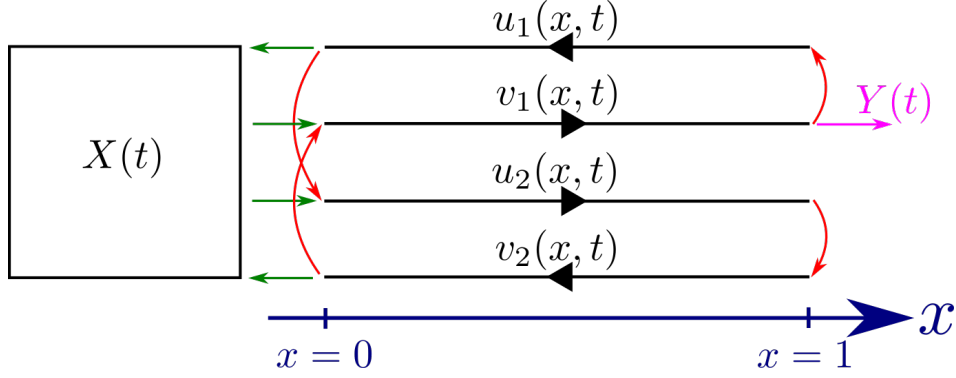


Figure 3.1: Schematic of Rijke tube system in Riemann coordinates. The green arrows are couplings between the ODE state and PDE states, the red arrows are boundary couplings between the PDE states and the magenta arrow represents the output signal.

$$\hat{u}_1(1, t) = d_0 y(t) \quad (3.17h)$$

$$\hat{v}_2(1, t) = d_1 y(t + \lambda_1^{-1} - \lambda_2^{-1}) + d_1 (\hat{u}_1(0, t - \lambda_2^{-1}) - \hat{v}_2(0, t - \lambda_2^{-1})). \quad (3.17i)$$

We state now the main result pertaining to the convergence properties of (3.17), before explaining the rationale behind the observer. A formal proof of the result is then given in Section 3.2.3.

Theorem 1. *Consider system (3.5), (3.8), (3.12), (3.14) and the state observer (3.17) using the measurement (3.15). We assume $|d_0|, |d_1| < 1$. Assume the states have initial conditions $(u_{i,0}, v_{i,0}, X_0) \in L^2(0, 1) \times L^2(0, 1) \times \mathbb{R}$ and $(\hat{u}_{i,0}, \hat{v}_{i,0}, \hat{X}_0) \in L^2(0, 1) \times L^2(0, 1) \times \mathbb{R}$, respectively. Then, the zero equilibrium of the dynamics of the estimation errors $\tilde{u}_i := u_i - \hat{u}_i$, $\tilde{v}_i := v_i - \hat{v}_i$, $\tilde{X} := X - \hat{X}$ is Globally Asymptotically Stable (GAS).*

This observer consists of a copy of the Rijke tube dynamics in Riemann coordinates (3.5), with the exception of (3.17i). While (3.17h) consists of injecting the measured output directly, Equation (3.17i) deserves more explanation. It is based on the following considerations. First, notice that substituting Equation (3.12b) into the general solution of u_2 in terms of the boundary at $x = 0$, $u_2(1, \cdot)$ rewrites

$$\begin{aligned} u_2(1, t) &= u_2(0, t - \lambda_2^{-1}) \\ &= u_1(0, t - \lambda_2^{-1}) + \mu \tilde{X}(t - \lambda_2^{-1}). \end{aligned} \quad (3.18)$$

Besides, using the expression for $v_1(0, \cdot)$ from (3.12a) together with the measurement $y(\cdot) = v_1(1, \cdot)$ yields

$$\mu \tilde{X}(t) = y(t + \lambda_1^{-1}) - v_2(0, t). \quad (3.19)$$

Combining (3.18)–(3.19) gives

$$v_2(1, t) = d_1 (u_1(0, t - \lambda_2^{-1}) - v_2(0, t - \lambda_2^{-1}) + y(t + \lambda_1^{-1} - \lambda_2^{-1})). \quad (3.20)$$

The boundary condition (3.17i) follows by considering estimates of $u_1(0, t - \lambda_2^{-1})$ and $v_2(0, t - \lambda_2^{-1})$ in lieu of the true values. As we show next in Section 3.2.3, the resulting error converges asymptotically to zero.

Remark 3. Notice that the observer is causal, in particular the signal $y(t + \lambda_1^{-1} - \lambda_2^{-1})$ is available at time t due to Remark 2.

3.2.3 Convergence analysis

The most critical boundary conditions in the error system for stability are $\tilde{u}_1(1, \cdot)$, $\tilde{v}_2(1, \cdot)$, so we derive their expressions first. It is trivial to see that $\tilde{u}_1(1, \cdot) = 0$, while subtracting (3.17i) from (3.20) yields

$$\tilde{v}_2(1, t) = d_1(\tilde{u}_1(0, t - \lambda_2^{-1}) - \tilde{v}_2(0, t - \lambda_2^{-1})). \quad (3.21)$$

The other terms in the observer (3.17) are copies of the corresponding terms in the original system (3.5) and hence their corresponding error dynamics are easily computed. Therefore, the state estimation error in $\tilde{u}_i, \tilde{v}_i, \tilde{X}$ satisfies the dynamics

$$\tilde{u}_{1,t}(x, t) = \lambda_1 \tilde{u}_{1,x}(x, t) \quad (3.22a)$$

$$\tilde{u}_{2,t}(x, t) = -\lambda_2 \tilde{u}_{2,x}(x, t) \quad (3.22b)$$

$$\tilde{v}_{1,t}(x, t) = -\lambda_1 \tilde{v}_{1,x}(x, t) \quad (3.22c)$$

$$\tilde{v}_{2,t}(x, t) = \lambda_2 \tilde{v}_{2,x}(x, t) \quad (3.22d)$$

$$\tilde{u}_1(1, t) = 0 \quad (3.22e)$$

$$\tilde{u}_2(0, t) = \tilde{u}_1(0, t) + \mu \tilde{X}(t) \quad (3.22f)$$

$$\tilde{v}_1(0, t) = \tilde{v}_2(0, t) + \mu \tilde{X}(t) \quad (3.22g)$$

$$\tilde{v}_2(1, t) = d_1(\tilde{u}_1(0, t - \lambda_2^{-1}) - \tilde{v}_2(0, t - \lambda_2^{-1})) \quad (3.22h)$$

$$\begin{aligned} \dot{\tilde{X}}(t) &= -a\tilde{X}(t) + b_1 \sqrt{|b_2 + b_3(u_1(0, t) - v_2(0, t))|} \\ &\quad - b_1 \sqrt{|b_2 + b_3(\hat{u}_1(0, t) - \hat{v}_2(0, t))|} \end{aligned} \quad (3.22i)$$

A schematic view of the error system is shown in Figure 3.2, illustrating the cascade structure of its dynamics which ensure the convergence of its states to zero. We are now ready to prove Theorem 1.

Proof of Theorem 1. From (3.22a), (3.22e) we see that $\tilde{u}_1(0, t - \lambda_2^{-1}) = 0$ for time $t \geq \lambda_1^{-1} + \lambda_2^{-1}$. Hence the boundary condition (3.22h) simplifies after this time to

$$\tilde{v}_2(1, t) = -d_1 \tilde{v}_2(0, t - \lambda_2^{-1}) \quad (3.23)$$

allowing us to conclude that

$$\tilde{v}_2(0, t) = -d_1 \tilde{v}_2(0, t - 2\lambda_2^{-1}). \quad (3.24)$$

Since $|d_1| < 1$, we can conclude that $\tilde{v}_2(0, t) \rightarrow 0$ exponentially as $t \rightarrow \infty$. Next, we can bound (3.22i) by the following inequality:

$$\dot{\tilde{X}}(t) \leq -a\tilde{X}(t) + b_1 \sqrt{|b_3[\tilde{u}_1(0, t) - \tilde{v}_2(0, t)]|}. \quad (3.25)$$

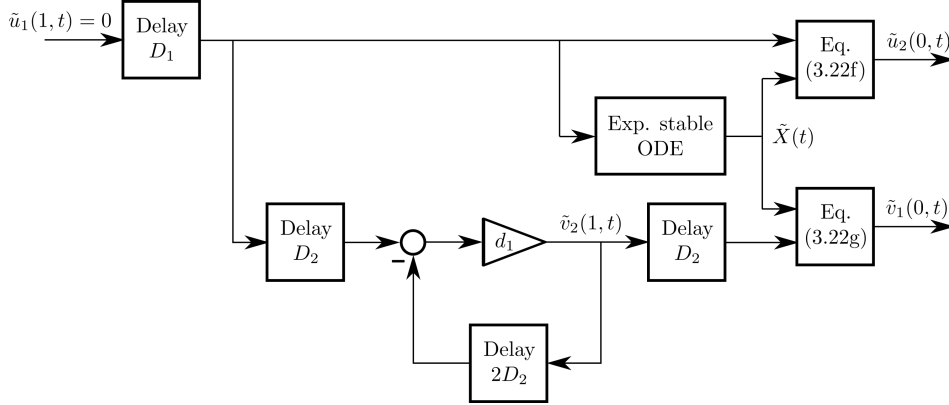


Figure 3.2: Schematic of the error system, where $D_i := \lambda_i^{-1}$ are time delays.

Define

$$g(t) := b_1 \sqrt{|b_3(\tilde{u}_1(0,t) - \tilde{v}_2(0,t))|} \quad (3.26)$$

where we know g tends to zero as $t \rightarrow \infty$. Also, defining the linear system in $\tilde{\Xi}$,

$$\dot{\tilde{\Xi}}(t) = -a\tilde{\Xi}(t) + g(t), \quad (3.27)$$

with initial condition $\tilde{\Xi}(0) = \tilde{X}(0)$, then $\tilde{\Xi}$ is Input-to-State Stable (ISS) with respect to g . More precisely (see [Khalil & Grizzle 2002]), we can establish the bound (where $0 \leq t_0 \leq t$),

$$|\tilde{\Xi}(t - t_0)| \leq e^{-a(t-t_0)} |\tilde{\Xi}(t_0)| + \frac{1}{a} \sup_{t_0 \leq \tau \leq t} |g(\tau)|. \quad (3.28)$$

Since $\dot{\tilde{X}} \leq \dot{\tilde{\Xi}}$ and $\tilde{X}(0) = \tilde{\Xi}(0)$, we can establish

$$\tilde{X}(t) \leq \tilde{\Xi}(t). \quad (3.29)$$

As g is exponentially vanishing as $t \rightarrow \infty$, we see the right hand side of (3.28) goes to zero and hence $\tilde{X} \rightarrow 0$ asymptotically as $t \rightarrow \infty$, which proves the Theorem. \square

3.2.4 Robustness to modelling error in boundary condition

In practice the acoustic impedances Z_0, Z_L appearing in Equations (2.43d)–(2.43e) are difficult to estimate correctly, implying the boundary coefficients d_0, d_1 appearing in (3.8) for the Riemann coordinate formulation is prone to being incorrectly modelled. Denote the estimates of d_0, d_1 as \hat{d}_0, \hat{d}_1 and define $\tilde{d}_0 := d_0 - \hat{d}_0, \tilde{d}_1 := d_1 - \hat{d}_1$ as the modelling errors.

When \hat{d}_0, \hat{d}_1 is used in place of d_0, d_1 in the observer (6.41), the expressions for $\tilde{u}_1(1, \cdot), \tilde{v}_2(1, \cdot)$, given by (3.22e), (3.22h), change to

$$\tilde{u}_1(1, t) = \tilde{d}_0 y(t) \quad (3.30)$$

$$\begin{aligned}\tilde{v}_2(1, t) &= \hat{d}_1(\tilde{u}_1(0, t - \lambda_2^{-1}) - \tilde{v}_2(0, t - \lambda_2^{-1})) \\ &\quad + \tilde{d}_1(\mu X(t - \lambda_2^{-1}) + u_1(0, t - \lambda_2^{-1}))\end{aligned}\quad (3.31)$$

with the rest of the error system (3.22) being unaffected. We state now a Proposition on the sensitivity of the state estimate error to errors in these boundary parameters.

Proposition 1. *Assume that the states of the original system are bounded, and the estimates \hat{d}_0, \hat{d}_1 of d_0, d_1 respectively satisfy*

$$|\hat{d}_0|, |\hat{d}_1| < 1. \quad (3.32)$$

Then all the error signals $\tilde{u}_i, \tilde{v}_i, \tilde{X}$ are bounded.

Proof. In the following we denote the Laplace transform of the time-domain signal f as \check{f} , i.e. $\check{f}(s) = \mathcal{L}(f(\cdot))$. With the signal h defined as

$$h(t) := u_1(0, t) + \mu X(t) \quad (3.33)$$

we find that

$$\begin{bmatrix} \check{\tilde{u}}_1(0, s) \\ \check{\tilde{v}}_2(0, s) \end{bmatrix} = H(s) \begin{bmatrix} \check{y}(s) \\ \check{h}(s) \end{bmatrix} \quad (3.34)$$

where

$$H(s) := \begin{bmatrix} e^{-\lambda_1^{-1}s} & 0 \\ \frac{\hat{d}_1 e^{-(2\lambda_2^{-1} + \lambda_1^{-1})s}}{1 + \hat{d}_1 e^{-2\lambda_2^{-1}s}} & \frac{e^{-2\lambda_2^{-1}s}}{1 + \hat{d}_1 e^{-2\lambda_2^{-1}s}} \end{bmatrix} \begin{bmatrix} \tilde{d}_0 & 0 \\ 0 & \tilde{d}_1 \end{bmatrix} \quad (3.35)$$

is a transfer matrix. This allows us to reconstruct the signal ι defined as

$$\iota(t) := \tilde{u}_1(0, t) - \tilde{v}_2(0, t) \quad (3.36)$$

in terms of signals y, h as

$$\iota(t) = \begin{bmatrix} 1 \\ -1 \end{bmatrix}^\top \mathcal{L}^{-1} \left(H(s) \begin{bmatrix} \check{y}(s) \\ \check{h}(s) \end{bmatrix} \right). \quad (3.37)$$

Since $|\hat{d}_0|, |\hat{d}_1| < 1$, Equation (3.35) implies that H is stable (see [Niculescu 2001] for a more extended treatment of transfer functions for systems with time delays), and since $y, h \in L^\infty$, one has $\iota, g \in L^\infty$, with g defined by (3.26).

Further, since $\tilde{u}_1(1, \cdot) = \tilde{d}_0 y(\cdot)$, $\tilde{u}_1(1, \cdot) \in L^\infty$ and hence all of \tilde{u}_1 is bounded. Besides, one has

$$\check{\tilde{v}}_2(1, s) = \frac{e^{-\lambda_2^{-1}s}}{1 + \hat{d}_1 e^{-\lambda_2^{-1}s}} \left(\tilde{d}_0 \hat{d}_1 e^{-\lambda_1^{-1}s} \check{y}(s) + \tilde{d}_1 \check{h}(s) \right) \quad (3.38)$$

which again using that $|\hat{d}_0|, |\hat{d}_1| < 1$ implies that $\tilde{v}_2(1, \cdot) \in L^\infty$ and therefore all of \tilde{v}_2 is bounded. Equation (3.25) further implies the following bound on \tilde{X} ,

$$\tilde{X}(t) \leq e^{-at} |\tilde{X}(0)| + \frac{1}{a} \|g\|_\infty. \quad (3.39)$$

Finally, (3.22f)–(3.22g) express $\tilde{u}_2(0, \cdot)$, $\tilde{v}_1(0, \cdot)$ as the sum of bounded signals, therefore $\tilde{u}_2(x, \cdot), \tilde{v}_1(x, \cdot) \in L^\infty, \forall x \in [0, 1]$. \square

3.3 Simulations

We test first the observer in a simulation setting, with parameters as presented in Table ii.1. In this chapter, the observer (3.17) is tested for the case when the boundary acoustic impedances Z_0, Z_L are incorrect. These simulations demonstrate the theoretical result of Proposition 1. In Chapter 4, after having estimated the boundary parameters, the observer with correct boundary parameters will be tested, demonstrating Theorem 1.

As a comparison, an observer we refer to as the “trivial” observer will be compared to (3.17) in the simulations. This observer is identical to (3.17), except instead of the boundary condition (3.17i), it uses

$$\hat{v}_2(1, t) = d_1 \hat{u}_2(1, t). \quad (3.40)$$

The “trivial” observer (3.17a)–(3.17h), (3.40) is the simplest observer one can construct for the Rijke tube modelled by (2.43) using the measurement (3.1), since it is simply a copy of the dynamics with the measurement injected in the corresponding boundary where it is taken. It does not have a convergence guarantee as one has a potentially unstable feedback loop in the interaction between \hat{u}_2, \hat{v}_2 and \hat{X} , but because it does not attempt to reconstruct $\hat{v}(1, \cdot)$ from known signals it does not introduce an exponentially converging error, which is a drawback of the observer (3.17) in the terms of its transient convergence properties.

Two different pairs of \hat{Z}_0, \hat{Z}_L are tested, namely one pair satisfying $|\hat{Z}_0| < |Z_0|, |\hat{Z}_L| < |Z_L|$, and the second pair satisfying $|\hat{Z}_0| > |Z_0|, |\hat{Z}_L| > |Z_L|$. The performance of the “trivial” observer (3.17a)–(3.17h), (3.40) is compared, and it uses the same parameters and measurement signal as the observer (3.17) in the respective tests. In the two tests, the simulation is run for $t_s = 2$ s, and the observers are turned on at $t = 0.5$ s.

3.3.1 First simulation - Smaller impedances

Here “estimates” $\hat{Z}_0 = -5, \hat{Z}_L = 5$ are used as values of the impedance in the observer. First the estimation errors for the observers are plotted against each other. For the pressure and velocity, the estimation error by the heater, at position $z = z_0$, is considered. In Figure 3.3, the pressure estimation error $\tilde{P}(z_0, \cdot)$ of the observer (3.17) is plotted in dark blue, versus the pressure estimation error $\tilde{P}_{trivial}(z_0, \cdot)$ of the “trivial” observer (3.17a)–(3.17h), which is plotted in a lighter shade of blue. Likewise, the velocity estimation errors $\tilde{V}(z_0, \cdot)$ and $\tilde{V}_{trivial}(z_0, \cdot)$ are plotted against each other in respectively dark and light grey in Figure 3.4. Lastly, the heat release estimation error $\tilde{Q}(\cdot)$ and $\tilde{Q}_{trivial}(\cdot)$, in respectively dark and light red, are plotted against each other in Figure 3.5. With the observer being turned on at $t = 0.5$ s, the plots are shown for $t \in [0.5, 0.7]$ and $t \in [1.8, 2.0]$, being respectively the first and last 200 ms of testing the observers. The plots are split up in this manner for ease of viewing, due to the relatively high frequency of the dynamics.

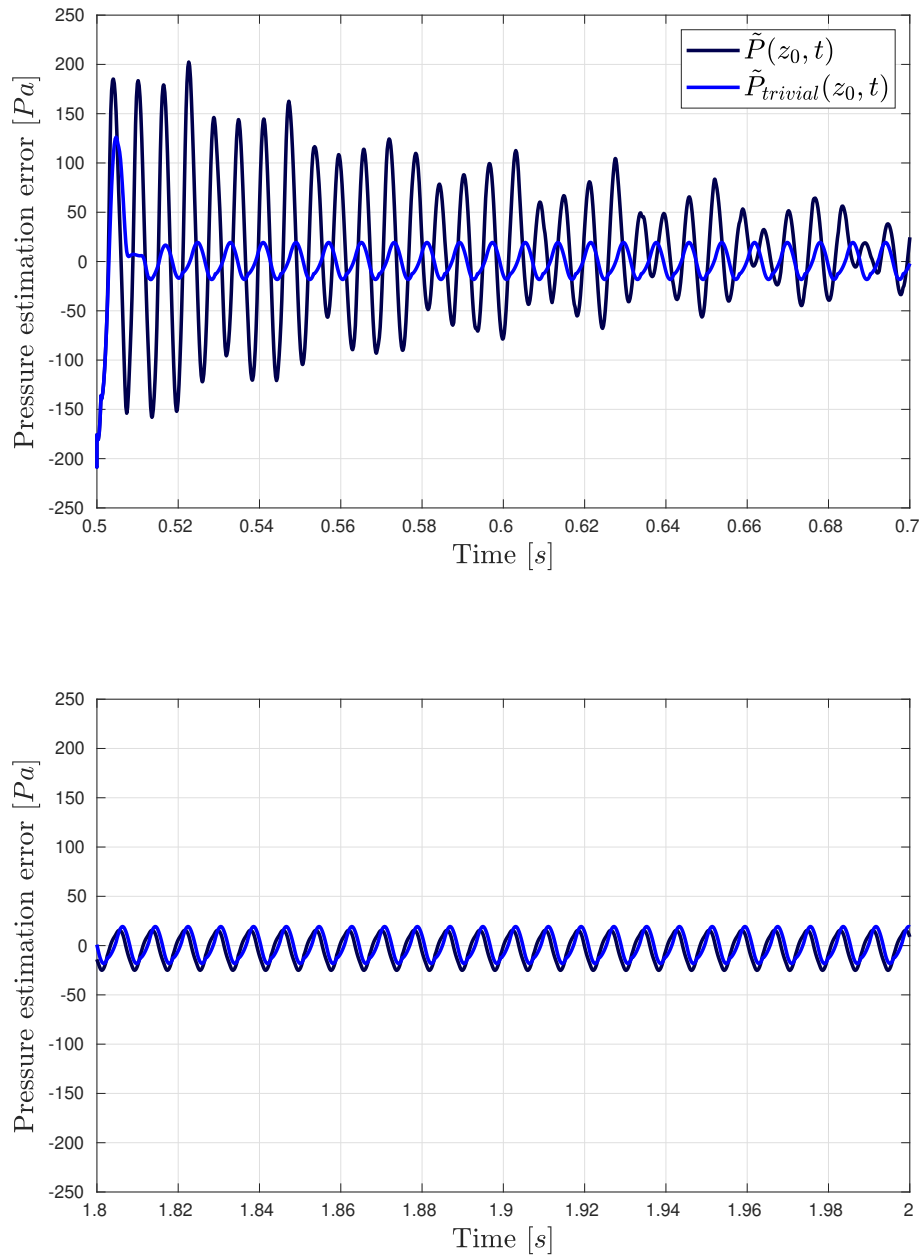


Figure 3.3: Pressure estimation errors. Initial transient (top) and converged estimates (bottom).

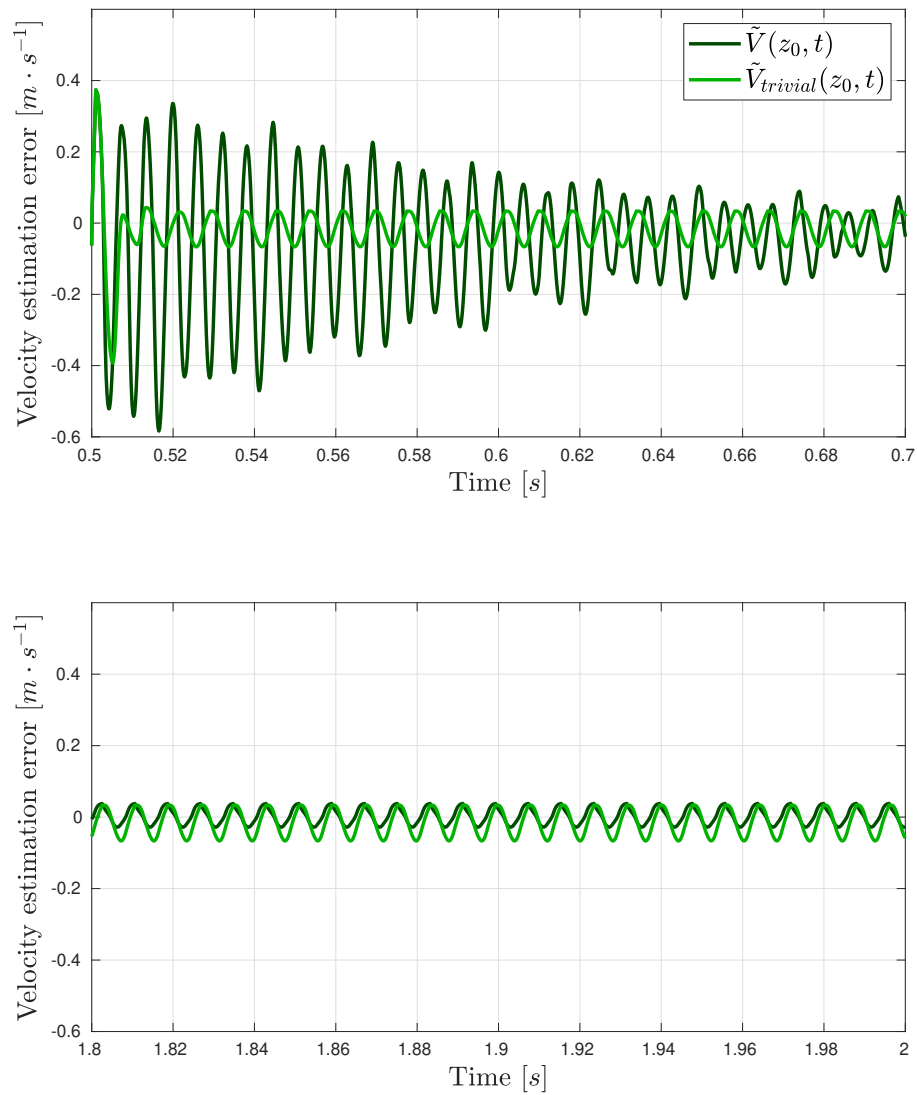


Figure 3.4: Velocity estimation errors. Initial transient (top) and converged estimates (bottom).

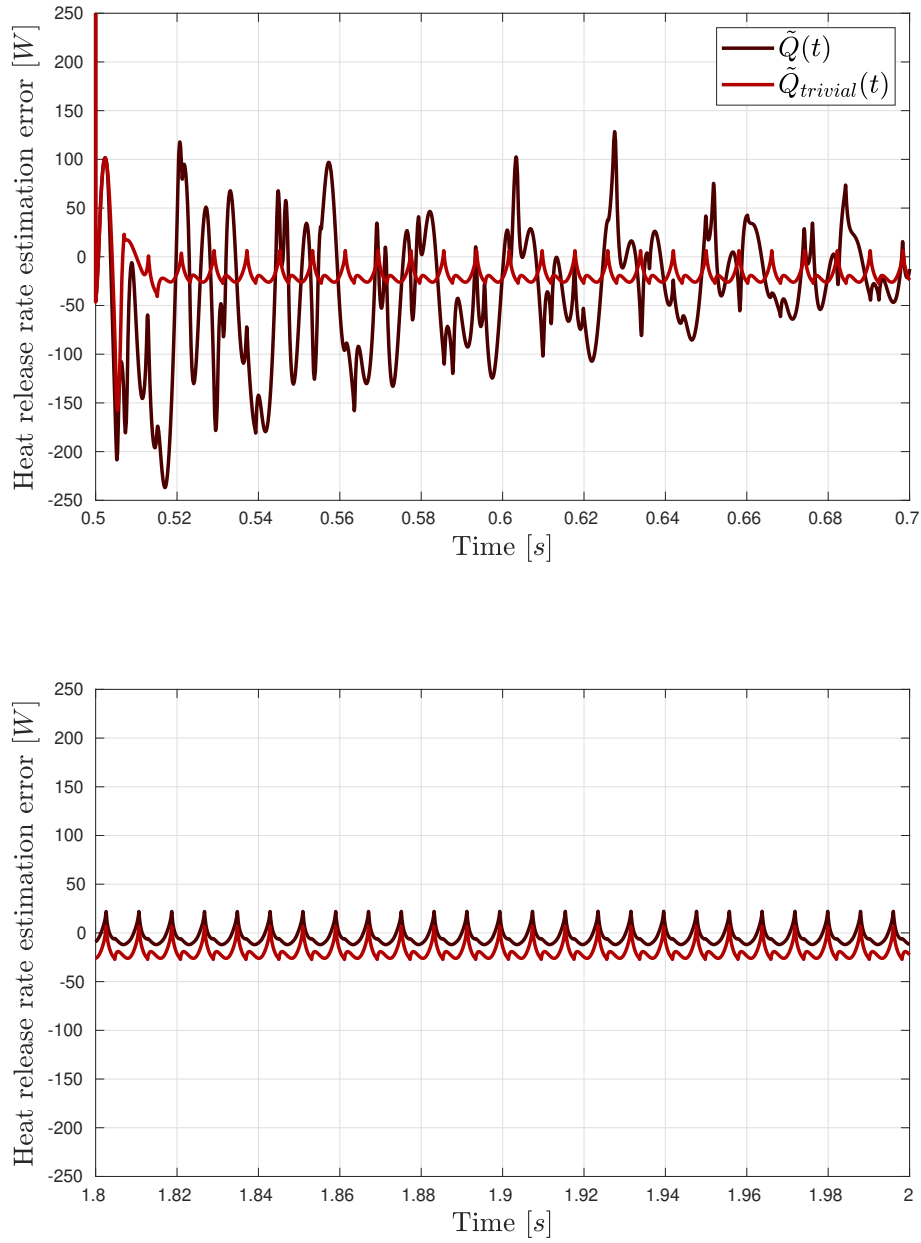


Figure 3.5: Heat release rate estimation errors. Initial transient (top) and converged estimates (bottom).

For both observers, the estimation error stays bounded throughout, with the “trivial” observer having approximately constant error for the duration of the simulation, but the observer (3.17) starting with a large error that converges to a bound. The pressure estimation errors $\tilde{P}_{trivial}(z_0, \cdot)$ in Figures 3.3 appears to be slightly closer to the origin than the estimation error $\tilde{P}(z_0, \cdot)$. However, the estimation errors $\tilde{V}(z_0, \cdot)$ and $\tilde{Q}(\cdot)$ appear to be much closer to the origin than $\tilde{V}_{trivial}(z_0, \cdot)$ and $\tilde{Q}_{trivial}(\cdot)$ in Figures 3.4–3.5. Since it can be difficult to see directly in Figures 3.3–3.5 which observer produces estimates that are on average closer to the true value, the steady-state estimation error norm $\|\tilde{f}\|$ after the initial transient response of the quantity \tilde{f} is estimated via

$$\|\tilde{f}\| \approx \sqrt{\frac{1}{T_2 - T_1} \int_{T_1}^{T_2} \tilde{f}^2(t) dt.}$$

Norm	Observer (3.17)	“Trivial” observer (3.17a)–(3.17h), (3.40)
$\ \tilde{P}(z_0)\ $	14.2	12.8
$\ \tilde{V}(z_0)\ $	2.25×10^{-2}	3.83×10^{-2}
$\ \tilde{Q}\ $	8.93	20.4

Table 3.1: Error norms.

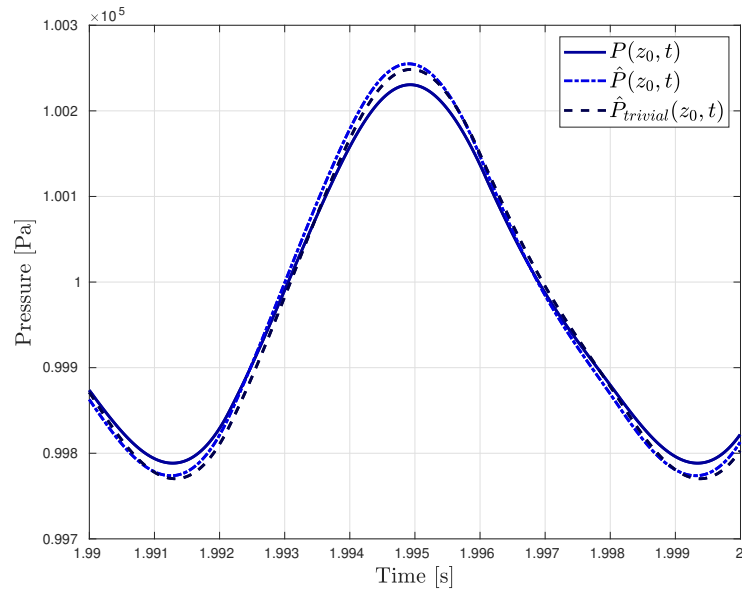
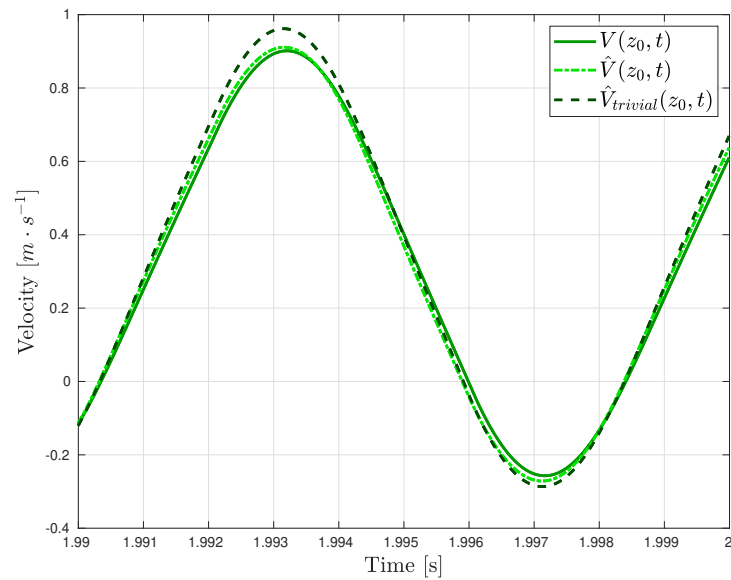
In Table 3.1 the estimates of the estimation error norms for the two observers is summarized to three significant digits, using $T_1 = 1.5$ s and $T_2 = 2$ s. The observer (3.17) has a norm $\|\tilde{P}(z_0)\|$ that is 11.0% higher than the one for the “trivial” observer. However, the norms $\|\tilde{V}(z_0)\|$ and $\|\tilde{Q}\|$ are respectively 69.9% and 128% higher for the “trivial” observer (3.17a)–(3.17h), (3.40) than for the observer (3.17).

Hence, despite the pressure estimation error norms being *slightly* higher for the the observer (3.17) compared to the “trivial” observer, the estimation error norm of the velocity and heat release rate is *significantly* higher for the “trivial” observer. We can thus conclude that overall the observer (3.17) has (after the initial transient) better performance than the “trivial observer” (3.17a)–(3.17h), (3.40) when $\hat{Z}_0 = -5$ and $\hat{Z}_L = 5$ are used in place of $Z_0 = -15$ and $Z_L = 20$ respectively.

To have a sense of the state estimates produced by the two observers as compared to the true states, after the initial transient, the estimates are plotted against the true states for $t \in [1.99, 2.00]$. In Figure 3.6 the pressure $P(z_0, \cdot)$ at z_0 is plotted against the estimate $\hat{P}(z_0, \cdot)$ produced by the observer (3.17) and the estimate $\hat{P}_{trivial}(z_0, \cdot)$ produced by the “trivial observer” (3.17a)–(3.17h), (3.40). Likewise, in Figure 3.7 the velocity $V(z_0, \cdot)$ compared to the estimate $\hat{V}(z_0, \cdot)$ produced by (3.17) and $\hat{V}_{trivial}(z_0, \cdot)$ produced by (3.17a)–(3.17h), (3.40) is plotted. Lastly, the heat release rate $Q(\cdot)$ is plotted against the estimate $\hat{Q}(\cdot)$ and $\hat{Q}_{trivial}(\cdot)$ in Figure 3.8.

3.3.2 Second simulation - Larger impedances

Here the case of incorrect “estimates” taking values $\hat{Z}_0 = -50$, $\hat{Z}_L = 50$ is considered. As in Section 3.3.1, the pressure and velocity estimation errors are plotted for $z = z_0$.

Figure 3.6: Pressure at $z = z_0$ compared to estimates.Figure 3.7: Velocity at $z = z_0$ compared to estimates.

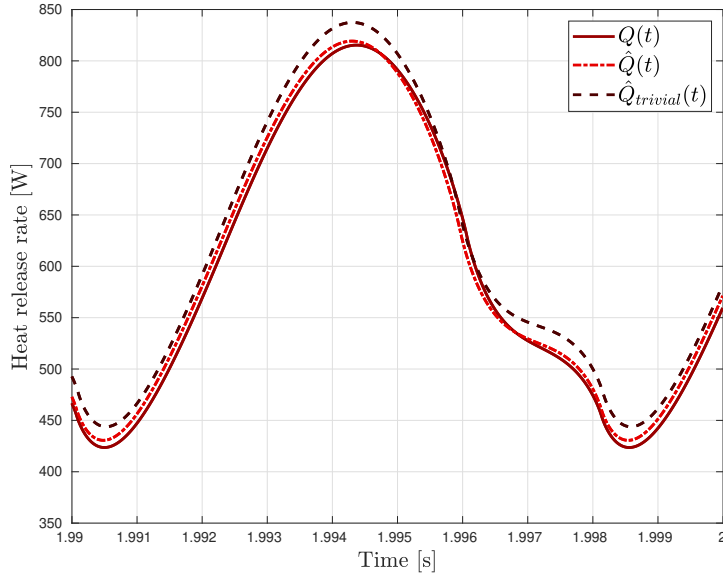


Figure 3.8: Heat release rate compared to estimates.

In Figure 3.9 the pressure estimation error $\tilde{P}(z_0, \cdot)$ for the observer (3.17) is plotted against the corresponding error $\tilde{P}_{trivial}(z_0, \cdot)$ for (3.17a)–(3.17h), (3.40) in dark and lighter blue, respectively. In Figure 3.10 the velocity estimation error $\tilde{V}(z_0, \cdot)$ is plotted in dark green against $\tilde{V}_{trivial}(z_0, \cdot)$ in light green. Lastly, the heat release estimation errors $\tilde{Q}(\cdot)$ and $\tilde{Q}_{trivial}(\cdot)$ are shown in Figure 3.11, in respectively dark and light red.

The pressure estimation errors plotted in Figure 3.9 are fairly similar to each other. However, for the velocity estimation errors in Figures 3.10, the estimation errors from the observer (3.17) have a tighter bound and appear to be closer to the origin after the initial transient as compared to the “trivial” observer (3.17a)–(3.17h), (3.40). The same can be said for the heat release rate estimation errors in Figure 3.11, where the observer (3.17) performs objectively better after the initial transient.

Norm	Observer (3.17)	“Trivial” observer (3.17a)–(3.17h), (3.40)
$\ \tilde{P}(z_0)\ $	32.0	29.0
$\ \tilde{V}(z_0)\ $	5.04×10^{-2}	8.60×10^{-2}
$\ \tilde{Q}\ $	25.7	49.0

Table 3.2: Error norms.

We summarize now the estimated estimation error norms of the observers for the three different plots in Figures 3.9–3.11, in Table 3.2. Similar to the situation in Section 3.3.1, the “trivial” observer performs better in estimating the pressure, but

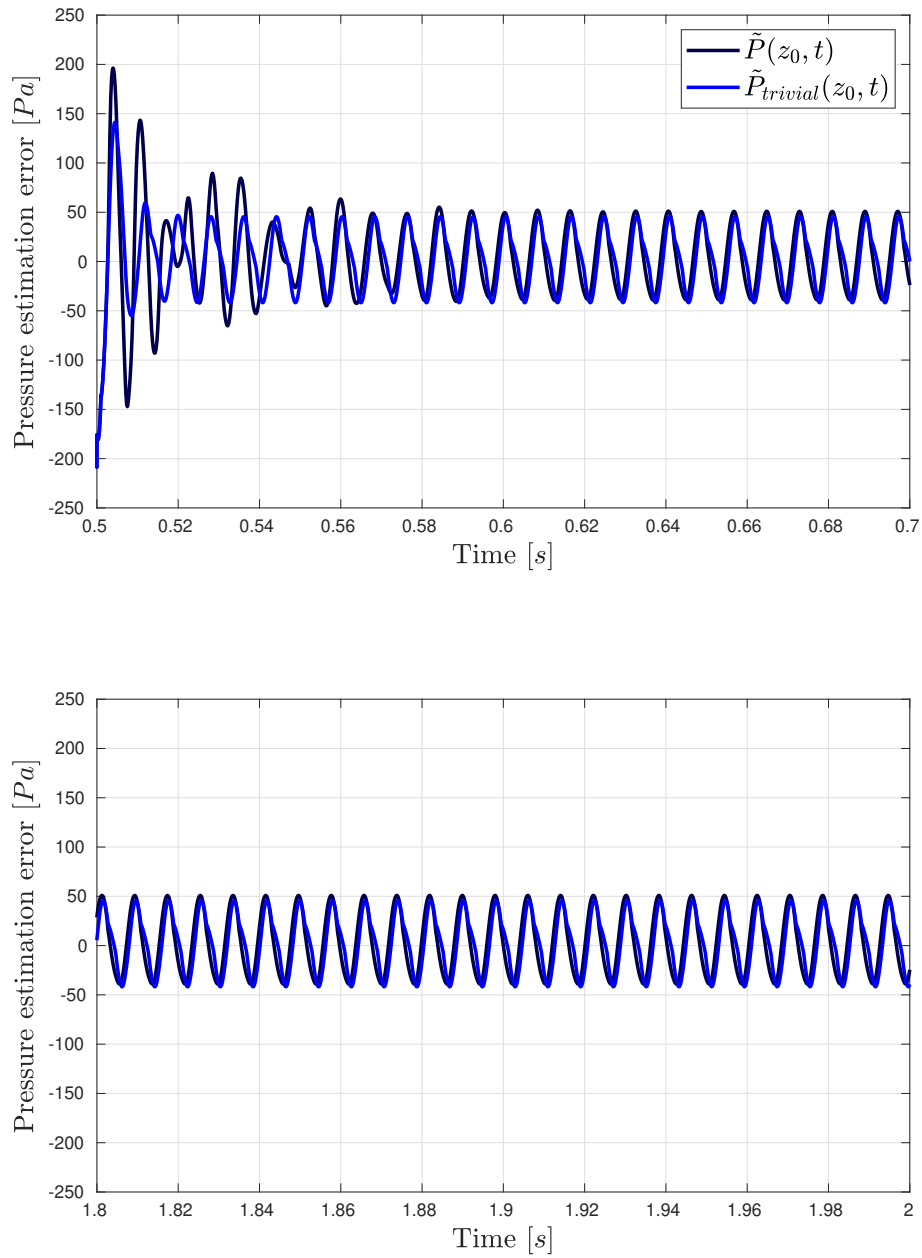


Figure 3.9: Pressure estimation error. Initial transient (top) and converged estimates (bottom).

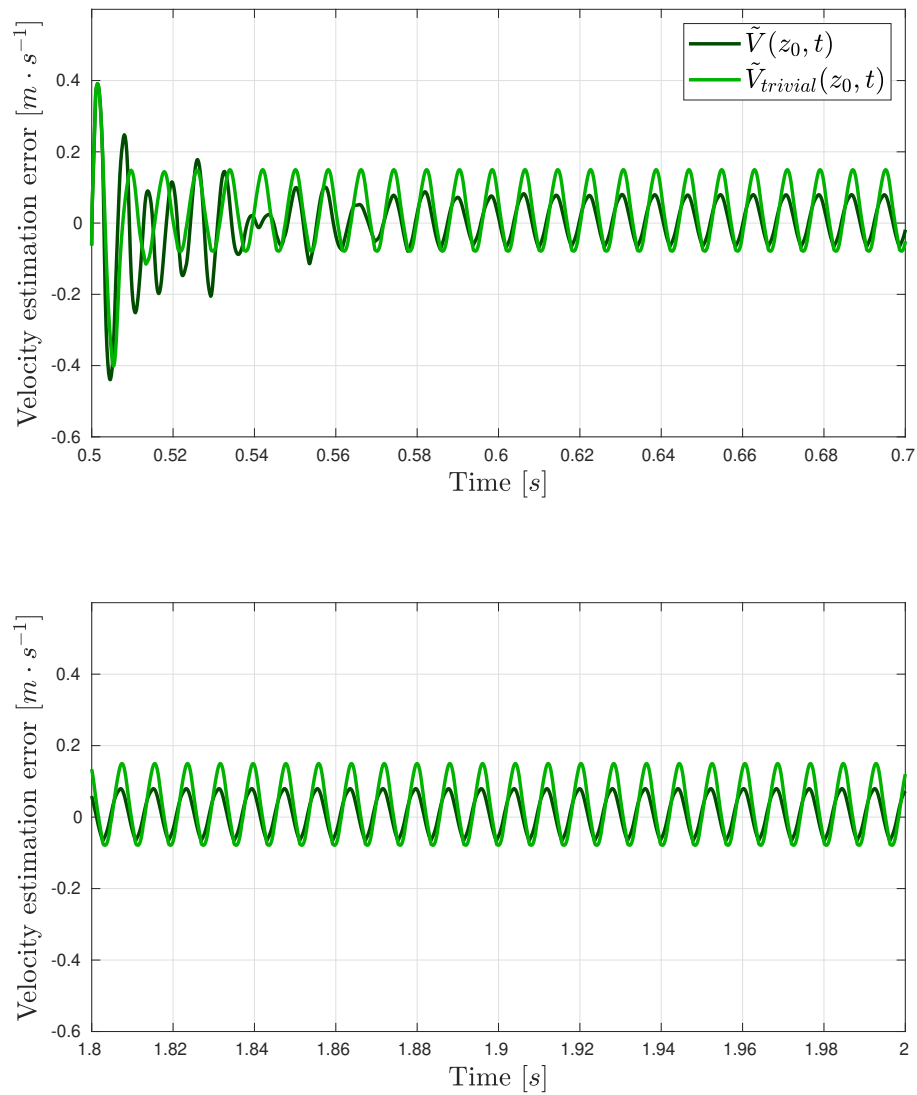


Figure 3.10: Velocity estimation error. Initial transient (top) and converged estimates (bottom).

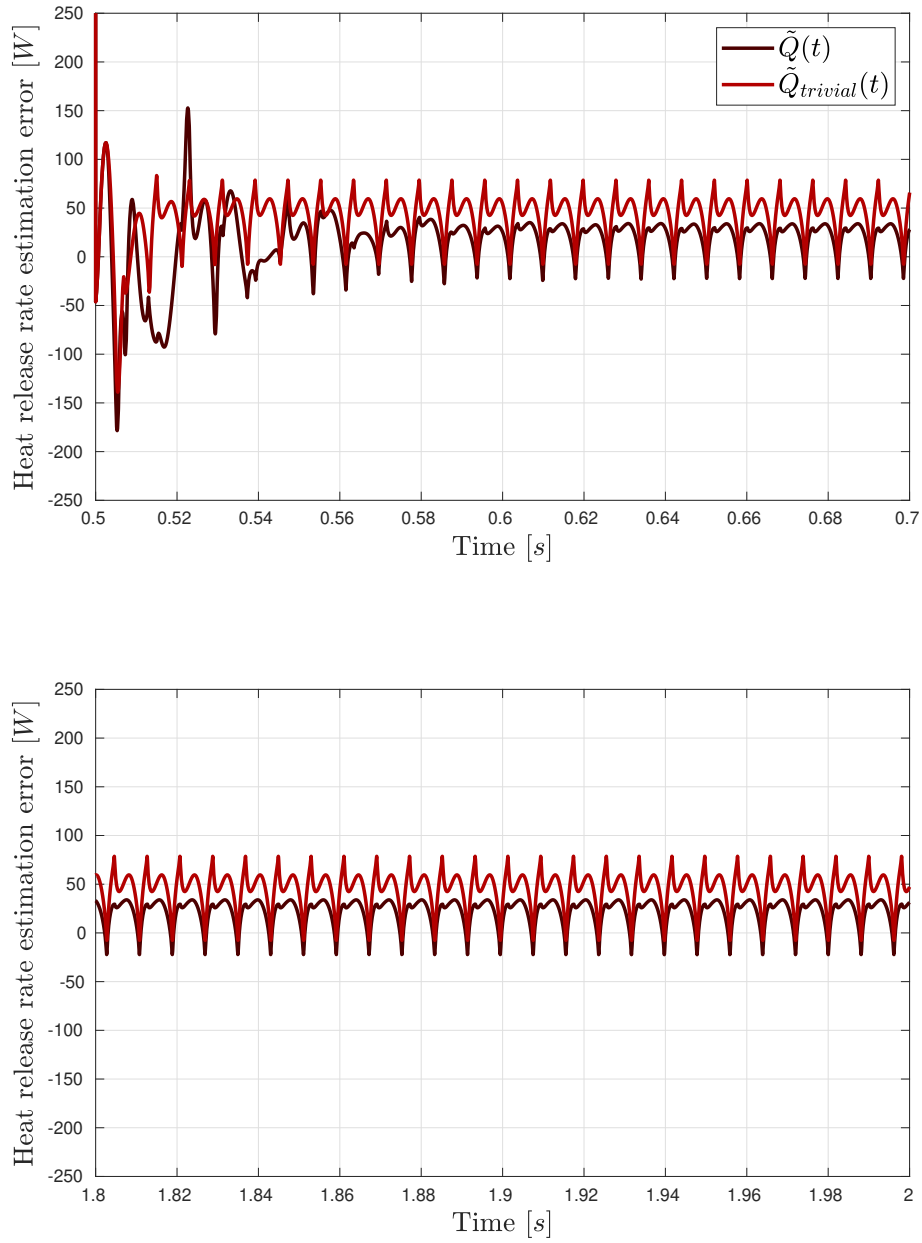


Figure 3.11: Heat release rate estimation error. Initial transient (top) and converged estimates (bottom).

worse in estimation of the velocity and heat release rate. Here, the observer (3.17) has error norm $\|\tilde{P}(z_0)\|$ that is estimated to be 10.0% higher than that for the “trivial” observer (3.17a)–(3.17h), (3.40). On the other hand, the norm $\|\tilde{V}(z_0)\|$ is 70.5% higher for the “trivial” observer. Finally, the estimate of the heat release rate estimation error norm is 90.7% higher for the “trivial observer”, when compared to the corresponding metric for the observer (3.17).

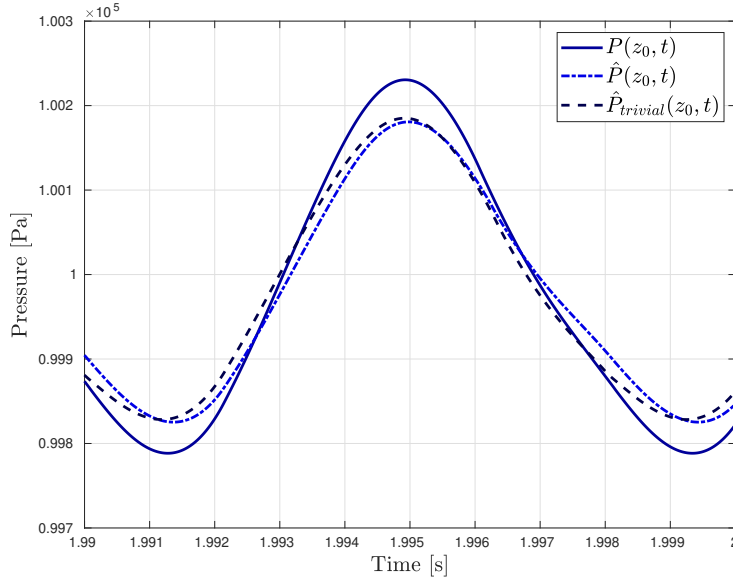


Figure 3.12: Pressure at $z = z_0$ compared to estimates.

Again, we show the state estimates versus the states for the last 10 *ms* of the simulation. In Figure 3.12 the pressure at $z = z_0$ is plotted against the estimates $\hat{P}(z_0, \cdot)$ and $\hat{P}_{trivial}(z_0, \cdot)$. From the Figure, their performance is nearly identical, with $\hat{P}_{trivial}(z_0, \cdot)$ being slightly closer to $P(z_0, \cdot)$ some of the time and $\hat{P}(z_0, \cdot)$ being slightly closer at other times, but overall they are approximately equally far away. In Figure 3.13, the velocity estimate $\hat{V}(z_0, \cdot)$ from (3.17) and the estimate $\hat{V}_{trivial}(z_0, \cdot)$ is plotted against the velocity $V(z_0, \cdot)$. Here it can be clearly seen that $\hat{V}(z_0, \cdot)$ is closer to the true state than $\hat{V}_{trivial}(z_0, \cdot)$ throughout. Lastly, in Figure 3.14, we see the heat release rate $Q(\cdot)$ compared to the estimates $\hat{Q}(\cdot)$ and $\hat{Q}_{trivial}(\cdot)$. As for the velocity, the estimate $\hat{Q}(\cdot)$ is closer to the true state throughout than $\hat{Q}_{trivial}(\cdot)$.

Here the observer (3.17) was tested and compared to the “trivial” observer (3.17a)–(3.17h), (3.40) for two cases when incorrect values of the acoustic impedances are used, firstly when the “estimates” are smaller in absolute value than the true parameters, and secondly when the “estimates” are larger in absolute value. Proposition 1 guarantees that the estimation errors from (3.17) remain bounded whenever these estimates are incorrect, as long as the reflection coefficients \hat{d}_0, \hat{d}_1 are smaller than unity in absolute value. The “trivial” observer (3.17a)–(3.17h),

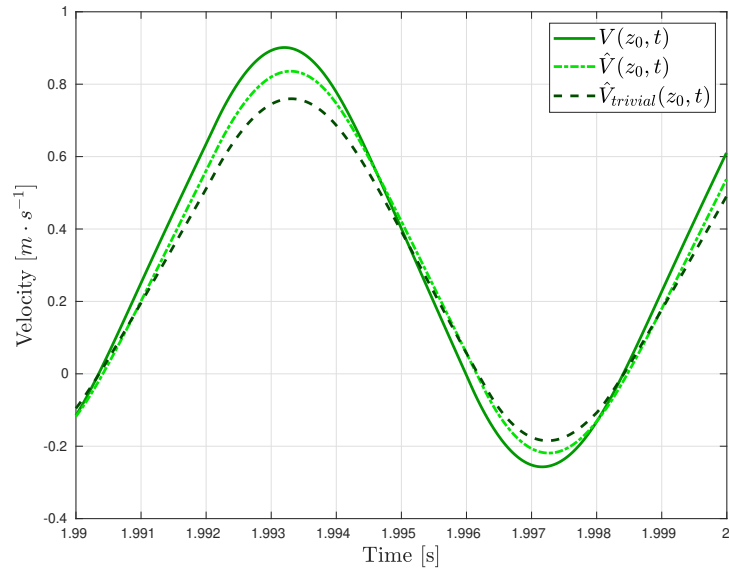
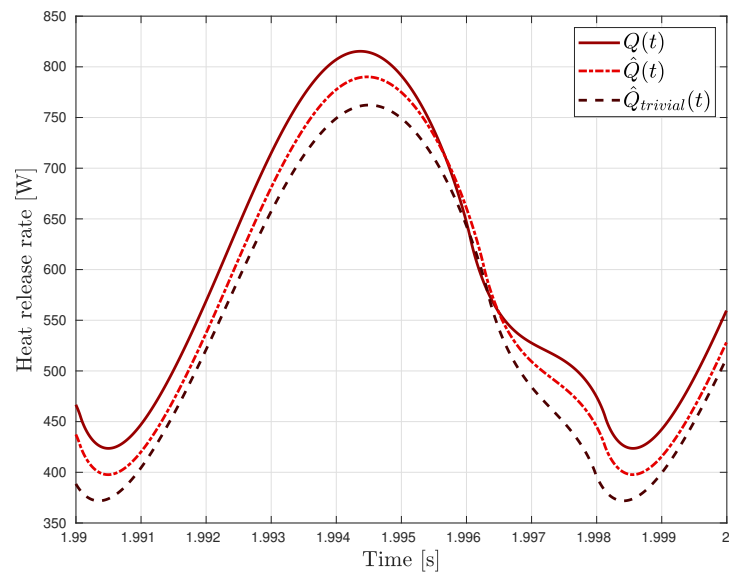
Figure 3.13: Velocity at $z = z_0$ compared to estimates.

Figure 3.14: Heat release rate compared to estimates.

(3.40) does however not have such a guarantee associated to it, but in the two cases considered, the error does indeed remain bounded as can be seen in Figures 3.3–3.5, 3.9–3.11. Despite this, the estimates from (3.17) have overall better performance when using incorrect values of the boundary acoustic impedances than the “trivial” observer.

Comparing Figures 3.6–3.8 to Figures 3.12–3.14, we see the estimates using \hat{Z}_0 , \hat{Z}_L smaller than Z_0 , Z_L in absolute value are in general larger than the true states, whereas the estimates using \hat{Z}_0 , \hat{Z}_L larger than Z_0 , Z_L in absolute value end up being smaller than the true states. This is to be expected as an impedance closer to the characteristic impedance k results the estimated reflection coefficients \hat{d}_0 , \hat{d}_1 being closer to zero, and hence introduces more damping into the system. Since using values of the acoustic impedances smaller than the true values causes the observer to exaggerate the estimates, and likewise using values larger than the true values causes the observer to underestimate the states, to achieve correct state estimates it is important to have as correct estimates of the acoustic impedances at hand, which is the focus of Chapter 4. We test next the state observer on experimental data.

3.4 Experiment

We consider in this section the experimental setup consisting of the Rijke tube as shown in Figure ii.5 together with the electrical heater shown in Figures ii.6–ii.7 placed in the interior of tube, as described in the introduction to Part II. Supplying power to the electrical heater via the power supply shown in Figure ii.8, thermoacoustic instabilities are incited within the tube. Recall that the measured and estimated physical parameters for the experimental setup are documented in Table ii.2.

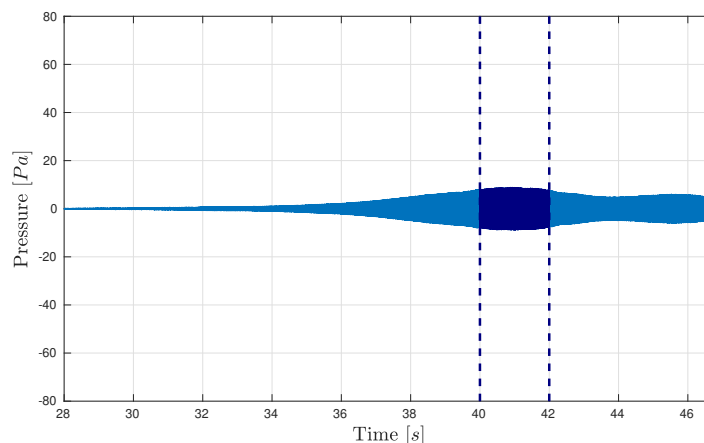


Figure 3.15: Boundary pressure measurement, taken at $z = 0$ m. See Figure ii.12 for sensor placement. Observer tested in dark blue region.

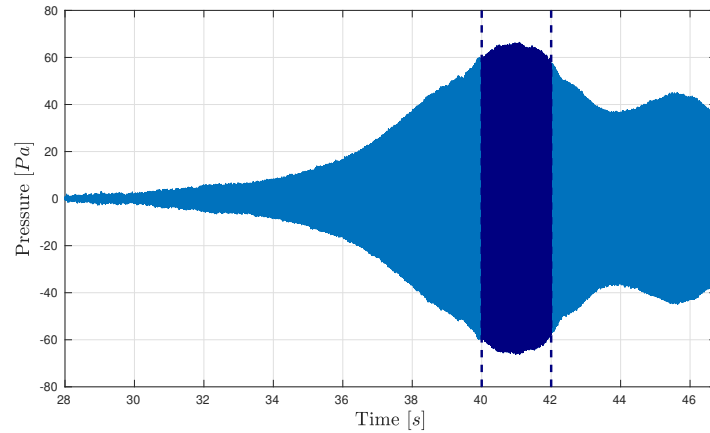


Figure 3.16: In-domain pressure measurement, taken at $z = 0.85 \text{ m}$. See Figure ii.13 for sensor placement. Observer tested in dark blue region.

Also as described in the introduction to Part II, two microphones positioned as shown in Figures ii.12–ii.13 pick up pressure time series data from the thermoacoustic instability. In Figure 3.15 the pressure measurement time series taken at the lower boundary ($z = 0$, corresponding to Figure ii.12) of the tube is plotted, while in Figure 3.16 we see the in-domain pressure measurement ($z = z_v$, corresponding to Figure ii.13) plotted. The plots are shown from time $t = 28 \text{ s}$ after the Rijke tube is turned on, as this is when thermoacoustic instabilities started to develop. The region in Figures 3.15–3.16 which is shown in dark blue is the time interval $t \in [40 \text{ } 42]$ over which the observer is to be tested. As expected, the boundary pressure measurement has a much smaller magnitude than the in-domain pressure measurement, since it is close to a node. We test now the observer (3.17) to see how well it uses the data shown in Figure 3.15 to estimate the data in Figure 3.16. For simplicity, only the observer (3.17) and not the “trivial” observer is tested here.

Since the boundary impedances Z_0, Z_L are here unknown, a range of values are tested. In Figure 3.17, the observer is tested using guessed values of the impedances set to $Z_z = \pm 5 \text{ Pa} \cdot \text{s} \cdot \text{m}^{-1}$ for $z \in \{0, L\}$. The estimate produced by the observer at position $z = z_v$ is plotted in grey and compared to the measured pressure at vertical position $z = z_v$. It is apparent that the pressure estimate overshoots the measured pressure by a significant amount. On the other, in Figure 3.18 the impedances are set to $Z_z = \pm 50 \text{ Pa} \cdot \text{s} \cdot \text{m}^{-1}$. Here the observer produces pressure estimates with amplitudes smaller than the measured pressure at $z = z_v$.

To have a clearer view of the discrepancy between measured and estimated pressure, in Figure 3.19 the estimates compared to the measured pressure at $z = z_v$ is plotted for a shorter interval of time $t \in [41.98 \text{ } 42]$, being the last 20 ms of the observer test. Here, in addition to $Z_z = \pm 5 \text{ Pa} \cdot \text{s} \cdot \text{m}^{-1}$ and $Z_z = \pm 50 \text{ Pa} \cdot \text{s} \cdot \text{m}^{-1}$, two values of impedance between these, namely $Z_z = \pm 10 \text{ Pa} \cdot \text{s} \cdot \text{m}^{-1}$ and

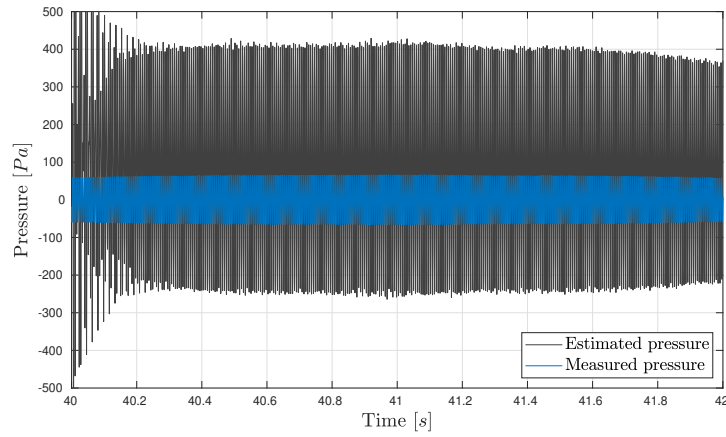


Figure 3.17: Measured (blue line) compared to estimated (grey line) gauge pressure using impedances $Z_z = \pm 5 \text{ Pa} \cdot \text{s} \cdot \text{m}^{-1}$, $z \in \{0, L\}$ at $z = z_v$.

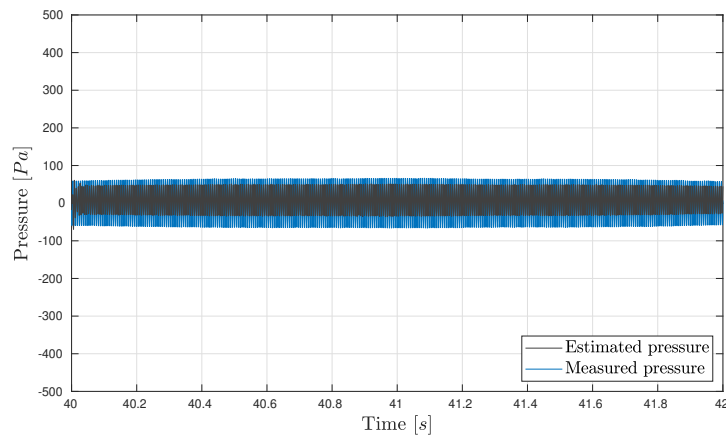


Figure 3.18: Measured (blue line) compared to estimated (grey line) gauge pressure using impedances $Z_z = \pm 50 \text{ Pa} \cdot \text{s} \cdot \text{m}^{-1}$, $z \in \{0, L\}$ at $z = z_v$.

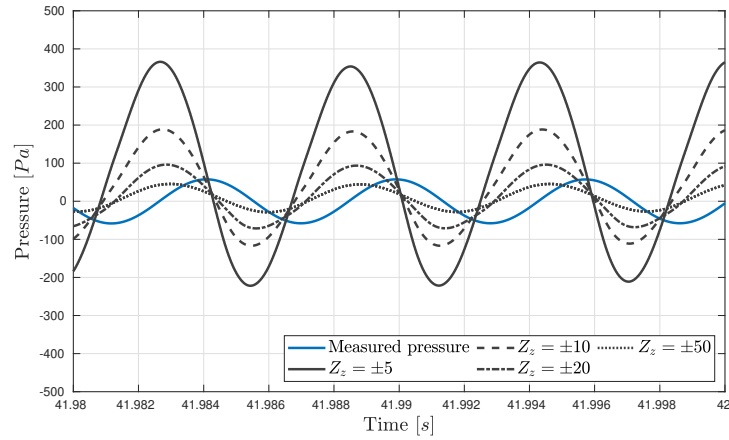


Figure 3.19: Measured (blue line) compared to estimated (grey lines) gauge pressure for multiple values of Z_z , $z \in \{0, L\}$ (see legend) at $z = z_v$. Shown for final 20 ms of observer test.

$Z_z = \pm 20 \text{ Pa} \cdot \text{s} \cdot \text{m}^{-1}$, are tested. As hinted at by Figures 3.17–3.18, one can see that the estimated amplitude is highly sensitive to the values of impedance used in the observer. This indicates that for more accurate estimation of the pressure, identification of the correct boundary impedance, being the focus of Chapter 4, is crucial. Additionally one sees in Figure 3.19 that the estimates are in general phase shifted and shifted away from the origin compared to the measured gauge pressure. This is further discussed in Section 3.5.

3.5 Discussion

The observer (3.17) features a nonlinear model of the heat release (2.43a) and has proven convergence, but with the tradeoff that an asymptotically convergent error is introduced into the dynamics. It has been tested and compared to the “trivial” observer which has no convergence guarantee, but does not introduce such an error into its dynamics.

The simulation results presented in Section 3.3 were in general as expected, although the “trivial observer” has in most cases surprisingly good performance. In the experimental part, Section 3.4, the results are more interesting. While using incorrect acoustic impedances the simulations causes *slight* offsets in the estimates compared to the true values, as can be seen in Figures 3.6–3.8, 3.12–3.14, in the experiments the variation in amplitude based on value of impedance used is much larger, as one can see in Figure 3.19.

In addition to the estimated amplitude being very sensitive to the acoustic impedance, the estimates shown in Figure 3.19 are phase-shifted compared to the measured pressure signal. There could be multiple reasons for this, a pos-

sible one being that the model (2.43) on which the algorithm design is based neglects certain aspects of the physics which are involved. With respect to the acoustic impedances, an assumption made in Chapter 2 is to model the acoustic impedances as constant scalars, hence leaving out possible reactive effects. However in practice one typically has reactive effects in the impedance of an open-ended tube [Levine & Schwinger 1948], and leaving this out in the modelling could be a possible explanation for the observed phase shift.

Another possible modelling error could be due to assumptions regarding heat transfer. In the particular experimental setup used here, the tube used is made of steel, which is a metal and hence conducts heat well. With the heater having been turned on for some time, inevitably the tube heats up, which then in turn influences the temperature T_g of the gas around the heater. As is seen in (2.43a), the rate of change of heat release rate is directly proportional to the difference between the wire and the gas temperature. The temperature of the gas documented in Table ii.2 is of approximate room temperature, which may in practice be wrong. Indeed, as is documented in the literature [Du *et al.* 2019], the temperature of the gas immediately surrounding the electrical heater tends to be significantly higher than the standard ambient room temperature surrounding the tube.

Therefore, in addition to the pressure measurement, a useful auxiliary sensor signal to use in the observer could be the temperature of the gas around the heater. Alternatively, observers that use more complicated models of the Rijke tube than (2.43) could be a viable research direction, with an observer that estimates the temperature distribution in the tube and its influence on the acoustics being an interesting idea.

The Rijke Tube – Parameter Identifier

Contents

4.1 Literature review	74
4.2 Parameter identifier	75
4.2.1 Model in Riemann coordinates	76
4.2.2 Regressor form	77
4.2.3 Identification scheme	78
4.3 Simulations	79
4.3.1 Parameter identification simulations	79
4.3.2 State observer simulations - Correct boundary coefficients	81
4.4 Experiments	87
4.4.1 Parameter identification experiment	87
4.4.2 State observer experiment - Estimated boundary coefficients	89
4.5 Discussion	90

Le tube de Rijke, modélisé comme ayant des extrémités ouvertes idéales, possède aux frontières des coefficients de réflexion $d_r = -1$. En pratique, il y a toujours un amortissement inconnu présent, ce qui implique $|d_r| < 1$. La sensibilité des estimations d'état de l'observateur proposé dans le chapitre 3 aux différentes valeurs des coefficients limites inconnus motive l'identification de ces paramètres. Après une revue de la littérature sur le sujet, nous proposons dans ce chapitre une méthode d'estimation de ces paramètres à partir d'une seule mesure de pression. Le modèle (2.44) qui, à section constante, modélise le tube de Rijke avec le réchauffeur éteint, est réécrit en coordonnées de Riemann. En utilisant la méthode des caractéristiques, nous exprimons le problème d'identification sous forme d'une régression linéaire. Nous proposons de résoudre ce problème par une méthode des moindres carrés avec un facteur d'oubli pour estimer les impédances acoustiques aux frontières. Nous effectuons d'abord des simulations, puis nous utilisons des données expérimentales. Nous testons l'observateur du chapitre 3 avec les valeurs identifiées des paramètres de frontière.

In theory the Rijke tube has ideal open ends with reflection coefficients $d_r = -1$; in practice there is always unknown damping present, which implies $|d_r| < 1$. Sensitivity of the state estimates from the observer proposed in Chapter 3 to different values of the unknown boundary coefficients motivates identification of these parameters in practice. After a literature review on the topic, we propose in this chapter a method for estimating these parameters from a single pressure measurement. The model (2.44) which, with constant cross-sectional area, models the Rijke tube with the heater turned off, is rewritten in Riemann coordinates. Using the Method Of Characteristics (MOC), a regressor form linear in the unknown parameters and their product is written. We propose applying this regressor form together with Least Squares (LS) with forgetting factor to estimate the boundary acoustic impedances. This is done first in simulations, and subsequently using experimental data. We test the observer from Chapter 3 with the identified values of the boundary parameters.

4.1 Literature review

In addition to design of state observers for estimating the pressure, velocity and heat release from sensor measurements, many of the parameters in the Rijke tube are by default unknown and need to be identified to implement the observers correctly. In [Epperlein *et al.* 2015] a range of classical system identification techniques are applied to estimate various parameters in the Rijke tube. As seen in Chapter 3, one class of parameters that can have a large impact on obtaining the correct estimates is the boundary acoustic impedances. These parameters appear in the acoustic boundary conditions (2.43d)–(2.43e) of the Rijke tube acoustic model.

In particular for combustion chambers susceptible to thermoacoustic instabilities, the chambers are in practice interfaced to complex turbomachinery during their operation, which in turn determines the impedances, making it a daunting task to analytically compute the quantities for all operating conditions [Poinsot 2017]. In the Rijke tube the acoustic impedances are in practice open ends with a bit of damping, and hence simpler than the impedances one finds in real combustion chambers. Hence, studying the problem of acoustic impedance estimation in the Rijke tube can be seen as a stepping stone towards understanding how to estimate the acoustic impedances in more complicated cases.

An early method for determination of boundary acoustic impedances developed is the Standing-Wave-Ratio (SWR) method [Kathuriya & Munjal 1975] where the positions of nodes and antinodes of a standing wave inside a tube connected to the acoustic boundary impedances of interest are identified by moving a microphone along the tube, and based on this information the acoustic impedances can be computed. Later, the now much used two-microphone method was introduced by [Seybert & Ross 1977]. The method consists of exciting the acoustic system at the boundary anticollocated to the unknown acoustic boundary with an acoustic source randomly fluctuating within a narrow bandwidth around the frequency one wishes to estimate the boundary impedance for. Two microphones are then placed

at different positions along the tube, and the boundary acoustic impedance is calculated based on the auto-spectral densities of the pressure at the respective points and their relative cross-spectral density. The original two-microphone method does not take into account uncertainty in the estimate, with an improved version doing this suggested in [Schultz *et al.* 2007].

The methods for estimating acoustic impedance mentioned above were designed to be applied with frequency domain data, assuming the impedance to be a general linear system with velocity as the input and pressure as the output, and hence typically giving a complex frequency response as the estimate of the impedance. For more complex cases it is necessary to describe the impedance in that manner, but in the Rijke tube acoustics (2.43) they are simply represented as real scalar quantities, with the pressure at the boundary being proportional to the velocity, rather than a convolution. To estimate these quantities, we propose in Section 4.2 a parameter identification scheme. The method is developed in the time domain and can hence be implemented in real-time.

4.2 Parameter identifier

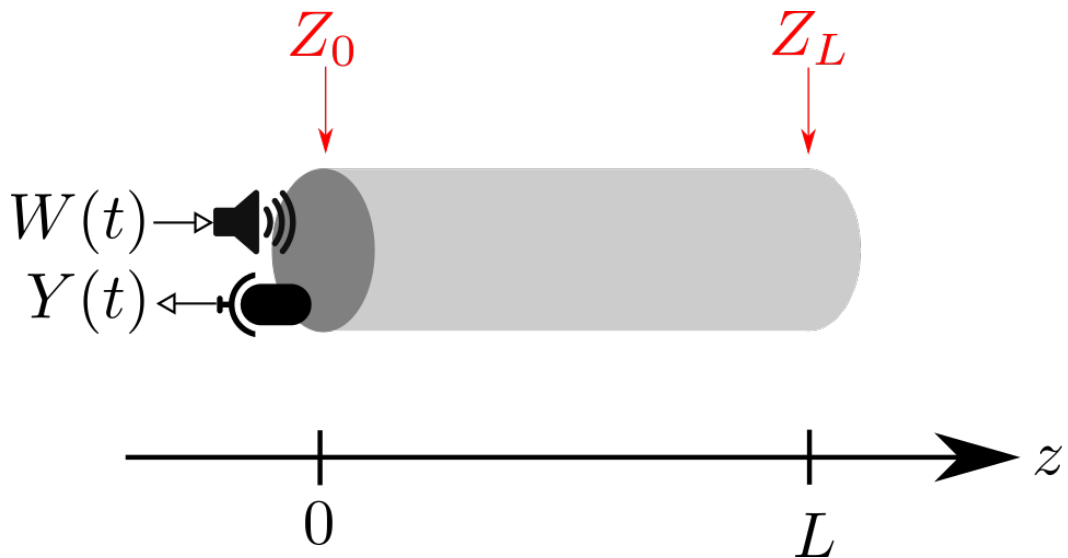


Figure 4.1: Diagram of setup for parameter identification of boundary impedances of cylindrical tube, for application to the Rijke tube. A pressure sensor collocated with a loudspeaker are placed at $z = 0$. Actuating the tube with a sufficiently rich signal and measuring the response, the aim of the parameter identifier is to estimate the unknown boundary impedances Z_0, Z_L .

In Section 3.2 we have proposed a state observer for the Rijke tube and proved that its corresponding estimation error dynamics are GAS with respect to the origin, if all model parameters are known. Also, a minor result was given with respect to

robustness of the observer estimates to error in knowledge of the acoustic reflection coefficients, which can in practice be challenging to compute or estimate accurately. In this section a simple estimation scheme for estimating these reflection coefficients is proposed.

4.2.1 Model in Riemann coordinates

We consider the same setup as shown in Figure ii.1, but with the electrical heater turned off. Also, we let there be a loudspeaker collocated with the pressure measurement at $z = 0$. This results in the setup illustrated in Figure 4.1, with the acoustic impedances Z_0, Z_L , which we are interested in estimating, labelled. The model (2.44) with $a'(\cdot) \equiv 0, W_L \equiv 0$ and $W_0 \equiv W$ can describe this scenario, where W is an identification signal. Note that this model is identical to (2.43b)–(2.43e) with $Q = \bar{Q} \equiv 0$, and can hence represent the Rijke tube with the heater turned off. We assume the measurement Y given by (3.1) is available.

Define the Riemann coordinates

$$u(x, t) = \check{P}(xl, t) + k\check{V}(xl, t) \quad (4.1a)$$

$$v(x, t) = \check{P}(xl, t) - k\check{V}(xl, t) \quad (4.1b)$$

where k the characteristic impedance of the air as given by (3.4). Note that unlike the observer design, where separate Riemann coordinates are needed for the part of the tube above and below the heater, only a single pair of Riemann coordinates are needed here due to the absence of folding the domain around the electrical heater.

Applying this transformation maps the system (2.44) with $a'(\cdot) \equiv 0$ into the system

$$u_t(x, t) = -\lambda u_x(x, t) \quad (4.2a)$$

$$v_t(x, t) = \lambda v_x(x, t) \quad (4.2b)$$

$$u(0, t) = d_0 v(0, t) + U(t) \quad (4.2c)$$

$$v(1, t) = d_1 u(1, t) \quad (4.2d)$$

with reflection coefficients d_0, d_1 given in (3.9) and λ defined by

$$\lambda := \frac{c}{L}. \quad (4.3a)$$

For the sake of obtaining the regressor form needed for parameter identification, we define the signal y as

$$y(t) := v(0, t) \quad (4.4)$$

as the output signal of (4.2). The respective I/O signals U and y from the boundary (4.2c) are related to the physical I/O signals W and Y from the boundary (2.44d) via the relations

$$U(t) = (1 - d_0)W(t) \quad (4.5a)$$

$$y(t) = \frac{2}{1+d_0}Y(t) - \frac{1-d_0}{1+d_0}W(t). \quad (4.5b)$$

Next in Section 4.2.2, the model in Riemann coordinates (4.2) is written in a regressor form suitable for parameter identification of the unknown reflection coefficients d_0 , d_1 using physical I/O signals W and Y .

4.2.2 Regressor form

The regressor form is given by the following Lemma.

Lemma 1. *Consider the duct acoustics described by (2.44) with $a'(\cdot) \equiv 0$, $W_0 = W$ and $W_L \equiv 0$, and output signal Y given by (3.1). Then the relation*

$$r(t) = \vartheta^\top R(t) \quad (4.6)$$

where r is defined by

$$r(t) := Y(t) - \frac{1}{2}W(t), \quad (4.7)$$

the parameter vector ϑ is written in terms of d_0 , d_1 , defined in (3.9), as

$$\vartheta := \begin{bmatrix} d_0 d_1 \\ d_0 \\ d_1 \end{bmatrix}, \quad (4.8)$$

and known signal vector R is

$$R(t) := \begin{bmatrix} r(t - 2\lambda^{-1}) \\ -\frac{1}{2}W(t) \\ \frac{1}{2}W(t - 2\lambda^{-1}) \end{bmatrix}, \quad (4.9)$$

holds true.

Proof. Applying the plant dynamics (4.2) and output signal definition (4.4), we have the relation between current and past characteristic I/O signals together with parameters

$$y(t) = d_1 d_0 y(t - 2\lambda^{-1}) + d_1 U(t - 2\lambda^{-1}). \quad (4.10)$$

Next, substituting (4.5) into (4.10) we obtain

$$\begin{aligned} \frac{2}{1+d_0}Y(t) - \frac{1-d_0}{1+d_0}W(t) &= d_1 d_0 \left(\frac{2}{1+d_0}Y(t - 2\lambda^{-1}) - \frac{1-d_0}{1+d_0}W(t - 2\lambda^{-1}) \right) \\ &\quad + d_1(1-d_0)W(t - 2\lambda^{-1}). \end{aligned} \quad (4.11)$$

With some algebraic manipulation, we end up with

$$\underbrace{Y(t) - \frac{1}{2}W(t)}_{=r(t)} = d_1 d_0 \underbrace{\left(Y(t - 2\lambda^{-1}) - \frac{1}{2}W(t - 2\lambda^{-1}) \right)}_{=r(t-2\lambda^{-1})} + d_0 \left(-\frac{1}{2}W(t) \right)$$

$$+ d_1 \left(\frac{1}{2} W(t - 2\lambda^{-1}) \right) + \underbrace{\frac{1}{2} d_1 d_0^2 W(t - 2\lambda^{-1}) - \frac{1}{2} d_1 d_0^2 W(t - 2\lambda^{-1})}_{=0} \quad (4.12)$$

which can be written as (4.6)–(4.9), and the proof is complete. \square

With the regressor form (4.6), a wide range of parameter identification schemes can be applied to estimate the parameter vector ϑ , given that the signal r and signal vector R are available. Next, in Section 4.2.3 we state sufficient conditions for the parameter estimates to converge when applying modified LS with forgetting factor.

4.2.3 Identification scheme

To apply the regressor form (4.6)–(4.9) to estimate the boundary acoustic impedances Z_0, Z_L via (3.9), we consider modified least squares with forgetting factor. Denote the estimate of ϑ defined in (4.8) as $\hat{\vartheta}$. We can then form an estimate \hat{r} of r as defined in (4.7), by replacing ϑ by $\hat{\vartheta}$ in (4.6), which lets us define

$$\hat{r}(t) := \hat{\vartheta}(t)^\top R(t). \quad (4.13)$$

Modified LS with forgetting factor proposes to update the estimate $\hat{\vartheta}$ via the adaptive law

$$\dot{\hat{\vartheta}}(t) = P(t) (r(t) - \hat{r}(t)) R(t) \quad (4.14a)$$

$$\dot{P}(t) = \begin{cases} \beta P(t) - P(t)R(t)R(t)^\top P(t), & \text{if } \|P(t)\| \leq \bar{P} \\ 0, & \text{otherwise} \end{cases} \quad (4.14b)$$

initialized from $\hat{\vartheta}(0) = \hat{\vartheta}_0 \in \mathbb{R}^{3 \times 1}$, $P(0) = P_0 \in \mathbb{R}^{3 \times 3}$, and $\beta, \bar{P} > 0$ are scalar tuning constants. The following Theorem presents the properties of the adaptive law (4.14).

Theorem 2. *Define $\tilde{r} := r - \hat{r}$. The adaptive law (4.14) guarantees that*

- $\tilde{r}, \hat{\vartheta}, \dot{\hat{\vartheta}} \in L^\infty$
- $\tilde{r}, \dot{\hat{\vartheta}} \in L^2$
- *If $\Psi \in L^\infty$ and Ψ is Persistently Exciting (PE), then $P, P^{-1} \in L^\infty$ and $\hat{\vartheta}(t) \rightarrow \vartheta$ exponentially.*

Proof. For the first two properties, see Proof of Theorem 4.3.5 in [Ioannou & Sun 2012], and for the final property see Proof of Corollary 4.3.2 in [Ioannou & Sun 2012]. \square

The parameter vector ϑ in (4.8) consists of three parameters, whereas we are only interested in estimating two. Hence, the regressor form (4.6) represents an overparametrized system in the unknown coefficients d_0 and d_1 . Denoting $\theta := d_0 d_1$ and $\hat{\theta}$ as the estimate of θ , we propose to solve the optimization problem

$$(\check{d}_0, \check{d}_1) = \arg \min(O(\check{d}_0, \check{d}_1)) \quad (4.15)$$

where $O : \mathbb{R}^2 \mapsto \mathbb{R}$ is given by

$$O(\check{d}_0, \check{d}_1) := \delta_1(\check{d}_0 \check{d}_1 - \hat{\theta})^2 + \delta_2(\check{d}_0 - \hat{d}_0)^2 + \delta_3(\check{d}_1 - \hat{d}_1)^2 \quad (4.16)$$

and

$$\delta_i = \begin{cases} 1, & \text{if } \rho_i \text{ is PE} \\ 0, & \text{otherwise .} \end{cases} \quad (4.17)$$

where ρ_i is the i^{th} component of R .

We test next the parameter estimation scheme in simulations and experiments. The obtained values are then applied together with the observer from Chapter 3.

4.3 Simulations

4.3.1 Parameter identification simulations

Here we apply the parameter estimation scheme proposed in Section 4.2 to estimate the acoustic impedances Z_0, Z_L listed in Table ii.1, testing the update law considered in Theorem 2.

To obtain sufficient information about the acoustic boundary impedances Z_0, Z_1 , the input signal W in (4.8) must be “sufficiently rich”, so that the PE condition in Theorem 2 is satisfied. For the simulations in this section, we choose W as

$$W(t) = 2 \cos\left(\frac{\lambda\pi}{3}t\right) + 2.5 \cos\left(\frac{\lambda\pi}{4}t\right) + 3 \cos(\lambda\pi t)$$

where λ is computed from (4.3a) and (3.7) using parameters in Table ii.1.

A plot of W versus the corresponding measurement signal Y from the simulation for $t \in [0.0, 0.2]$ is shown in Figure 4.2. Using these two signals, the parameter estimation scheme presented in Theorem 2 is implemented with the tuning parameters

$$\beta = 5, \quad \bar{P} = 10^3,$$

and initialized from

$$\hat{\vartheta}_0 = \begin{bmatrix} 0.56 \\ -0.80 \\ -0.70 \end{bmatrix}, \quad P_0 = \begin{bmatrix} 1 & 0 & 0 \\ 0 & 1 & 0 \\ 0 & 0 & 1 \end{bmatrix}.$$

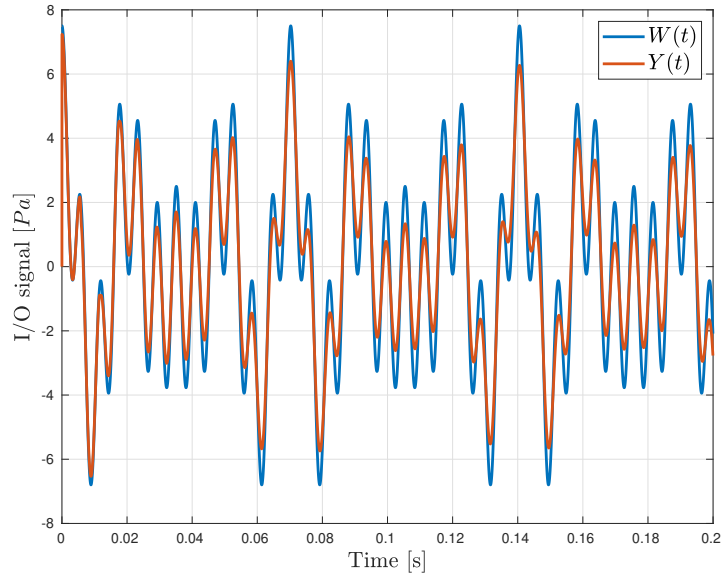


Figure 4.2: Pressure input signal W (in blue) versus pressure output signal Y (in orange) used for parameter identification.

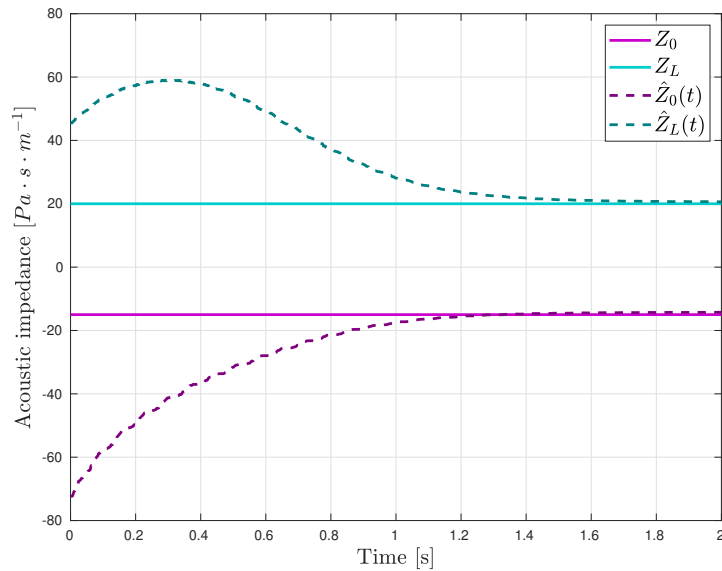


Figure 4.3: Acoustic impedance estimates versus true values.

For each time step, after updating the parameter estimate using (4.14), the optimization problem (4.16) is solved with

$$\delta_1 = 1, \quad \delta_2 = 1, \quad \delta_3 = 1,$$

using the `fminunc` function from MATLAB. The resultant acoustic impedance estimates as a function of time for $t \in [0, 2]$ are plotted in dashed lines against the true parameters, which are represented by solid lines, in Figure 4.3. The impedance Z_0 and its corresponding estimate are in magenta, whereas Z_L and its estimate is plotted in cyan. With the given tuning parameters, the estimates converge to a steady state solution close to the true values within 2 s.

Parameter estimate	Expected value	Variance
\hat{Z}_0	-14.4	6.40×10^{-3}
\hat{Z}_L	20.8	3.58×10^{-2}

Table 4.1: Acoustic impedance estimates.

To obtain values of the acoustic impedances which can be applied to the observer, the expected value and variance of the estimates for the last 0.5 s of the simulation are computed, summarized in Table 4.1. The estimates are not perfect, but are close to the true values tabulated in Table ii.1. The true test of the parameter estimates is in assisting the observer to produce correct state estimates, which is tested next in Section 4.3.2.

4.3.2 State observer simulations - Correct boundary coefficients

The observer (3.17) is now compared to the “trivial observer” (3.17a)–(3.17h), (3.40) when using the estimates of Z_0 , Z_L presented as expected values of $\hat{Z}_0(\cdot)$, $\hat{Z}_L(\cdot)$ documented in Table 4.1. In Figure 4.4, the pressure estimation error $\tilde{P}(z_0, \cdot)$, shown in dark blue, from the observer (3.17) is plotted against the error $\tilde{P}_{trivial}(z_0, \cdot)$, shown in light blue, associated with the “trivial” observer (3.17a)–(3.17h). As done in Chapter 3, the first and last 200 ms of the observer being active is plotted. Also, shown in Figure 4.5 is the estimation error $\tilde{V}(z_0, \cdot)$, in dark green, of the velocity from (3.17) plotted against $\tilde{V}_{trivial}(z_0, \cdot)$ from the “trivial” observer, which is shown in light green. Lastly, in Figure 4.6 we see the heat release rate errors $\tilde{Q}(\cdot)$, in dark red, and $\tilde{Q}_{trivial}(\cdot)$, in light red, plotted against each other.

Comparing Figures 4.4–4.6 to the corresponding Figures 3.3–3.5, 3.9–3.11 from Chapter 3, we see the estimates of Z_0 , Z_L has a profound impact on the correctness of the state estimates, after the initial transient. Indeed, the errors from last 200 ms of the simulation as plotted in Figures 4.4–4.6 are almost at the origin. The estimates of the error norm, computed in the same way as in Chapter 3, is summarized in Table 4.2. Compared to the norms documented in Tables 3.1–3.2, the error norms in Table 4.2 are much smaller in magnitude, as expected. However, in this case the “trivial” observer has better performance for all three state estimates. This

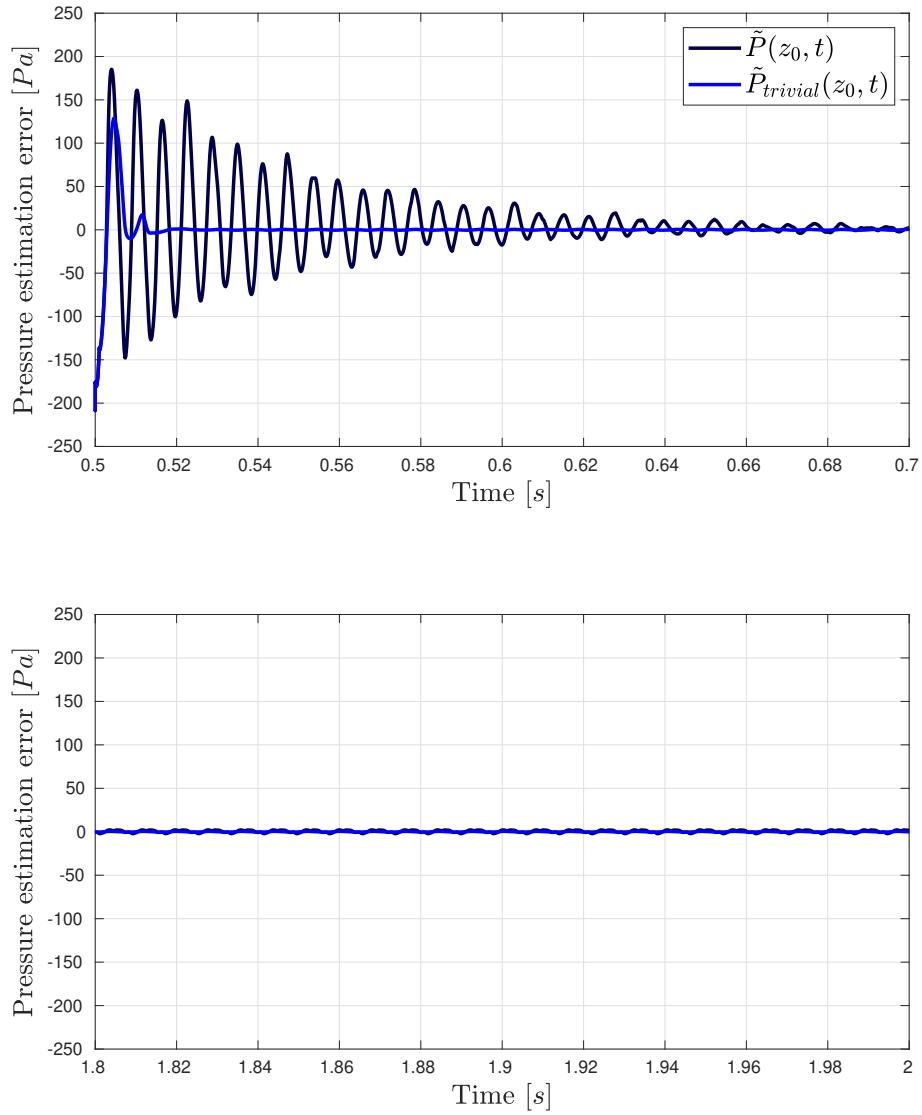


Figure 4.4: Pressure estimation error. Initial transient (top) and converged estimates (bottom).

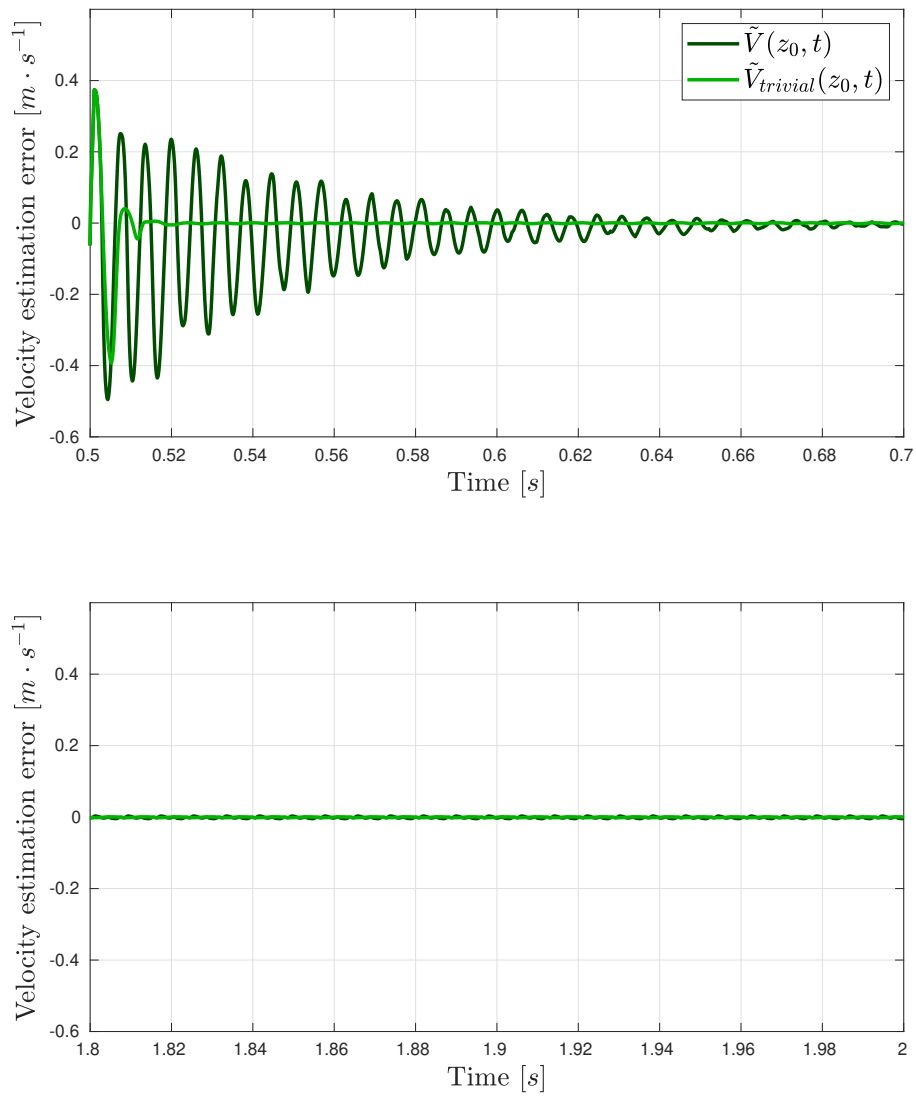


Figure 4.5: Velocity estimation error. Initial transient (top) and converged estimates (bottom).

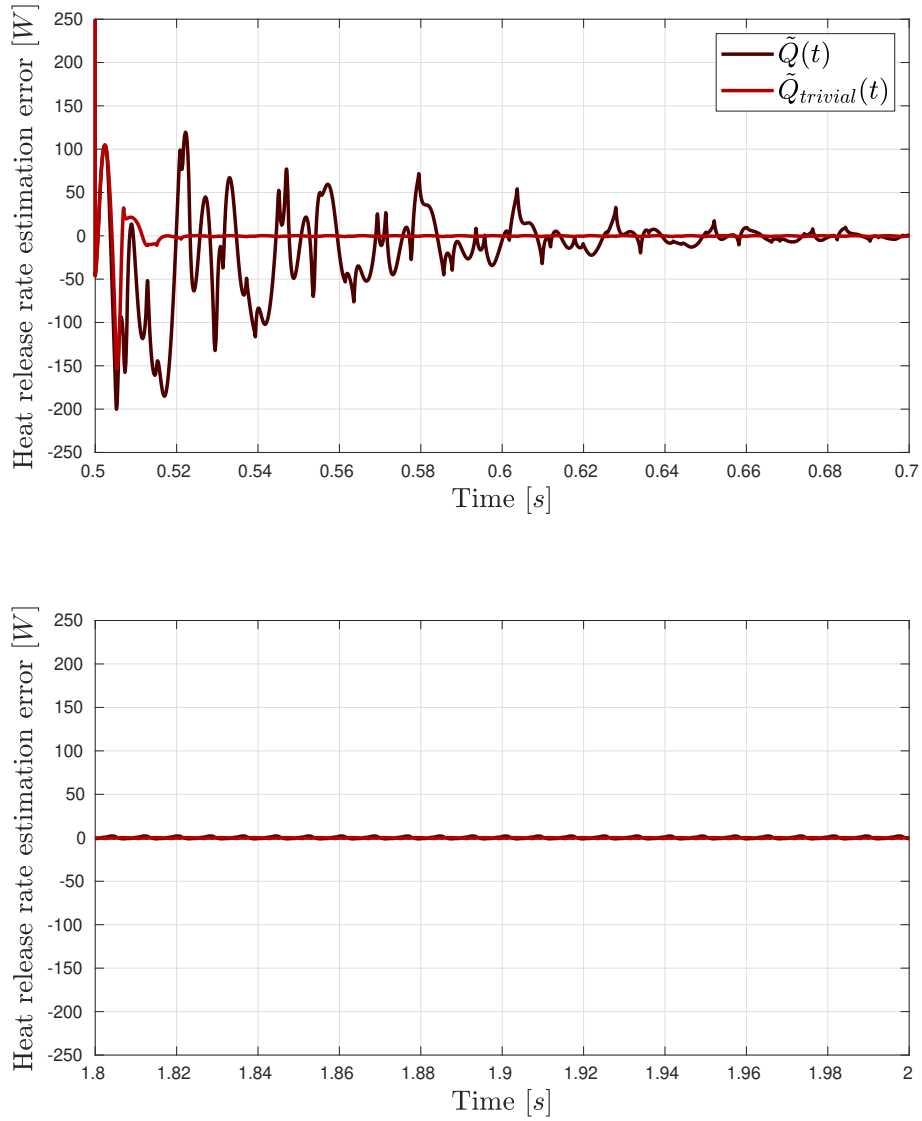
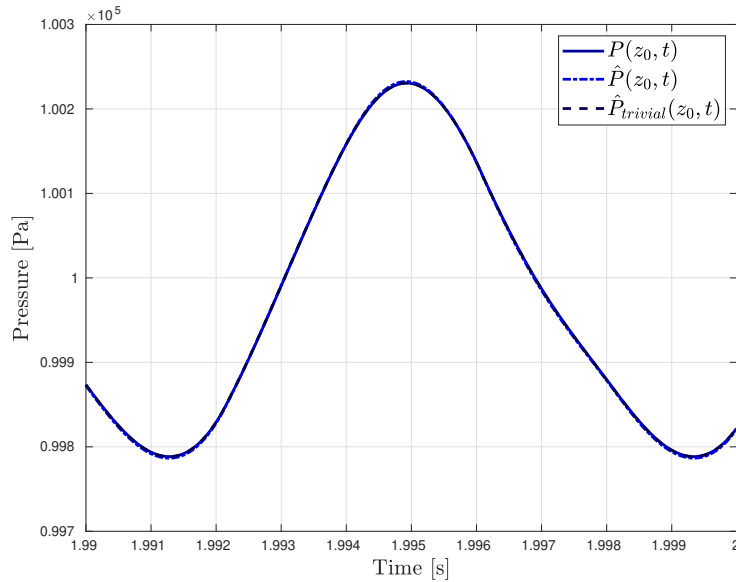


Figure 4.6: Heat release rate estimation errors. Initial transient (top) and converged estimates (bottom).

Norm	Observer (3.17)	“Trivial” observer (3.17a)–(3.17h), (3.40)
$\ \tilde{P}(z_0)\ $	1.44	0.305
$\ \tilde{V}(z_0)\ $	2.3×10^{-3}	9.31×10^{-4}
$\ \tilde{Q}\ $	1.08	0.399

Table 4.2: Error norms.

can be attributed to the asymptotically convergent error that is introduced into the observer (3.17) from reconstructing the unmeasured boundary, which is done in order to be able to guarantee global convergence. This shows there is a trade-off involved, with the global convergence guarantee coming with a possible performance penalty.

Figure 4.7: Pressure at $z = z_0$ compared to estimates.

To see the estimates compared to the true states, they are plotted for the last 10 ms of the simulation in Figure 4.7, which shows the pressure $P(z_0, \cdot)$ versus the estimates $\hat{P}(z_0, \cdot)$ and $\hat{P}_{trivial}(z_0, \cdot)$, Figure 4.8 which shows the velocity $V(z_0, \cdot)$ versus the estimates $\hat{V}(z_0, \cdot)$ and $\hat{V}_{trivial}(z_0, \cdot)$, and Figure 4.9 which shows the heat release $Q(\cdot)$ versus estimates $\hat{Q}(\cdot)$ and $\hat{Q}_{trivial}(\cdot)$. In all three cases, the estimates are almost identical to the states, showing that the error norms documented in Table 4.2 have marginal importance for state estimation purposes.

With the parameter identification algorithm tested on a simulation example in Section 4.3.1 and the parameter estimates subsequently applied to the observer from Chapter 3, we now do the same with the experimental data.

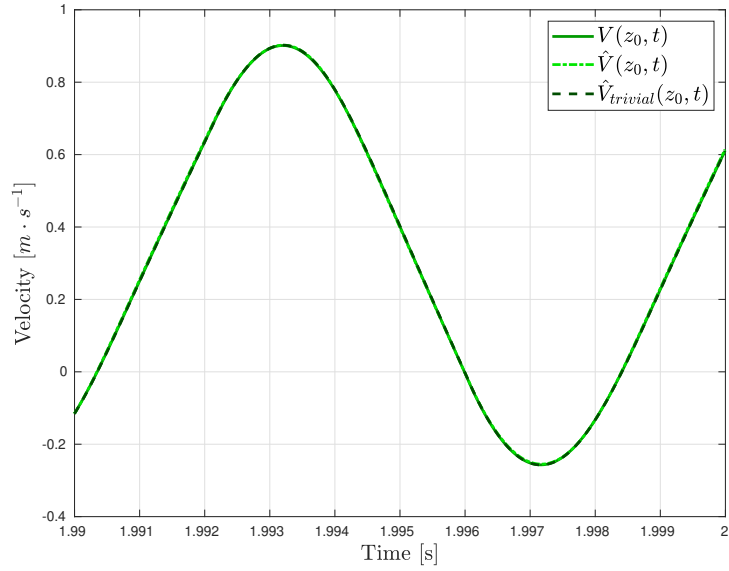
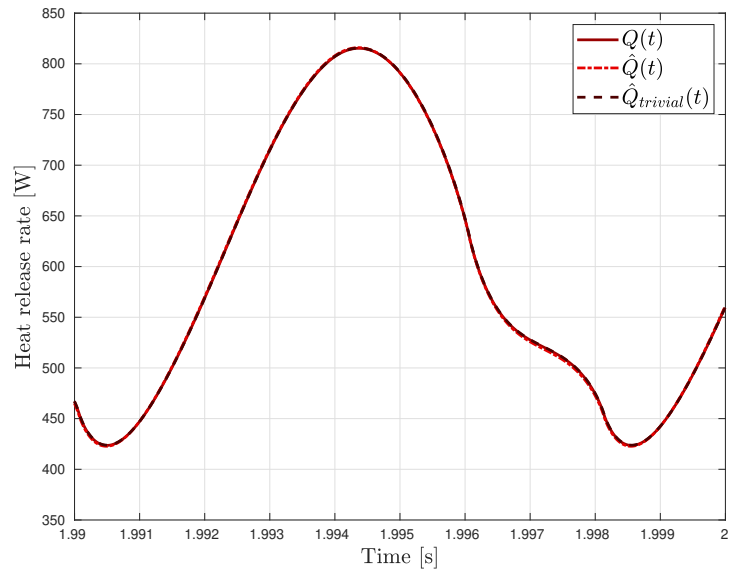
Figure 4.8: Velocity at $z = z_0$ compared to estimates.

Figure 4.9: Heat release rate compared to estimates.

4.4 Experiments

We test in this section the parameter identification method developed in Section 4.2 experimentally. The values obtained are then used in the observer from Chapter 3 to see if any improvement is made over the experimental estimates documented in Section 3.4. For the parameter identification experiment, we use the experimental setup shown in Figure ii.15, with a collocated loudspeaker and microphone. An acoustic identification signal is measured sent into the tube, and the resultant response from the tube is picked up with a microphone.

4.4.1 Parameter identification experiment

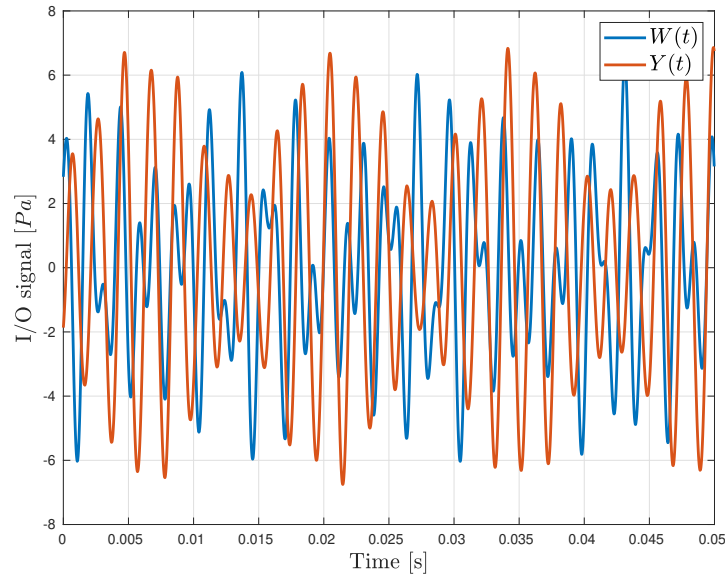


Figure 4.10: Pressure input signal W (in blue) versus pressure output signal Y (in orange) used for parameter identification.

For parameter identification, to excite the tube, we sent in a signal consisting of three separate frequencies, namely $f_1 = 440 \text{ Hz}$, $f_2 = 510 \text{ Hz}$ and $f_3 = 750 \text{ Hz}$. The resultant I/O signals used for parameter identification, as measured by the microphone setup shown in Figure ii.15, are shown for the first 50 ms in Figure 4.10. Using these signals, the parameter estimation scheme from Theorem 2 is implemented with the tuning parameters

$$\beta = 2, \quad \bar{P} = 10^3.$$

The parameter estimation scheme is initialized from three different initial conditions

$$\hat{\vartheta}_0^1 = \begin{bmatrix} 0.25 \\ -0.50 \\ -0.50 \end{bmatrix}, \quad \hat{\vartheta}_0^2 = \begin{bmatrix} 0.25 \\ 0.50 \\ 0.50 \end{bmatrix}, \quad \hat{\vartheta}_0^3 = \begin{bmatrix} -0.1875 \\ -0.25 \\ 0.75 \end{bmatrix}$$

but the same value for P_0 as used in Section 4.3.1.

For each time step, after updating the parameter estimate using (4.14), the optimization problem (4.16) is solved with

$$\delta_1 = 1, \quad \delta_2 = 0, \quad \delta_3 = 1.$$

The resultant acoustic impedances as a function of time are plotted in Figure 4.11

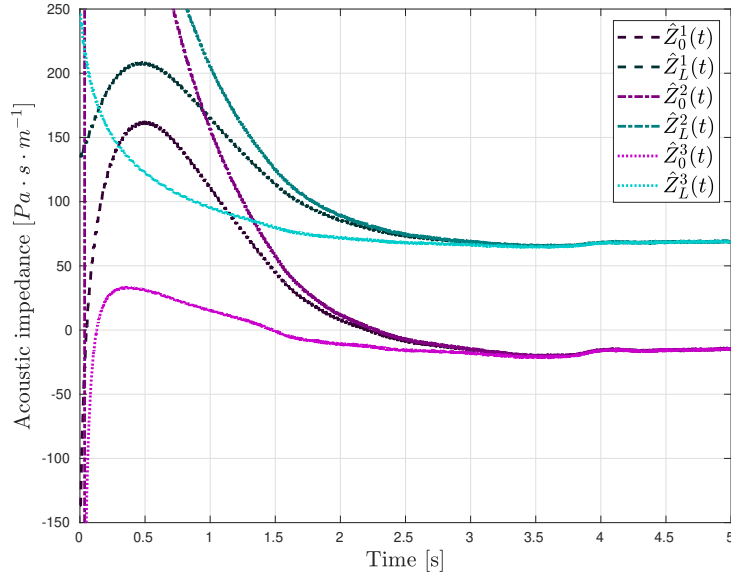


Figure 4.11: Acoustic impedance estimates.

for time $t \in [0, 5]$, with the dashed magenta lines showing the estimates $\hat{Z}_0^i(\cdot)$ ¹ for $i \in \{1, 2, 3\}$ (see legend) of Z_0 , and the dashed cyan lines showing the estimates $\hat{Z}_L^i(\cdot)$ for $i \in \{1, 2, 3\}$ (see legend) of Z_L . Compared to the estimates found in Figure 4.3, the estimates in Figure 4.11 appear to have a higher variance, despite the lower value of forgetting factor used. It appears that the estimates reach a steady state region at around $t = 4$ s, and the expected value and variance of the estimates computed over the last 1 s of the simulation is recorded in Table 4.3. Compared to the estimates in Table 4.1, the estimates in Table 4.3 do indeed have a larger variance. Next, in Section 4.4.2, the observer (3.3) is tested again, using the expected values (which converged to very similar values) of the estimates in Table 4.3 as \hat{Z}_0 , \hat{Z}_L .

¹The notation \hat{Z}_z^i denotes the estimate of the boundary impedance at location z initialized from $\hat{\vartheta}_0^i$.

Parameter estimate	Expected value	Variance
\hat{Z}_0^1	-15.4	0.579
\hat{Z}_L^1	68.5	0.443
\hat{Z}_0^2	-15.4	0.577
\hat{Z}_L^2	68.5	0.440
\hat{Z}_0^3	-15.5	0.599
\hat{Z}_L^3	68.4	0.461

Table 4.3: Acoustic impedance estimates.

4.4.2 State observer experiment - Estimated boundary coefficients

We repeat here the observer experiment from Section 3.4 using values of the impedances estimated in Section 4.4.1. Precisely, we use the mean of the expected values of the estimated impedances documented in Table 4.3 in the observer. The observer is tested on the data shown in Figures 3.15–3.16.

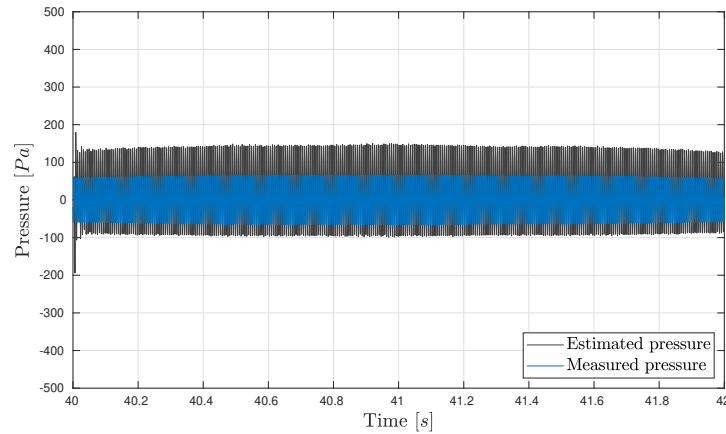


Figure 4.12: Measured (blue line) compared to estimated (grey line) gauge pressure at $z = z_v$ using values of impedance estimated in Section 4.4.1.

In Figure 4.12 the estimated value of gauge pressure at $z = z_v$ is plotted in grey, and compared to the measured value which is plotted in blue. A closer view of the estimated gauge pressure compared to the measured gauge pressure is shown in Figure 4.13, showing the last 20 *ms* of the observer test. Considering the discrepancy in estimated and measured amplitude in Figure 4.12, sensitivity of the estimated gauge pressure to assumed locations z_v of the in-domain validation microphone is considered in Figure 4.13 by plotting estimates for $z_v \in [0.8 \text{ } 0.9]$ around the estimate corresponding to the measured value of $z_v = 0.85 \text{ m}$. As is seen, the amplitude of the estimated gauge pressure is highly sensitive to accurate knowledge of the in-domain microphone position z_v , and uncertainty in this could hence be a

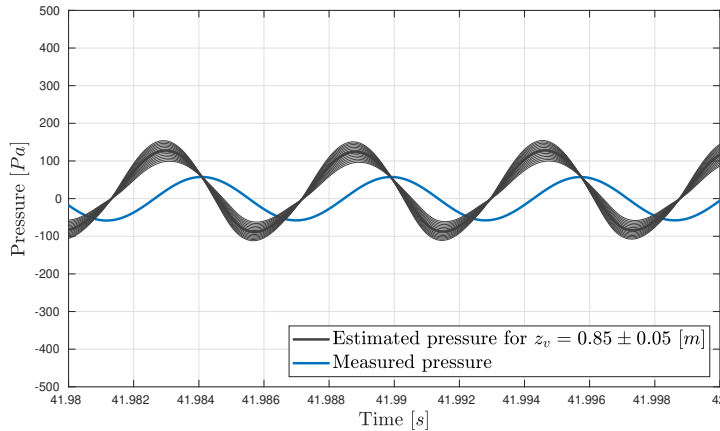


Figure 4.13: Measured (blue line) compared estimated (grey lines) gauge pressure for validation microphone locations $z_v \in [0.8 \ 0.9]$. Using values of impedance estimated in Section 4.4.1. Shown for final 20 *ms* of observer test.

contributing factor in inaccurate estimation of the pressure amplitude. In addition to this possible contributions from modelling error will be discussed in Section 4.5. As was the case in Chapter 3, the estimates are however still phase-shifted compared to the measured pressure signal and as seen from Figure 4.13 possible uncertainty in the measured microphone position does not influence this greatly.

4.5 Discussion

Compared to existing results in the literature, the parameter identifier (4.14) has the advantage that it estimates both acoustic impedances simultaneously with a single pressure measurement, but with the regressor form (4.6) being overparametrized. Since the acoustic impedances are estimated indirectly via the reflection coefficients d_0 , d_1 , an accurate knowledge of the characteristic impedance k is needed to get accurate knowledge of the impedances.

In the parameter identification experiment presented in Section 4.4.1, the estimate of \hat{Z}_L converges to a larger absolute value than the estimate of \hat{Z}_0 . This is surprising as they should in theory be as similar as possible, with each of them representing an open end with a slight amount of damping. However, the estimates are both significantly smaller than the characteristic impedance k in absolute value, which represent physically feasible solutions. With a value closer to k in absolute value representing more damping, and the acoustics model (2.43) used in the algorithm design assuming there is no in-domain damping in the Rijke tube, one possible explanation for acoustic impedance estimate \hat{Z}_L being larger than \hat{Z}_0 in absolute value is that in-domain damping from the tube is inadvertently lumped together with the acoustic impedance anticollocated with the I/O signals.

Also, a possible source of error in the experimental technique used is that the microphones shown in Figure ii.15 are fairly close to each other. With the pressure node in practice extending approximately $\Delta L = 0.61r$ outside of the tube end [Levine & Schwinger 1948], the microphone that is supposed to only pick up the loudspeaker signal could also accidentally pick up some of the tube acoustic response. Also, the loudspeaker signal is attenuated slightly as it travels from the loudspeaker into the tube, so the exact microphone placements could impact the resultant parameter estimate.

Although the parameters found in Section 4.4.1 made an improvement to the observer state estimates, the estimate shown in Figure 4.13 is still far from perfect. As discussed in Section 3.5, there could be multiple reasons, such as possible modelling error, for this. Two probable causes of modelling errors are mentioned, namely the lack of modelling heat transfer between the air inside the Rijke tube and tube walls and also modelling the impedances as having a resistive component, only. The former could cause errors in the sense that extra damping from a heated tube that is not included in the model might cause the observer to overestimate the amplitude of the thermoacoustic instabilities. Indeed, this could possibly explain the estimated pressure amplitude in Figures 4.12–4.13 being larger than that of the measured pressure despite using estimated rather than guessed values of the boundary impedances. Also as discussed in Section 3.5, the latter modelling error is a probable cause for the observed phase shift in Figures 3.19, 4.13. In addition to sensitivity of the estimate to validation microphone position as explored in Figure 4.13, the author has considered sensitivity of the estimates to other uncertain parameters, some examples being the electrical heater position and electrical heater time constant. However no significant variation in the phase shift has been observed from varying parameters currently in the model, suggesting modelling error is the probable cause for this error.

Some direct further work building on what is presented here is to investigate robustness of the parameter identifier (4.14) in estimating accurately the boundary acoustic impedances of the Rijke tube. It should be investigated to what extent in-domain damping influences the estimate of the anti-located acoustic impedance, and the sensitivity of the method to microphone placement in relation to the loudspeaker and tube boundary. Also, possibilities for combining the observer and parameter identifier into an adaptive observer should be looked into.

As has been seen, the Rijke tube is a rather simple setup, and the algorithm designs based on the model (2.43) and (2.44) with constant cross-sectional area reflects that. Thermoacoustic instabilities in combustors can feature highly complicated dynamics that is difficult to understand from studying basic laboratory setups such as the Rijke tube. Next, in Part III of this thesis, some research efforts attempting to move beyond the Rijke tube are considered.

Part III

Towards Combustors

Introduction to Part III

The work that was considered in Part II dealt with the Rijke tube, which is a laboratory setup. Although studying this setup is useful for understanding the rudiments of thermoacoustics as a physical phenomenon, designing algorithms to estimate the states and parameters for the Rijke tube can not be directly applied to practical combustors. There are, in addition to other factors, two important reasons for this. Firstly, the Rijke tube uses either a heated gauze or an electrical heater, which are simpler to model than flames in principal. Secondly, the Rijke tube has very simple geometry, whereas many important aspects of thermoacoustics in combustors are a direct consequence of their more complicated geometry [Poinsot 2017].

Therefore, to work towards model-based state and parameter estimation algorithms for combustors, the unique aspects of combustor dynamics need to be taken into account in the models used. In Part III of the thesis we aim to take some steps, however small, towards this. Only longitudinal modes and laminar flame dynamics are considered, but we hope the contributions presented can be built upon towards the realization of estimation algorithms using more realistic descriptions of the combustor dynamics in future work. We start in Chapter 5 by considering the problem of generalizing the parameter estimation scheme from Chapter 4, which assumes the cross-sectional area of the duct is constant, to the case when the duct has spatially varying geometry. This is done by using the acoustics described by (2.44) with $a'(\cdot) \neq 0$ in general as a basis. In Chapters 6 and 7, the state estimation problem for the model (2.45), representing longitudinal oscillations in a can combustor with spatially varying geometry, is considered. Here we use spatially compact flame models to describe the heat release. In Chapter 6 the flame model is linearized, but in Chapter 7 a nonlinear flame model is considered.

Boundary Parameter Estimation

Contents

5.1	Background	98
5.1.1	Problem statement	98
5.1.2	Literature review	98
5.2	Boundary parameter estimation 2×2 hyperbolic systems .	100
5.2.1	Mapping to target system	100
5.2.2	Regressor form	102
5.2.3	Adaptive law	104
5.3	Simulations	106
5.3.1	Simulation example	106
5.3.2	Robustness to noise	109
5.4	Application to estimation of acoustic impedance in duct with spatially varying cross section	110
5.4.1	Model in Riemann coordinates	110
5.4.2	Regressor form	112
5.5	Discussion	114

Dans ce chapitre, nous présentons un schéma d'identification des paramètres permettant d'estimer les coefficients limites d'un système hyperbolique linéaire 2×2 . La conception est similaire au schéma d'identification des paramètres suggéré au chapitre 4 pour le tube de Rijke, mais les coefficients de couplage dans le domaine rendent l'application de la même approche non triviale. Pour surmonter ce problème, une transformation de type backstepping est employée pour transformer le système hyperbolique linéaire 2×2 en un système cible piloté par les signaux entrée/sortie en chaque point du domaine spatial. La méthode des caractéristiques est ensuite appliquée pour trouver une forme de régresseur pour laquelle les méthodes standard d'estimation des paramètres peuvent être appliquées. Nous illustrons cette approche par des simulations sur un exemple théorique. Ensuite, il est démontré que le modèle (2.44) de l'acoustique dans un conduit dont la section transversale varie dans l'espace peut être écrit comme un système hyperbolique linéaire 2×2 . Cela permet d'appliquer la forme de régresseur trouvée pour les systèmes hyperboliques linéaires 2×2 généraux afin de trouver une forme similaire pour l'estimation des impédances acoustiques de frontière dans les conduits dont la géométrie varie dans

l'espace.

In this chapter, a parameter identification scheme for estimating the boundary coefficients of a 2×2 linear hyperbolic system is presented. The design is similar to the parameter identification scheme suggested in Chapter 4 for the Rijke tube, but the in-domain coupling coefficients make applying the same approach non-trivial. To overcome this issue, a backstepping transformation is employed to map the 2×2 linear hyperbolic system into a target system driven by the I/O signals at each point in the spatial domain. The MOC is then applied to find a regressor form for which standard parameter estimation methods can be applied. The design is demonstrated in simulations on a theoretical example. Next, it is shown that the model (2.44) of acoustics in a duct with spatially varying cross-sectional area can be written as a 2×2 linear hyperbolic system. This allows the regressor form found for general 2×2 linear hyperbolic systems to be applied to find a similar form for estimation of boundary acoustic impedances in ducts with spatially varying geometry.

5.1 Background

5.1.1 Problem statement

We are here concerned with systems of the form

$$u_t(x, t) = -\lambda(x)u_x(x, t) + \sigma^+(x)v(x, t) \quad (5.1a)$$

$$v_t(x, t) = \mu(x)v_x(x, t) + \sigma^-(x)u(x, t) \quad (5.1b)$$

$$u(0, t) = d_0v(0, t) \quad (5.1c)$$

$$v(1, t) = d_1u(1, t) + U(t), \quad (5.1d)$$

where u, v are distributed states defined over $(x, t) \in [0, 1] \times [0, \infty)$, and the boundary reflection coefficients d_0, d_1 are unknown. The transport speeds $\lambda, \mu \in C^1(0, 1)$ and in-domain coupling coefficients $\sigma^+, \sigma^- \in C^0(0, 1)$ are all assumed known, and $U : [0, \infty) \mapsto \mathbb{R}$ is a boundary input signal. We assume the initial conditions $u_0, v_0 \in L^2(0, 1)$.

Given knowledge of the boundary measurement

$$y(t) := u(1, t), \quad (5.2)$$

only, the main goal is to design a parameter identification scheme for estimating the unknown coefficients d_0, d_1 and to choose the input signal U so that parameter convergence is achieved.

5.1.2 Literature review

Linear hyperbolic 2×2 systems of the form (5.1) model a wide range of systems commonly found in engineering applications, such as open channel

flow [Coron *et al.* 1999], gas dynamics [Marchesin & Paes-Leme 1986], leak detection in pipes [Aamo 2015] and oil well drilling [Di Meglio & Aarsnes 2015]. They consist of two distributed one-dimensional states convecting in opposite directions through a first-order transport equation and coupled in-domain and at the boundaries. In order to actuate and sense these systems, the most feasible access points in many practical applications are the boundaries, and hence much research has been devoted to observer and controller design within this setting over the past years.

A successful technique for boundary observer and controller design for many distributed parameter systems is the backstepping methodology, which was first developed for stabilization of certain classes of finite dimensional nonlinear systems (see [Krstić *et al.* 1995, Khalil & Grizzle 2002]) and later generalized to design stabilizing boundary control laws for infinite dimensional systems, the design first fully mastered in [Liu 2003] for a parabolic PDE. The technique was later applied to hyperbolic PDEs in [Krstić & Smyshlyaev 2008a] and later to systems of first-order hyperbolic PDEs in [Vazquez *et al.* 2011].

In early contributions it is assumed all system parameters are known, but following on the research effort for control and observer backstepping designs, research into adaptive controllers and parameter identifiers for parabolic PDEs has been considered, culminating in the seminal text [Smyshlyaev & Krstić 2010]. In [Mechhoud *et al.* 2013] estimation of the source terms in a parabolic PDE describing plasma heat transport is considered, and in [Baudouin *et al.* 2014], a parameter estimation problem for the Korteweg-De Vries equation modelling shallow water waves is considered.

After multiple contributions for parabolic PDEs, research on adaptive designs for hyperbolic systems was initiated in [Bernard & Krstić 2014]. Building on this, much research has been done on systems of hyperbolic PDEs; in the two-part paper [Anfinsen & Aamo 2016a, Anfinsen & Aamo 2016b] uncertain in-domain coupling coefficients are estimated assuming distributed measurements are available, while in [Anfinsen *et al.* 2016] an uncertain boundary reflection coefficient at the boundary anti-located with sensing is estimated for $n + 1$ systems. In [Ghousein *et al.* 2020] the temperature distribution in a heat exchanger is estimated by posing the problem as estimation of the amplitude of a distributed in-domain disturbance with known profile, via considering the problem as an estimation problem for 2×2 linear hyperbolic systems. Many of the current designs available for adaptive control and parameter identification of hyperbolic PDE systems are covered in [Anfinsen & Aamo 2019].

A scheme for estimating both reflection coefficients d_0, d_1 in the 2×2 linear hyperbolic system (5.1), given the boundary measurement (5.2) only is presented in Section 5.2. Both reflection coefficients of such systems are estimated in [Anfinsen & Aamo 2017], but assuming both boundaries are available for measurement. Here, we only require one measurement. The methodology applied here is based on using a Volterra integral transformation, a vital ingredient in the infinite dimensional backstepping technique (see [Krstić & Smyshlyaev 2008b]), to map the system we are studying into a target system. Using this target system, the measure-

ment signal is written in a regressor form linear in the unknown coefficients and their product, allowing standard parameter identification techniques to be applied. The results from Section 5.2 are then applied in Section 5.4 to suggest an algorithm for estimating the boundary impedances of a duct with spatially varying cross section, such as the one modelled by (2.44).

5.2 Boundary parameter estimation 2×2 hyperbolic systems

5.2.1 Mapping to target system

We apply the Volterra integral transformation

$$\alpha(x, t) = u(x, t) + \int_x^1 K^{uu}(x, \xi)u(\xi, t) + K^{uv}(x, \xi)v(\xi, t)d\xi \quad (5.3a)$$

$$\beta(x, t) = v(x, t) + \int_x^1 K^{vu}(x, \xi)u(\xi, t) + K^{vv}(x, \xi)v(\xi, t)d\xi \quad (5.3b)$$

with kernels satisfying the PDE system

$$-\lambda(x)K_x^{uu}(x, \xi) - \lambda(\xi)K_\xi^{uu}(x, \xi) = \lambda'(\xi)K^{uu}(x, \xi) + \sigma^-(\xi)K^{uv}(x, \xi) \quad (5.4a)$$

$$-\lambda(x)K_x^{uv}(x, \xi) + \mu(\xi)K_\xi^{uv}(x, \xi) = -\mu'(\xi)K^{uv}(x, \xi) + \sigma^+(\xi)K^{uu}(x, \xi) \quad (5.4b)$$

$$-\mu(x)K_x^{vu}(x, \xi) + \lambda(\xi)K_\xi^{vu}(x, \xi) = -\lambda'(\xi)K^{vu}(x, \xi) - \sigma^-(\xi)K^{vv}(x, \xi) \quad (5.4c)$$

$$-\mu(x)K_x^{vv}(x, \xi) - \mu(\xi)K_\xi^{vv}(x, \xi) = \mu'(\xi)K^{vv}(x, \xi) - \sigma^+(\xi)K^{vu}(x, \xi) \quad (5.4d)$$

defined over the the upper triangular domain $\mathcal{T}_u := \{(x, \xi) \mid 0 \leq x \leq \xi \leq 1\}$, and having boundary conditions

$$K^{uu}(x, 1) = f^u(x) \quad (5.5a)$$

$$K^{uv}(x, x) = \frac{\sigma^+(x)}{\lambda(x) + \mu(x)} \quad (5.5b)$$

$$K^{vu}(x, x) = \frac{-\sigma^-(x)}{\lambda(x) + \mu(x)} \quad (5.5c)$$

$$K^{vv}(x, 1) = f^v(x) \quad (5.5d)$$

Here the boundary data f^u, f^v can be chosen freely, as long as it is sufficiently smooth for (5.4)–(5.5) to have a well-posed solution. In Figure 5.1, a schematic representation of the characteristics of the kernel equations (5.4)–(5.5) is shown.

Remark 4. Note that unlike the standard backstepping transformation considered in e.g. [Vazquez et al. 2011], the kernels defined by (5.4)–(5.5) do not depend on the boundary coefficients d_0, d_1 . This is achieved, as can be seen in (5.5) and Figure 5.1, by defining the boundary condition of K^{uu}, K^{vv} along the line $\xi = 1$ rather than $x = 0$, as is conventional in backstepping designs for observer and controller designs.

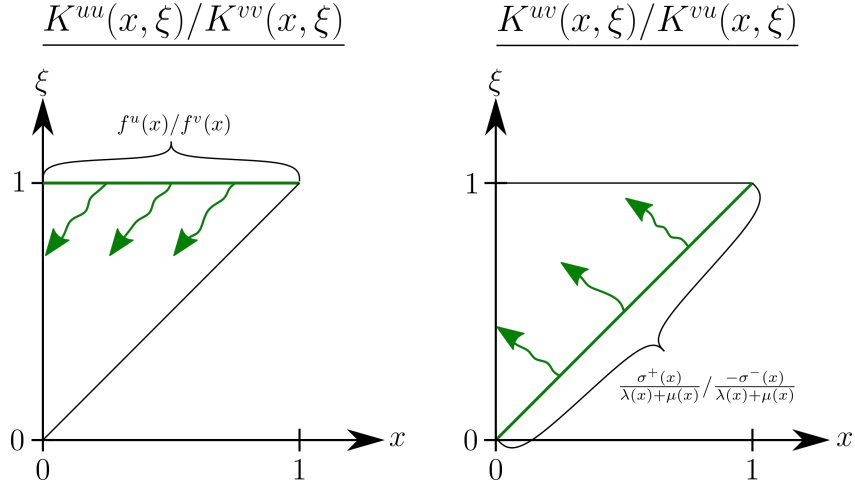


Figure 5.1: Schematic of kernel equations (5.4)–(5.5). Characteristics in green, originating in boundary data as indicated.

We present now a Lemma equating the system (5.1) with a target system. The proof is standard and hence omitted.

Lemma 2. *The invertible Volterra integral transformation (5.3)–(5.5) maps the system (5.1) into the target system*

$$\alpha_t(x, t) + \lambda(x)\alpha_x(x, t) = l_1^y(x)y(t) + l_1^U(x)U(t) \quad (5.6a)$$

$$\beta_t(x, t) - \mu(x)\beta_x(x, t) = l_2^y(x)y(t) + l_2^U(x)U(t) \quad (5.6b)$$

$$\alpha(0, t) = d_0\beta(0, t) + \int_0^1 M(x)\alpha(x, t) + N(x)\beta(x, t)dx \quad (5.6c)$$

$$\beta(1, t) = d_1\alpha(1, t) + U(t) \quad (5.6d)$$

with the I/O gains defined as

$$l_1^y(x) := d_1\mu(1)K^{uv}(x, 1) - \lambda(1)K^{uu}(x, 1) \quad (5.7)$$

$$l_2^y(x) := d_1\mu(1)K^{vv}(x, 1) - \lambda(1)K^{vu}(x, 1) \quad (5.8)$$

$$l_1^U(x) := \mu(1)K^{uv}(x, 1) \quad (5.9)$$

$$l_2^U(x) := \mu(1)K^{vv}(x, 1) \quad (5.10)$$

and M, N given by

$$M(x) := K^{uu}(0, x) - d_0K^{vu}(0, x) - \int_0^x M(s)K^{uu}(s, x) + N(s)K^{uv}(s, x)ds \quad (5.11)$$

$$N(x) := K^{uv}(0, x) - d_0K^{vv}(0, x) - \int_0^x M(s)K^{vu}(s, x) + N(s)K^{vv}(s, x)ds \quad (5.12)$$

5.2.2 Regressor form

We denote here by ϕ_ε the injective function

$$\phi_\varepsilon(x) := \int_0^x \frac{d\xi}{\varepsilon(\xi)} \quad (5.13)$$

for any $\varepsilon \in C^1(0, 1)$, $\varepsilon > 0$. We denote also $\bar{\phi}_\varepsilon(x) := \phi_\varepsilon(1) - \phi_\varepsilon(x)$. Note that l_1^y , l_2^y , N and M can be factorized as

$$l_1^y(x) = \bar{l}_1^y(x) + d_1 l_1^U(x) \quad (5.14)$$

$$l_2^y(x) = \bar{l}_2^U(x) + d_1 l_2^U(x) \quad (5.15)$$

$$M(x) = M_1(x) + d_0 M_2(x) \quad (5.16)$$

$$N(x) = N_1(x) + d_0 N_2(x) \quad (5.17)$$

with component functions defined as

$$\bar{l}_1^y(x) := -\lambda(1)K^{uu}(x, 1) \quad (5.18)$$

$$\bar{l}_2^y(x) := -\lambda(1)K^{vu}(x, 1) \quad (5.19)$$

$$M_1(x) := K^{uu}(0, x) - \int_0^1 M_1(s)K^{uu}(s, x) + N_1(s)K^{uv}(s, x)ds \quad (5.20)$$

$$M_2(x) := -K^{vu}(0, x) - \int_0^x M_2(s)K^{uu}(s, x) + N_2(s)K^{uv}(s, x)ds \quad (5.21)$$

$$N_1(x) := K^{uv}(0, x) - \int_0^x M_1(s)K^{vu}(s, x) + N_1(s)K^{vv}(s, x)ds \quad (5.22)$$

$$N_2(x) := -K^{vv}(0, x) - \int_0^x M_2(s)K^{vu}(s, x) + N_2(s)K^{vv}(s, x)ds \quad (5.23)$$

Consider also the integral terms I_i^y , I_j^U given by

$$\begin{aligned} I_1^y[y](t) &:= \int_0^1 -M_2(s)F_{11}^y[y](s, t) + N_2(s)F_{12}^y[y](s, t)ds \\ &\quad + \int_0^{\phi_\mu(1)} l_2^U(\phi_\mu^{-1}(\phi_\mu(1) - s))y(t - \phi_\lambda(1) - \phi_\mu(1) + s)ds \end{aligned} \quad (5.24)$$

$$\begin{aligned} I_2^y[y](t) &:= \int_0^1 M_2(s)F_{21}^y[y](s, t) + N_2(s)F_{22}^y[y](s, t)ds \\ &\quad + \int_0^{\phi_\mu(1)} \bar{l}_2^y(\phi_\mu^{-1}(\phi_\mu(1) - s))y(t - \phi_\lambda(1) - \phi_\mu(1) + s)ds \end{aligned} \quad (5.25)$$

$$\begin{aligned} I_2^U[U](t) &:= \int_0^1 M_2(s)F_{21}^U[U](s, t) + N_2(s)F_{22}^U[U](s, t)ds \\ &\quad + \int_0^{\phi_\mu(1)} l_2^U(\phi_\mu^{-1}(\phi_\mu(1) - s))U(t - \phi_\lambda(1) - \phi_\mu(1) + s)ds \end{aligned} \quad (5.26)$$

$$I_3^y[y](t) := \int_0^1 -M_1(s)F_{11}^y[y](s, t) + N_1(s)F_{12}^y[y](s, t)ds$$

$$+ \int_0^{\phi_\lambda(1)} l_1^U(\phi_\lambda^{-1}(s))y(t - \phi_\lambda(1) + s)ds \quad (5.27)$$

$$\begin{aligned} I_4^y[y](t) &:= \int_0^1 M_1(s)F_{21}^y[y](s, t) + N_1(s)F_{22}^y[y](s, t)ds \\ &+ \int_0^{\phi_\lambda(1)} \bar{l}_1^y(\phi_\lambda^{-1}(s))y(t - \phi_\lambda(1) + s)ds \end{aligned} \quad (5.28)$$

$$\begin{aligned} I_4^U[U](t) &:= \int_0^1 M_1(s)F_{21}^U[U](s, t) + N_1(s)F_{22}^U[U](s, t)ds \\ &+ \int_0^{\phi_\lambda(1)} l_1^U(\phi_\lambda^{-1}(s))U(t - \phi_\lambda(1) + s)ds \end{aligned} \quad (5.29)$$

which in turn depend on F_{ij}^y, F_{ij}^U , given by

$$F_{11}^y[y](s, t) := \int_0^{\bar{\phi}_\lambda(s)} l_1^U(\phi_\lambda^{-1}(\phi_\lambda(s) + \sigma))y(t - \phi_\lambda(1) + \sigma)d\sigma \quad (5.30)$$

$$\begin{aligned} F_{12}^y[y](s, t) &:= y(t - \bar{\phi}_\mu(s)) \\ &+ \int_0^{\bar{\phi}_\mu(s)} l_2^U(\phi_\mu^{-1}(\phi_\mu(1) - \sigma))y(t - \bar{\phi}_\mu(s) - \phi_\lambda(1) + \sigma)d\sigma \end{aligned} \quad (5.31)$$

$$F_{21}^y[y](s, t) := y(t - \phi_\lambda(s)) - \int_0^{\bar{\phi}_\lambda(s)} \bar{l}_1^y(\phi_\lambda^{-1}(\phi_\lambda(s) + \sigma))y(t - \phi_\lambda(1) + \sigma)d\sigma \quad (5.32)$$

$$F_{21}^U[U](s, t) := - \int_0^{\bar{\phi}_\lambda(s)} l_1^U(\phi_\lambda^{-1}(\phi_\lambda(s) + \sigma))U(t - \phi_\lambda(1) + \sigma)d\sigma \quad (5.33)$$

$$F_{22}^y[y](s, t) := \int_0^{\bar{\phi}_\mu(s)} \bar{l}_2^y(\phi_\mu^{-1}(\phi_\mu(1) - \sigma))y(t - \bar{\phi}_\mu(s) - \phi_\lambda(1) + \sigma)d\sigma \quad (5.34)$$

$$\begin{aligned} F_{22}^U[U](s, t) &:= U(t - \bar{\phi}_\mu(s) - \phi_\lambda(1)) \\ &+ \int_0^{\bar{\phi}_\mu(s)} l_2^U(\phi_\mu^{-1}(\phi_\mu(1) - \sigma))U(t - \bar{\phi}_\mu(s) - \phi_\lambda(1) + \sigma)d\sigma \end{aligned} \quad (5.35)$$

Lemma 3. *The output signal y defined in (5.2) can be written as*

$$y(t) = d_0d_1\omega_1(t) + d_0\omega_2(t) + d_1\omega_3(t) + \omega_4(t) \quad (5.36)$$

with ω_i defined as

$$\omega_1(t) := y(t - \phi_\lambda(1) - \phi_\mu(1)) + I_1^y[y](t) \quad (5.37)$$

$$\omega_2(t) := U(t - \phi_\lambda(1) - \phi_\mu(1)) + I_2^y[y](t) + I_2^U[U](t) \quad (5.38)$$

$$\omega_3(t) := I_3^y[y](t) \quad (5.39)$$

$$\omega_4(t) := I_4^y[y](t) + I_4^U[U](t) \quad (5.40)$$

being functions only of known signals and gains defined in (5.24)–(5.35).

Proof. Applying the MOC and transformation (5.3a), we write the measurement as

$$y(t) = \alpha(1, t)$$

$$\begin{aligned}
&= \alpha(0, t - \phi_\lambda(1)) + \int_0^{\phi_\lambda(1)} l_1^y(\phi_\lambda^{-1}(s))y(t - \phi_\lambda(1) + s)ds \\
&\quad + \int_0^{\phi_\lambda(1)} l_1^U(\phi_\lambda^{-1}(s))U(t - \phi_\lambda(1) + s)ds. \tag{5.41}
\end{aligned}$$

Further, using the MOC for α from the boundary at $x = 1$

$$\begin{aligned}
\alpha(x, t - \phi_\lambda(1)) &= y(t - \phi_\lambda(x)) - \int_0^{\bar{\phi}_\lambda(x)} l_1^y(\phi_\lambda^{-1}(\phi_\lambda(x) + s))y(t - \phi_\lambda(1) + s)ds \\
&\quad - \int_0^{\bar{\phi}_\lambda(x)} l_1^U(\phi_\lambda^{-1}(\phi_\lambda(x) + s))U(t - \phi_\lambda(1) + s)ds. \tag{5.42}
\end{aligned}$$

Applying the boundary condition (5.6c), using the MOC to solve for the dynamics (5.6b), substituting in (5.6d) and also applying (5.42) allows us to express

$$\begin{aligned}
\alpha(0, t - \phi_\lambda(1)) &= d_0 \left(d_1 y(t - \phi_\mu(1) - \phi_\lambda(1)) + U(t - \phi_\mu(1) - \phi_\lambda(1)) \right. \\
&\quad + \int_0^{\phi_\mu(1)} l_2^y(\bar{\phi}_\mu^{-1}(s))y(t - \phi_\mu(1) - \phi_\lambda(1) + s)ds \\
&\quad + \left. \int_0^{\phi_\mu(1)} l_2^U(\bar{\phi}_\mu^{-1}(s))U(t - \phi_\mu(1) - \phi_\lambda(1) + s)ds \right) \\
&\quad + \int_0^1 M(s) \left(y(t - \phi_\lambda(s)) \right. \\
&\quad - \int_0^{\bar{\phi}_\lambda(s)} l_1^y(\phi_\lambda^{-1}(\phi_\lambda(s) + \sigma))y(t - \phi_\lambda(1) + \sigma)d\sigma \\
&\quad - \left. \int_0^{\bar{\phi}_\lambda(s)} l_1^U(\phi_\lambda^{-1}(\phi_\lambda(s) + \sigma))U(t - \phi_\lambda(1) + \sigma)d\sigma \right) ds \\
&\quad + \int_0^1 N(s) \left(d_1 y(t - \phi_\lambda(1) - \bar{\phi}_\mu(s)) + U(t - \phi_\lambda(1) - \bar{\phi}_\mu(s)) \right. \\
&\quad + \int_0^{\bar{\phi}_\mu(s)} l_2^y(\bar{\phi}_\mu^{-1}(\sigma))y(t - \bar{\phi}_\mu(s) - \phi_\lambda(1) + \sigma)d\sigma \\
&\quad + \left. \int_0^{\bar{\phi}_\mu(s)} l_2^U(\bar{\phi}_\mu^{-1}(\sigma))U(t - \bar{\phi}_\mu(s) - \phi_\lambda(1) + \sigma)d\sigma \right) ds \tag{5.43}
\end{aligned}$$

Hence substituting (5.43) into (5.41) and applying (5.14)–(5.17), by factoring out the unknown coefficients and grouping terms one obtains the expression (5.36). \square

5.2.3 Adaptive law

Denoting by ϖ the signal

$$\varpi(t) := y(t) - \omega_4(t) \tag{5.44}$$

we see that (5.36) can be expressed in the regressor form

$$\varpi(t) = \vartheta^\top \Omega(t) \quad (5.45)$$

with ϑ as defined in (4.8) but Ω given by

$$\Omega(t) := \begin{bmatrix} \omega_1(t) \\ \omega_2(t) \\ \omega_3(t) \end{bmatrix}. \quad (5.46)$$

Similar to the case in Section 4.2, a large number of standard adaptive schemes can be applied with the regressor form (5.45) to estimate the unknown parameters in ϑ . As was done there, we suggest applying modified least-squares with forgetting factor. We form an estimate $\hat{\varpi}$ of the signal ϖ by applying the parameter estimate vector $\hat{\vartheta}$

$$\hat{\varpi}(t) := \hat{\vartheta}(t)^\top \Omega(t), \quad (5.47)$$

and together with forgetting factor $\beta > 0$, the adaptive law reads

$$\dot{\hat{\vartheta}}(t) = P(t)(\varpi(t) - \hat{\varpi}(t))\Omega(t) \quad (5.48a)$$

$$\dot{P}(t) = \begin{cases} \beta P(t) - P(t)\Omega(t)\Omega(t)^\top P(t), & \text{if } \|P(t)\| \leq \bar{P} \\ 0, & \text{otherwise.} \end{cases} \quad (5.48b)$$

initialized from $P(0) = P_0$, $\hat{\vartheta}(0) = \hat{\vartheta}_0$ and \bar{P} an upper bound imposed on P . The following Theorem is almost identical to Theorem 2 (only difference being different signals), but is stated for completeness.

Theorem 3. Define $\tilde{\varpi} := \varpi - \hat{\varpi}$. The adaptive law (5.48) guarantees that

- $\tilde{\varpi}, \hat{\vartheta}, \dot{\hat{\vartheta}} \in L_\infty$.
- $\tilde{\varpi}, \dot{\hat{\vartheta}} \in L_2$.
- If $\Omega \in L_\infty$ and Ω is PE, then $P, P^{-1} \in L_\infty$ and $\hat{\vartheta}(t) \rightarrow \vartheta$ exponentially.

Since the same parameter vector is used in (5.45) as was the case for (4.6), the optimization problem (4.15)–(4.16) with δ_i assigned as

$$\delta_i = \begin{cases} 1, & \text{if } \omega_i \text{ is PE} \\ 0, & \text{otherwise.} \end{cases} \quad (5.49)$$

is solved to obtain unique estimates \check{d}_0, \check{d}_1 .

Remark 5. Given a vector of signals Ω defined as (5.46), checking whether it and its components are PE is relatively straightforward. Recalling from [Ioannou & Sun 2012] that a signal $\varphi : [0, \infty) \mapsto \mathbb{R}^n$ is PE if it satisfies

$$\alpha_1 I \geq \frac{1}{T_0} \int_t^{t+T_0} \varphi(\tau)\varphi^\top(\tau) d\tau \geq \alpha_0 I \quad (5.50)$$

for some $T_0, \alpha_0, \alpha_1 > 0$, whether the signal is *PE* or not can be verified by applying the condition directly. However, the question of how to choose the input signal U so that Ω and its components are *PE* is more tricky and will in practice most likely need to be found by trial and error, before the parameter identifier can be applied to a given plant. As discussed in [Ioannou & Sun 2012], a “rule of thumb” is to choose U to be sufficiently rich of order equal to the number of unknown parameter, which in the case of U being the sum of sinusoids corresponds to the signal consisting of at least half as many distinct frequencies as there are unknown parameters. One could then apply (5.50) to verify that the regressor signal Ω and its components are *PE* for this choice of U .

5.3 Simulations

5.3.1 Simulation example

The system (5.1) is implemented in MATLAB with the coefficients

$$\begin{aligned} \lambda(x) &= 1, & \mu(x) &= 1 \\ \sigma^+(x) &= 1, & \sigma^-(x) &= 1 \\ d_0 &= 0.1, & d_1 &= 0.2 \end{aligned}$$

and simulated for a total time of $t_s = 20$ seconds, starting from the initial conditions

$$u_0(x) = 0, \quad v_0(x) = 0.$$

Spatial and temporal discretization of $dx = 10^{-3}$ and $dt = 10^{-3}$, respectively, are used. To solve the PDEs forwards in time, a first-order upwind scheme is applied. The trapezoidal method is used to approximate all integrals.

As the system parametrization (5.45) is linear in three parameters, the input signal U must be sufficiently rich in frequencies to allow the signal vector Ω to be *PE* and be able to distinguish between the parameters. To excite the system to generate sufficient output information for parameter convergence, the input signal U defined by

$$U(t) = \sin(t) + \sin\left(\frac{t}{2}\right)$$

is chosen.

In order to compute the signals ω_i , $i \in \{1, \dots, 4\}$, defined by (5.37)–(5.40), the kernel PDE system (5.4)–(5.5) is solved using Uniformly Gridded Discretization (UGD) (see [Anfinson & Aamo 2019]) with boundary data $f^u = 0$ and $f^v = 0$. Hence, using these solutions the signals ω_i are computed after $\phi_\lambda(1) + \phi_\mu(1) = 2$ s of I/O data has been collected.

Remark 6. *The choice of boundary data f^u, f^v “tunes” the exact shape (as functions of I/O data) of the respective signal components $d_0 d_1 \omega_1$, $d_0 \omega_2$, $d_1 \omega_3$ and ω_4 , that decompose the measurement signal y in (5.36). In the example presented here,*

choosing $f^u = f^v = 0$ is sufficient to obtain parameter convergence, but in certain cases where Ω does not satisfy the PE property with this choice, one could choose f^u and f^v differently to make Ω PE, given that U is sufficiently rich. There is no guarantee, however, that this will work in all cases, and further investigation is necessary to establish the exact conditions for this to be possible.

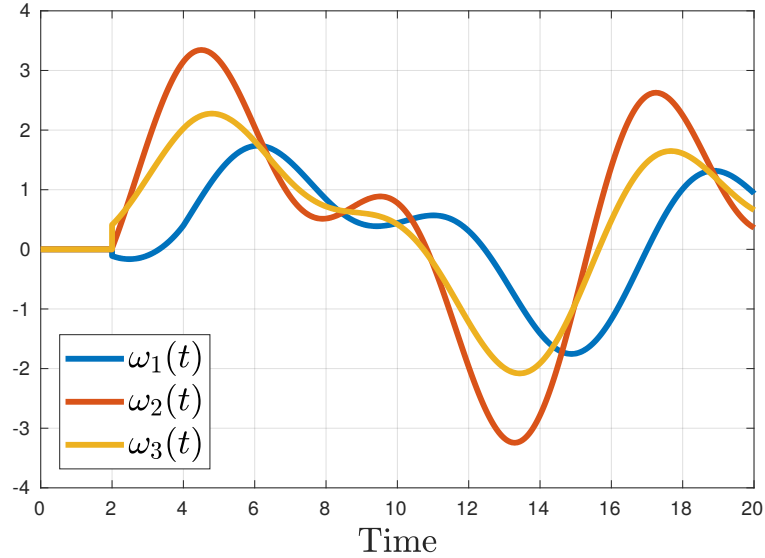


Figure 5.2: Component signals of Ω .

The three component signals of Ω are plotted in Figure 5.2. With the ω_i signals computed, the adaptive law (5.48) is implemented with

$$\beta = 2, \quad \bar{P} = 10^3.$$

The parameter estimate vector $\hat{\vartheta}$ and covariance matrix P are respectively initialized at

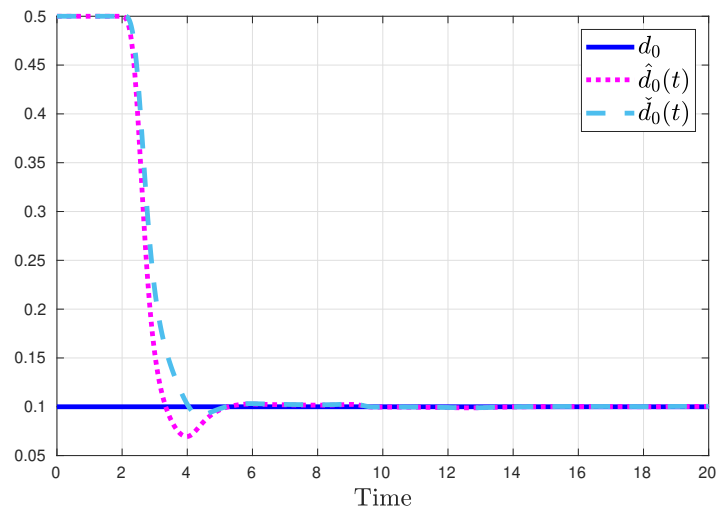
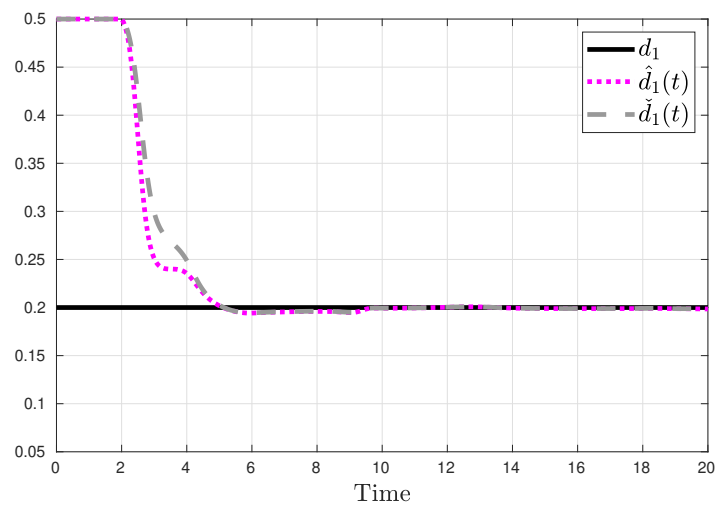
$$\hat{\vartheta}_0 = \begin{bmatrix} 0.25 \\ 0.5 \\ 0.5 \end{bmatrix}, \quad P_0 = \begin{bmatrix} 1 & 0 & 0 \\ 0 & 1 & 0 \\ 0 & 0 & 1 \end{bmatrix}.$$

For each time step, after updating the parameter estimate using (5.48), the optimization problem (4.15)–(4.16) is solved with

$$\delta_1 = 1, \quad \delta_2 = 1, \quad \delta_3 = 1,$$

using the `fminunc` function from MATLAB.

A plot showing the parameter d_0 plotted against \hat{d}_0 directly from the update law and \check{d}_0 after the optimization step is plotted in Figure 5.3. Likewise, Figure 5.4 shows a plot of d_1 against \hat{d}_1 and \check{d}_1 . As can be seen, both estimates from before

Figure 5.3: Plot of d_0 versus estimates.Figure 5.4: Plot of d_1 versus estimates.

and after the optimization step converge to their true values. In particular for the estimation of d_0 , the optimization step forces the estimate \check{d}_0 to stay closer throughout, compared to \hat{d}_0 which has a small overshoot initially.

5.3.2 Robustness to noise

In situations where one has sensor data that is corrupted by high levels of noise, the forgetting factor β appearing in (5.48) has the effect of amplifying the noise, as it discounts past data in preference for current data, and can hence give poor parameter estimates if β and/or the maximum covariance norm \bar{P} are chosen to be too high. One faces in any case a trade-off between flexibility offered by the forgetting factor and robustness to noise.

The system (5.1) is simulated with the same settings as in Section 5.3.1, but with the measurement y originally defined as (5.2), now corrupted by an additive white Gaussian noise process with power¹ of $0.1 W$, yielding a comparatively high level of noise for this example. Instead of forgetting factor and maximum covariance used in Section 5.3.1, these constants are here set to significantly lower values of

$$\beta = 0.1, \quad \bar{P} = 2$$

to not amplify the noise too much. Using these new values, the adaptive law (5.48) is implemented. A plot of the resultant parameter estimates is given in Figure 5.5.

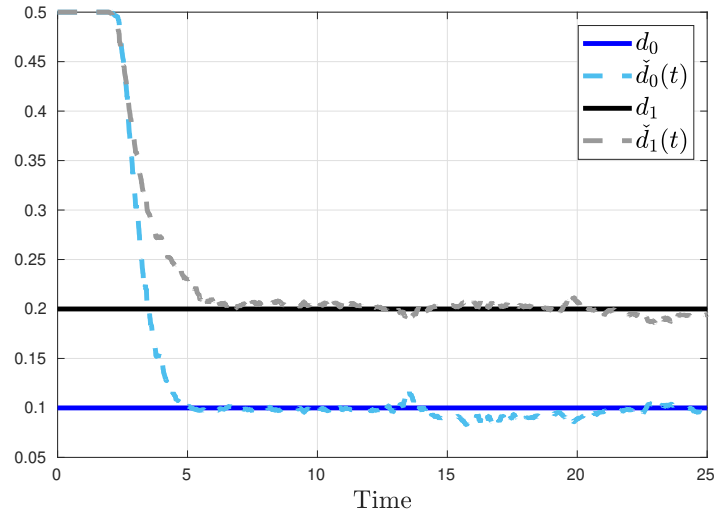


Figure 5.5: Plot of d_0 and d_1 versus estimates. With measurement noise.

The quality of the parameter estimates are deteriorated due to the noise, but despite

¹The unit Watt [W] to quantify the “size” of the noise is used here with the conventional meaning, as used by the `wgn` function [`wgn`] used to implement it in `MATLAB`, that if a voltage with equal numerical value, in Volts [V], to the noise signal generated is placed over a resistor with resistance 1Ω , a power equal to the number of Watts specified would be dissipated.

this the estimates remain in the neighbourhood of the correct parameter values. One should however note that parametrization (5.45) used will cause the estimates produced by applying LS to be biased when faced with measurement noise. Hence with significant amounts of noise the estimates could diverge, rather than converge to the true parameters as they would in the corresponding noiseless case with identical input signal. It could be beneficial to instead apply an update law more robust to noise, such as Instrumental Variables (IV) (see e.g. [Ljung 1987]), rather than LS in such a scenario.

5.4 Application to estimation of acoustic impedance in duct with spatially varying cross section

5.4.1 Model in Riemann coordinates

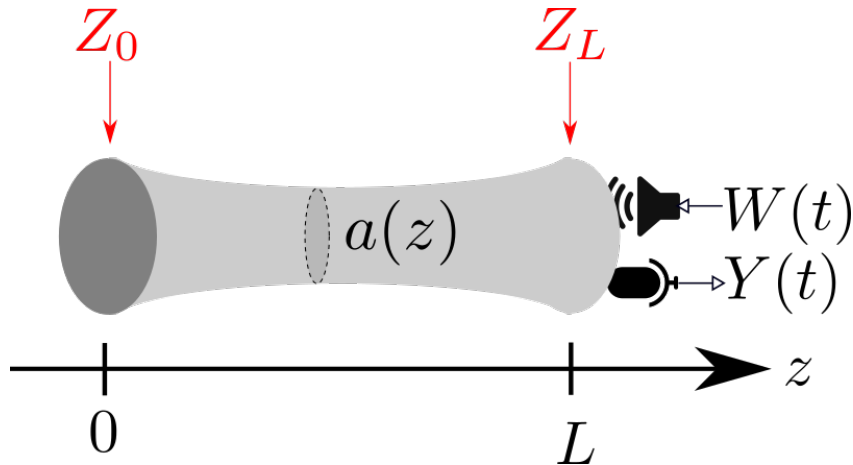


Figure 5.6: Acoustic impedance estimation in duct with spatially varying cross-sectional area.

Consider the setup shown in Figure 5.6. It consists of a similar setup to that shown in Figure 4.1, but rather than having a duct with constant cross-sectional area, the cross section is here described by a spatially varying function $a(z)$ for $z \in [0, L]$. We let there be a loudspeaker located at $z = L$ sending in signal $W_L = W$ that it is collocated to a pressure measurement. Also, it is assumed the air inside the duct is stationary, so that $\bar{V} = 0$, and standard atmospheric conditions apply. As shown in Chapter 2, such a scenario can be modelled by (2.44) with $W_0 = 0$. The pressure measurement Y is given by

$$Y(t) = \check{P}(L, t) \quad (5.51)$$

and together with knowledge of W , the aim is to estimate unknown boundary acoustic impedances Z_0, Z_L . We proceed in the following steps. First, we show that (2.44)

can be written in the form (5.1) by mapping into Riemann coordinates. Then, applying results from Section 5.2, we suggest a regressor form for (2.44) that can be used for parameter identification.

Lemma 4. *Consider the change of variables*

$$u(x, t) := (\check{P}(xL, t) + k\check{V}(xL, t)) \exp\left(\frac{L}{c} \int_0^x \sigma(\xi) d\xi\right) \quad (5.52a)$$

$$v(x, t) := (\check{P}(xL, t) - k\check{V}(xL, t)) \exp\left(\frac{L}{c} \int_0^x \sigma(\xi) d\xi\right) \quad (5.52b)$$

where σ is defined by

$$\sigma(x) := \frac{\gamma \bar{P} a'(xL)}{2k a(xL)} \quad (5.53)$$

and the speed of sound c and characteristic impedance k are respectively defined in (3.7), (3.4). The change of coordinates (5.52) maps (2.44) into (5.1) with transport speeds

$$\lambda(x) := \frac{c}{L}, \quad (5.54a)$$

$$\mu(x) := \frac{c}{L} \quad (5.54b)$$

in-domain coupling coefficients

$$\sigma^+(x) = \sigma(x), \quad (5.55a)$$

$$\sigma^-(x) = -\sigma(x) \quad (5.55b)$$

reflection coefficients

$$d_0 := \frac{Z_0 + k}{Z_0 - k} \quad (5.56a)$$

$$d_1 := \frac{Z_L - k}{Z_L + k} \quad (5.56b)$$

$$(5.56c)$$

and input signal

$$U(t) := (1 - d_1)\alpha_W W(t) \quad (5.57)$$

where

$$\alpha_W := \exp\left(\frac{L}{c} \int_0^1 \sigma(\xi) d\xi\right) \quad (5.58)$$

is known.

Proof. Consider first the intermediate change of variables

$$\bar{u}(x, t) := \check{P}(xL, t) + k\check{V}(xL, t) \quad (5.59a)$$

$$\bar{v}(x, t) := \check{P}(xL, t) - k\check{V}(xL, t) \quad (5.59b)$$

which lets us rewrite (2.44a)–(2.44b) as

$$\frac{1}{2k} (\bar{u}_t(x, t) - \bar{v}_t(x, t)) = -\frac{1}{2L\bar{\rho}} (\bar{u}_x(x, t) + \bar{v}_x(x, t)) \quad (5.60a)$$

$$\begin{aligned} \frac{1}{2} (\bar{u}_t(x, t) + \bar{v}_t(x, t)) &= -\frac{\gamma\bar{P}}{2kL} (\bar{u}_x(x, t) - \bar{v}_x(x, t)) \\ &\quad - \frac{\gamma\bar{P}}{2k} \frac{a'(xL)}{a(xL)} (\bar{u}(x, t) - \bar{v}(x, t)) \end{aligned} \quad (5.60b)$$

Multiplying (5.60a) by k and adding and subtracting from (5.60b) gives the following expressions for the temporal partial derivatives \bar{u}_t, \bar{v}_t

$$\begin{aligned} \bar{u}_t(x, t) &= -\frac{1}{2L} \left(\frac{k}{\bar{\rho}} + \frac{\gamma\bar{P}}{k} \right) \bar{u}_x(x, t) + \frac{1}{2L} \left(-\frac{k}{\bar{\rho}} + \frac{\gamma\bar{P}}{k} \right) \bar{v}_x(x, t) - \frac{\gamma\bar{P}}{2k} \frac{a'(xL)}{a(xL)} \bar{u}(x, t) \\ &\quad + \frac{\gamma\bar{P}}{2k} \frac{a'(xL)}{a(xL)} \bar{v}(x, t), \end{aligned} \quad (5.61a)$$

$$\begin{aligned} \bar{v}_t(x, t) &= \frac{1}{2L} \left(\frac{k}{\bar{\rho}} - \frac{\gamma\bar{P}}{k} \right) \bar{u}_x(x, t) + \frac{1}{2L} \left(\frac{k}{\bar{\rho}} + \frac{\gamma\bar{P}}{k} \right) \bar{v}_x(x, t) - \frac{\gamma\bar{P}}{2k} \frac{a'(xL)}{a(xL)} \bar{u}(x, t) \\ &\quad + \frac{\gamma\bar{P}}{2k} \frac{a'(xL)}{a(xL)} \bar{v}(x, t). \end{aligned} \quad (5.61b)$$

Applying the definitions of k, c and σ , we write (5.61) as

$$\bar{u}_t(x, t) = -\frac{c}{L} \bar{u}_x(x, t) - \sigma(x) \bar{u}(x, t) + \sigma(x) \bar{v}(x, t) \quad (5.62a)$$

$$\bar{v}_t(x, t) = \frac{c}{L} \bar{v}_x(x, t) - \sigma(x) \bar{u}(x, t) + \sigma(x) \bar{v}(x, t) \quad (5.62b)$$

Next, substituting the subsequent change of variables

$$u(x, t) = \bar{u}(x, t) \exp\left(\frac{L}{c} \int_0^x \sigma(\xi) d\xi\right) \quad (5.63a)$$

$$v(x, t) = \bar{v}(x, t) \exp\left(\frac{L}{c} \int_0^x \sigma(\xi) d\xi\right) \quad (5.63b)$$

into (5.62) we obtain (5.1a)–(5.1b) with λ, μ as given in (5.54) and σ^+, σ^- as given in (5.55).

Composing (5.59) with (5.63) gives the complete change of coordinates (5.52). Substituting this into the boundary conditions (5.1c)–(5.1d), by assigning d_0, d_1 and U as in (5.56)–(5.57) we see (2.44c)–(2.44d) maps into (5.1c)–(5.1d) with $W_0 = 0$, and the proof is complete. \square

5.4.2 Regressor form

Having shown that the acoustics mathematical model (2.44) fits into the form (5.1), we combine here Lemmas 3–4 to suggest a regressor form for estimating the boundary impedances Z_0, Z_L in (2.44).

Lemma 5. Consider the acoustics described by (2.44) and I/O signals W and Y given by (2.44c) and (5.51) respectively. Then the relation

$$\chi(t) = \iota^\top \Psi(t) \quad (5.64)$$

where the signal χ is defined by

$$\chi(t) := 2(Y(t) - I_4^y[Y](t)) + \alpha_W (I_4^y[W](t) - W(t) - I_4^U[W](t)) \quad (5.65)$$

the parameter vector ι is given by

$$\iota := \begin{bmatrix} d_0 d_1^2 \\ d_1^2 \\ d_0 d_1 \\ d_0 \\ d_1 \end{bmatrix} \quad (5.66)$$

and the vector of signals Ψ , which is given by

$$\Psi(t) := \begin{bmatrix} \psi_1(t) \\ \psi_2(t) \\ \psi_3(t) \\ \psi_4(t) \\ \psi_5(t) \end{bmatrix} \quad (5.67)$$

consists of the component signals ψ_i defined by

$$\psi_1(t) := \alpha_W (I_1^y[W](t) - I_2^U[W](t)) \quad (5.68)$$

$$\psi_2(t) := \alpha_W (I_3^y[W](t) - I_4^U[W](t)) \quad (5.69)$$

$$\begin{aligned} \psi_3(t) := & 2(Y(t - \phi_\lambda(1) - \phi_\mu(1)) + I_1^y[Y](t)) \\ & + \alpha_W (I_2^y[W](t) - W(t - \phi_\lambda(1) - \phi_\mu(1)) - I_1^y[W](t)) \end{aligned} \quad (5.70)$$

$$\psi_4(t) := 2I_2^y[Y](t) + \alpha_W (W(t - \phi_\lambda(1) - \phi_\mu(1)) + I_2^U[W](t) - I_2^y[W](t)) \quad (5.71)$$

$$\psi_5(t) := 2I_3^y[Y](t) + \alpha_W (I_4^y[W](t) - W(t) - I_3^y[W](t)) \quad (5.72)$$

holds true.

Proof. The relation between U and W is given in (5.57), and applying this together with (5.51)–(5.52) we write the characteristics measurement y , defined in (5.2), in terms of Y , W and system parameters as

$$y(t) = \frac{2}{1 + d_1} Y(t) - \frac{1 - d_1}{1 + d_1} \exp\left(\frac{L}{c} \int_0^1 \sigma(\xi) d\xi\right) W(t). \quad (5.73)$$

Substituting (5.57), (5.73) into (5.37)–(5.40) gives

$$\omega_1(t) = \frac{2}{1 + d_1} (Y(t - \phi_\lambda(1) - \phi_\mu(1)) + I_1^y[Y](t))$$

$$- \frac{1-d_1}{1+d_1} \exp\left(\frac{L}{c} \int_0^1 \sigma(\xi) d\xi\right) (W(t - \phi_\lambda(1) - \phi_\mu(1)) + I_1^y[W](t)) \quad (5.74)$$

$$\begin{aligned} \omega_2(t) &= (1-d_1) \exp\left(\frac{L}{c} \int_0^1 \sigma(\xi) d\xi\right) (W(t - \phi_\lambda(1) - \phi_\mu(1)) + I_2^U[W](t)) \\ &\quad + \frac{2}{1+d_1} I_2^y[Y](t) - \frac{1-d_1}{1+d_1} \exp\left(\frac{L}{c} \int_0^1 \sigma(\xi) d\xi\right) I_2^y[W](t) \end{aligned} \quad (5.75)$$

$$\omega_3(t) = \frac{2}{1+d_1} I_3^y[Y](t) - \frac{1-d_1}{1+d_1} \exp\left(\frac{L}{c} \int_0^1 \sigma(\xi) d\xi\right) I_3^y[W](t) \quad (5.76)$$

$$\begin{aligned} \omega_4(t) &= \frac{2}{1+d_1} I_4^y[Y](t) - \frac{1-d_1}{1+d_1} \exp\left(\frac{L}{c} \int_0^1 \sigma(\xi) d\xi\right) I_4^y[W](t) \\ &\quad + (1-d_1) \exp\left(\frac{L}{c} \int_0^1 \sigma(\xi) d\xi\right) I_4^U[W](t). \end{aligned} \quad (5.77)$$

Substituting (5.74)–(5.77) into the regressor form (5.45) and multiplying both sides by $(1+d_1)$ yields

$$\begin{aligned} &2Y(t) - (1-d_1) \exp\left(\frac{L}{c} \int_0^1 \sigma(\xi) d\xi\right) W(t) - 2I_4^y[Y](t) \\ &\quad + (1-d_1) \exp\left(\frac{L}{c} \int_0^1 \sigma(\xi) d\xi\right) I_4^y[W](t) - (1-d_1^2) \exp\left(\frac{L}{c} \int_0^1 \sigma(\xi) d\xi\right) I_4^U[W](t) \\ &= d_0 d_1 \left(2(Y(t - \phi_\lambda(1) - \phi_\mu(1)) + I_1^y[Y](t)) \right. \\ &\quad \left. - (1-d_1) \exp\left(\frac{L}{c} \int_0^1 \sigma(\xi) d\xi\right) (W(t - \phi_\lambda(1) - \phi_\mu(1)) + I_1^y[W](t)) \right) \\ &\quad + d_0 \left((1-d_1^2) \exp\left(\frac{L}{c} \int_0^1 \sigma(\xi) d\xi\right) (W(t - \phi_\lambda(1) - \phi_\mu(1)) + I_2^U[W](t)) \right. \\ &\quad \left. + 2I_2^y[Y](t) - (1-d_1) \exp\left(\frac{L}{c} \int_0^1 \sigma(\xi) d\xi\right) I_2^y[W](t) \right) \\ &\quad + d_1 \left(2I_3^y[Y](t) - (1-d_1) \exp\left(\frac{L}{c} \int_0^1 \sigma(\xi) d\xi\right) I_3^y[W](t) \right). \end{aligned}$$

Rearranging gives us the regressor form (5.64), and the proof is complete. \square

With the regressor form (5.64), it should in principle be possible to apply a wide range of different parameter identification schemes to estimate the unknown reflection coefficients d_0 , d_1 and hence Z_0 , Z_L in (2.44). However, the parameter vector ι appearing in (5.64) is more overparametrized than the parameter vector ϑ appearing in (4.6) and (5.45).

5.5 Discussion

We solved in this chapter the problem of estimating both reflection coefficients of 2×2 linear hyperbolic systems of the form (5.1) using a single boundary measurement.

The approach used was similar to the one for boundary estimation in the Rijke tube in Chapter 4, but to deal with the in-domain coupling coefficients the plant was mapped into target system (5.6) for which the MOC is applied to obtain the regressor form (5.45).

Applying a standard parameter estimation scheme, such as least-squares with forgetting factor as suggested, on the system written in regressor form should in theory result in the parameters converging to their correct values, given that the input signal is chosen to be “sufficiently rich” for the signals in the regressor form to be PE. However, as the parameter vectors ϑ given in (4.8), and especially ι in (5.66), are overparametrized, obtaining unique estimates \check{d}_0, \check{d}_1 that are consistent with all the estimates in the parameter vectors is not necessarily guaranteed by the procedure suggested. The solutions could in practice end up in local minima or saddle points that are not representative of the true solution. More investigation needs to go into choice of the input signal and update law for the parameters to be able to guarantee global convergence.

In Section 4.2, the overparametrization comes about as a result of there being unknown boundary coefficients in the relationship (4.5) between physical pressure I/O signals (Y, W) and characteristic coordinate I/O signals (y, U). On the other hand, in Section 5.2 the same overparametrization results from the presence of in-domain coupling coefficients, and in Section 5.4 an even more complicated overparametrization comes about due to both factors. Compared to frequency-domain estimation methods such as the two-microphone method [Seybert & Ross 1977], part of the value in designing time-domain parameter estimation scheme is their application to real-time applications, such as adaptive observers and controllers. Also, to implement the parameter estimation schemes considered here online in a system suffering from thermoacoustic instabilities, the algorithms need to be extended to work in tandem with heat release included in the model.

As mentioned in Chapter 2, the acoustic impedance is often within the paradigm of locally reacting linear surfaces considered to be a general linear system. The parameter estimation schemes presented here consider it as the even more special case of being modelled by a constant scalar, as this formulation is convenient to work with in the time domain. In an analogue to purely resistive networks in electric circuit theory, this formulation only takes the resistive part of the impedance into account and disregards possible reactive parts. As considered in e.g. [Rienstra & Hirschberg 2004], one could model the impedance as a mass-spring-damper system, where the damper represents the resistive part that is currently modelled, and the mass and spring model reactive parts of the impedance, analogous to inductors and capacitors modelling the reactive parts of the impedance in electric circuit theory. With such a model, the parameter estimation scheme would have three parameter to estimate at each boundary, namely the unknown mass, spring constant and damping coefficient. The problem would then formulate as parameter identification for a coupled hyperbolic PDE–ODE system.

So far we considered in Section 5.4 the estimation of acoustic impedances in a duct with spatially varying geometry, but the acoustic properties of the duct

walls was not explicitly taken into account. For the sake of boundary acoustic impedance estimation, modelling of the acoustics where such distributed damping due to the particular material is taken into account would be a useful further step from the model (2.44), as this could prevent possible distributed contributions from the acoustic properties of the material to be inadvertently lumped into the boundary impedance estimates.

Linear Combustor

Contents

6.1	Background	118
6.1.1	Literature review	118
6.1.2	Model in Riemann coordinates	119
6.1.3	Problem statement	122
6.2	Control Design	123
6.2.1	Mapping into simpler cascade	124
6.2.2	Analysis of kernels	126
6.2.3	Full control law	128
6.3	Observer Design	130
6.3.1	Mapping into stable cascade	130
6.3.2	Analysis of kernels	132
6.3.3	Observer	133
6.4	Output Feedback Controller	134
6.5	Simulations	135
6.5.1	Simulation parameters	135
6.5.2	Simulation results	137
6.6	Discussion	139

Dans ce chapitre, un contrôleur par retour de sortie est proposé pour stabiliser les instabilités thermoacoustiques longitudinales dans un modèle mathématique d'une chambre de combustion de la forme (2.45), avec le sous-système décrivant la flamme linéarisé. Après avoir montré que (2.45) avec un dégagement de chaleur linéarisé peut être écrit comme un système d'EDP hyperbolique linéaire 2×2 couplé à un sous-système d'EDO avec retard, une commande par retour d'état est proposée. Elle est conçue grâce à un changement de variables transformant le système considéré en une cascade EDP-EDO simplifiée, pour laquelle la conception de la commande est un problème résolu. Ensuite, l'observateur est conçu en transformant la dynamique de l'erreur d'estimation en une cascade stable EDP-EDO. En combinant la loi de contrôle par retour d'état et l'observateur, on obtient un commande par retour de sortie. Un exemple de simulation pour illustrer la théorie est présenté.

In this chapter an output-feedback controller to stabilize longitudinal thermoacoustic instabilities in a mathematical model of a can combustor as given by (2.45),

with the flame subsystem linearised, is proposed. After showing that (2.45) with linearized heat release can be written as a 2×2 linear hyperbolic PDE coupled to an ODE subsystem with instantaneous and time-delayed interaction, a full-state feedback law is proposed. It is designed by mapping the considered plant into a simplified PDE–ODE cascade, for which control design is a solved problem. Subsequently, the observer is designed by mapping the estimation error dynamics directly into a stable target PDE–ODE cascade. Combining the full-state feedback control law and observer we arrive at an output feedback controller. A simulation example to demonstrate the theory is presented, where the full-state feedback controller, observer and output feedback controller are shown to stabilize and estimate the pressure, velocity and heat release rate.

6.1 Background

6.1.1 Literature review

Much of the early work on combustion instability focused on developing methods to passively dampen [Culick 1988, Putnam 1971] out the instabilities by ad-hoc physical augmentation of the system. Although it is advantageous to have an inherently stable system, passive methodologies to stabilize thermoacoustic instabilities can turn out to be incredibly expensive, the infamous Apollo F-1 project [Oefelein & Yang 1993] being an example of this. Also as noted in [Dowling & Morgans 2005], even though a passive method works well within a given operating region, it might have limited applicability to other operating conditions.

An alternative to passive stabilization of thermoacoustic instabilities is active stabilization. The interest of this approach amongst researchers in the field has gone in and out of fashion since the problem first started being studied, with one of the earliest contributions [Tsien 1952] being from the beginning of the 1950s. A few decades later active feedback control of combustion instabilities was demonstrated experimentally, firstly on the Rijke tube [Dines 1984, Heckl 1988] and gradually on more complex rigs [Lang *et al.* 1987, Neumeier *et al.* 1996, Johnson *et al.* 2001], via empirically designed *phase-shift controllers*. These are based on feeding back an amplified and phase-shifted measurement signal¹, tuned via a trial-and-error approach. More sophisticated control algorithms, both in the form of data-driven [Kemal & Bowman 1996, Blonbou *et al.* 2000, Murugappan *et al.* 2003] and model-based [Yang *et al.* 1992, Krstić *et al.* 1999, Annaswamy *et al.* 2000] design approaches have been explored.

Many of the model-based control algorithms in the literature rely on truncating the infinite dimensional model of the thermoacoustic instability into a finite number of modes, arguing that the lower order modes are most significant for the instability and the higher order modes can thus be disregarded. This

¹This is usually a pressure measurement but other metrics such as CH^* radicals or soot formation can be used.

approach reduces the plant model to be stabilized as a set of ODEs, and a finite-dimensional control law can then be developed to stabilize these lower order modes. Unfortunately, a problem with this approach is that although the modes included in the truncated model are stabilized, instabilities at higher frequencies that were not present initially may inadvertently occur as a result of the intervention [Bloxsidge *et al.* 1987, Gulati & Mani 1992].

Additionally, it is typically assumed that the duct acoustics can be modelled by an ideal wave equation, which in reality requires that the duct has constant cross-sectional area relative to the propagation of the acoustic waves and no internal damping. This is a reasonable assumption for many laboratory setups, where the ducts are purposefully made to be straight, but since real combustion chambers tend to have more complex geometry, for them it is not necessarily the case. As pointed out in [Poinsot 2017], the chamber geometry is a highly significant determining factor for combustion instability, and is thus important to take into account when considering the suppression of thermoacoustic instabilities in real combustion chambers. In [de Andrade *et al.* 2018b, de Andrade *et al.* 2018a], an infinite-dimensional full-state feedback control law and boundary observer for stabilizing thermoacoustic instabilities in the Rijke tube are designed, respectively. Although the acoustics model considered contains all modes of the system, the Rijke tube has straight geometry and the design is therefore not directly applicable to real combustion chambers.

The objective of this chapter is to propose a model-based output-feedback control law for stabilizing thermoacoustic instabilities that takes into account the infinite-dimensional nature of the duct acoustics and effects from spatially varying geometry. A linear flame response is assumed, which is a reasonable assumption for early stages of the instability, and hence if the instability is suppressed fast enough nonlinear effects are unnecessary to take into account. As part of the design process, an observer that estimates pressure, velocity and heat release in the combustion chamber from a pressure measurement is derived. As a contribution on its own, the observer could have applications within early warning systems to detect thermoacoustic instabilities before they grow unstable.

6.1.2 Model in Riemann coordinates

Consider the setup shown in Figure 6.1. It consists of a duct of length L and spatially varying cross-sectional area $a(z)$, where $z \in [0, L]$. It is assumed a premixed flame is burning at $z = 0$, being fed by a fuel injector. At the far end of the duct, at $z = L$, a loudspeaker is assumed to be collocated with a pressure sensor. This setup can be modelled by the can combustor model (2.45), where the input signal W comes in via the boundary condition (2.45e), and the output signal Y is as defined in (5.51).

In this chapter, we consider the special case when the flame subsystem (2.45a)–(2.45b) is linearised. We present now a Lemma mapping the model considered into a form suitable for algorithm design and analysis.

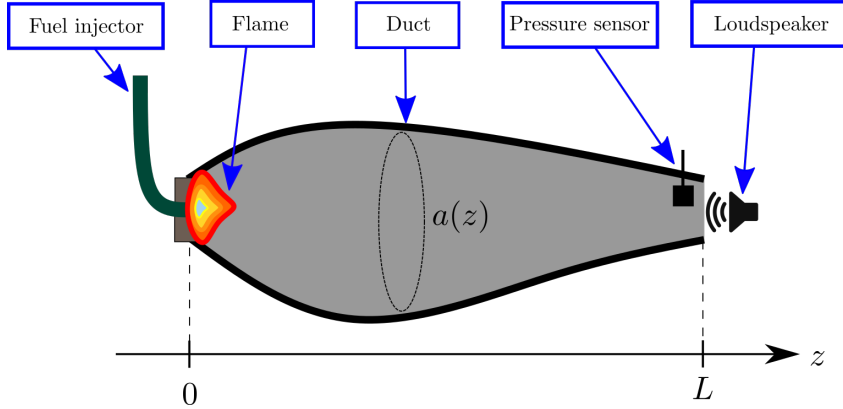


Figure 6.1: Sketch of combustor setup considered.

Lemma 6. Consider the system (2.45), where $f(\cdot)$, $g_0(\cdot)$, $g_1(\cdot)$ in (2.45a) and $h(\cdot)$ in (2.45b) take the particular form

$$f(X) := AX, \quad \bar{g}_0(X) := \bar{B}_0, \quad \bar{g}_1(X) := \bar{B}_1, \quad \bar{h}(X) := \bar{C}X,$$

with $A \in \mathbb{R}^{n \times n}$, $\bar{B}_0, \bar{B}_1 \in \mathbb{R}^{n \times 1}$ and $\bar{C} \in \mathbb{R}^{1 \times n}$ constant matrices. With the change of variables

$$u(x, t) := \left(\check{P}(xL, t) + k(xL)\check{V}(xL, t) \right) \exp \left(-L \int_0^x \frac{\bar{\sigma}^{++}(\xi)}{c(\xi L)} d\xi \right) \quad (6.1a)$$

$$v(x, t) := \left(\check{P}(xL, t) - k(xL)\check{V}(xL, t) \right) \exp \left(L \int_0^x \frac{\bar{\sigma}^{--}(\xi)}{c(\xi L)} d\xi \right) \quad (6.1b)$$

the system satisfies the dynamics

$$\dot{X}(t) = AX(t) + B_0v(0, t) + B_1v(0, t - \tau) \quad (6.2a)$$

$$u_t(x, t) = -\lambda(x)u_x(x, t) + \sigma^+(x)v(x, t) \quad (6.2b)$$

$$v_t(x, t) = \mu(x)v_x(x, t) + \sigma^-(x)u(x, t) \quad (6.2c)$$

$$u(0, t) = d_0v(0, t) + CX(t) \quad (6.2d)$$

$$v(1, t) = d_1u(1, t) + U(t), \quad (6.2e)$$

with transport speeds

$$\lambda(x) := \frac{c(xL)}{L} \quad (6.3a)$$

$$\mu(x) := \frac{c(xL)}{L} \quad (6.3b)$$

in-domain coupling coefficients

$$\sigma^+(x) := \bar{\sigma}^{+-}(x) \exp \left(-L \int_0^x \frac{\bar{\sigma}^{++}(\xi) + \bar{\sigma}^{--}(\xi)}{c(\xi L)} d\xi \right), \quad (6.4a)$$

$$\sigma^-(x) := \bar{\sigma}^{-+}(x) \exp\left(L \int_0^x \frac{\bar{\sigma}^{++}(\xi) + \bar{\sigma}^{--}(\xi)}{c(\xi L)} d\xi\right) \quad (6.4b)$$

reflection coefficients

$$d_0 := \frac{1 - \alpha}{1 + \alpha}, \quad (6.5a)$$

$$d_1 := \frac{Z - k(L)}{Z + k(L)} \exp\left(L \int_0^1 \frac{\bar{\sigma}^{++}(\xi) + \bar{\sigma}^{--}(\xi)}{c(\xi L)} d\xi\right), \quad (6.5b)$$

boundary input signal

$$U(t) := \frac{2k(L)}{k(L) + Z} \exp\left(L \int_0^1 \frac{\bar{\sigma}^{--}(\xi)}{c(\xi L)} d\xi\right) W(t) \quad (6.6)$$

and matrix-valued parameters B_0 , B_1 , C given by

$$B_0 := -\frac{1}{2k(0)} \bar{B}_0 \quad (6.7)$$

$$B_1 := -\frac{1}{2k(0)} \bar{B}_1 \quad (6.8)$$

$$C := \frac{2k(0)}{1 + \alpha} \theta \bar{C} \quad (6.9)$$

where

$$\bar{\sigma}^{++}(x) := -\frac{1 + \gamma}{2} \bar{V}'(xL) - \frac{1}{2k(xL)} \left(\bar{P}'(xL) + \left(\frac{a'(xL)}{a(xL)} - \frac{k'(xL)}{k(xL)} \right) \gamma \bar{P}(xL) \right) \quad (6.10a)$$

$$\bar{\sigma}^{+-}(x) := \frac{1 - \gamma}{2} \bar{V}'(xL) + \frac{1}{2k(xL)} \left(\bar{P}'(xL) + \left(\frac{a'(xL)}{a(xL)} - \frac{k'(xL)}{k(xL)} \right) \gamma \bar{P}(xL) \right) \quad (6.10b)$$

$$\bar{\sigma}^{-+}(x) := \frac{1 - \gamma}{2} \bar{V}'(xL) - \frac{1}{2k(xL)} \left(\bar{P}'(xL) + \left(\frac{a'(xL)}{a(xL)} - \frac{k'(xL)}{k(xL)} \right) \gamma \bar{P}(xL) \right) \quad (6.10c)$$

$$\bar{\sigma}^{--}(x) := -\frac{1 + \gamma}{2} \bar{V}'(xL) + \frac{1}{2k(xL)} \left(\bar{P}'(xL) + \left(\frac{a'(xL)}{a(xL)} - \frac{k'(xL)}{k(xL)} \right) \gamma \bar{P}(xL) \right) \quad (6.10d)$$

and

$$k(z) := \sqrt{\gamma \bar{\rho}(z) \bar{P}(z)}, \quad (6.11)$$

$$c(z) := \sqrt{\frac{\gamma \bar{P}(z)}{\bar{\rho}(z)}}. \quad (6.12)$$

Proof. The part of the Proof regarding mapping of the acoustics (2.45c)–(2.45d) into the PDE dynamics (6.2b)–(6.2c) and boundary condition (2.45e) into (6.2e) is almost identical to steps followed in the proof of Lemma 4, so it is omitted.

Evaluating the change of variables (6.1) at $x = 0$, and denoting by $u^-(0, \cdot), v^-(0, \cdot)$ characteristic variables directly upstream of the flame and area jump, $u^+(0, \cdot), v^+(0, \cdot)$ characteristic variables directly downstream of the flame, we rewrite (2.45f)–(2.45g) as

$$\frac{1}{2} (u^+(0, t) + v^+(0, t)) = \frac{1}{2} (u^-(0, t) + v^-(0, t)) \quad (6.13a)$$

$$\frac{1}{2} (u^+(0, t) - v^+(0, t)) = \frac{\alpha}{2} (u^-(0, t) - v^-(0, t)) + k(0)\theta\bar{C}X(t). \quad (6.13b)$$

Adding and subtracting (6.13a) respectively to and from (6.13b), after some algebra we have the boundary conditions

$$u^+(0, t) = \frac{1-\alpha}{1+\alpha}v^+(0, t) + \frac{2\alpha}{1+\alpha}u^-(0, t) + \frac{2k(0)\theta}{1+\alpha}\bar{C}X(t), \quad (6.14a)$$

$$v^-(0, t) = \frac{-1+\alpha}{1+\alpha}u^-(0, t) + \frac{2}{1+\alpha}v^+(0, t) + \frac{2k(0)\theta}{1+\alpha}\bar{C}X(t). \quad (6.14b)$$

Substituting characteristic variables into the linearized flame model followed by boundary conditions (6.14) gives

$$\dot{X}(t) = AX(t) + \bar{B}_0 \frac{u^-(0, t) - v^+(0, t)}{2k(0)} + \bar{B}_1 \frac{u^-(0, t - \tau) - v^+(0, t - \tau)}{2k(0)}. \quad (6.15)$$

Thanks to Assumption 15, a non-reflective section is upstream of the boundary (6.14), so we can in (6.14)–(6.15) set $u^-(0, \cdot) = 0$. Also, since $v^-(0, \cdot)$ exits the system the boundary condition (6.14b) is disregarded in the final model. Hence, denoting $u(0, \cdot) = u^+(0, \cdot), v(0, \cdot) = v^+(0, \cdot)$ gives respectively (6.2d) with d_0 assigned in (6.5a), C assigned in (6.9) and (6.2a) with B_0, B_1 assigned in (6.7)–(6.8). \square

Remark 7. *Note that for the physical control signal W in (6.6) to be implementable in practice, the proportionality constant between U and W must be non-zero. Physically this corresponds to the case when the actuated boundary is not an ideal rigid wall, which in theory would correspond to a velocity node and hence an infinite specific impedance Z .*

6.1.3 Problem statement

We consider in this chapter boundary controller and observer design of the plant (6.2). In Section 6.2–6.3 the problems of full-state feedback control design and observer design for the plant is considered in general. These designs are then combined into an output-feedback controller in Section 6.4 which is applied to stabilize longitudinal thermoacoustic instabilities in a simulation example presented in Section 6.5.

The plant (6.2) consists of a linear ODE subsystem (6.2a) with state $X \in \mathbb{R}^n$ defined for $t \in [0, \infty)$, where $A \in \mathbb{R}^{n \times n}$, and having both instantaneous and time-delayed input signals entering via $B_0, B_1 \in \mathbb{R}^{n \times 1}$, respectively. It is coupled via the boundary (6.2d), with $C \in \mathbb{R}^{1 \times n}$ and $d_0 \in \mathbb{R}$, to a 2×2 linear hyperbolic PDE

system (6.2b)–(6.2c), with states $u, v \in L^2(0, 1)$ defined over $(x, t) \in [0, 1] \times [0, \infty)$. The parameters of the PDE system are the transport speeds $\lambda, \mu \in C^1(0, 1)$, $\lambda, \mu > 0$, and in-domain coupling coefficients $\sigma^+, \sigma^- \in L^\infty(0, 1)$. The plant is actuated by the signal $U : [0, \infty) \mapsto \mathbb{R}$ via the boundary condition (6.2e), where $d_1 \in \mathbb{R}$, and we assume a collocated measurement signal y , defined as in (5.2) is available. For the purpose of the control and observer designs we make the following assumption.

Assumption 17. *The transport speeds $\lambda, \mu \in C^1(0, 1)$ and time delay $\tau \in \mathbb{R}$ in (6.2) satisfy the inequalities*

- $\lambda(x), \mu(x), \tau > 0$,
- $\tau \geq \int_0^1 \frac{dx}{\lambda(x)}, \int_0^1 \frac{dx}{\mu(x)}$.

Additionally, to facilitate the control and observer design we introduce the artificial state w , defined according to

$$w_t(x, t) = -\frac{1}{\tau}w_x(x, t), \quad (6.16a)$$

$$w(0, t) = v(0, t). \quad (6.16b)$$

The plant ODE (6.2a) is then rewritten as

$$\dot{X}(t) = AX(t) + B_0v(0, t) + B_1w(1, t). \quad (6.17)$$

The problem of boundary control and observer design for interconnected PDE–ODE systems has been widely studied in the literature the past decade, both for parabolic PDEs [Tang & Xie 2011] and hyperbolic PDEs [Di Meglio *et al.* 2018]. These build on contributions for stabilization of PDEs, which for hyperbolic PDEs was firstly achieved with the backstepping method in [Vazquez *et al.* 2011]. Alternative methods to backstepping have also been considered, such as Lyapunov-based methods [Castillo *et al.* 2013]. In [Castillo *et al.* 2012] Lyapunov based methods are considered for hyperbolic PDEs with dynamic boundary conditions.

With $B_1 = 0$ in (6.2) the collocated controller and observer design from [Di Meglio *et al.* 2018] can be applied to stabilize (6.2), but when $B_1 \neq 0$ the delayed input signal causes extra difficulties. As an isolated subsystem with $v(0, \cdot)$ considered as the input signal, stabilization of (6.2a) is considered in [Kwon & Pearson 1980, Artstein 1982]. The plant considered in [de Andrade *et al.* 2018b] can be written to look similar to (6.2), but only a scalar ODE is considered and the PDE subsystems have no in-domain couplings. Likewise, the plant considered in [Auriol *et al.* 2020a] can be written to look similar to (6.2) but instead of a term proportional to the delayed $v(0, \cdot)$ signal one would have a term related to the delayed ODE state $X(\cdot)$.

6.2 Control Design

The control design is performed in two steps. First, (6.2) is mapped into a simpler cascade for which the control design is known. Subsequently, the control law for

the simpler cascade is written out and the expression for U that stabilizes (6.2) is recovered.

6.2.1 Mapping into simpler cascade

Consider the cascade system

$$\dot{Z}(t) = AZ(t) + \bar{B}\beta(0, t) \quad (6.18a)$$

$$\alpha_t(x, t) = -\lambda(x)\alpha_x(x, t) \quad (6.18b)$$

$$\beta_t(x, t) = \mu(x)\beta_x(x, t) \quad (6.18c)$$

$$\alpha(0, t) = d_0\beta(0, t) \quad (6.18d)$$

$$\beta(1, t) = d_1\alpha(1, t) + V(t) \quad (6.18e)$$

where \bar{B} and V are to be defined, and the change of coordinates

$$Z(t) = X(t) - \int_0^1 r(\xi)w(\xi, t)d\xi \quad (6.19a)$$

$$\begin{aligned} \alpha(x, t) = & u(x, t) - \nu_u(x)^\top X(t) - \int_0^x K^{uu}(x, \xi)u(\xi, t)d\xi \\ & - \int_0^x K^{uv}(x, \xi)v(\xi, t)d\xi - \int_0^1 R^u(x, \xi)w(\xi, t)d\xi \end{aligned} \quad (6.19b)$$

$$\begin{aligned} \beta(x, t) = & v(x, t) - \nu_v(x)^\top X(t) - \int_0^x K^{vv}(x, \xi)v(\xi, t)d\xi \\ & - \int_0^x K^{vu}(x, \xi)u(\xi, t)d\xi - \int_0^1 R^v(x, \xi)w(\xi, t)d\xi \end{aligned} \quad (6.19c)$$

where r satisfies for $\xi \in [0, 1]$

$$r'(\xi) = \tau Ar(\xi) + \frac{\tau}{d_0}\bar{B}R^u(0, \xi), \quad (6.20a)$$

$$r(1) = -\tau B_1, \quad (6.20b)$$

ν_u, ν_v satisfy for $x \in [0, 1]$

$$\nu'_u(x) = -\frac{1}{\lambda(x)}A^\top \nu_u(x) - \frac{\lambda(0)}{\lambda(x)}K^{uu}(x, 0)C^\top \quad (6.21a)$$

$$\nu'_v(x) = \frac{1}{\mu(x)}A^\top \nu_v(x) + \frac{\lambda(0)}{\mu(x)}K^{vv}(x, 0)C^\top \quad (6.21b)$$

$$\nu_u(0) = C^\top \quad (6.21c)$$

$$\nu_v(0) = 0, \quad (6.21d)$$

R^u, R^v are for $(x, \xi) \in \mathcal{S}$, the square domain $\mathcal{S} := \{(x, \xi) \mid 0 \leq x, \xi \leq 1\}$, given by

$$\frac{1}{\tau}R_\xi^u(x, \xi) = -\lambda(x)R_x^u(x, \xi) \quad (6.22a)$$

$$\frac{1}{\tau}R_\xi^v(x, \xi) = \mu(x)R_x^v(x, \xi) \quad (6.22b)$$

$$R^u(x, 1) = \tau \nu_u(x)^\top B_1 \quad (6.22c)$$

$$R^u(1, \xi) = 0 \quad (6.22d)$$

$$R^v(x, 1) = \tau \nu_v(x)^\top B_1 \quad (6.22e)$$

$$R^v(0, \xi) = \frac{1}{d_0} R^u(0, \xi) \quad (6.22f)$$

and finally $K^{uu}, K^{uv}, K^{vu}, K^{vv}$ are for $(x, \xi) \in \mathcal{T}_l$, the lower triangular domain $\mathcal{T}_l := \{(x, \xi) \mid 0 \leq \xi \leq x \leq 1\}$, given by

$$\lambda(x)K_x^{uu}(x, \xi) + \lambda(\xi)K_\xi^{uu}(x, \xi) = -\lambda'(\xi)K^{uu}(x, \xi) - \sigma^-(\xi)K^{uv}(x, \xi) \quad (6.23a)$$

$$\lambda(x)K_x^{uv}(x, \xi) - \mu(\xi)K_\xi^{uv}(x, \xi) = \mu'(\xi)K^{uv}(x, \xi) - \sigma^+(\xi)K^{uu}(x, \xi) \quad (6.23b)$$

$$\mu(x)K_x^{vu}(x, \xi) - \lambda(\xi)K_\xi^{vu}(x, \xi) = \lambda'(\xi)K^{vu}(x, \xi) + \sigma^-(\xi)K^{vv}(x, \xi) \quad (6.23c)$$

$$\mu(x)K_x^{vv}(x, \xi) + \mu(\xi)K_\xi^{vv}(x, \xi) = -\mu'(\xi)K^{vv}(x, \xi) + \sigma^+(\xi)K^{vu}(x, \xi) \quad (6.23d)$$

$$\begin{aligned} K^{uu}(x, 0) &= \frac{\mu(0)}{d_0 \lambda(0)} K^{uv}(x, 0) - \frac{1}{d_0 \lambda(0)} \nu_u(x)^\top B_0 \\ &\quad - \frac{1}{d_0 \lambda(0) \tau} R^u(x, 0) \end{aligned} \quad (6.23e)$$

$$K^{uv}(x, x) = \frac{\sigma^+(x)}{\lambda(x) + \mu(x)} \quad (6.23f)$$

$$K^{vu}(x, x) = -\frac{\sigma^-(x)}{\lambda(x) + \mu(x)} \quad (6.23g)$$

$$\begin{aligned} K^{vv}(x, 0) &= \frac{\lambda(0)d_0}{\mu(0)} K^{vu}(x, 0) + \frac{1}{\mu(0)} \nu_v(x)^\top B_0 \\ &\quad + \frac{1}{\mu(0)\tau} R^v(x, 0). \end{aligned} \quad (6.23h)$$

The vector \bar{B} in (6.18a) is defined in terms of the solution to (6.20) as

$$\bar{B} := B_0 - \frac{1}{\tau} r(0). \quad (6.24)$$

We have the following Lemma.

Lemma 7. *With U in (6.2e) given by*

$$\begin{aligned} U(t) &= V(t) + (\nu_v(1)^\top - d_1 \nu_u(1)^\top) X(t) + \int_0^1 (K^{vu}(1, \xi) - d_1 K^{uu}(1, \xi)) u(\xi, t) d\xi \\ &\quad + \int_0^1 (K^{vv}(1, \xi) - d_1 K^{uv}(1, \xi)) v(\xi, t) d\xi + \int_0^1 R^v(1, \xi) w(\xi, t) d\xi, \end{aligned} \quad (6.25)$$

the transformation (6.19)–(6.23) maps (6.2) into (6.18), (6.24), whenever (6.20)–(6.23) has a unique, smooth solution.

Proof. Differentiating (6.19a) with respect to time, (6.19b)–(6.19c) with respect to time and space, integrating by parts and substituting the resultant expressions into

target dynamics (6.18a)–(6.18c), applying (6.20), (6.21a)–(6.21b), (6.22a)–(6.22c), (6.22e), (6.23) and (6.24) we recover (6.2a)–(6.2c).

Furthermore, evaluating (6.19b)–(6.19c) at $x = 0$ and substituting into (6.18d), from applying (6.21c)–(6.21d), (6.22f) we recover (6.2d). Finally, evaluating (6.19b)–(6.19c) at $x = 1$, substituting into (6.18e) and applying (6.22d) we obtain (6.2e), (6.25). \square

Remark 8. Note that $\nu_v(0)$ and $R^u(1, \cdot)$ do not necessarily need to be assigned to zero as in (6.21d), (6.22d), respectively; their values are an extra degree of freedom in the design. However, in assigning a non-zero value to these boundary conditions, \bar{B} defined in (6.24) will be the solution to a nonlinear matrix equation, which may or may not have a unique solution, depending on the system parameters. As is shown further down, picking them as (6.21d), (6.22d) lets \bar{B} be solved as the solution to a linear matrix equation.

6.2.2 Analysis of kernels

As mentioned in Lemma 7, in order to map (6.2) into (6.18) via a transformation of the form (6.19), the kernels (6.20)–(6.23), in addition to \bar{B} defined as (6.24), must have a well-posed solution. We show here that this is the case under Assumption 17 and sufficiently smooth model parameters in (6.2).

Firstly, the general solution of (6.20) is for $\xi \in [0, 1]$ given by

$$r(\xi) = -\tau \left(e^{\tau A(\xi-1)} B_1 + \frac{1}{d_0} \int_{\xi}^1 e^{-\tau A s} \bar{B} R^u(0, s) ds \right). \quad (6.26)$$

Evaluating then (6.26) at $\xi = 0$ and substituting into (6.24), with the matrix E defined as

$$E := I - \frac{1}{d_0} \int_0^1 e^{\tau A s} R^u(0, s) ds, \quad (6.27)$$

and I denoting the identity matrix, we uniquely solve for \bar{B} as

$$\bar{B} = E^{-1} (B_0 + e^{-A\tau} B_1). \quad (6.28)$$

Note that this requires the following Assumption:

Assumption 18. The matrix E defined by (6.27) is invertible.

Applying the MOC, under Assumption 17 we have the solution of (6.22) given by

$$R^u(x, \xi) = \begin{cases} \tau \nu_u (\phi_\lambda^{-1} (\phi_\lambda(x) + \tau(1 - \xi)))^\top B_1, & \text{if } \xi > 1 - \frac{1}{\tau} (\phi_\lambda(1) - \phi_\lambda(x)) \\ 0, & \text{if } \xi \leq 1 - \frac{1}{\tau} (\phi_\lambda(1) - \phi_\lambda(x)) \end{cases} \quad (6.29a)$$

$$R^v(x, \xi) = \begin{cases} \tau \nu_v (\phi_\mu^{-1} (\phi_\mu(x) + \tau(\xi - 1)))^\top B_1, & \text{if } \xi > 1 - \frac{1}{\tau} \phi_\mu(x) \\ \frac{1}{d_0} R^u(0, \xi + \frac{1}{\tau} \phi_\mu(x)), & \text{if } \xi \leq 1 - \frac{1}{\tau} \phi_\mu(x). \end{cases} \quad (6.29b)$$

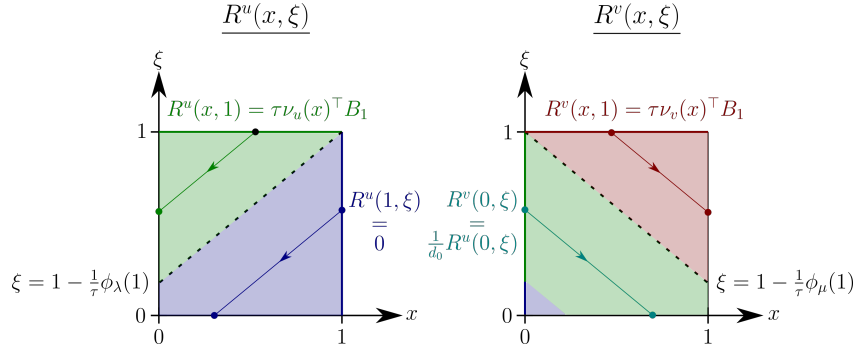


Figure 6.2: Sketch of solutions to R^u and R^v . The region shaded in green has characteristics originating from the boundary condition along $R^u(\cdot, 1)$, the region shaded in blue has characteristics with data originating in $R^u(1, \cdot)$, and the region shaded in red has characteristics coming from the boundary condition of $R^v(\cdot, 1)$. The line of discontinuity in the solution of R^u terminates along $x = 0$ at the point $\xi = 1 - \frac{1}{\tau}\phi_\lambda(1)$, while the main line of discontinuity in the solution to R^v terminates along $x = 1$ at the point $\xi = 1 - \frac{1}{\tau}\phi_\mu(1)$.

where ϕ_λ, ϕ_μ are functions of the form (5.13).

The solutions to R^u, R^v are illustrated in Figure 6.2. Thus, evaluating (6.29a) at $\xi = 0$ and substituting into (6.23e) we have

$$K^{uu}(x, 0) = \frac{\mu(0)}{d_0\lambda(0)}K^{uv}(x, 0) + \nu_u(x)^\top \left(-\frac{1}{d_0\lambda(0)}B_0 \right). \quad (6.30)$$

Subsequently, substituting (6.30) into (6.21a) gives us

$$\nu_u'(x) = \left(-\frac{1}{\lambda(x)}A^\top + \frac{1}{d_0\lambda(x)}CB_0^\top \right) \nu_u(x) + K^{uv}(x, 0) \left(-\frac{\mu(0)}{d_0\lambda(x)}C^\top \right). \quad (6.31)$$

Then, (6.30)–(6.31) together with (6.21c), (6.23a)–(6.23b), (6.23f) forms a coupled system of equations to solve for (K^{uu}, K^{uv}, ν_u) .

Likewise, evaluating (6.29b) at $\xi = 0$ and substituting into (6.23h) yields

$$K^{vv}(x, 0) = \frac{\lambda(0)d_0}{\mu(0)}K^{vu}(x, 0) + \nu_v(x)^\top \left(\frac{1}{\mu(0)}B_0 \right) + \frac{1}{d_0\mu(0)\tau}R^u \left(0, \frac{1}{\tau}\phi_\mu(x) \right). \quad (6.32)$$

From (6.29a) we see R^u is only dependent on the solution to ν_u , and hence (6.32) together with (6.21b), (6.21d), (6.23c)–(6.23d), (6.23g) forms a coupled system of equations to solve for (K^{vv}, K^{vu}, ν_v) . To assess the regularity of solutions to the systems of equations for (K^{uu}, K^{uv}, ν_u) , (K^{vv}, K^{vu}, ν_v) , respectively, we need the following Lemma.

Lemma 8. *The coupled system*

$$\varepsilon_1(x)G_x^1(x, \xi) + \varepsilon_1(\xi)G_\xi^1(x, \xi) = c_{11}(x, \xi)G^1(x, \xi) + c_{12}(x, \xi)G^2(x, \xi) \quad (6.33a)$$

$$\varepsilon_1(x)G_x^2(x, \xi) - \varepsilon_2(\xi)G_\xi^2(x, \xi) = c_{21}(x, \xi)G^1(x, \xi) + c_{22}(x, \xi)G^2(x, \xi) \quad (6.33b)$$

$$G^1(x, 0) = aG^2(x, 0) + \gamma(x)^\top F + b_1(x) \quad (6.33c)$$

$$G^2(x, x) = b_2(x) \quad (6.33d)$$

$$\gamma'(x) = D(x)\gamma(x) + G^2(x, 0)E(x) \quad (6.33e)$$

$$\gamma(0) = H \quad (6.33f)$$

with parameters satisfying $\varepsilon_1, \varepsilon_2 \in C^1(0, 1)$, $\varepsilon_1, \varepsilon_2 > 0$, $a \in \mathbb{R}$, $b_1, b_2 \in C(0, 1)$, $c_{11}, c_{12}, c_{21}, c_{22} \in C(\mathcal{T}_l)$, $D \in C((0, 1); \mathbb{R}^{n \times n})$, $E \in C((0, 1); \mathbb{R}^{n \times 1})$, $F, H \in \mathbb{R}^{n \times 1}$ has a unique solution $G^1, G^2 \in L^\infty(\mathcal{T}_l)$, $\gamma \in (L^\infty[0, 1])^n$.

The proof of this Lemma is almost identical to the proof of Lemma 1 in [Auriol *et al.* 2018], and hence omitted.

Through comparison we see the systems of equations for (K^{uu}, K^{uv}, ν_u) , (K^{vv}, K^{vu}, ν_v) can be written in the form (6.33) with appropriate coefficient assignment, and hence by Lemma 8 we establish that $K^{uu}, K^{uv}, K^{vu}, K^{vv} \in L^\infty(\mathcal{T}_l)$, $\nu_u, \nu_v \in (L^\infty[0, 1])^n$.

6.2.3 Full control law

We present now the main result of this section.

Theorem 4. *Let Assumption 17 and 18 be satisfied, and assume that (A, \bar{B}) is a controllable pair, $\mathcal{K} \in \mathbb{R}^{1 \times n}$ chosen so that $(A + \bar{B}\mathcal{K})$ is Hurwitz. Denote by Φ_α, Φ_β the state transition matrices defined via*

$$\frac{\partial}{\partial x} \Phi_\alpha(x, \sigma) = -\frac{1}{\lambda(x)} A^\top \Phi_\alpha(x, \sigma), \quad \Phi_\alpha(\sigma, \sigma) = I \quad (6.34a)$$

$$\frac{\partial}{\partial x} \Phi_\beta(x, \sigma) = \frac{1}{\mu(x)} A^\top \Phi_\beta(x, \sigma), \quad \Phi_\beta(\sigma, \sigma) = I. \quad (6.34b)$$

Then the full-state feedback control law

$$U(t) = \Pi^\top X(t) + \int_0^1 \pi_u(\xi) u(\xi, t) d\xi + \int_0^1 \pi_v(\xi) v(\xi, t) d\xi + \int_0^1 \pi_w(\xi) w(\xi, t) d\xi \quad (6.35)$$

with

$$\Pi := N^X + \nu_v(1)^\top - d_1 \nu_u(1)^\top \quad (6.36a)$$

$$\pi_u(x) := N^u(x) + K^{vu}(1, x) - d_1 K^{uu}(1, x) \quad (6.36b)$$

$$\pi_v(x) := N^v(x) + K^{vv}(1, x) - d_1 K^{uv}(1, x) \quad (6.36c)$$

$$\pi_w(x) := N^w(x) + R^v(1, x) \quad (6.36d)$$

with N^X, N^u, N^v, N^w defined by

$$N^u(\xi) := \mathcal{M}^\alpha(\xi) - \int_\xi^1 \mathcal{M}^\alpha(s) K^{uu}(s, \xi) ds - \int_\xi^1 \mathcal{M}^\beta(s) K^{vu}(s, \xi) ds \quad (6.37a)$$

$$N^v(\xi) := \mathcal{M}^\beta(\xi) - \int_\xi^1 \mathcal{M}^\alpha(s)K^{uv}(s, \xi)ds - \int_\xi^1 \mathcal{M}^\beta(s)K^{vv}(s, \xi)ds \quad (6.37b)$$

$$N^w(\xi) := -\mathcal{M}^Z r(\xi) - \int_0^1 \mathcal{M}^\alpha(s)R^u(s, \xi)ds - \int_0^1 \mathcal{M}^\beta(s)R^v(s, \xi)ds \quad (6.37c)$$

$$N^X := \mathcal{M}^Z - \int_0^1 \mathcal{M}^\alpha(\xi)\nu_u(\xi)^\top d\xi - \int_0^1 \mathcal{M}^\beta(\xi)\nu_v(\xi)^\top d\xi \quad (6.37d)$$

and \mathcal{M}^Z , \mathcal{M}^α , \mathcal{M}^β defined by

$$\mathcal{M}^\alpha(\xi) := \frac{d_1}{\lambda(0)} \exp\left(-\int_0^{\phi_\lambda(\xi)} \lambda'(\phi_\lambda^{-1}(\sigma))d\sigma\right) \mathcal{K}\Phi_\alpha(\phi_\lambda^{-1}(\phi_\lambda(1) - \phi_\lambda(\xi)), 0)^\top \bar{B} \quad (6.38a)$$

$$\mathcal{M}^\beta(\xi) := \frac{1}{\mu(0)} \exp\left(-\int_0^{\phi_\mu(\xi)} \mu'(\phi_\mu^{-1}(\sigma))d\sigma\right) \mathcal{K}\Phi_\beta(\phi_\mu^{-1}(\phi_\mu(1) - \phi_\mu(\xi)), 0)^\top \bar{B} \quad (6.38b)$$

$$\mathcal{M}^Z := \mathcal{K}\left(\Phi_\beta(1, 0)^\top - d_1 d_0 \Phi_\alpha(1, 0)^\top\right) \quad (6.38c)$$

stabilizes (6.2) exponentially to the origin.

Proof. By applying the backstepping transformation and computing the kernels explicitly, obtain that V given by

$$V(t) = \int_0^1 \mathcal{M}^\alpha(\xi)\alpha(\xi, t)d\xi + \int_0^1 \mathcal{M}^\beta(\xi)\beta(\xi, t)d\xi + \mathcal{M}^Z Z(t) \quad (6.39)$$

exponentially stabilizes (6.18) to the origin. Substituting in the transformation (6.19) and rearranging, we can rewrite V in plant coordinates as

$$V(t) = \int_0^1 N^u(\xi)u(\xi, t)d\xi + \int_0^1 N^v(\xi)v(\xi, t)d\xi + \int_0^1 N^w(\xi)w(\xi, t)d\xi + N^X X(t). \quad (6.40)$$

Substituting this into (6.25) we have the expression (6.35). By Lemma 7 and by the fact that (6.19) is invertible the Proof is complete. \square

Remark 9. *It should be noted that the problem of boundary stabilization of (6.18) is a well-known problem, with several controllers in the literature (some examples presented in [Auriol et al. 2018, Bekiaris-Liberis & Krstić 2014]). In principle one could apply any controller that stabilizes (6.18) and combine it with the transformation (6.19) to obtain a stabilizing controller for (6.2).*

In practice, implementing the control law requires full knowledge of the states (u, v, X) , which are often unknown in practice. In the next section we design an observer that produces exponentially convergent estimates of these states.

6.3 Observer Design

We design in this section an observer of the form

$$\dot{\hat{X}}(t) = A\hat{X}(t) + B_0\hat{v}(0, t) + B_1\hat{w}(1, t) + L[y(t) - \hat{u}(1, t)] \quad (6.41a)$$

$$\hat{u}_t(x, t) = -\lambda(x)\hat{u}_x(x, t) + \sigma^+(x)\hat{v}(x, t) + P^+(x)[y(t) - \hat{u}(1, t)] \quad (6.41b)$$

$$\hat{v}_t(x, t) = \mu(x)\hat{v}_x(x, t) + \sigma^-(x)\hat{u}(x, t) + P^-(x)[y(t) - \hat{u}(1, t)] \quad (6.41c)$$

$$\hat{w}_t(x, t) = -\frac{1}{\tau}\hat{w}_t(x, t) + P^w(x)[y(t) - \hat{u}(1, t)] \quad (6.41d)$$

$$\hat{u}(0, t) = d_0\hat{v}(0, t) + C\hat{X}(t) \quad (6.41e)$$

$$\hat{v}(1, t) = d_1y(t) + U(t) \quad (6.41f)$$

$$\hat{w}(0, t) = \hat{v}(0, t) \quad (6.41g)$$

using the measurement signal y as defined in (5.2), where L , P^+ , P^- , P^w are gains to be found such that $(\hat{u}, \hat{v}, \hat{w}, \hat{X})$ converge to their true values (u, v, w, X) in some sense.

With state estimation errors defined as $\tilde{u} := u - \hat{u}$, $\tilde{v} := v - \hat{v}$, $\tilde{w} := w - \hat{w}$ and $\tilde{X} := X - \hat{X}$, we find the state estimation error dynamics

$$\dot{\tilde{X}}(t) = A\tilde{X}(t) + B_0\tilde{v}(0, t) + B_1\tilde{w}(1, t) - L\tilde{u}(1, t) \quad (6.42a)$$

$$\tilde{u}_t(x, t) = -\lambda(x)\tilde{u}_x(x, t) + \sigma^+(x)\tilde{v}(x, t) - P^+(x)\tilde{u}(1, t) \quad (6.42b)$$

$$\tilde{v}_t(x, t) = \mu(x)\tilde{v}_x(x, t) + \sigma^-(x)\tilde{u}(x, t) - P^-(x)\tilde{u}(1, t) \quad (6.42c)$$

$$\tilde{w}_t(x, t) = -\frac{1}{\tau}\tilde{w}_x(x, t) - P^w(x)\tilde{u}(1, t) \quad (6.42d)$$

$$\tilde{u}(0, t) = d_0\tilde{v}(0, t) + C\tilde{X}(t) \quad (6.42e)$$

$$\tilde{v}(1, t) = 0 \quad (6.42f)$$

$$\tilde{w}(0, t) = \tilde{v}(0, t). \quad (6.42g)$$

6.3.1 Mapping into stable cascade

Consider the target error system

$$\dot{\tilde{Z}}(t) = (A - \Gamma C)\tilde{Z}(t) \quad (6.43a)$$

$$\tilde{\alpha}_t(x, t) = -\lambda(x)\tilde{\alpha}_x(x, t) \quad (6.43b)$$

$$\tilde{\beta}_t(x, t) = \mu(x)\tilde{\beta}_x(x, t) \quad (6.43c)$$

$$\tilde{\omega}_t(x, t) = -\frac{1}{\tau}\tilde{\omega}_x(x, t) \quad (6.43d)$$

$$\tilde{\alpha}(0, t) = d_0\tilde{\beta}(0, t) + C\tilde{Z}(t) + \int_0^1 F(\xi)\tilde{\omega}(\xi, t)d\xi \quad (6.43e)$$

$$\tilde{\omega}(0, t) = \tilde{\beta}(0, t) + \int_0^1 H(\xi)\tilde{\beta}(\xi, t)d\xi \quad (6.43f)$$

$$\tilde{\beta}(1, t) = 0 \quad (6.43g)$$

where Γ is picked so that $(A - \Gamma C)$ is Hurwitz, and F, H are to be defined further down. We assess the convergence properties of (6.43) in the following Lemma.

Lemma 9. *The states $(\tilde{\alpha}, \tilde{\beta}, \tilde{\omega}, \tilde{Z})$ of (6.43) converge exponentially fast to the origin.*

Proof. Due to (6.43c), (6.43g), we have that $\tilde{\beta} \equiv 0$ for time $t \geq \phi_\mu(1)$. Hence, after this (6.43f) is reduced to $\tilde{\omega}(0, \cdot) = 0$, which together with (6.43d) implies $\tilde{\omega} \equiv 0$ for time $t \geq \phi_\mu(1) + \tau$. Thereafter the target system is reduced to the autonomous ODE (6.43a) cascading into the transport PDE (6.43b), via the boundary condition (6.43e) which is reduced to $\tilde{\alpha}(0, \cdot) = C\tilde{Z}(\cdot)$. Because Γ is picked so that $A - \Gamma C$ is Hurwitz, $(\tilde{\alpha}, \tilde{Z})$ converge to the origin exponentially fast and the Proof is complete. \square

Consider next the change of coordinates

$$\tilde{X}(t) = \tilde{Z}(t) + \int_0^1 \eta_\alpha(\xi) \tilde{\alpha}(\xi, t) d\xi + \int_0^1 \eta_\beta(\xi) \tilde{\beta}(\xi, t) d\xi + \int_0^1 \eta_\omega(\xi) \tilde{\omega}(\xi, t) d\xi \quad (6.44a)$$

$$\tilde{w}(x, t) = \tilde{\omega}(x, t) + \int_0^1 S^\alpha(x, \xi) \tilde{\alpha}(\xi, t) d\xi \quad (6.44b)$$

$$\tilde{u}(x, t) = \tilde{\alpha}(x, t) + \int_x^1 M^{\alpha\alpha}(x, \xi) \tilde{\alpha}(\xi, t) d\xi + \int_x^1 M^{\alpha\beta}(x, \xi) \tilde{\beta}(\xi, t) d\xi \quad (6.44c)$$

$$\tilde{v}(x, t) = \tilde{\beta}(x, t) + \int_x^1 M^{\beta\alpha}(x, \xi) \tilde{\alpha}(\xi, t) d\xi + \int_x^1 M^{\beta\beta}(x, \xi) \tilde{\beta}(\xi, t) d\xi \quad (6.44d)$$

where η_ω satisfies for $\xi \in [0, 1]$

$$\eta'_\omega(\xi) = \tau(A - \Gamma C)\eta_\omega(\xi) \quad (6.45a)$$

$$\eta_\omega(1) = -\tau B_1, \quad (6.45b)$$

η_α satisfies for $\xi \in [0, 1]$

$$\eta'_\alpha(\xi) = \frac{1}{\lambda(\xi)} \left((A - \lambda'(\xi)I) \eta_\alpha(\xi) + B_0 M^{\beta\alpha}(0, \xi) + B_1 S^\alpha(1, \xi) \right) \quad (6.46a)$$

$$\eta_\alpha(0) = \frac{1}{\lambda(0)} \Gamma, \quad (6.46b)$$

η_β satisfies for $\xi \in [0, 1]$

$$\eta'_\beta(\xi) = -\frac{1}{\mu(\xi)} \left((A + \mu'(\xi)I) \eta_\beta(\xi) + (B_0 - \frac{1}{\tau} \eta_\omega(0)) M^{\beta\beta}(0, \xi) \right) \quad (6.47a)$$

$$\eta_\beta(0) = \frac{1}{\mu(0)} \left(\frac{1}{\tau} \eta_\omega(0) + \lambda(0) d_0 \eta_\alpha(0) - B_0 \right), \quad (6.47b)$$

S^α satisfies for $(x, \xi) \in \mathcal{S}$

$$\lambda(\xi) S'_\xi^\alpha(x, \xi) + \frac{1}{\tau} S'_x^\alpha(x, \xi) = -\lambda'(\xi) S^\alpha(x, \xi) \quad (6.48a)$$

$$S^\alpha(x, 0) = 0 \quad (6.48b)$$

$$S^\alpha(0, \xi) = M^{\beta\alpha}(0, \xi), \quad (6.48c)$$

and $M^{\alpha\alpha}, M^{\alpha\beta}, M^{\beta\alpha}, M^{\beta\beta}$ are for $(x, \xi) \in \mathcal{T}_u := \{(x, \xi) \mid 0 \leq x \leq \xi \leq 1\}$ given by

$$\lambda(\xi)M_\xi^{\alpha\alpha}(x, \xi) + \lambda(x)M_x^{\alpha\alpha}(x, \xi) = -\lambda'(\xi)M^{\alpha\alpha}(x, \xi) + \sigma^+(x)M^{\beta\alpha}(x, \xi) \quad (6.49a)$$

$$-\mu(\xi)M_\xi^{\alpha\beta}(x, \xi) + \lambda(x)M_x^{\alpha\beta}(x, \xi) = \mu'(\xi)M^{\alpha\beta}(x, \xi) + \sigma^+(x)M^{\beta\beta}(x, \xi) \quad (6.49b)$$

$$\lambda(\xi)M_\xi^{\beta\alpha}(x, \xi) - \mu(x)M_x^{\beta\alpha}(x, \xi) = -\lambda'(\xi)M^{\beta\alpha}(x, \xi) + \sigma^-(x)M^{\alpha\alpha}(x, \xi) \quad (6.49c)$$

$$-\mu(\xi)M_\xi^{\beta\beta}(x, \xi) - \mu(x)M_x^{\beta\beta}(x, \xi) = \mu'(\xi)M^{\beta\beta}(x, \xi) + \sigma^-(x)M^{\alpha\beta}(x, \xi) \quad (6.49d)$$

$$M^{\alpha\alpha}(0, \xi) = d_0M^{\beta\alpha}(0, \xi) + C\eta_\alpha(\xi) \quad (6.49e)$$

$$M^{\alpha\beta}(x, x) = -\frac{\sigma^+(x)}{\lambda(x) + \mu(x)} \quad (6.49f)$$

$$M^{\beta\alpha}(x, x) = \frac{\sigma^-(x)}{\lambda(x) + \mu(x)} \quad (6.49g)$$

$$M^{\beta\beta}(0, \xi) = \frac{1}{d_0}(M^{\alpha\beta}(0, \xi) - C\eta_\beta(\xi)). \quad (6.49h)$$

The terms F, H appearing in (6.43e)–(6.43f) are defined as

$$F(\xi) := C\eta_\omega(\xi), \quad H(\xi) := M^{\beta\beta}(0, \xi). \quad (6.50)$$

We have the following Lemma.

Lemma 10. *The change of coordinates (6.44) maps (6.43) into (6.42), provided that*

$$P^+(x) = \lambda(1)M^{\alpha\alpha}(x, 1), \quad (6.51a)$$

$$P^-(x) = \lambda(1)M^{\beta\alpha}(x, 1), \quad (6.51b)$$

$$P^w(x) = \lambda(1)S^\alpha(x, 1), \quad (6.51c)$$

$$L = \lambda(1)\eta_\alpha(1). \quad (6.51d)$$

6.3.2 Analysis of kernels

As was done for the controller kernels in Section 6.2.2, we show here that under Assumption 17 and sufficiently smooth model parameters in (6.2), the kernel equations (6.45)–(6.49) have a well-posed solution.

Firstly, (6.45) is solved explicitly as

$$\eta_\omega(\xi) = -\tau \exp(\tau(A - \Gamma C)(\xi - 1))B_1. \quad (6.52)$$

Also, as a function of $M^{\beta\alpha}$, the solution to S^α is written as

$$S^\alpha(x, \xi) = \begin{cases} \exp(-\int_0^{\tau x} \lambda'(\sigma + \phi_\lambda(\xi) - \tau x)d\sigma)M^{\beta\alpha}(0, \xi - \lambda\tau x), & \text{if } \xi \geq \phi_\lambda^{-1}(\tau x) \\ 0, & \text{if } \xi < \phi_\lambda^{-1}(\tau x). \end{cases} \quad (6.53)$$

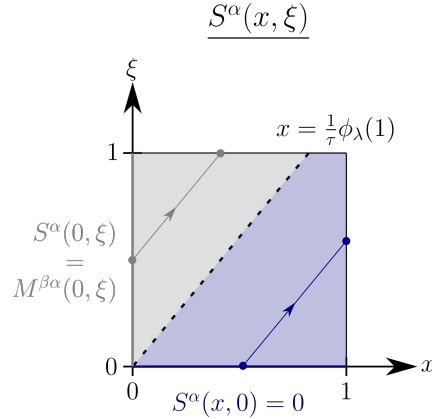


Figure 6.3: Sketch of solution to S^α . The region shaded in grey has characteristics originating along the line $x = 0$, while the region shaded in blue has characteristics from $\xi = 0$. The line of discontinuity, represented by the dashed line, intersects $\xi = 1$ at the point $x = \frac{1}{\tau}\phi_\lambda(1)$.

The solution to S^α is illustrated in Figure 6.3. Evaluating (6.53) at $x = 1$ and substituting into (6.46a), we have

$$\eta'_\alpha(\xi) = \frac{1}{\lambda(\xi)} (A - \lambda'(\xi)I) \eta_\alpha(\xi) + \frac{1}{\lambda(\xi)} B_0 M^{\beta\alpha}(0, \xi). \quad (6.54)$$

Then (6.54) together with (6.46b), (6.49a), (6.49c), (6.49e), (6.49g) constitutes an independent system of equations to solve for $(M^{\alpha\alpha}, M^{\beta\alpha}, \eta_\alpha)$.

Likewise, evaluating (6.52) at $\xi = 0$ and substituting this together with (6.46b), (6.49h) into (6.47) we have

$$\eta'_\beta(\xi) = \left(-\frac{1}{\mu(\xi)} (A + \mu'(\xi)I) + \frac{1}{\mu(\xi)} \underline{BC} \right) \eta_\beta(\xi) - \frac{1}{d_0 \mu(\xi)} \underline{B} M^{\alpha\beta}(0, \xi) \quad (6.55a)$$

$$\eta_\beta(0) = \frac{d_0}{\mu(0)} \Gamma - \frac{1}{\mu(0)} \underline{B} \quad (6.55b)$$

with

$$\underline{B} := B_0 + \exp(-\tau(A - \Gamma C)B_1). \quad (6.56)$$

This gives us that (6.55) together with (6.49b), (6.49d), (6.49f), (6.49h) is a coupled system of equations for $(M^{\beta\beta}, M^{\alpha\beta}, \eta_\beta)$.

Swapping $x \rightarrow \xi$, $\xi \rightarrow x$ in the systems of equations (6.46b), (6.49a), (6.49c), (6.49e), (6.49g), (6.54) for $(M^{\alpha\alpha}, M^{\beta\alpha}, \eta_\alpha)$ and (6.49b), (6.49d), (6.49f), (6.49h), (6.55) for $(M^{\beta\beta}, M^{\alpha\beta}, \eta_\beta)$, we mirror the equations over the line $x = \xi$ such that they are defined over $(\mathcal{T}_l)^2 \times [0, 1]$ rather than $(\mathcal{T}_u)^2 \times [0, 1]$. Lemma 8 is then applied to establish that $M^{\alpha\alpha}, M^{\alpha\beta}, M^{\beta\alpha}, M^{\beta\beta} \in L^\infty(\mathcal{T}_u)$ and $\eta_\alpha, \eta_\beta \in (L^\infty[0, 1])^n$.

6.3.3 Observer

We present now the main result of this section.

Theorem 5. *The observer (6.41) with gains (6.51) produces state estimates $(\hat{u}, \hat{v}, \hat{w}, \hat{X})$ that converge exponentially to the states (u, v, w, X) of the plant (6.2), (6.16).*

Proof. Because the change of coordinates (6.44) is invertible, by combining Lemmas 9–10, we see the observer error system (6.42) with gains (6.51) converges to the origin exponentially. Due to the definition of the error state, we write $\hat{u} = u - \tilde{u}$, $\hat{v} = v - \tilde{v}$, $\hat{w} = w - \tilde{w}$, $\hat{X} = X - \tilde{X}$, and indeed because $(\tilde{u}, \tilde{v}, \tilde{w}, \tilde{X}) \rightarrow 0$ exponentially, we have $(\hat{u}, \hat{v}, \hat{w}, \hat{X}) \rightarrow (u, v, w, X)$ exponentially. \square

Combining then Lemma 6 and Theorem 5, we see estimates for the pressure, velocity and heat release rate perturbations $(\hat{P}, \hat{V}, \hat{Q})$ in the thermoacoustic system (2.45) are computed based on $\hat{u}, \hat{v}, \hat{X}$ as

$$\begin{aligned} \hat{P}(z, t) := & \frac{1}{2} \left(\hat{u} \left(\frac{z}{L}, t \right) \exp \left(L \int_0^{\frac{z}{L}} \frac{\bar{\sigma}^{++}(\xi)}{c(\xi L)} d\xi \right) \right. \\ & \left. + \hat{v} \left(\frac{z}{L}, t \right) \exp \left(-L \int_0^{\frac{z}{L}} \frac{\bar{\sigma}^{--}(\xi)}{c(\xi L)} d\xi \right) \right) \end{aligned} \quad (6.57a)$$

$$\begin{aligned} \hat{V}(z, t) := & \frac{1}{2k(z)} \left(\hat{u} \left(\frac{z}{L}, t \right) \exp \left(L \int_0^{\frac{z}{L}} \frac{\bar{\sigma}^{++}(\xi)}{c(\xi L)} d\xi \right) \right. \\ & \left. - \hat{v} \left(\frac{z}{L}, t \right) \exp \left(-L \int_0^{\frac{z}{L}} \frac{\bar{\sigma}^{--}(\xi)}{c(\xi L)} d\xi \right) \right) \end{aligned} \quad (6.57b)$$

$$\hat{Q}(t) := \frac{\bar{Q}}{\bar{V}(0)} \bar{C} \hat{X}(t). \quad (6.57c)$$

6.4 Output Feedback Controller

We combine here the results from Section 6.2–6.3 to propose an output feedback controller to stabilize (6.2), whenever the output signal (5.2) is known. This is then applied to make an acoustic boundary output feedback controller for the thermoacoustic model (2.45).

Corollary 1. *Assume the output signal y as defined in (5.2) is available. Then the control law*

$$U(t) = \Pi^\top \hat{X}(t) + \int_0^1 \pi_u(\xi) \hat{u}(\xi, t) d\xi + \int_0^1 \pi_v(\xi) \hat{v}(\xi, t) d\xi + \int_0^1 \pi_w(\xi) \hat{w}(\xi, t) d\xi, \quad (6.58)$$

with Π, π_u, π_v, π_w given in (6.36)–(6.38) and $\hat{X}, \hat{u}, \hat{v}, \hat{w}$ are produced by (6.41) stabilizes (6.2) exponentially to the origin.

The proof of Corollary 1 is omitted for sake of brevity. Intuitively, the convergence of the output feedback controller can be seen by rewriting the closed loop system as a cascade of the observer system into the observer dynamics.

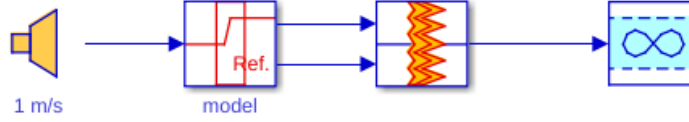


Figure 6.4: Flame identification experiment block diagram.

To apply the control law (6.58) to stabilize (2.45), assume pressure measurement Y given in (5.51) is available. Then, applying (6.2e), (6.1) and (6.6) we find y can be expressed as

$$y(t) = \frac{2\check{P}(L, t) - \frac{2k(L)}{k(L)+Z}W(t)}{\exp(L \int_0^1 \frac{\bar{\sigma}^{++}(\xi)}{c(\xi L)} d\xi) + d_1 \exp(-L \int_0^1 \frac{\bar{\sigma}^{--}(\xi)}{c(\xi L)} d\xi)}. \quad (6.59)$$

Hence, by Corollary 1 a stabilizing feedback U is calculated from (6.41), (6.58), where coefficients are assigned according to Lemma 6. The acoustic forcing signal W to apply to stabilize (2.45) is then computed from (6.6).

6.5 Simulations

We demonstrate the theory in Sections 6.2–6.4 on an example of the thermoacoustic system (2.45). Next, in Section 6.5.1 the model parameters are presented, before in Section 6.5.2 the output feedback controller from Corollary 1 is verified to stabilize the plant (6.2) in a MATLAB simulation.

6.5.1 Simulation parameters

Firstly, to obtain the flame model, a `taX` model (see [Emmert *et al.* 2014] for more details on `taX`) of the considered flame being excited by an acoustic source was set up. The `Simulink` block diagram of this setup is shown in Figure 6.4. Applying the `MATLAB` system identification toolbox, a transfer function for the flame was fitted to the transfer function produced by `taX`. The fit is shown in Figure 6.5, and is given by the transfer function

$$F(s) = \frac{0.03412}{2.251 \times 10^{-6}s^2 + 0.0008245s + 1} e^{-0.002s}.$$

Calculating a state space realization in controller canonical form of this transfer function gives the matrices

$$A = \begin{bmatrix} -366.3014 & -4.4427 \times 10^5 \\ 1 & 0 \end{bmatrix},$$

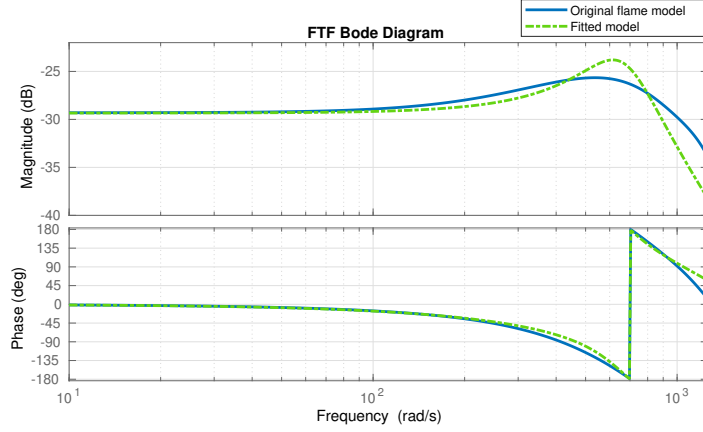


Figure 6.5: Bode plot of flame versus fitted transfer function model.

$$\begin{aligned} \bar{B}_0 &= \begin{bmatrix} 0 \\ 0 \end{bmatrix}, & \bar{B}_1 &= \begin{bmatrix} 1 \\ 0 \end{bmatrix}, \\ \bar{C} &= [0 \quad 1.5159 \times 10^4]. \end{aligned}$$

for a model of the form (2.16), and the input time delay $\tau = 0.002$ s. Since the parameters in the resultant model matrices vary largely in terms of order of magnitude, it is in practice beneficial to scale the matrices to have more well-conditioned numerical behaviour. We define the matrix $P := \text{Diag}\{1/\beta, \beta\}$ where β is a tuning constant, and consider a second tuning constant δ . We define then new matrices

$$A' := PAP^{-1}, \quad B'_1 := \frac{1}{\delta}PB_1, \quad C' := \delta CP^{-1} \quad (6.60)$$

where B_1 and C are calculated from \bar{B}_1 and \bar{C} according to (6.8)–(6.9). From trial and error values of $\beta = 25$ and $\delta = \frac{10^{-4}}{k(0)}$ are found, resulting in the matrices

$$A' = \begin{bmatrix} -366.3014 & -710.8327 \\ 625 & 0 \end{bmatrix}, \quad B'_1 = \begin{bmatrix} -200 \\ 0 \end{bmatrix}, \quad C' = [0 \quad 316.6565]$$

The new matrices A' , B'_1 and C' are then used in the simulation in place of A , B_1 and C . Note that when scaling with δ , one must multiply the right-hand side of (6.57a)–(6.57b) by $\frac{1}{\delta}$ to compensate for the scaling when recovering the pressure and velocity from the characteristic coordinates.

Consider next a duct of length $L = 2.5$ m with cross-sectional area expressed as a function of z as

$$a(z) = 1 + 0.2 \tanh(-20z + 12.5) + 0.2 \tanh(20z - 37.5) \quad [m^2]. \quad (6.61)$$

is considered. The cross-sectional area is plotted in Figure 6.6. The area jump upstream of the flame at the combustor inlet has an area ratio of $\alpha = 0.12$, and a specific resistive impedance of $Z = 1.011 \times 10^5 \left[\frac{Pa \cdot s}{m} \right]$ is used for the outlet boundary at the downstream end of the combustor.

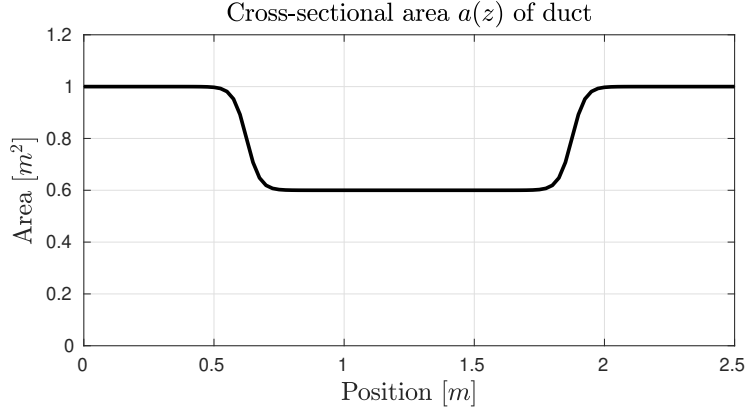


Figure 6.6: Cross-sectional area of duct.

Directly downstream of the flame, the mean density $\bar{\rho}_0$, velocity \bar{V}_0 and pressure \bar{P}_0 are set to be

$$\bar{\rho}_0 = 1.2 \left[\frac{kg}{m^3} \right], \quad \bar{V}_0 = 75 \left[\frac{m}{s} \right], \quad \bar{P}_0 = 4 \times 10^6 [Pa].$$

Using $\gamma = 1.4$, the IVP (2.23) is solved with the aforementioned values as initial conditions, yielding the flow steady state solution plotted in Figure 6.7.

The resultant transport speeds λ, μ computed from (6.3), (6.11)–(6.12) are approximately constant, with the maximum value approximately 0.016% higher than the minimum value. For simplicity, they are assumed constant and their mean values are used in the simulation, so that $\lambda(x) \equiv \lambda$, $\mu(x) \equiv \mu$. It can be verified that $\lambda\tau = \mu\tau \approx 1.73 > 1$ and hence satisfies Assumption 17. For the coupling of the heat release into the flow, the temperature ratio $\frac{T_h}{T_c} \approx \frac{c_h^2}{c_c^2}$, where c_h, c_c is the speed of sound directly down- and upstream of the flame. A speed of sound $c_c = 341 \left[\frac{m}{s} \right]$ upstream of the flame is used.

To compute the controller and observer gains, the poles of the target ODE matrices $p_c := \text{eig}(A + \bar{B}K)$, $p_o := \text{eig}(A - \Gamma C)$ are set as

$$p_c = \begin{bmatrix} -1 \times 10^5 \\ -2 \times 10^5 \end{bmatrix}, \quad p_o = \begin{bmatrix} -1 - 2j \\ -1 + 2j \end{bmatrix}.$$

The kernels are approximated with UGD by discretizing the spatial domain into a uniform grid with discretization step of $\Delta x = \Delta \xi = 10^{-2}$. The resultant distributed controller and observer gains are respectively plotted in Figures 6.8–6.9, and the ODE gains are given by

$$\Pi = \begin{bmatrix} -3.21 \times 10^6 \\ 7.43 \times 10^5 \end{bmatrix}, \quad L = \begin{bmatrix} 9.00 \times 10^{-3} \\ -1.71 \end{bmatrix}.$$

6.5.2 Simulation results

To simulate the plant (6.2) with parameters defined via Lemma 6 using coefficients as stated in Section 6.5.1, the normalized spatial domain $[0, 1] \ni x$ is discretized with

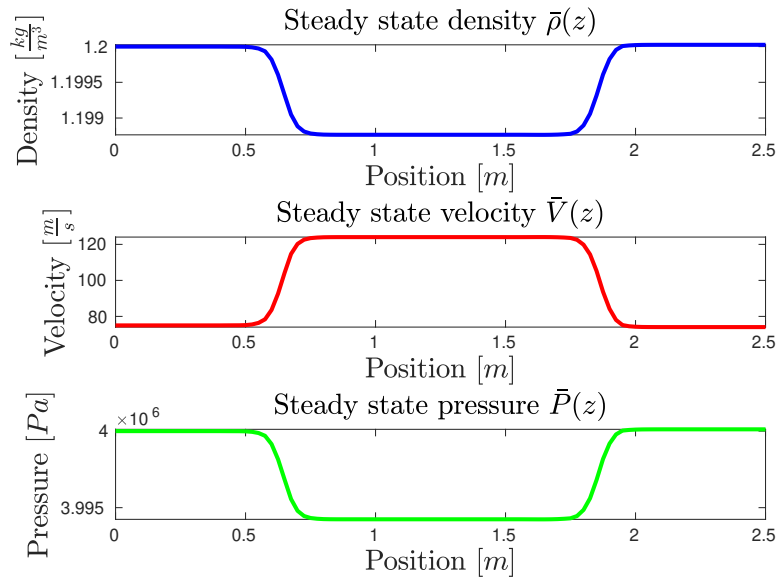


Figure 6.7: Steady-state density, velocity and pressure along duct.

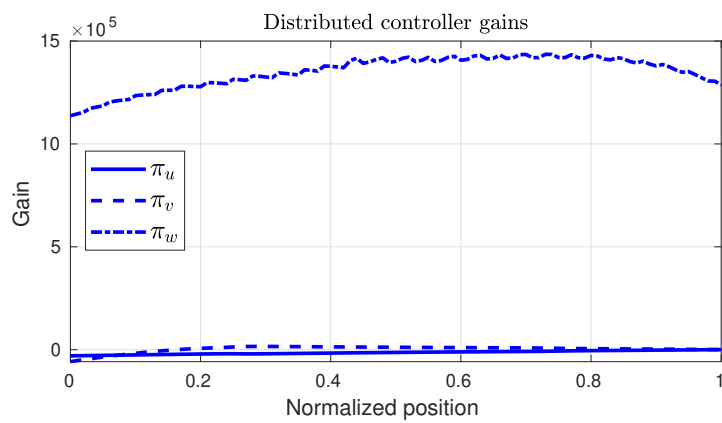


Figure 6.8: Distributed controller gains.

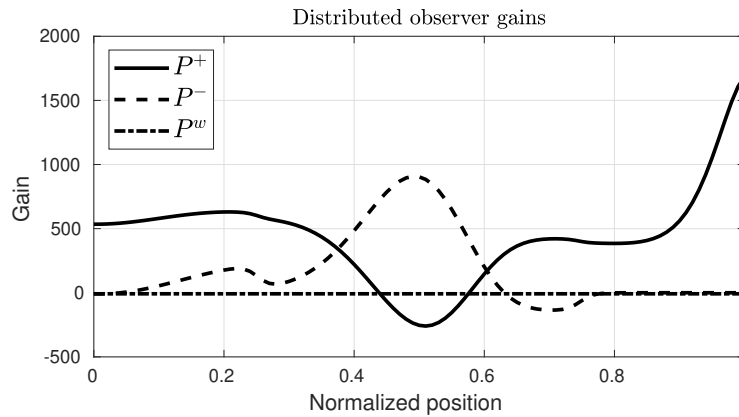


Figure 6.9: Distributed observer gains.

a uniform discretization step $\Delta x = 10^{-2}$. A Differential-Algebraic Equation (DAE) is then obtained which is solved using the `ode23t` solver in MATLAB. The initial conditions used are

$$u_0(x) \equiv 0, \quad v_0(x) \equiv 0, \quad w_0(x) \equiv 0, \quad X_0 = \begin{bmatrix} 0 \\ 1.25 \times 10^{-7} \end{bmatrix}$$

and results in an open-loop response of the plant as plotted in Figures 6.10–6.12. As can be seen, after 0.25 s the amplitude of the pressure fluctuations are almost 5000 Pa, which corresponds to a Sound Pressure Level (SPL) of around 170 dB.

Firstly, the full-state feedback controller from Theorem 4 is implemented. The closed-loop response of this controller is plotted in Figures 6.13–6.15. In Figure 6.16 the control signal U is plotted. Next, the observer from Theorem 5 is implemented to estimate the open-loop states plotted in Figures 6.10–6.12. The estimation errors are plotted in Figure 6.17–6.19. Lastly, the output-feedback controller from Corollary 1 is implemented to stabilize the unstable plant only using knowledge of the pressure estimate at the downstream boundary of the combustor. The closed-loop response of this controller is shown in Figure 6.20–6.22, and the corresponding boundary control signal U is plotted in Figure 6.23.

As the simulations demonstrate, the output-feedback controller is successful in stabilizing the thermoacoustic instability present in the open-loop plant. Comparing the output feedback control signal in Figure 6.23 to the full-state feedback control signal in Figure 6.16, we see the observer dynamics in the loop causes the signal to be more “uneven” and with higher amplitude.

6.6 Discussion

In this chapter an output-feedback controller for stabilizing a model of thermoacoustic instabilities in a duct with spatially varying geometry coupled to a linear flame model with a simultaneous instantaneous and time-delayed velocity input has been proposed. It senses and actuates the acoustics at the boundary opposite from

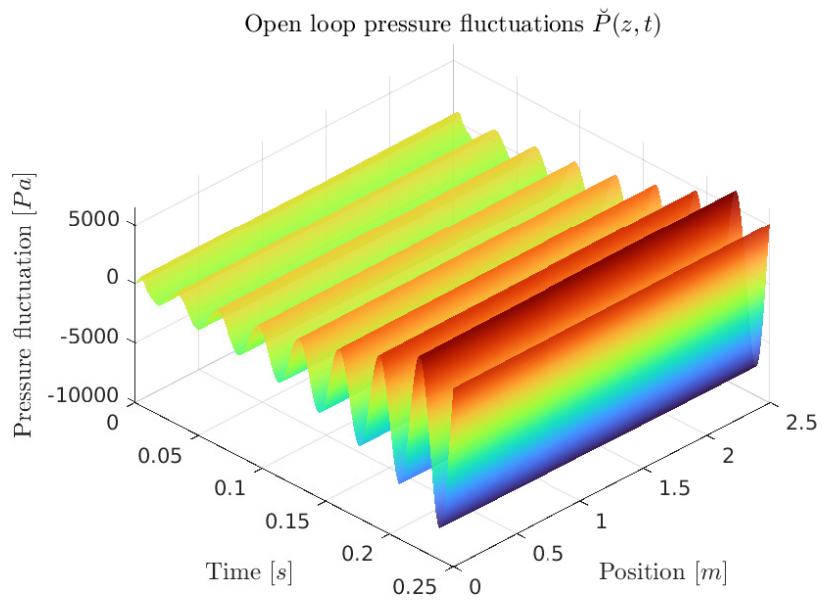


Figure 6.10: Open-loop pressure fluctuations.

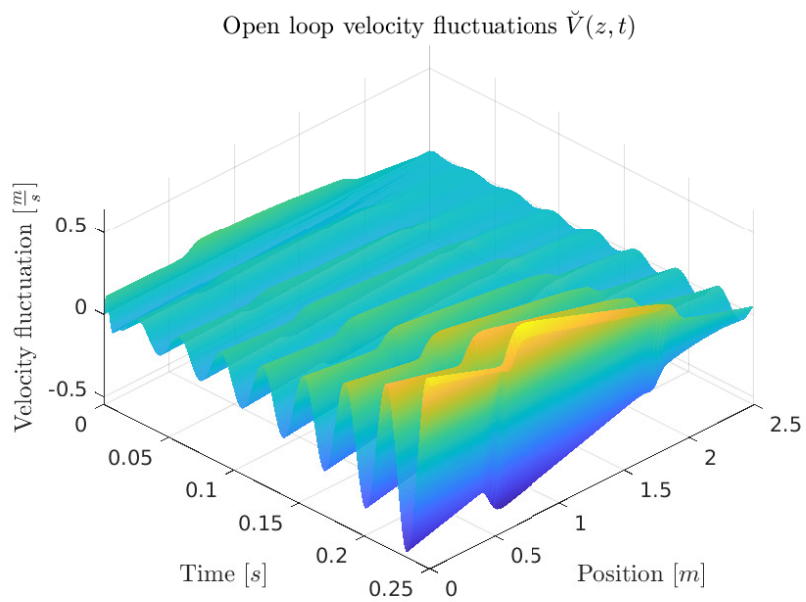


Figure 6.11: Open-loop velocity fluctuations.

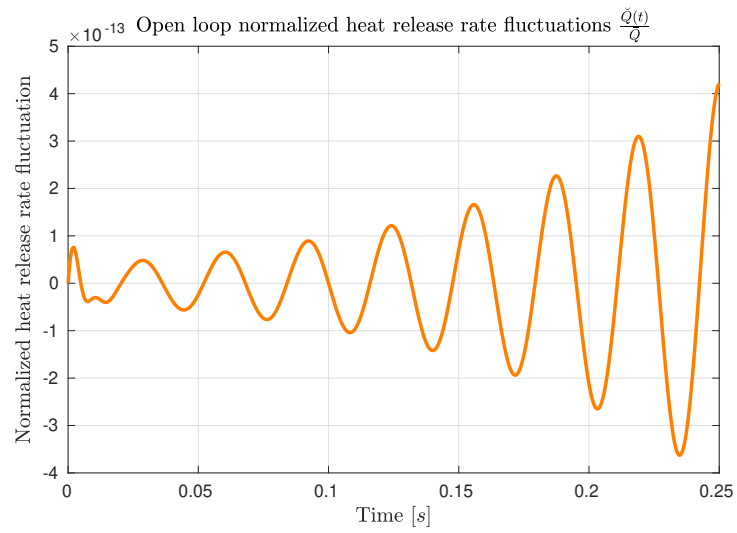


Figure 6.12: Open-loop heat release rate fluctuations.

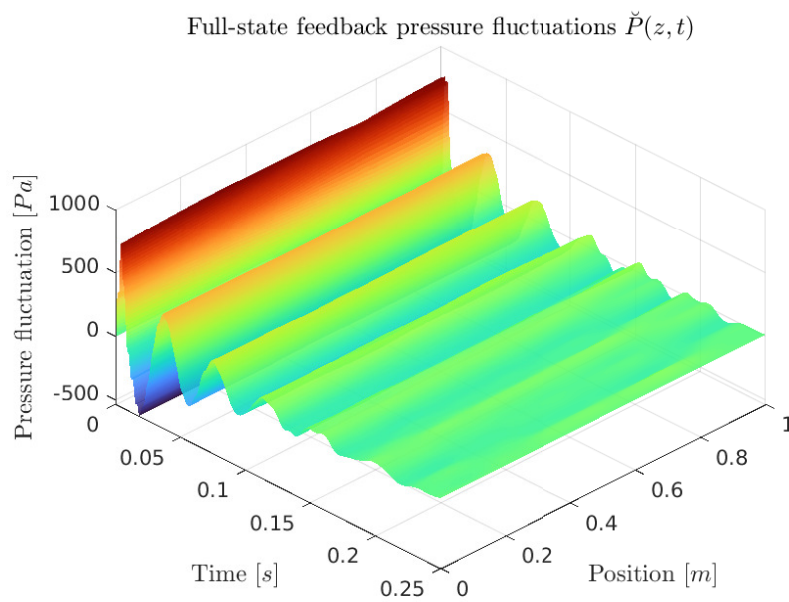


Figure 6.13: Full-state feedback control pressure fluctuations.

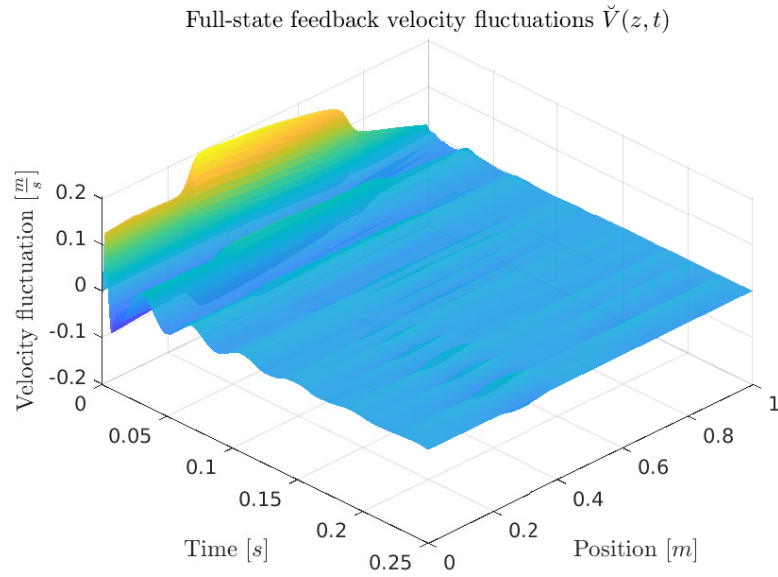


Figure 6.14: Full-state feedback control velocity fluctuations.

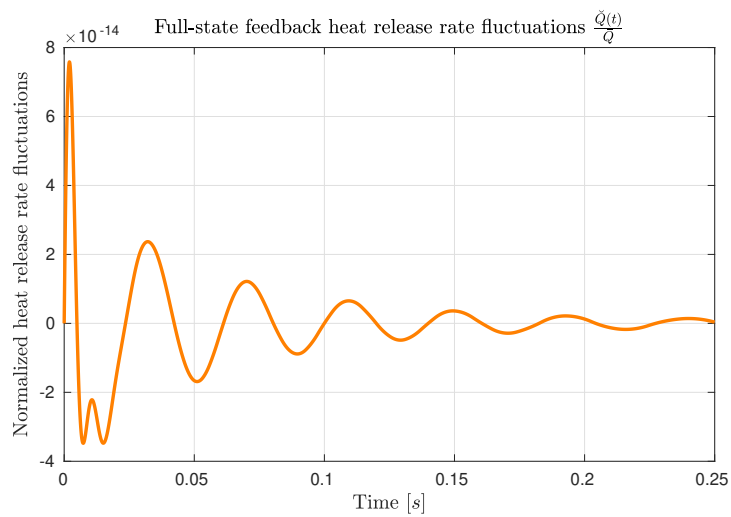


Figure 6.15: Full-state feedback control heat release rate fluctuations.

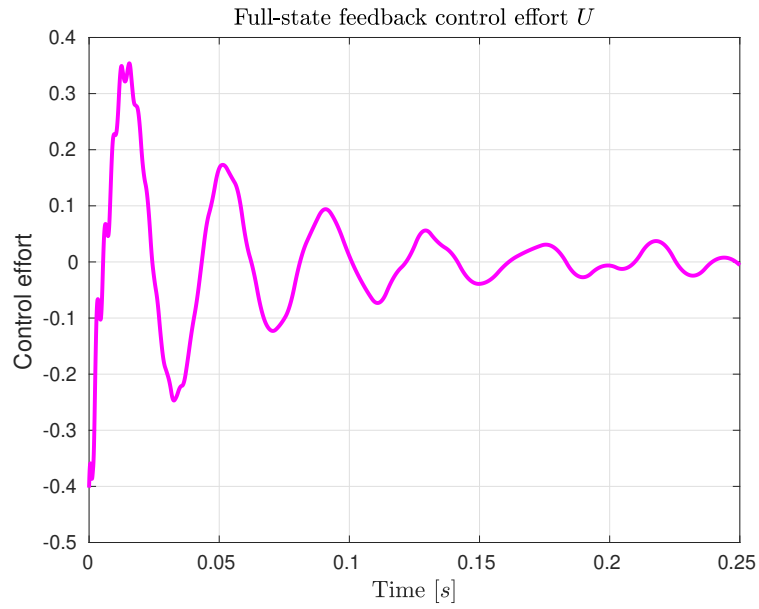


Figure 6.16: Full-state feedback control signal.

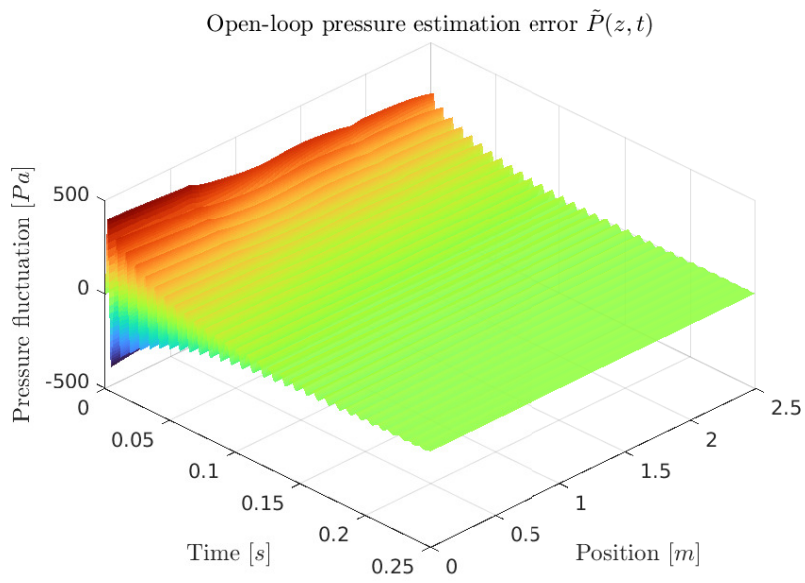


Figure 6.17: Estimation error of open-loop pressure.

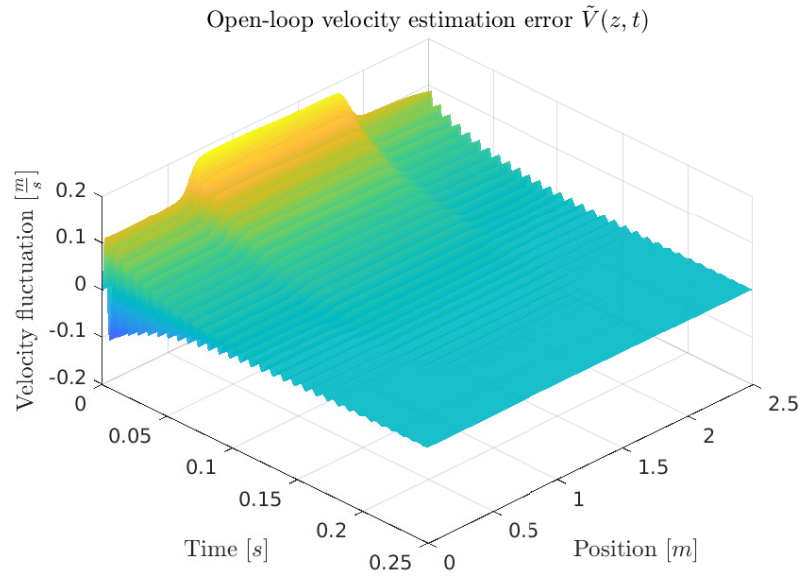


Figure 6.18: Observer estimation error of open-loop velocity.

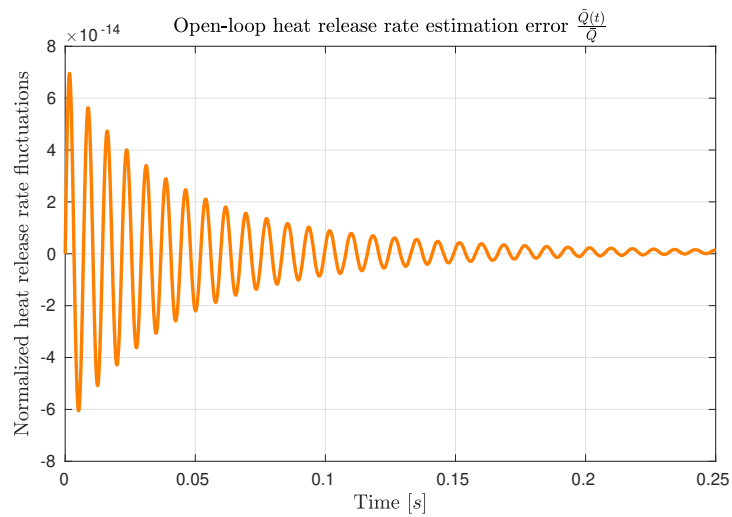


Figure 6.19: Estimation error of open-loop heat release rate.

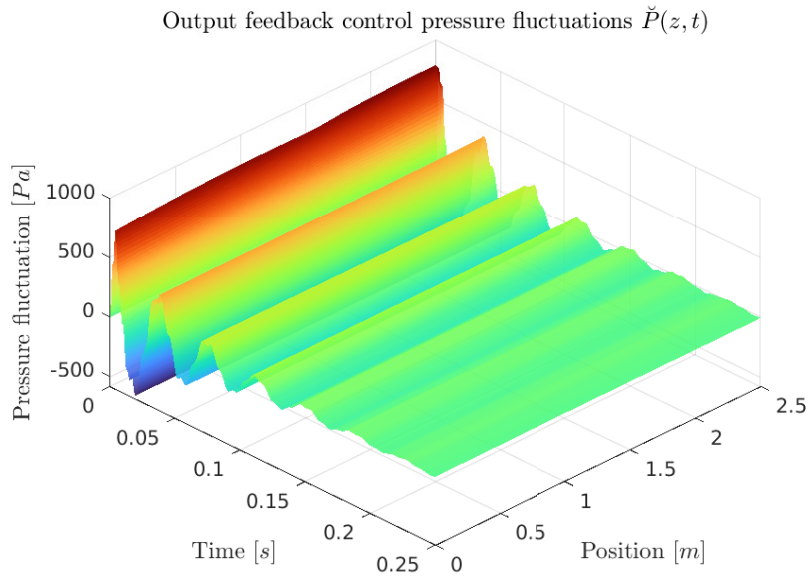


Figure 6.20: Output feedback stabilized pressure fluctuations.

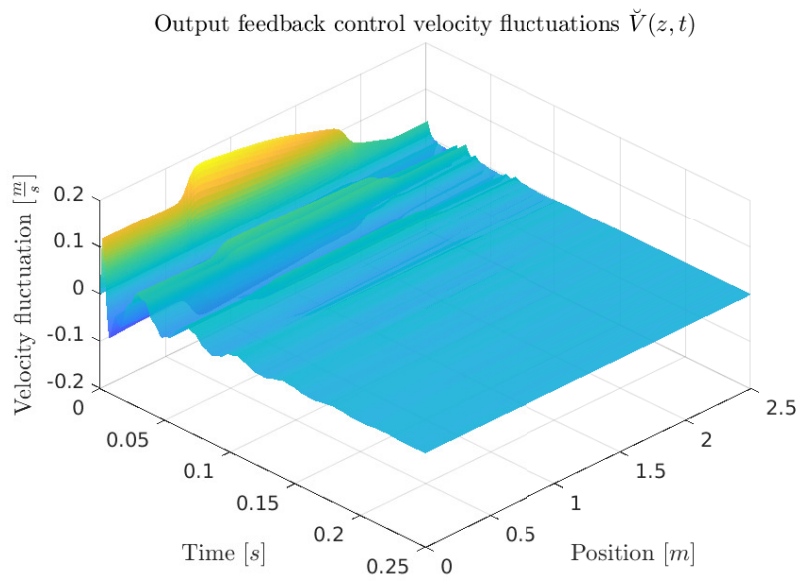


Figure 6.21: Output feedback stabilized velocity fluctuations.

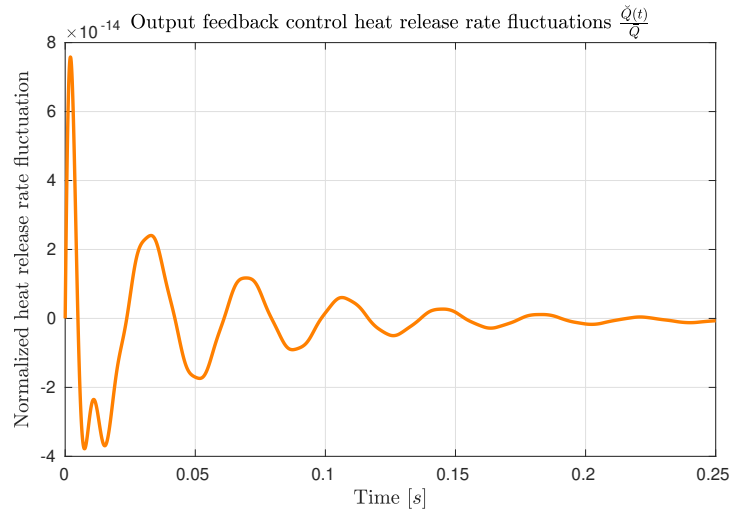


Figure 6.22: Output feedback stabilized heat release rate fluctuations.

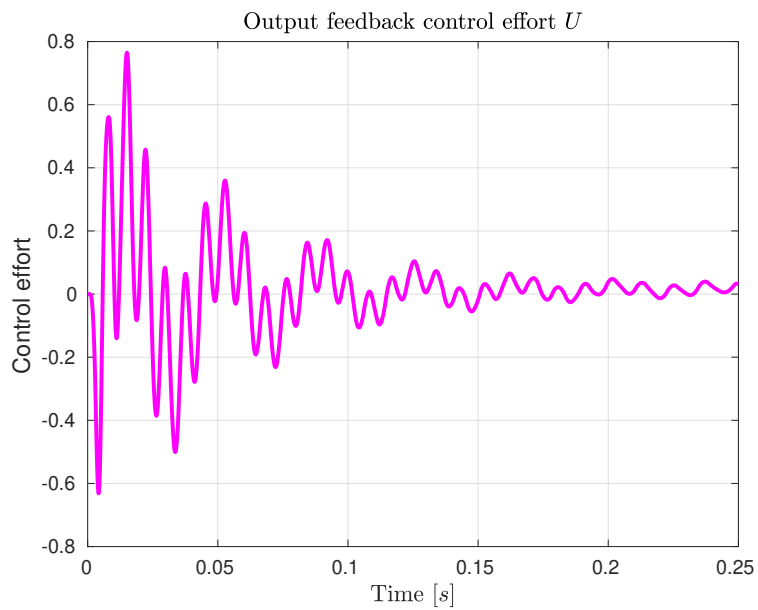


Figure 6.23: Output feedback control signal.

the location of the flame. The output feedback controller is composed of two parts, an exponentially converging full-state feedback control law connected in-the-loop to an observer providing exponentially converging internal state estimates. To design the control law, the plant is first mapped to a simplified cascade system, for which a control law is known and can be explicitly found. Subsequently the full-state feedback control law is recovered.

On the other hand, the observer is designed by mapping the estimation error dynamics directly into an exponentially convergent target cascade system. Both the controller and observer kernels are analysed and found to have a well-posed solution given certain assumptions are satisfied. Results from a simulation testing first the full-state feedback control law and observer independently, and finally the combined output feedback control law, is presented and shown to successfully stabilize and estimate the pressure, velocity and heat release fluctuations, which are unstable in the open-loop plant.

From a theoretical perspective, investigating if and how the second part of Assumption 17 can be removed would be valuable. Also, design of observers and controllers for plants with more complicated dynamics in place of the “ w -subsystem” (6.16) is a direction this research can be continued. Controller and observer designs for plants with nonlinear extensions of (6.2a), such as an input-affine ODE as natural first step, would be valuable both for theoretical understanding and practical application. Next in Chapter 7 the observer problem for such a nonlinear generalization is considered, but using a considerably different approach to that taken here.

In practice, if the necessary control effort to stabilize the thermoacoustic instability gets too large, the loudspeaker could saturate due to physical limitations. Hence, further work should focus on modifying the controller presented here to stabilize the instabilities in face of actuator saturations. Future work should hence also focus on modelling and design of a controller that stabilizes the plant by actuation the ODE subsystem directly, and combining this with the observer in an anti-collocated setup. A fuel modulation controller could also be used together with the acoustic actuating controller proposed here, and studying ways of combining these would also be a useful research direction.

Nonlinear Flame

Contents

7.1	Background	150
7.1.1	Problem statement	150
7.1.2	Observer for nonlinear ODE coupled to hyperbolic PDE system	151
7.1.3	KKL observers	153
7.2	Numerical design of observer for Kornilov's flame	155
7.2.1	Methodology	155
7.2.2	Generation of training data	159
7.2.3	Training of neural networks	162
7.2.4	Resultant transformation	166
7.3	Simulation and verification	167
7.3.1	Direct observer tests	167
7.3.2	Verification on Kornilov's flame data	170
7.4	Discussion	173

Dans ce chapitre, nous nous intéressons au problème d'estimation des états du modèle de chambre de combustion (2.45) décrivant les instabilités thermoacoustiques longitudinales. Contrairement au chapitre 6 le modèle de flamme considéré ici a une réponse dynamique non linéaire. Deux résultats utiles de la littérature sont rappelés. Le premier résultat réduit le problème de la conception d'un observateur pour l'interconnection EDP-EDO au problème de la conception d'un observateur pour le sous-système non linéaire EDO uniquement. Le deuxième résultat réduit le problème de la conception d'un observateur pour les EDO non linéaires en un problème d'approximation d'une fonction statique et de son inverse à gauche. Une procédure pour générer des données numériques représentant des points dans le domaine de définition de la fonction et de son inverse à gauche est proposée, avant d'être appliquée pour générer numériquement des données basées sur le modèle de flamme non linéaire. Avec ces données, des réseaux de neurones représentant les transformations directe et inverse sont entraînés. Les transformations estimées sont d'abord testées dans une implémentation d'observateur estimant les états internes du modèle de flamme non linéaire EDO, puis dans l'estimation du taux de dégagement de chaleur à partir des données originales entrée/sortie sur lesquelles le modèle de flamme est basé.

The observation problem of estimating the states of the can combustor model (2.45) describing longitudinal thermoacoustic instabilities is considered, but unlike Chapter 6 the flame model considered here has a nonlinear dynamic response. Two useful results from the literature are recalled. The first result reduces the problem of designing an observer for the fully coupled PDE–ODE plant to the problem of designing an observer for the nonlinear ODE subsystem only. The second result reduces the problem of observer design for the nonlinear ODE into a problem of approximating a static function and its left-inverse. A procedure to generate numerical data representing points in the domain and co-domain of the function and its left-inverse is proposed, before being applied to numerically generate data based on the nonlinear flame model. With this data, neural networks representing the forward and left-inverse transformations necessary to implement the nonlinear observer are trained. The estimated transformations are tested first in an observer implementation estimating the internal states of the nonlinear ODE flame model, and thereafter in estimation of the heat release rate from the original I/O data on which the flame model is based.

7.1 Background

7.1.1 Problem statement

We consider in this chapter the same setup as that shown in Figure 6.1, which can be modelled by (2.45). However, differently from Chapter 6, we do here not linearise dynamics of the flame subsystem (2.45a)–(2.45b). Assuming the boundary pressure signal (5.51) is available for measurement, the aim of this chapter is to design an observer to estimate the duct acoustics together with heat release (and internal states of the flame model) from knowledge of this output signal. The control problem is not studied in this chapter, so the loudspeaker signal W in (2.45e) at $z = L$ can be considered an arbitrary and optional input to the system.

Lemma 6 from Chapter 6 can easily be modified to write (2.45) without any restrictions on (2.45a)–(2.45b) in the form (6.2), but with

$$\dot{X}(t) = f(X(t)) + g_0(X(t))v(0, t) + g_1(X(t))v(0, t - \tau) \quad (7.1a)$$

$$u(0, t) = d_0v(0, t) + h(X(t)) \quad (7.1b)$$

in place of (6.2a), (6.2d). Hence, we consider the problem of designing a state observer for the coupled PDE–ODE system (6.2b)–(6.2c), (6.2e), (7.1) using knowledge of the output signal (5.2), only.

Due to the nonlinearity of the flame model, performing a similar analysis to that presented in Chapter 6 is highly nontrivial. Instead, we take a significantly different approach. First, in Section 7.1.2 a generic observer design for a 2×2 linear hyperbolic PDE system coupled to a nonlinear ODE, from [Irscheid *et al.* 2021], is presented. This observer design allows an observer for the coupled PDE–ODE system to be designed, given that one has an observer for the ODE subsystem. Hence, instead

of designing an observer directly for the complete plant (6.2b)–(6.2c), (6.2e), (7.1), we design it for the ODE subsystem (7.1a). This reduces the problem of observer design for the complete PDE–ODE plant to that of observer design for just the ODE subsystem.

The observer for the nonlinear ODE subsystem is designed as a Kazantzis-Kravaris-Luenberger (KKL) observer, the literature and theory of which is reviewed in Section (7.1.3). To implement the KKL observer in practice, one needs to compute a nonlinear injective mapping between the plant state space and observer state space. Although the conditions for the existence of such a transformation are relatively weak, there is no general methodology for calculating the transformation in practice. Similar to the work done in [da Costa Ramos *et al.* 2020], we train neural networks to approximate the transformation.

Since the resultant observer design problem considered here is of a highly numerical nature, in contrast to the analytical approach taken for the linear design in Chapter 6, a specific nonlinear ODE flame model must be applied during the design stage. For this, a nonlinear input-affine Reduced Order Model (ROM) of Kornilov’s flame [Kornilov *et al.* 2009], a premixed laminar conical flame, is considered. This ROM is described in [da Costa Ramos 2021] and is constructed using the Dynamic ROM tool in the Twin Builder software [twi] by Ansys Inc., based on CFD data of the flame as considered in [Jaensch *et al.* 2017]. Exact expressions of the flame model are the property of Ansys Inc. and can hence not be reproduced here, but for the reader it is sufficient to know they are an input-affine nonlinear model of the form (2.17), with internal state $X \in \mathbb{R}^5$.

7.1.2 Observer for nonlinear ODE coupled to hyperbolic PDE system

We state here the main result from [Irscheid *et al.* 2021] that gives a generic methodology for implementing observers for a 2×2 linear hyperbolic PDE coupled to a nonlinear ODE. The design is based on the following assumption.

Assumption 19. *Let*

$$\dot{X}(t) = F(X(t), \bar{U}(t)) \quad (7.2a)$$

$$\bar{Y}(t) = h(X(t)) \quad (7.2b)$$

be a nonlinear ODE with input \bar{U} and output \bar{Y} . We assume:

- *An observer*

$$\dot{\hat{X}}(t) = \bar{F}(\hat{X}(t), \bar{U}(t), \bar{Y}(t)) \quad (7.3)$$

initialized from $\hat{X}(0) = \hat{X}_0 \in \mathbb{R}^n$ exists such that $\lim_{t \rightarrow \infty} \|\hat{X}(t) - X(t)\| = 0$.

- *The vector field F is sufficiently locally Lipschitz for the IVP (7.2a), initialized from some $X(0) = X_0$, to have a well-posed solution for all $t \geq 0$.*

The first part of Assumption 19 implies that as long as one has an observer for the ODE subsystem at hand, an observer for the coupled PDE–ODE system can be implemented. The second part is necessary to construct the observer presented in the following Theorem. The observer is given for the case of constant transport speeds, but Remark 1 of [Irscheid *et al.* 2021] claims that the observer can be adjusted to the case of spatially varying transport speeds with minor modification.

Theorem 6 (Theorem 1 in [Irscheid *et al.* 2021]). *Let Assumption 19 hold. Consider the observer*

$$\dot{\hat{X}}(t) = \bar{F}(\hat{X}(t), \hat{U}(t), \hat{Y}(t)) \quad (7.4a)$$

$$\hat{u}_t(x, t) = -\lambda \hat{u}_x(x, t) + \sigma^+(x) \hat{v}(x, t) + P^+(x) \tilde{y}(t) \quad (7.4b)$$

$$(7.4c)$$

$$\hat{v}_t(x, t) = \mu \hat{v}_x(x, t) + \sigma^-(x) \hat{u}(x, t) + P^-(x) \tilde{y}(t) \quad (7.4d)$$

$$\hat{u}(0, t) = d_0 \hat{v}(0, t) + h(\hat{X}(t)) \quad (7.4e)$$

$$\hat{v}(1, t) = d_1 y(t) + U(t) \quad (7.4f)$$

with

$$\hat{U}(t) = \hat{v}\left(0, t - \frac{1}{\lambda}\right) + \int_0^1 M^{\beta\alpha}(0, \xi) \tilde{y}\left(t - \frac{1}{\lambda}\xi\right) d\xi \quad (7.5)$$

$$\hat{Y}(t) = h\left(\hat{X}\left(t - \frac{1}{\lambda}\right)\right) - \tilde{y}(t) \quad (7.6)$$

$$\tilde{y}(t+s) = \begin{cases} \hat{u}(1, t+s) - y(t+s), & \text{if } s \in [-\frac{1}{\lambda}, 0] \\ h\left(\hat{X}\left(t+s - \frac{1}{\lambda}\right)\right) - h\left(X_p\left(s - \frac{1}{\lambda}; t\right)\right), & \text{if } s \in (0, \frac{1}{\lambda}] \end{cases} \quad (7.7)$$

$$X_p(s; t) = \Phi\left(t+s, \hat{U}\Big|_t^{t+\frac{1}{\lambda}+s}; \hat{X}(t)\right) \quad (7.8)$$

$$\hat{X}(t) = X_p(0; t) \quad (7.9)$$

and observer gains given by

$$P^+(x) = \lambda M^{\alpha\alpha}(x, 1) \quad (7.10a)$$

$$P^-(x) = \lambda M^{\beta\alpha}(x, 1) \quad (7.10b)$$

where $M^{\alpha\alpha}$, $M^{\beta\alpha}$ are the solution to (6.49a), (6.49c), (6.49e), (6.49g) with $\lambda(x) \equiv \lambda$, $\mu(x) \equiv \mu$, $C \equiv 0$ and Φ in (7.8) denotes the solution to the IVP (7.2a) initialized from $\hat{X}(t)$ with input (7.5). This observer guarantees that $(\hat{u}, \hat{v}, \hat{X})$ converges to the states (u, v, X) of the plant

$$\dot{X}(t) = F(X(t), v(0, t)) \quad (7.11a)$$

$$u_t(x, t) = -\lambda u_x(x, t) + \sigma^+(x) v(x, t) \quad (7.11b)$$

$$v_t(x, t) = \mu v_x(x, t) + \sigma^-(x) u(x, t) \quad (7.11c)$$

$$u(0, t) = d_0 v(0, t) + h(X(t)) \quad (7.11d)$$

$$v(1, t) = d_1 u(1, t) + U(t). \quad (7.11e)$$

Setting

$$F(X(t), v(0, \cdot)) := f(X(t)) + g_1(X(t))v(0, t) + g_2(X(t))v(0, t - \tau) \quad (7.12)$$

in (7.11a) we can apply the observer (7.4) to estimate the states of (6.2b)–(6.2c), (6.2e), (7.1), given that we have an observer

$$\dot{\hat{X}}(t) = \bar{F}(\hat{X}(t), v(0, t), h(X(t))). \quad (7.13)$$

for the flame subsystem. For this we design a KKL observer, and the background for such observers is given next in Section 7.1.3.

Remark 10. *The observer given by Theorem 6 can be applied to implement an observer for the plant (6.2) considered in Chapter 6, whenever the ODE subsystem is observable. This is because the ODE subsystem there is linear and hence trivially satisfies the Lipschitzness condition required by the second part of Assumption 19. However, the observer (6.41) does not require the computation of an integral of the form (7.5) or to solve an IVP such as (7.8) at each time step as required by (7.4), but instead can be implemented directly after the gains (6.51) have been computed once offline. This suggests the observer (6.41) would be more computationally efficient than (7.4) in practice, and hence more suitable for real-time implementation.*

7.1.3 KKL observers

The theory of KKL observers originates in the original, linear *Luenberger* observer design presented in [Luenberger 1964]. There, a state observer is designed for a finite-dimensional Linear Time Invariant (LTI) state-space system by mapping the plant into a target system driven by known I/O signals. Conditions are given for the existence of an invertible linear transformation between the plant and target state, which is computed from solving a Sylvester matrix equation. State estimates are then recovered by mapping the target state into the plant state space via the inverse transformation.

A generalization of this observer design for autonomous nonlinear ODEs was discovered independently by [Shoshitaishvili 1992] and [Kazantzis & Kravaris 1998]. As for the linear case, the plant is mapped into a linear target system driven by the measurement signal, but because the original plant is nonlinear, a nonlinear transformation is required. Rather than being the solution to a Sylvester matrix equation, the nonlinear transformation is here the solution to a “Sylvester-like” PDE. General sufficient conditions for the existence and injectivity of this mapping are given in [Andrieu & Praly 2006].

The extension of this one step further to nonautonomous nonlinear ODEs is treated in [Bernard & Andrieu 2018]. In the general case a nonlinear, time-varying transformation is required here, rather than a static one which was sufficient for the autonomous nonlinear case. However, the flame model of the form (2.17) we consider here falls within a special class of nonautonomous nonlinear ODEs, namely input-affine nonlinear ODEs. As shown in [Bernard & Andrieu 2018], for this particular

class of nonautonomous nonlinear ODEs it is sufficient to use a static, rather than time-varying transformation in a KKL observer design, and the transformation is the same as for the corresponding autonomous *drift*¹ system. The result is based on the following assumption.

Assumption 20. *Let the system*

$$\dot{X}(t) = f(X(t)) + g(X(t))\bar{U}(t) \quad (7.14a)$$

$$\bar{Y}(t) = h(X(t)) \quad (7.14b)$$

be initialized from some $X_0 \in \chi_0 \subset \mathbb{R}^n$, and \mathcal{S} be an open subset of \mathbb{R}^n containing χ_0 . The system (7.14) is assumed to be uniformly instantaneously observable on \mathcal{S} and its drift system is strongly differentially observable of order n on \mathcal{S} .

The following result from [Bernard & Andrieu 2018] provides the theoretical basis for the numerical observer design presented in Section 7.2.

Theorem 7 (Theorem 4 in [Bernard & Andrieu 2018]). *Let $\lambda_1, \dots, \lambda_n$ be any distinct positive real numbers such that $\min(\lambda_1, \dots, \lambda_n) = \lambda_{\min} > 0$ sufficiently large, D the Hurwitz matrix $\text{Diag}(-\lambda_1, \dots, -\lambda_n)$ in $\mathbb{R}^{n \times n}$, F the vector $(1, \dots, 1)^\top$ in \mathbb{R}^n . Then, for any positive real number \underline{U} , any bounded open subset χ of \mathbb{R}^n such that*

- $cl(\chi) \subset \mathcal{S}$,
- For any \bar{U} in \mathcal{U} , for all t in $[0, \infty)$ and for all X_0 in χ_0 , $|\bar{U}(t)| \leq \underline{U}$ and $\Phi(t, \bar{U}|_0^t; X_0)$ is in χ ,

there exists a strictly positive number $\bar{\lambda}$ such that for any $\lambda_{\min} > \bar{\lambda}$:

- *There exists a function $T : \mathbb{R}^n \mapsto \mathbb{R}^n$, which is a diffeomorphism on $cl(\chi)$ and is solution to the PDE associated to the drift dynamics*

$$\frac{\partial T}{\partial X}(X)f(X) = DT(X) + Fh(X), \quad \forall X \in \chi. \quad (7.15)$$

- *There exists a Lipschitz function $\bar{\varphi}$ defined on \mathbb{R}^n satisfying*

$$\bar{\varphi}(T(X)) := \frac{\partial T}{\partial X}(X)g(X), \quad \forall X \in \chi \quad (7.16)$$

and such that, for any function $T^ : \mathbb{R}^n \mapsto \mathbb{R}^n$ satisfying*

$$T^*(T(X)) = X \quad (7.17)$$

the system

$$\dot{Z}(t) = DZ(t) + F\bar{Y}(t) + \bar{\varphi}(Z(t))\bar{U}(t) \quad (7.18)$$

is an observer for system (7.14) initialized in χ_0 .

¹The drift system of an input-affine ODE plant is the autonomous ODE which results from setting the input $\bar{U} \equiv 0$.

Hence, to design a KKL observer for the system (7.14), it suffices to find a solution T to the PDE (7.15) and its corresponding left-inverse satisfying (7.17). Finding such transformation numerically is the focus of Section 7.2. Note that the ODE subsystem (2.45a) can be written in the form (7.14a) with

$$g(X) := \begin{bmatrix} g_1(X) \\ g_2(X) \end{bmatrix}^\top, \quad \bar{U}(t) := \begin{bmatrix} \check{V}(0, t) \\ \check{V}(0, t - \tau) \end{bmatrix}.$$

7.2 Numerical design of observer for Kornilov's flame

7.2.1 Methodology

We propose here a methodology for data generation to train neural networks to estimate a static transformation satisfying (7.15), linking states of the input-affine system (7.14a) to states of the corresponding observer (7.18). In [da Costa Ramos *et al.* 2020] it was proposed to train a time varying transformation for input-affine nonlinear systems, which introduces an extra dimension (time) into the transformation to be found. The approach was feasible there since toy examples of dimension $n = 2$ were considered; here we consider a state space model of dimension $n = 5$ for a practically applied problem. At this dimension, finding a static transformation is already challenging enough due to the ‘‘curse of dimensionality’’, let alone finding a spatially varying transformation. Also, the approach previously considered relies on exploring the state space using a single nominal input signal, which for higher dimensional state spaces could be difficult to achieve sufficiently well in practice.

In light of Theorem 7, it is sufficient to train a static transformation between the drift system and the observer dynamics it cascades into, as given by

$$\dot{X}(t) = f(X(t)), \quad (7.19a)$$

$$\dot{Z}(t) = DZ(t) + Fh(X(t)). \quad (7.19b)$$

To achieve this, data consisting of corresponding $\{X, Z\}$ pairs in respectively the plant and observer compact states spaces of interest χ and \mathcal{Z} needs to be established. However, since the flame model (2.45a) describes flame behaviour under a locally changing velocity field, simulating the drift system (7.19a) will not necessarily cause the system to follow the trajectories in χ that the plant follows under acoustic forcing. Rather, one wants to sample $\{X, Z\}$ at points corresponding to where the states go under the influence of input signals one could expect in practice.

Having picked a D and F matrix for use in (7.18), we suggest applying the following steps to generate the $\{X, Z\}$ pairs necessary to train the static transformation.

1. Choose a representative set of N input signals $\{\bar{U}^i\}_{1 \leq i \leq N}$ for the system.
2. For each \bar{U}^i , solve the following IVP for $t \in [0, t_s]$:

$$\dot{X}^i(t) = f(X^i(t)) + g(X^i(t))\bar{U}^i(t), \quad X^i(0) = X^{i,0} \in \chi_0. \quad (7.20)$$

3. Sample state trajectories at M points in time $0 \leq t_1 < \dots < t_M \leq t_s$ to obtain $N \times M$ points $\{X^i(t_j)\}_{1 \leq i \leq N, 1 \leq j \leq M}$.
4. Solve $N \times M$ IVPs

$$\dot{X}^{b,ij}(t) = -f(X^{b,ij}(t)), \quad X^{b,ij}(0) = X^i(t_j) \quad (7.21)$$

for $t \in [0, t_o]$, with t_o being the estimated convergence time² of the observer, and $\varepsilon > 0$ a time-scaling constant.

5. Solve the following $N \times M$ IVPs for $t \in [0, t_o]$:

$$\dot{X}^{f,ij}(t) = f(X^{f,ij}(t)), \quad X^{f,ij}(0) = X^{b,ij}(t_o), \quad (7.22a)$$

$$\dot{Z}^{ij}(t) = DZ^{ij}(t) + Fh(X^{f,ij}(t)), \quad Z^{ij}(0) = Z^{ij,0} \in \mathcal{Z}_0. \quad (7.22b)$$

6. Store $N \times M$ training data pairs as $\{X^{f,ij}(t_o), Z^{ij}(t_o)\}$.

In Step 1, the objective is to pick a set of input signals representing what the plant would be subjected to in a practical setting. This is so that in Step 2, the generated trajectories explore the regions of the state space we expect the plant to visit during practical operating conditions, so that an observer able to estimate states in this region is trained sufficiently well. Thereafter, Step 3 starts collecting data points that will be used during training of the neural networks by sampling the trajectories generated during Step 2. However, at this stage we only have half of the data necessary to train the neural networks – the other half needs to come from sampling of the observer state space at points corresponding to transformations of the plant states through the unknown transformation T . This is what Steps 4–5 of the data generation procedure are for. Since knowledge of T is needed to calculate $\bar{\varphi}$ defined by (7.16), the input signals chosen in Step 1 cannot be directly used to drive the observer dynamics (7.18). Hence the data from the observer state space must be generated without using the input signals directly. To do this, we consider finding points in the plant state space, which when used as initial conditions to the drift dynamics (7.19a), end up at the points sampled in Step 3 after being integrated for the time equal to the observer convergence time t_o . Finding these points is akin to backwards integration of the drift system, hence Step 4. Then, when the cascade (7.19) is solved from these initial conditions for a time of duration t_o , the plant states will move back to the initial values they were sampled at in Step 3, while the observer states will be integrated to points $Z^{ij} = T(X^{ij})$ in the observer state space. This is achieved through Step 5. With the complete set of data generated, the data generated in Step 5 is stored for further use in Step 6.

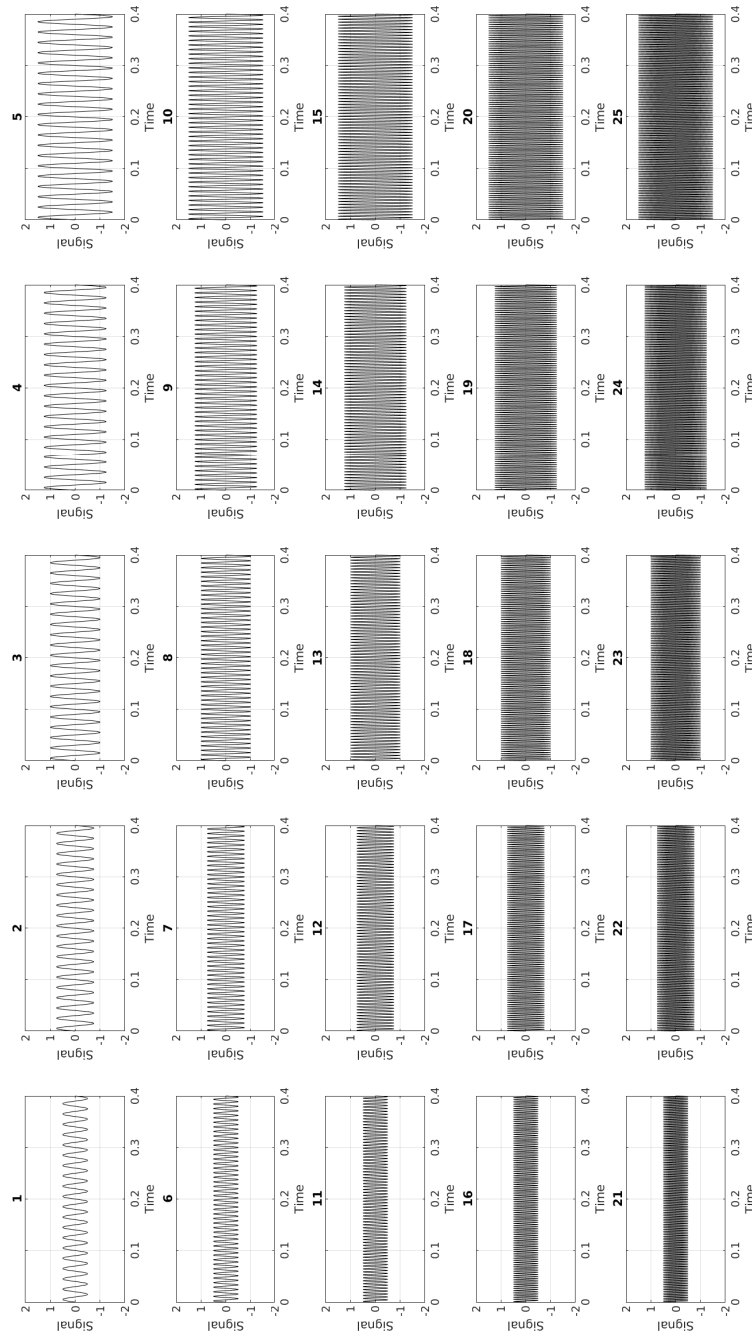


Figure 7.1: Monofrequent input signals to generate training data.

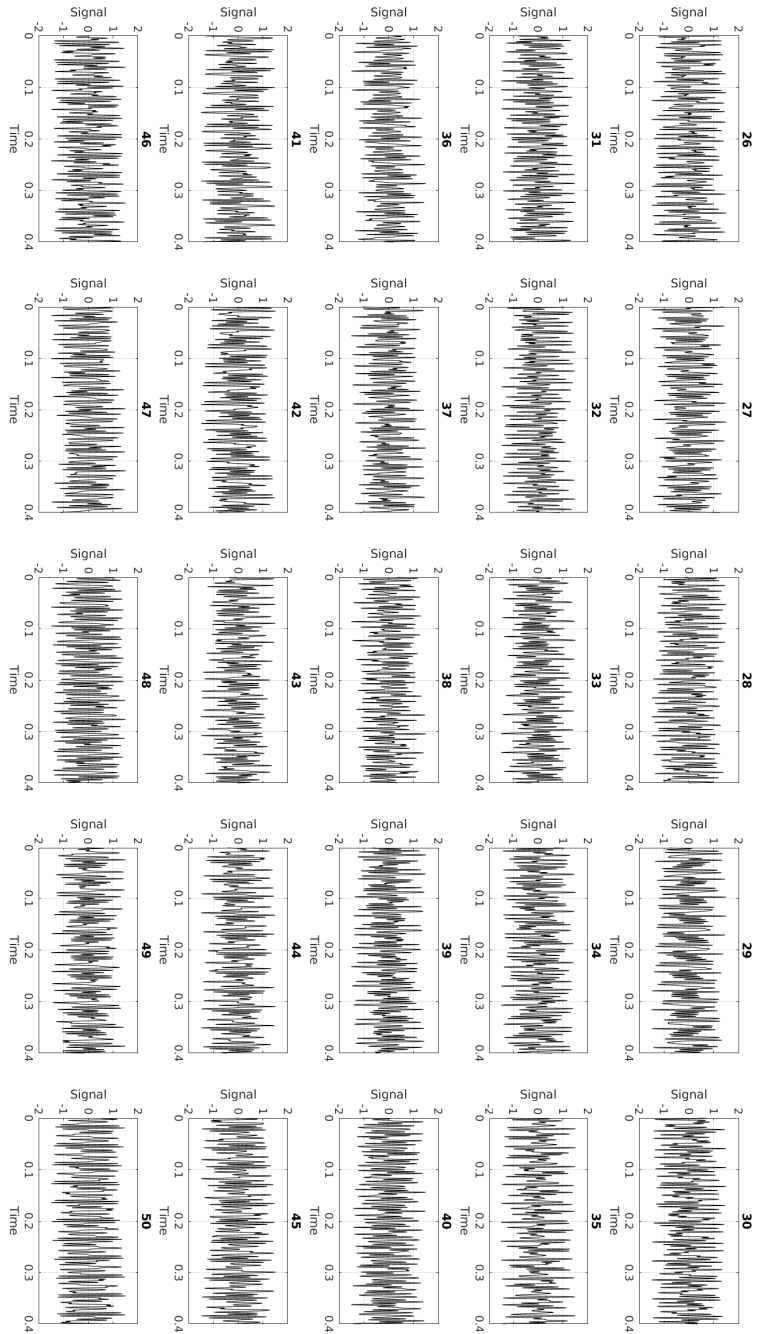


Figure 7.2: Broadband input signals to generate training data.

7.2.2 Generation of training data

To generate the data for Step 1, $N = 50$ input signals \bar{U}^i are chosen to simulate trajectories X^i of IVP (7.20) for $t \in [0, t_s]$, where $t_s = 0.4$ s. To be representative of what the flame might be exposed to in a practical setting, the input signals are selected as a mix of monofrequent and broadband signals containing frequencies between $f_l = 50$ Hz and $f_h = 300$ Hz, and amplitudes between $a_l = 0.5$ and $a_h = 1.5$. For $i \in \{1, \dots, 25\}$, the signals are monofrequent and are plotted in Figure 7.1. The remaining signals for $i \in \{26, \dots, 50\}$ are broadband, generated with the MATLAB `idinput` function and are plotted in Figure 7.2. Using the set of input signals $\{\bar{U}^i\}_{i=1}^N$ shown in Figures 7.1–7.2, Step 2 of the procedure is performed to generate a set of trajectories $\{X^i\}_{i=1}^N$ in χ with the `ode45` function from MATLAB, initialized from the same initial state $X^{i,0} = X^0 \in \mathbb{R}^5$ given by the Dynamic ROM model.

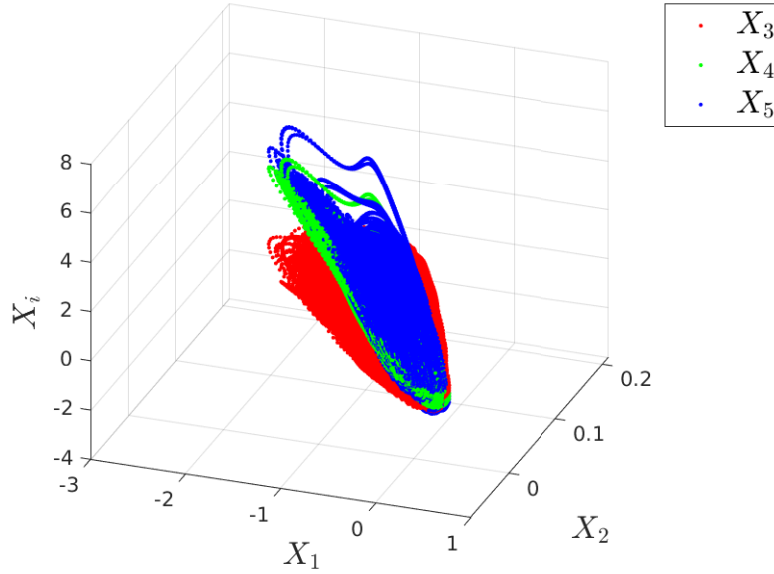


Figure 7.3: Three orthogonal 3-D projections of 5-D point cloud representing sampled trajectories in $\chi \subset \mathbb{R}^5$.

In accordance with Step 3, each of these trajectories are sampled. This was done at each time step giving $M = 8001$ samples for each of the $N = 50$ trajectories, for a total of $N \times M = 400050$ points in $\chi \subset \mathbb{R}^5$. Three different 3-D projections of the resultant 5-D point cloud are visualized in Figure 7.3. The red point cloud represents the points projected onto the X_1 – X_2 – X_3 subspace of χ , the green point cloud the points projected to the X_1 – X_2 – X_4 subspace and the blue point cloud the

²We use here the estimate used in [da Costa Ramos *et al.* 2020], namely $t_o := \frac{k}{\lambda_{min}}$ where $k = 3$ or 5.

points projected into the X_1 - X_2 - X_5 subspace.

With these points in \mathbb{R}^5 as initial conditions, $N \times M = 400050$ IVPs of the form (7.21) are solved for Step 4 of the data generation procedure. To perform this step we need an estimate of the observer convergence time, and to estimate this we need the observer eigenvalues. These are picked to correspond to a sixth-order Bessel filter, and are calculated using the `besself` function in MATLAB. This results in observer D and F matrices given by

$$D = \begin{bmatrix} -4285.38 & -875.10 & 0 & 0 & 0 & 0 \\ 875.10 & -4285.38 & 0 & 0 & 0 & 0 \\ 0 & 0 & -3768.3 & -2649.18 & 0 & 0 \\ 0 & 0 & 2649.18 & -3768.3 & 0 & 0 \\ 0 & 0 & 0 & 0 & -2537.76 & -4531.86 \\ 0 & 0 & 0 & 0 & 4531.86 & -2537.76 \end{bmatrix},$$

$$F = [600 \ 600 \ 600 \ 600 \ 600 \ 600]^\top$$

and using $k = 3$ an estimated observer convergence time of

$$t_o \approx 1.18 \times 10^{-3} \text{ s.}$$

Remark 11. *The resultant observer matrix $D \in \mathbb{R}^{6 \times 6}$ has complex eigenvalues and implies the set \mathcal{Z} for which the trajectories of (7.18) will be contained in is a subset of \mathbb{R}^6 , which is of one dimension higher than \mathbb{R}^5 which contains χ . However, Theorem 7 states that \mathcal{Z} should be contained in \mathbb{R}^5 and have real eigenvalues. These are, however, the strictest necessary conditions and in some practical scenarios (such as the one considered here) it is possible to use an observer state space of dimension $p > n$ and matrix D with complex eigenvalues. In the case considered here we found choosing $p = n + 1$ and complex eigenvalues in D gave better numerical performance. Investigating the exact conditions under which this design flexibility is possible would be valuable and interesting further work.*

The IVPs (7.21) are solved using the `ode45` solver. To visualize this step, the solution to 150 of the IVPs are plotted in Figure 7.4, using initial conditions $X^{30}(t_j)$ for $j \in \{1, \dots, 150\}$. Subsequently, in Step 5 the IVP (7.22) is solved $N \times M = 400050$ times using `ode45` with initial data generated from Step 4 for $X^{f,ij}$ but $Z^{ij,0} = 0$. This step is visualized in Figure 7.6 by showing the observer states for 150 of the IVPs, namely $Z^{30,j}$ for $j \in \{1, \dots, 150\}$. Step 5 results in $N \times M = 400050$ points Z_{ij} in $\mathcal{Z} \subset \mathbb{R}^6$. These are represented by four 3-D point clouds as shown in Figure 7.6, where the black point cloud represents points in the Z_1 - Z_2 - Z_3 subspace of \mathcal{Z} , the cyan point cloud is for the Z_1 - Z_2 - Z_4 subspace, the magenta point cloud represents points in the Z_1 - Z_2 - Z_5 subspace and the yellow point cloud is for Z_1 - Z_2 - Z_6 .

Next, in Section 7.2.3 the data shown in Figures 7.3, 7.6 is used to train nonlinear transformations between the two point clouds (one forward transformation $T : \mathbb{R}^5 \mapsto \mathbb{R}^6$ and one left-inverse $T^* : \mathbb{R}^6 \mapsto \mathbb{R}^5$), with each triplet of points in 7.3 (one

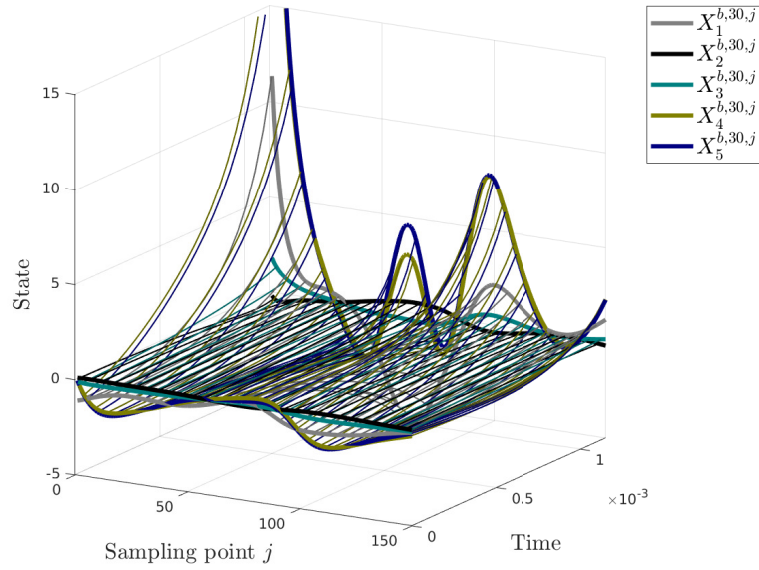


Figure 7.4: Solutions $X^{b,30,j}$ for $j \in \{1, \dots, 150\}$ of (7.21). Represents backwards integration of the drift system. For ease of viewing only state component number ($j \bmod 5$) is shown for each sampling point j .

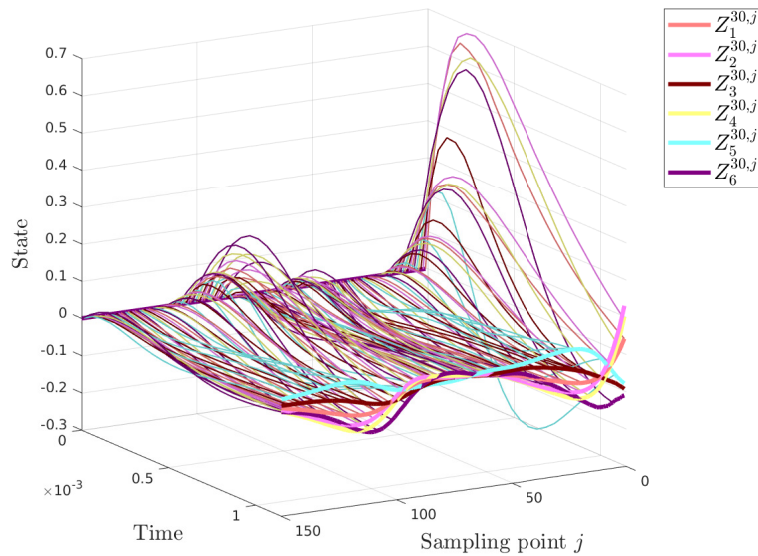


Figure 7.5: Solutions $Z^{30,j}$ for $j \in \{1, \dots, 150\}$ of (7.22). Represents integration of the observer driven by the drift system. For ease of viewing only state component number ($j \bmod 6$) is shown for each sampling point j .

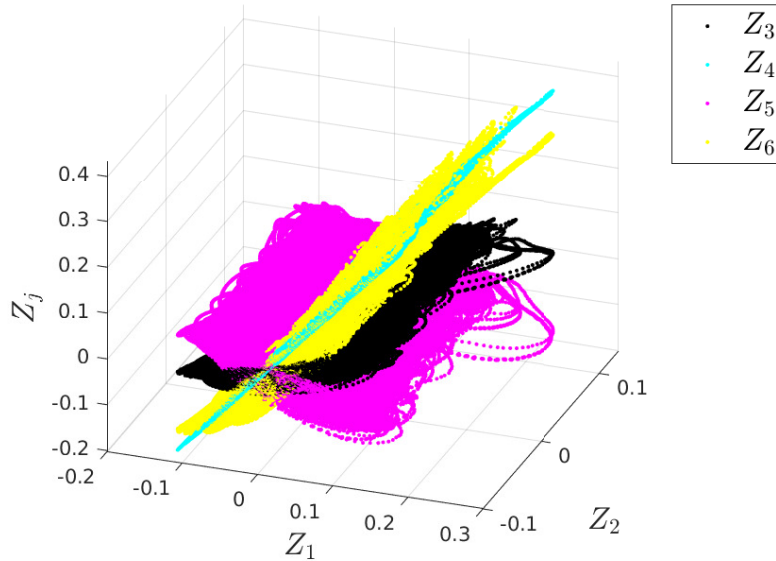


Figure 7.6: Four orthogonal 3-D projections of 6-D point cloud representing sampled trajectories in $\mathcal{Z} \subset \mathbb{R}^6$.

component from each of the three 3-D point clouds) together corresponding to a quadruple of points in 7.6 (one component from each of the four 3-D point clouds). An example of points corresponding to each other is shown in Figure 7.7, which shows a set of points $\{X^{f,45,j}(t_o), Z^{45,j}(t_o)\}$ for $j \in \{1, \dots, 300\}$.

7.2.3 Training of neural networks

We employ neural networks to approximate the nonlinear transformation T and its left-inverse T^* necessary to implement the observer presented in Theorem 7. Using a shallow network with a single hidden layer of sigmoid functions and a linear output layer is sufficient to approximate any function with a finite number of discontinuities arbitrarily well [Beale *et al.* 2010], and because we have reduced our observer design problem to a problem of approximating two static functions $T : \mathbb{R}^5 \mapsto \mathbb{R}^6$, $T^* : \mathbb{R}^6 \mapsto \mathbb{R}^5$, such an architecture is employed.

A diagram of the architecture used to approximate T is shown in Figure 7.8, whereas the neural network architecture used to approximate T^* is shown in Figure 7.9. They are both initialized using the `feedforwardnet` function in MATLAB, and both consist of a hidden layer of 8 `tansig` functions, a type of sigmoid function defined by

$$\text{tansig}(x) := \frac{2}{1 + \exp(-2x)} - 1. \quad (7.23)$$

The input to each of the `tansig` functions is a weighted sum of the inputs (5 inputs in the case of T and 6 in the case of T^*) in addition to a bias. All of the input

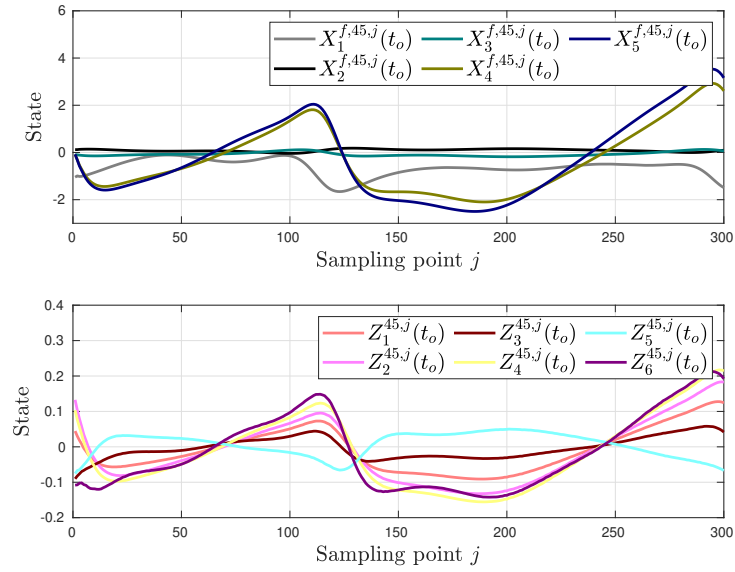


Figure 7.7: Example of corresponding X and Z points for training of transformation.

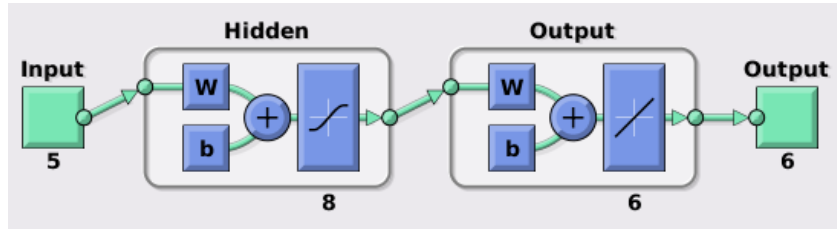


Figure 7.8: Architecture of neural networks used to approximate forward transformation T .

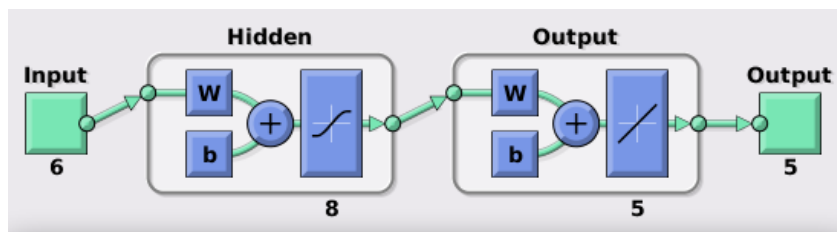


Figure 7.9: Architecture of neural networks used to approximate left-inverse transformation T^* .

weights are summarized in a matrix denoted W^1 , of dimension 8×5 for T and 8×6 for T^* , and the biases in the first layer are stored in a vector of dimension 8 denoted b^1 . Linear combinations of the 8 `tansig` functions are passed into an output layer, which consists of 6 passthrough functions in the case of T and 5 passthrough functions in the case of T^* . A bias is also added to each of the linear combinations of outputs from the `tansig` functions. In the case of T , 6 different linear combinations are performed so the weights in the second layer are stored in a matrix denoted W^2 of dimension 6×8 , whereas the second bias vector denoted b^2 is of dimension 6. On the other hand, for T^* the second weight matrix W^2 is of dimension 5×8 and the bias vector b^2 is of dimension 5. This gives a total of 101 hyperparameters to fit for T^* and 102 hyperparameters for T .

When initializing the neural networks, the parameters in W^1 , W^2 , b^1 and b^2 in each of the networks is randomized. Then, using the training data visually represented in Figures 7.3, 7.6, a backpropagation algorithm is employed to update the network parameters to approximate the functions T and T^* . For this purpose, conjugate gradient backpropagation with Polak-Ribière updates is used. Because

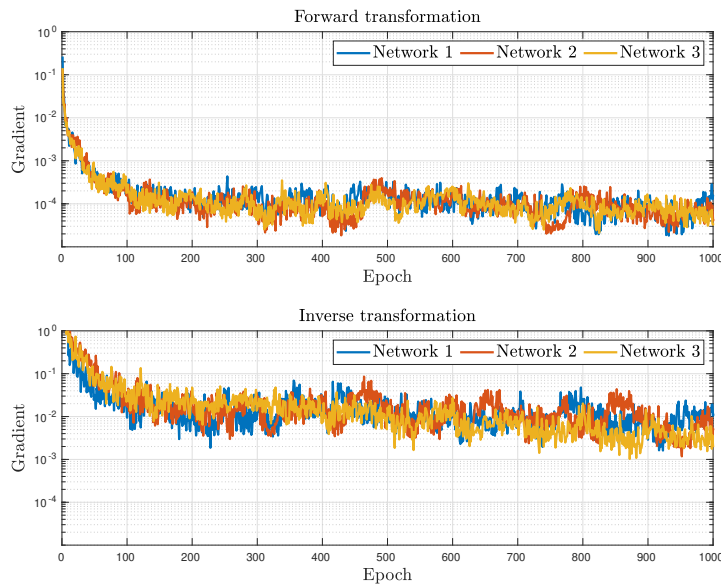


Figure 7.10: Gradient of the hyperparameter search vector during backpropagation training of neural networks. Shown for forward transformation (top) and inverse transformation (bottom).

the training of neural networks is a randomized process and consists of solving a relatively complex optimization problem, three separate neural networks are trained for the sake of replication. Before training each the neural networks, 10% of the training data shown in Figures 7.3, 7.6 was picked out at random, and is used in Section 7.2.4 to check how well the trained transformations predict data not used

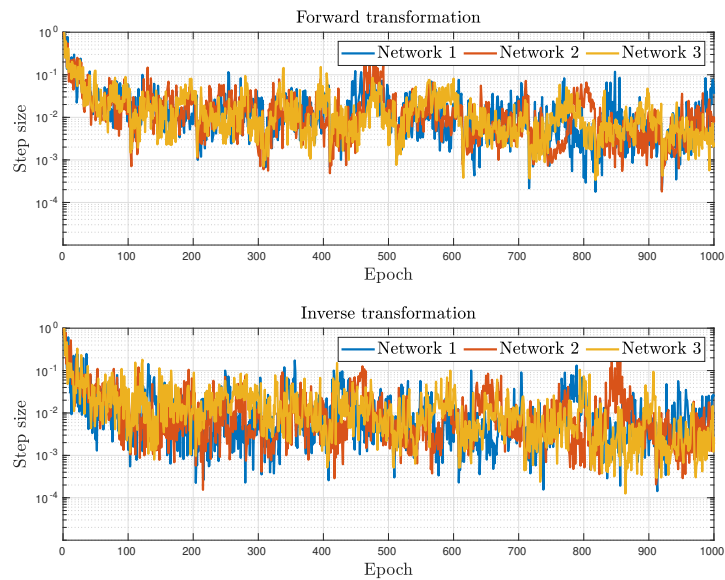


Figure 7.11: Step size of the hyperparameter search vector during backpropagation training of neural networks. Shown for forward transformation (top) and inverse transformation (bottom).

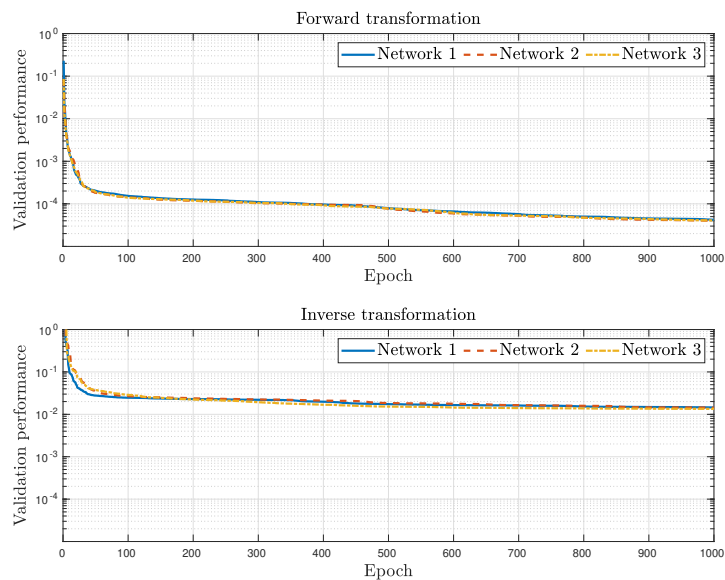


Figure 7.12: Validation performance of neural networks during backpropagation training. Shown for forward transformation (top) and inverse transformation (bottom).

in the training.

The neural networks were trained with an upper limit of 1000 epochs, with the training consistently running up to the limit. In Figure 7.10, the gradient of the parameter update vector at each epoch is plotted for the three networks trained, and in Figure 7.11 the corresponding step size is shown. Also, in Figure 7.12 the validation performance at each epoch is compared for the three different neural networks trained for each transformation. The three networks for the forward transformation have similar gradient, step size and validation performance throughout the training, and the same can be said for the left-inverse transformations. However, the left-inverse transformations systematically had larger gradients and mean square errors in the validation performance tests throughout training, indicating that training of these networks was more challenging. This is consistent with the results of [Andrieu & Praly 2006] which give smoothness guarantees for T but not for T^* .

7.2.4 Resultant transformation

The hyperparameters in the weight and bias matrices W^1 , W^2 , b^1 and b^2 obtained at the end of the training for each of the six networks is documented in Appendix A. Despite approximating the same transformation and being trained with the same data (disregarding the 10% that is randomly taken out before training each network), the resultant hyperparameters take different values over the three networks for each transformation in general. This indicates that the networks converged to different local minima or did not fully converge to a minimal point in the hyperparameter search space during training. To test the performance of the resultant

Quantity	Neural network 1	Neural network 2	Neural network 3
$\ \tilde{X}_1\ /\ X_1\ $	3.68×10^{-1}	3.67×10^{-1}	3.51×10^{-1}
$\ \tilde{X}_2\ /\ X_2\ $	5.02×10^{-1}	5.14×10^{-1}	5.07×10^{-1}
$\ \tilde{X}_3\ /\ X_3\ $	4.51×10^{-1}	4.42×10^{-1}	4.79×10^{-1}
$\ \tilde{X}_4\ /\ X_4\ $	8.77×10^{-2}	8.61×10^{-2}	8.40×10^{-2}
$\ \tilde{X}_5\ /\ X_5\ $	1.58×10^{-2}	2.33×10^{-2}	2.65×10^{-2}
$\ \tilde{Z}_1\ /\ Z_1\ $	2.37×10^{-2}	3.72×10^{-2}	3.01×10^{-2}
$\ \tilde{Z}_2\ /\ Z_2\ $	6.06×10^{-2}	5.33×10^{-2}	6.11×10^{-2}
$\ \tilde{Z}_3\ /\ Z_3\ $	2.93×10^{-1}	2.96×10^{-1}	2.99×10^{-1}
$\ \tilde{Z}_4\ /\ Z_4\ $	3.11×10^{-2}	2.91×10^{-2}	3.47×10^{-2}
$\ \tilde{Z}_5\ /\ Z_5\ $	2.48×10^{-1}	2.46×10^{-1}	2.45×10^{-1}
$\ \tilde{Z}_6\ /\ Z_6\ $	1.37×10^{-1}	1.33×10^{-1}	1.32×10^{-1}

Table 7.1: Euclidean norms of scaled prediction errors.

transformations, after training the transformations are tested on the remaining 10% of the data that is not used during training. Firstly, for the left-inverse transformation, 120015 predictions $\hat{X}^{kl} = \hat{T}_l^*(Z^{kl})$ for $k \in \{1, \dots, 40005\}$ and $l \in \{1, 2, 3\}$ are

made by evaluating the three neural networks \hat{T}_l^* at the points Z^{kl} in the validation data set. Subtracting the predictions from the corresponding X^{kl} data points gives the prediction errors $\tilde{X}^{kl} := X^{kl} - \hat{X}^{kl}$. Scaling each of the components of \tilde{X}^{kl} by the Euclidean norm $\|X_i^l\| := \sqrt{\sum_{k=1}^{40005} |X_i^{kl}|^2}$, the prediction errors for the components can be compared. The same is done for the forward transformation, namely 120015 predictions are made by computing $\hat{Z}^{kl} = \hat{T}_l(X^{kl})$ for each X^{kl} in the validation data set, \hat{T}_l being the neural network estimate l of T .

The Euclidean norm of these values are summarized in Table 7.1. The neural networks have systematically relatively smaller prediction errors in X_4 , X_5 , Z_1 , Z_2 and Z_4 than in the remaining state components. None of the neural networks have overall better performance in prediction of all state components than the others.

7.3 Simulation and verification

7.3.1 Direct observer tests

With the transformation T satisfying the ‘‘Sylvester-like’’ PDE (7.15) and its left-inverse T^* having been approximated in Section 7.2, it is natural to test the transformation in an implementation of the observer from Theorem 7. The same plant and observer parameters as used for training are applied. For the input signal \bar{U} to (7.14), we use the signal

$$\bar{U}(t) = 0.4 \sin(200\pi t) + 0.6 \sin(300\pi t) \quad (7.24)$$

which was not part of the signals used to generate the training data, plotted in Figures 7.1–7.2. To approximate $\bar{\varphi}$ defined as (7.16) appearing in (7.18), a finite difference approximation with $\Delta X_i = 10^{-2}$ is used to approximate the Jacobian $\frac{\partial T}{\partial X}$. The observer dynamics (7.18) are initialized from $Z_0 = 0$ in all three tests, and the property (7.17) of the left-inverse transformation is applied to generate estimates \hat{X} from values of Z via

$$\hat{X}(t) = T^*(Z(t)). \quad (7.25)$$

In Figure 7.13, the plant states for the observer test simulations are plotted in solid black versus the estimates produced by the observers using the three different transformations trained in Section 7.2, which are dashed and colour coded (see the Figure legend). From the plot, all three observers estimate the state components X_4 and X_5 fairly well, but have more error in estimating X_1 , X_2 and X_3 . This corresponds to what is seen during the transformation validation tests in Section 7.2.4. Next, in Figure 7.14 the estimation errors $\tilde{X}_i := X_i - \hat{X}_i$ are plotted to more easily compare the performances between the three observers. Overall the three observers feature similar error magnitudes. However, in estimating X_4 and especially in X_5 observer number 1 has a slightly larger error compared to observer 2 and 3 at various points throughout the simulation.

Part of the reason in estimating the 5 internal states of the observer is for their contribution in estimating the heat release rate from the Kornilov flame. The

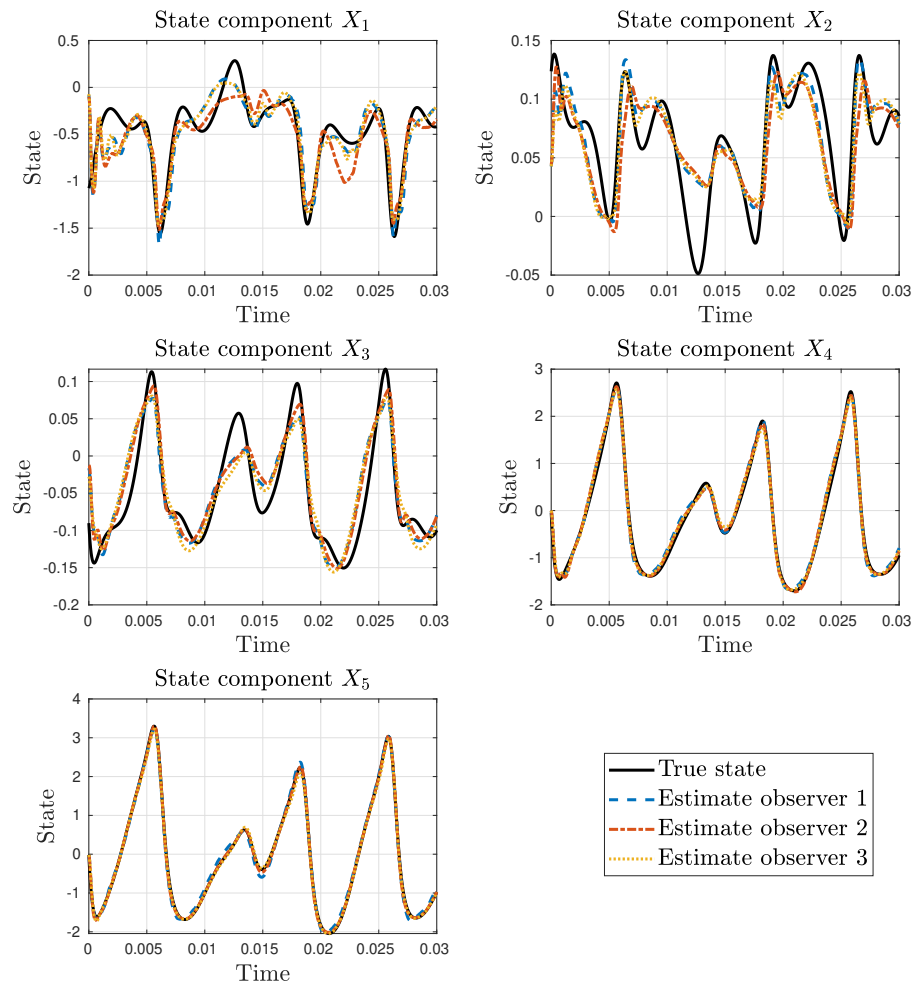


Figure 7.13: Plant states versus observer estimates.

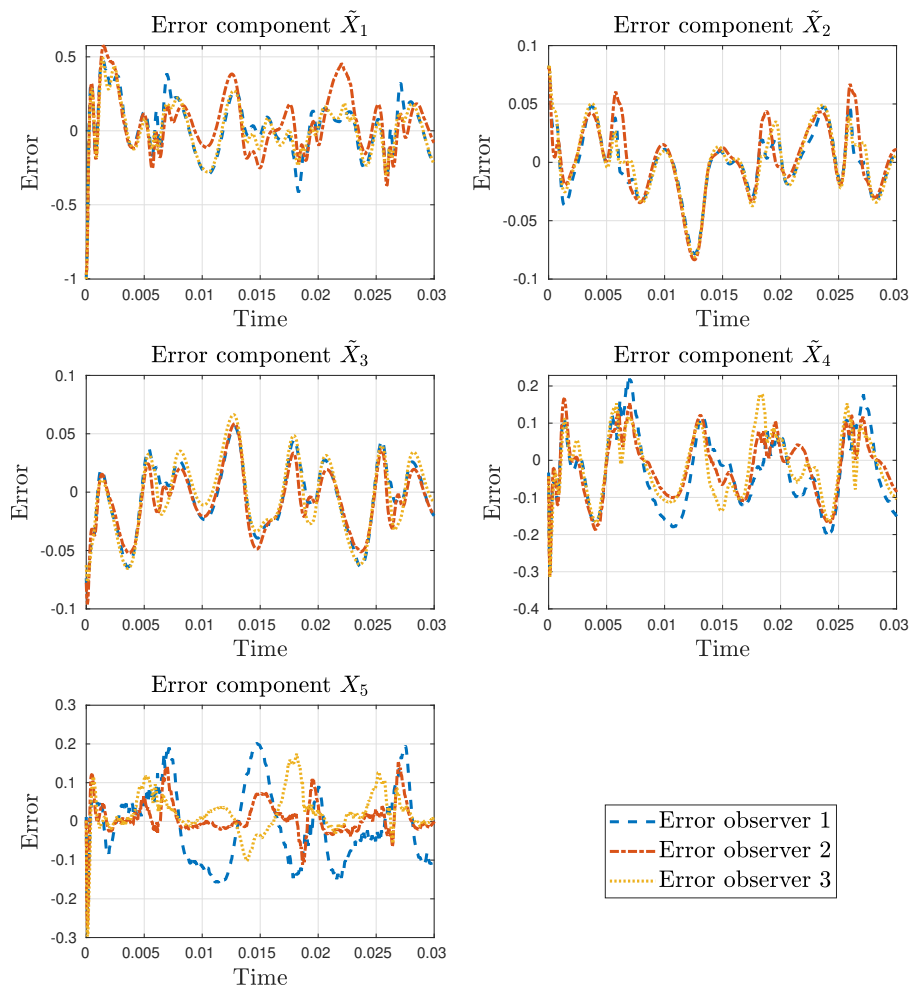


Figure 7.14: Observer estimation errors.

observer can then be placed as a subsystem in the combustor network model (6.2b)–(6.2c), (6.2e), (7.1), and used in a PDE–ODE observer such as the one presented in Theorem 6 to estimate heat release rate (together with pressure and velocity perturbations) using a pressure measurement taken from afar. Another reason the internal state estimates of the Dynamic ROM Kornilov flame model are of interest could be for control purposes, where a complete knowledge of the state might be needed for implementation of a control law, but this is outside the scope of this chapter as we do not consider control design here. Since the internal states of the Dynamic ROM ODE model are in a sense “synthetic” (they do not necessarily have a physical meaning), it is interesting to verify how well the observer estimates the heat release in the original CFD data on which the Dynamic ROM is based. This is the focus of Section 7.3.2.

7.3.2 Verification on Kornilov’s flame data

In this Section, the three observers are tested in their ability to reproduce the original I/O data on which the nonlinear flame ODE model is based. In Figure 7.15, the

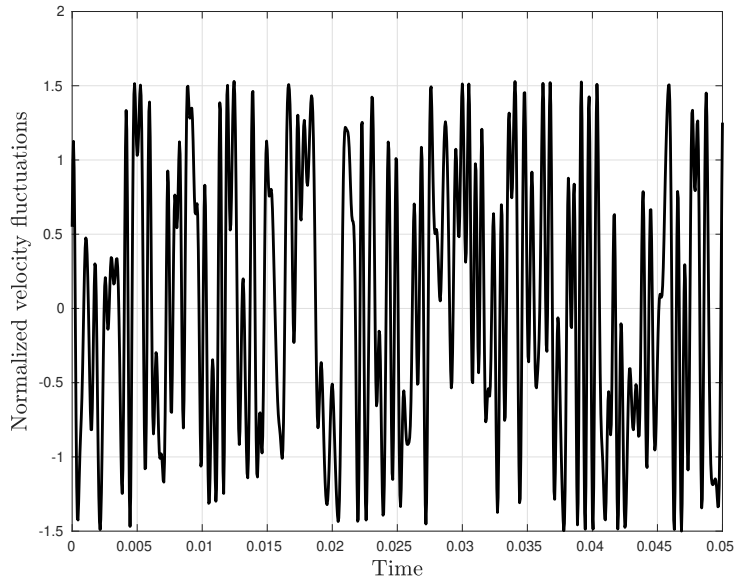


Figure 7.15: Velocity fluctuation signal from CFD data used for testing.

input signal from the CFD data that is passed into the observers is plotted. This data is firstly passed as the input signal \bar{U} , together with the corresponding heat-release fluctuation data as the output signal \bar{Y} , into the observer dynamics (7.18). Then, the output estimate

$$\hat{Y}(t) = h(T^*(Z(t))) \quad (7.26)$$

is computed. The resultant estimates using the three different neural networks

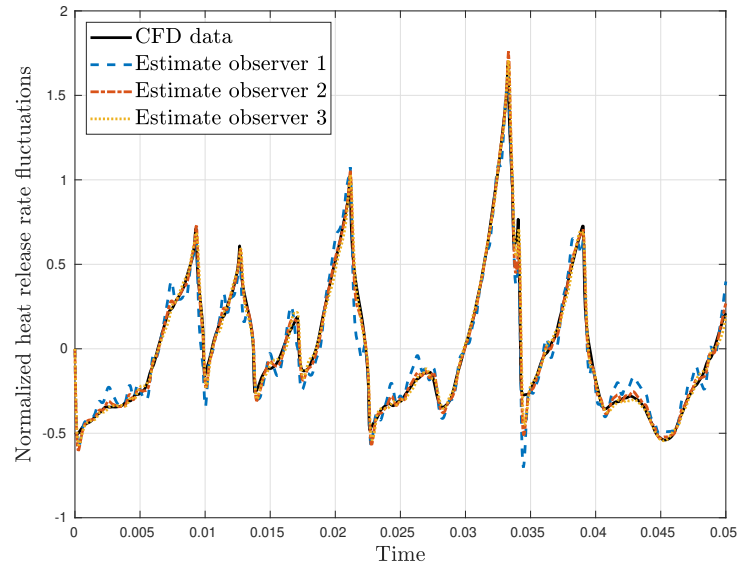


Figure 7.16: Observer estimates of heat release versus CFD data. Using both I/O signals from CFD as input to observer dynamics (7.18).

trained in Section 7.2 is plotted in Figure 7.16. In general the estimates track the CFD data fairly well, but have a tendency to overshoot at times of abrupt change. To more easily visualize and compare the performance, Figure 7.17 plots the estimation error from the three respective observers. Indeed, at times when the heat release fluctuations abruptly change corresponds to jumps in the error.

Next, it is of interest to test how well the observer estimates the heat release rate fluctuations when the input signal \bar{Y} is not directly from the Kornilov CFD data, but rather generated via the Dynamic ROM ODE model, by passing the input signal data shown in Figure 7.15 as the input \bar{U} to (7.14a), and then generating the output data \bar{Y} from evaluating the measurement function h in (7.14b).

In Figure 7.18 the heat release rate from the CFD data, plotted in solid black, is compared to the resultant estimates from the three observers. Compared to Figure 7.16, there is more error in the estimation of the heat release rate, especially at points where the heat release rate experiences ‘spikes’. This is as expected, since an extra source of error is introduced by generating the output data fed into the observer via the Dynamic ROM model. In Figure 7.19 the estimation errors computed from subtracting the observer estimates in Figure 7.18 from the CFD output data is plotted. Compared to Figure 7.17 the errors are larger at points where the heat release changes quickly, but overall the estimation error stays close to the origin.

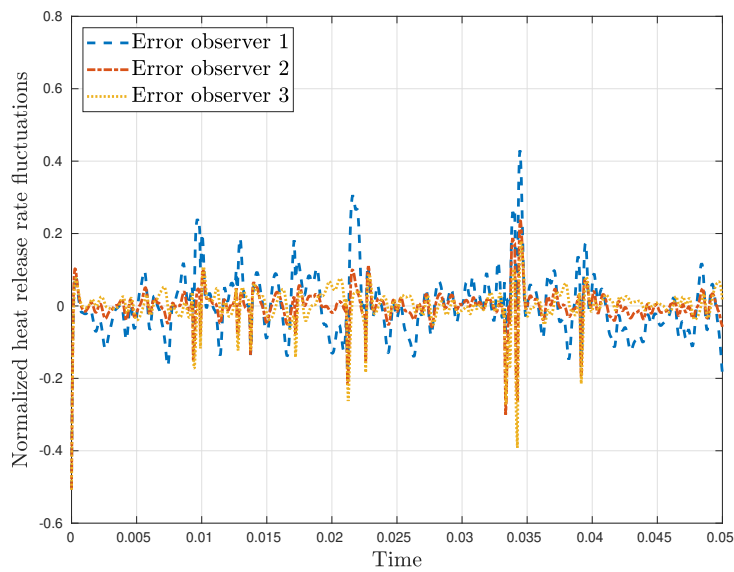


Figure 7.17: Observer estimation errors. Using both I/O signals from CFD as input to observer dynamics (7.18).

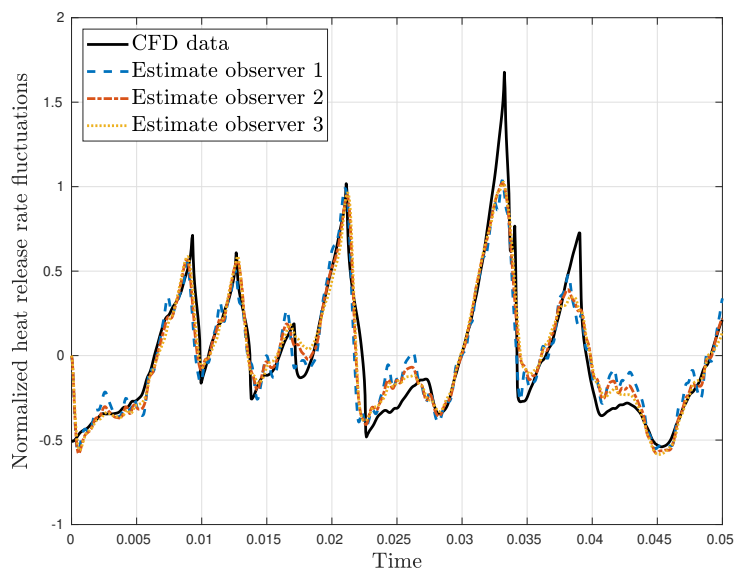


Figure 7.18: Observer estimates of heat release versus CFD data. Using data from CFD as input and output data from nonlinear ODE flame model as I/O data for observer dynamics (7.18).

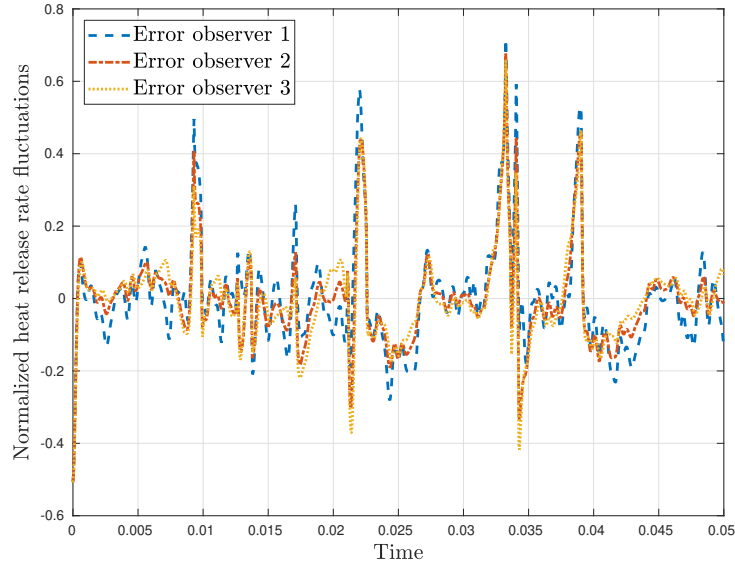


Figure 7.19: Observer estimation errors. Using data from CFD as input and output data from nonlinear ODE flame model as I/O data for observer dynamics (7.18).

7.4 Discussion

We have in this chapter numerically designed a KKL observer for a nonlinear state-space ROM of Kornilov’s flame. The observer was tested in reproducing firstly the states of the state-space model, and subsequently in estimating the heat release in the data on which the state-space model was based. Its performance, although not perfect, is fair and for the most part gives a decent prediction of the quantities of interest. One thing that could be tested to see if the observer performance improves is to design the observer to have equal dimension as the plant, as is possible according to Theorem 7. This would reduce the complexity of the problem as one less dimension needs to be considered in the target system space, and the forward and inverse transformations would be of equal size. Reducing the dimension of the target space has implications for both the data generation, since the number of points needed to sample a compact space of equal radius increases exponentially for each added dimension, and also for hyperparameter optimization, since fewer parameters would be needed, all else being equal. Alternatively, if one is only interested in estimating the heat release, the step of designing an ODE with “synthetic” states could be bypassed by only considering the output prediction directly with the I/O data describing the flame generated from CFD simulations, as for instance very recently studied for autonomous systems in [Janny *et al.* 2021]. To apply this to the problem considered in this chapter, the framework there would need to be extended to input-affine systems. Taking this approach could be more flexible as no *a priori*

restrictions on the structure of the f , g and h matrices in the plant model (7.14) need to be taken, eliminating a possible source of error.

Although more complicated neural network architectures can be tested, the more complex ones already tested by the author suffered from overfitting, in which regularization techniques must be applied. However, going in this direction could make the problem more complicated than it needs to be, especially in light of the use case of the neural network here being function approximation and hence in theory a single hidden layer being sufficient. Keeping a single hidden layer, future investigations could go into finding the most suitable number of nodes in the hidden layer, as well as testing alternative sigmoid functions. Also, during training the maximum number of epochs was capped at 1000, and especially for the forward transformation the gradient and validation performance still had a slight downward trend in all cases at this point in the training, as seen in Figures 7.10, 7.12. This indicates that the training might have been stopped before a minimum in the hyperparameter search space was reached, and investigating whether increasing this upper bound has an impact on the observer performance could be a worthwhile further step.

From a testing point of view, a natural next step would be to integrate the observer developed in this chapter into the PDE–ODE observer from Theorem 7.4, and see how well it estimates heat release rate, pressure and velocity based on a pressure measurement taken from afar. This observer could be compared to the linear observer from Theorem 5, and conclusions about the advantages and disadvantages of the two different approaches could be drawn. It would be reasonable to expect to find a trade-off between computational efficiency and estimation accuracy. In addition to testing how well the observers perform in a pure monitoring application, the use of the linear and nonlinear observer approaches that have been explored could be tested in the loop with a full-state feedback control law. One could start with the linear control law from Theorem 4, before proceeding to designing a control law taking into account nonlinearities in the heat release rate. Lastly, it is important to not forget to mention that during development of the nonlinear observer in this chapter, possible noise in the I/O signals was not taken into account. From a practical point of view, studying the sensitivity to noise of the observer is an important direction in which to further develop this work.

Part IV

Backmatter

Conclusion and Perspectives

Contents

8.1 Summary	177
8.2 Discussion	178

Dans ce chapitre final, nous résumons les travaux réalisés dans la thèse. Des perspectives et des suggestions pour des travaux futurs sont offertes.

In this final chapter, we take a bird’s-eye view of what has been achieved in the thesis and make concluding statements. Perspectives and suggestions for further work are offered.

8.1 Summary

We have in this thesis, in response to the objectives stated in Chapter 1, proposed state and parameter estimation algorithms for thermoacoustic instabilities with distributed acoustics and, whenever possible, nonlinear heat release dynamics. The first part of the work dealt with the electrically heated Rijke tube, a laboratory setup for reproducing thermoacoustic instabilities. Here, an observer relying on a boundary measurement is designed to provide globally convergent estimates of the pressure, velocity and heat release rate using a model with distributed acoustics and nonlinear heat release. It is identified that the state estimates are sensitive to the knowledge of boundary acoustic impedances, a parameter that is difficult to know or compute a priori. In response to this, we suggest a parameter identification method for estimating these parameters, also using a single pressure measurement.

As stated in the introductory Chapter 1, the literature on the topic of thermoacoustic instabilities has heavily relied on laboratory setups, and for model-based estimation and active control this is not an exception. We have therefore proposed to further the development of model-based estimation algorithms for thermoacoustics, using network models containing distributed models of the acoustics, towards cases more directly applicable to industrial settings. This is here mainly via our proposed model of distributed acoustics in ducts with variable cross-sectional area. As noted in [Poinsot 2017] the combustor geometry is a first-order factor with regards to thermoacoustics, and therefore taking this into account in the estimation algorithm design is important for correct estimation in practical combustors outside of

the laboratory. With the more general infinite-dimensional acoustics model, to avoid possible occurrence of the spillover effect we use it as basis for infinite-dimensional algorithm design, rather than lumping it into an ODE system first.

An extension of the parameter identification method used for the Rijke tube is considered next, firstly in a theoretical setting by suggesting a boundary parameter identification method for 2×2 linear hyperbolic PDE systems where a single boundary measurement is available. It is then suggested how this can be applied to boundary parameter estimation in a duct with spatially varying cross section. With the spatially varying acoustics coupled via a network model to a heuristically designed linear flame model, which we suggest can model the thermoacoustics in a can combustor, we design an observer for estimating the distributed velocity and pressure together with heat release from the flame. This state estimator design is paired with a collocated control law, which together can be used as an output feedback controller for the thermoacoustic oscillations. In the final core Chapter, we consider how a state estimator for a combustor can be designed when the flame model considered is nonlinear rather than linear. The mathematical analysis used in Chapter 6 is not as straightforward for this case, so instead we take a different approach where the problem is, using previous results from the literature, simplified to that of a nonlinear multidimensional function approximation problem. Data is generated, and neural networks are trained to approximate the mapping. With the learned mapping, an observer for the nonlinear flame ODE subsystem is implemented and first tested in estimating the internal states, before being tested on estimating the heat release rate from CFD data.

8.2 Discussion

Concerning the performance of the algorithms from Part II in simulations and experiments, there were mixed results. Although, to the best of the author's knowledge, this Rijke tube observer is the first globally convergent observer for the electrically heated Rijke tube that uses fully distributed acoustics and nonlinear heat release to model the dynamics, the observer design was unconventional in the sense that no tuning is possible. To prove the global convergence, an exponentially decreasing error was introduced into the system. In the simulations this slowed the convergence down compared to a "trivial observer" which, without any convergence guarantees, converged much faster. Indeed, the heat release model used is self-stabilizing when the conditions allow for it, with the nonlinear contribution coming from the coupling to the acoustics. Despite this, the observer proposed had better robustness properties with respect to uncertainty in the boundary acoustic parameters, something which was verified in simulations. For the experimental tests, the estimate of the pressure was phase-shifted away from the measured verification signal. Also, compared to the difference seen in the simulations, the difference in response was rather large when different values for the acoustic impedance are tested. After the acoustic impedances were estimated using the method from Chapter 4, the amplitude of the

estimated pressure signal was fairly close to the measured verification signal. However, the estimate was still phase-shifted away from the measured pressure signal, indicating that some modelling error might be present. Hence, as further work, a model validation step needs to be taken to isolate the main causes of the issue. Since the tube used in the construction of the Rijke tube was built of steel, one possible cause of the error which had been neglected in the modelling step is heat transfer between the gas and the tube, which could heat up the temperature of the gas. Further work that could address this issue would be to include a model of the heat evolution in the tube, and couple this to the acoustics model currently in place. Within the framework used in this thesis, this could be formulated as a problem of hyperbolic PDE system coupled in-domain to a parabolic PDE.

The parameter identification method suggested for 2×2 systems of linear hyperbolic PDEs in Chapter 5 is tested on a theoretical example and shown to work well there. The extension required to apply it for ducts with spatially varying cross-sectional area results in a parameter vector that is overparametrized with five parameters to estimate two parameters, rather than three parameters to estimate two as was the case previously. For further work, it would be interesting to test this on a practical example of a duct with spatially varying cross section. It should be compared to an algorithm that does not take into account the spatially varying geometry, and the parameter estimates compared to a benchmark example.

For the state estimation of distributed pressure and velocity in a combustor, two cases were considered - namely the case of a linear flame model and the more general scenario where a nonlinear input-affine flame model is considered. Since a different approach was taken in considering these two cases, their performance on practical examples should be compared. As discussed, we expect the state observer from Chapter 6 to be more computationally efficient than the one from Chapter 7, but in cases where strong nonlinearities in the heat release model are present it could be at a disadvantage. For practical implementation of these state estimators in practice, it is also expected that model validation steps need to be taken to ensure the model used for observer design matches the behaviour of the combustor the observer is being applied to. Control design, which was considered for the combustor with the linear flame using acoustic actuation collocated with the pressure sensor, should also be studied when the actuation is via fuel modulation at the flame. Indeed, from the literature [Dowling & Morgans 2005] we know this type of actuation is more feasible to implement in practice. The control design for the case of nonlinear flame should also be studied.

Overall, as stated in Chapter 1, this thesis has only considered longitudinal modes of thermoacoustic instabilities. Modelling and designing estimation schemes for these is, however, a crucial step in developing estimation schemes for more general models. Although the work presented here only scratches the surface of what is possible and necessary to do, we believe many of the ideas the work in this thesis is based on, as well as the contributions offered, can together form a basis for extending the results here to more complex cases. One important extension that should be considered in future work is the development of estimation algorithms

for the thermoacoustic instabilities encountered in annular combustors, which are featured in many modern combustion systems. Also, future extensions of this work should consider noise robustness and methods of modifying the algorithms suggested to such cases, if necessary and possible. Additionally, we believe the algorithms suggested here can be built on in the form of incorporating more realistic effects, in the form of effects such as internal damping contributions from the combustor material or intrinsic instabilities in the flame front, which could in certain settings be important to describe the system dynamics more accurately.

Appendix

Trained Neural Network Coefficients

The hyperparameters for the neural networks described in Section 7.2.3 of Chapter 7, as a result of the backpropagation training visualized in Figures 7.10–7.12, are documented here. As described, three pairs of neural networks for the forward and left-inverse transformations, T and T^* respectively, are trained on simulation data generated in Section 7.2.2. Due to the neural network architectures as shown in Figures 7.8–7.9, the hyperparameters are summarized in six sets of weight and bias matrices W^1 , W^2 , b^1 and b^2 , with three of the sets being for the forward transformation and the remaining three being for the left-inverse transformation.

We document here first the hyperparameters for the forward transformations, and then the left-inverse transformations. In Tables 1.1–1.3, W^1 for the forward transformation is shown, in Tables 1.4–1.6 W^2 is documented, and lastly in Tables 1.7–1.9 the bias values b^1 and b^2 for T is shown. Likewise, in Tables 1.10–1.12 W^1 for the left-inverse transformations is shown, in Tables 1.13–1.15 we have W^2 documented, and finally the bias vectors b^1 and b^2 for T^* are in Tables 1.16–1.18.

–	$w_{1,i}^1$	$w_{2,i}^1$	$w_{3,i}^1$	$w_{4,i}^1$	$w_{5,i}^1$
$w_{j,1}^1$	0.3334	0.2224	–0.2287	1.4581	0.6641
$w_{j,2}^1$	1.3027	–0.0620	0.0938	0.6231	–0.7262
$w_{j,3}^1$	0.6840	–0.5221	–0.8297	1.5006	–1.6470
$w_{j,4}^1$	0.1602	–0.1410	–0.7295	2.9956	–1.8192
$w_{j,5}^1$	–1.4785	–1.2168	–0.8630	1.5563	–1.3585
$w_{j,6}^1$	0.3796	–0.5499	0.4790	–0.8672	–0.6523
$w_{j,7}^1$	–0.6092	–0.9651	–0.3413	–1.2453	1.6277
$w_{j,8}^1$	–0.7007	–1.1893	0.2531	1.1828	–0.8958

Table 1.1: W^1 parameters forward transformation 1.

—	$w_{1,i}^1$	$w_{2,i}^1$	$w_{3,i}^1$	$w_{4,i}^1$	$w_{5,i}^1$
$w_{j,1}^1$	0.5038	-1.3071	-0.8413	-0.9842	1.3483
$w_{j,2}^1$	-0.6279	-0.3470	0.4370	1.0616	-0.0459
$w_{j,3}^1$	0.5308	0.1614	-1.1873	0.0820	-0.0649
$w_{j,4}^1$	-0.8655	-0.4273	0.5800	-3.7819	2.6945
$w_{j,5}^1$	-0.2274	-0.3042	-0.3390	0.4651	0.3101
$w_{j,6}^1$	-1.4720	-1.4519	-0.8186	1.1868	-0.7636
$w_{j,7}^1$	0.8490	0.8823	1.4739	-1.3427	1.6188
$w_{j,8}^1$	1.1381	1.1290	0.4961	-1.1869	1.4154

Table 1.2: W^1 parameters forward transformation 2.

—	$w_{1,i}^1$	$w_{2,i}^1$	$w_{3,i}^1$	$w_{4,i}^1$	$w_{5,i}^1$
$w_{j,1}^1$	0.4813	0.7649	0.3005	0.3120	-1.5745
$w_{j,2}^1$	-0.8229	-1.6009	-0.3431	-0.8548	0.3393
$w_{j,3}^1$	-0.2052	-0.2204	0.0617	2.0540	-1.6516
$w_{j,4}^1$	1.1871	0.8884	0.1848	2.3388	-0.7672
$w_{j,5}^1$	0.1331	0.1593	0.1144	-1.0263	2.0278
$w_{j,6}^1$	-0.7291	0.0582	-0.4825	1.4118	-0.8644
$w_{j,7}^1$	-0.7070	-1.0129	-1.6697	2.4584	-1.6323
$w_{j,8}^1$	-0.7438	-0.6170	-0.1600	-0.9175	-0.7153

Table 1.3: W^1 parameters forward transformation 3.

—	$w_{1,i}^2$	$w_{2,i}^2$	$w_{3,i}^2$	$w_{4,i}^2$	$w_{5,i}^2$	$w_{6,i}^2$	$w_{7,i}^2$	$w_{8,i}^2$
$w_{j,1}^2$	0.3201	-0.0228	0.2226	1.8772	0.5404	-0.0168	0.0592	0.7399
$w_{j,2}^2$	0.6274	0.3354	0.6133	2.4500	0.9959	0.2755	-0.3686	0.5105
$w_{j,3}^2$	-0.6225	-1.0955	-1.3432	-0.8923	-1.2631	0.0999	1.4896	0.2985
$w_{j,4}^2$	0.4113	0.1303	0.3624	2.0790	0.7718	0.0373	-0.0811	0.6946
$w_{j,5}^2$	-0.5021	-0.8032	-0.7103	-1.9424	-1.9465	0.1564	0.1971	0.3595
$w_{j,6}^2$	-0.5429	-0.7936	-1.1580	-0.1304	-0.6629	-0.2023	1.4700	0.1597

Table 1.4: W^2 parameters forward transformation 1.

—	$w_{1,i}^2$	$w_{2,i}^2$	$w_{3,i}^2$	$w_{4,i}^2$	$w_{5,i}^2$	$w_{6,i}^2$	$w_{7,i}^2$	$w_{8,i}^2$
$w_{j,1}^2$	-0.1657	0.2266	-0.0863	-0.9835	0.8930	0.6365	-0.1912	0.0722
$w_{j,2}^2$	0.8318	0.4713	0.0949	-2.0117	0.6943	1.0213	-0.7738	-0.5028
$w_{j,3}^2$	-0.5509	-0.8292	-0.1115	1.9340	1.6156	-0.4174	1.1387	0.5838
$w_{j,4}^2$	0.5264	0.3620	0.0301	-1.4995	0.7621	0.9535	-0.5283	-0.1632
$w_{j,5}^2$	0.2782	-0.9275	-0.4293	1.8116	0.3824	-1.9266	0.9844	-0.2666
$w_{j,6}^2$	-1.2426	-0.2833	-0.9066	1.3566	1.2610	0.1815	0.8920	1.4710

Table 1.5: W^2 parameters forward transformation 2.

—	$w_{1,i}^2$	$w_{2,i}^2$	$w_{3,i}^2$	$w_{4,i}^2$	$w_{5,i}^2$	$w_{6,i}^2$	$w_{7,i}^2$	$w_{8,i}^2$
$w_{j,1}^2$	-0.7112	0.2200	0.7772	0.4105	0.1178	0.1325	0.8600	-0.7485
$w_{j,2}^2$	-0.6024	0.2641	1.1636	1.0484	-0.5394	-0.1591	1.7484	-0.8470
$w_{j,3}^2$	-0.5409	0.8519	-0.4701	-1.3555	2.0236	0.2848	-1.2966	0.1467
$w_{j,4}^2$	-0.6578	0.3702	1.0166	0.6543	-0.1407	0.0385	1.3305	-0.7560
$w_{j,5}^2$	0.3574	-1.2891	-1.5860	-0.5538	0.5337	-1.2078	-1.7268	0.7355
$w_{j,6}^2$	-0.7526	0.4911	0.0123	-1.2909	1.9136	0.8269	-1.0718	-0.3092

Table 1.6: W^2 parameters forward transformation 3.

b_i^1	b_i^2
-0.8955	0.1458
-1.9130	-0.0853
0.5532	-0.4572
0.5941	0.1767
-0.1266	-0.1982
1.7945	-0.4110
0.0560	—
-2.1165	—

Table 1.7: Bias parameters forward transformation 1.

b_i^1	b_i^2
2.1270	0.3248
1.7084	0.0677
2.2616	-0.1119
0.0332	-0.0001
0.1129	-0.1299
-0.0705	0.3702
0.9312	—
0.8654	—

Table 1.8: Bias parameters forward transformation 2.

b_i^1	b_i^2
1.6039	-0.0442
1.5545	-0.2280
0.3010	-0.2339
-0.2271	-0.1887
0.0090	0.4389
-1.1221	0.0612
-0.0589	-
-1.9612	-

Table 1.9: Bias parameters forward transformation 3.

-	$w_{1,i}^1$	$w_{2,i}^1$	$w_{3,i}^1$	$w_{4,i}^1$	$w_{5,i}^1$	$w_{6,i}^1$
$w_{j,1}^1$	1.3826	1.0679	0.1349	-0.7569	-0.5219	-0.3797
$w_{j,2}^1$	-0.6859	-0.3986	-1.0253	-0.0161	-0.9710	0.6847
$w_{j,3}^1$	-0.5155	1.2254	1.8056	0.3121	2.7780	0.0689
$w_{j,4}^1$	0.3854	-1.2561	0.0912	0.4432	-1.6349	-2.0053
$w_{j,5}^1$	0.0584	-0.0800	-1.0154	-1.2928	0.0253	1.2015
$w_{j,6}^1$	-0.2386	0.2284	-0.9416	-0.8623	-1.1179	-0.6938
$w_{j,7}^1$	-0.0494	-0.4422	0.7741	-0.6775	3.1059	1.1577
$w_{j,8}^1$	-0.8241	-0.3227	-0.3424	-0.0287	-0.5628	-0.8046

Table 1.10: W^1 parameters inverse transformation 1.

-	$w_{1,i}^1$	$w_{2,i}^1$	$w_{3,i}^1$	$w_{4,i}^1$	$w_{5,i}^1$	$w_{6,i}^1$
$w_{j,1}^1$	0.1975	0.4069	0.6537	0.7793	0.6590	-1.2193
$w_{j,2}^1$	-0.4519	-0.7778	0.0474	-0.5526	0.5512	-0.6582
$w_{j,3}^1$	-0.5670	-1.3320	-0.9198	0.9287	0.3282	0.9070
$w_{j,4}^1$	-0.9230	-0.0982	-2.3961	0.6542	-3.4710	-0.1798
$w_{j,5}^1$	1.3613	0.5629	0.5792	0.0593	0.9104	-0.2677
$w_{j,6}^1$	0.0718	0.0249	-0.6638	0.3127	-0.2835	-1.0733
$w_{j,7}^1$	0.1668	-0.0269	1.9695	0.1153	3.1783	-0.0413
$w_{j,8}^1$	-0.0951	-0.4528	-0.1362	1.4943	1.2534	0.6423

Table 1.11: W^1 parameters inverse transformation 2.

—	$w_{1,i}^1$	$w_{2,i}^1$	$w_{3,i}^1$	$w_{4,i}^1$	$w_{5,i}^1$	$w_{6,i}^1$
$w_{j,1}^1$	0.1902	-1.1442	1.0069	-0.9719	-0.9339	-0.8522
$w_{j,2}^1$	-0.1182	-0.3627	-0.6432	-0.5649	-2.9620	-1.4441
$w_{j,3}^1$	-0.9654	1.1340	-0.6392	0.0968	-1.1007	0.0047
$w_{j,4}^1$	1.9488	-0.3202	-0.1038	0.2299	0.5180	0.1598
$w_{j,5}^1$	-2.1316	0.2331	-1.7588	0.5451	-3.9605	-0.4333
$w_{j,6}^1$	0.9969	-1.0412	-0.4697	-0.5067	0.0790	-0.1248
$w_{j,7}^1$	-0.1513	1.1165	0.6779	0.4360	0.3397	-0.5085
$w_{j,8}^1$	0.6043	0.7650	-0.9803	-1.0399	-3.7434	-0.9613

Table 1.12: W^1 parameters inverse transformation 3.

—	$w_{1,i}^2$	$w_{2,i}^2$	$w_{3,i}^2$	$w_{4,i}^2$	$w_{5,i}^2$	$w_{6,i}^2$	$w_{7,i}^2$	$w_{8,i}^2$
$w_{j,1}^2$	1.1111	0.8534	2.0054	2.2950	-1.2870	-0.1903	-1.2689	0.4631
$w_{j,2}^2$	0.4474	0.7015	-0.8695	-0.4933	0.4701	-0.0433	1.0553	-0.5836
$w_{j,3}^2$	0.8366	-0.0170	0.4281	0.1099	-0.4090	-0.1221	-0.6932	-0.4362
$w_{j,4}^2$	0.2744	0.7040	0.1797	-0.0099	-1.3376	0.0481	-0.1195	-0.1050
$w_{j,5}^2$	0.2606	-0.2738	-0.0238	0.0416	-1.2495	0.1155	-0.0256	-0.2391

Table 1.13: W^2 parameters inverse transformation 1.

—	$w_{1,i}^2$	$w_{2,i}^2$	$w_{3,i}^2$	$w_{4,i}^2$	$w_{5,i}^2$	$w_{6,i}^2$	$w_{7,i}^2$	$w_{8,i}^2$
$w_{j,1}^2$	1.1268	-0.6254	0.7815	-1.5400	1.2364	1.1251	-1.9268	-0.5410
$w_{j,2}^2$	-0.1764	-0.0426	0.1778	0.7056	-0.6279	-0.1831	0.9001	-0.5989
$w_{j,3}^2$	1.5557	0.1448	0.3831	-0.3140	1.1849	-0.5831	-0.8169	-0.2207
$w_{j,4}^2$	-0.5958	-0.2105	-0.8427	-0.1496	0.2332	0.0031	-0.2307	0.4189
$w_{j,5}^2$	-0.1629	-0.1393	-0.8389	-0.0055	0.2325	0.0040	-0.0400	0.8848

Table 1.14: W^2 parameters inverse transformation 2.

—	$w_{1,i}^2$	$w_{2,i}^2$	$w_{3,i}^2$	$w_{4,i}^2$	$w_{5,i}^2$	$w_{6,i}^2$	$w_{7,i}^2$	$w_{8,i}^2$
$w_{j,1}^2$	-0.7805	2.2374	-1.1451	1.5314	-1.8960	1.1208	0.7387	1.5783
$w_{j,2}^2$	0.0553	0.3161	0.7729	-0.2290	0.3677	-0.4795	-0.3732	-1.1368
$w_{j,3}^2$	-0.5033	-0.2137	-0.2097	-0.3307	-0.1289	-0.3757	0.3793	0.5064
$w_{j,4}^2$	0.1085	0.2132	0.0440	0.4149	-0.2165	-0.4756	0.6471	0.1822
$w_{j,5}^2$	0.0967	-0.0341	0.1440	0.4536	-0.0403	-0.2991	0.7472	0.0289

Table 1.15: W^2 parameters inverse transformation 3.

b_i^1	b_i^2
-2.0478	-0.8218
1.0630	0.2832
-0.4552	-0.2070
0.3042	-0.4213
0.1500	0.2391
-1.6803	-
-2.0752	-
-1.8550	-

Table 1.16: Bias parameters inverse transformation 1.

b_i^1	b_i^2
-2.4217	-0.9896
1.8845	0.2451
-0.0358	0.1923
1.0175	-0.5396
1.2121	0.3051
0.5690	-
-1.6330	-
-1.2409	-

Table 1.17: Bias parameters inverse transformation 2.

b_i^1	b_i^2
-1.7773	-1.1882
0.8481	0.3159
0.8387	-0.9366
-1.1999	-0.1873
0.9280	-0.1259
0.2137	-
0.7320	-
1.9011	-

Table 1.18: Bias parameters inverse transformation 3.

Bibliography

- [Aamo 2015] O.M. Aamo. *Leak detection, size estimation and localization in pipe flows*. IEEE Transactions on Automatic Control, vol. 61, no. 1, pages 246–251, 2015. (Cited on page 99.)
- [Agostino *et al.* 2002] F. Agostino, G. Baldini, S. Bittanti, A. De Marco, G. Poncia, W. Prandoni and M. Scarpellini. *Nonlinear identification of thermoacoustic instabilities with limit cycles in a rijke tube*. In Proceedings of the International Conference on Control Applications, volume 2, pages 1147–1152. IEEE, 2002. (Cited on page 48.)
- [Andrieu & Praly 2006] V. Andrieu and L. Praly. *On the existence of a Kazantzis-Kravaris/Luenberger observer*. SIAM Journal on Control and Optimization, vol. 45, no. 2, pages 432–456, 2006. (Cited on pages 153 and 166.)
- [Anfinsen & Aamo 2016a] H. Anfinsen and O.M. Aamo. *Stabilization of linear 2×2 hyperbolic systems with uncertain coupling coefficients-Part I: Identifier-based design*. In 2016 Australian Control Conference (AuCC), pages 93–98. IEEE, 2016. (Cited on page 99.)
- [Anfinsen & Aamo 2016b] H. Anfinsen and O.M. Aamo. *Stabilization of linear 2×2 hyperbolic systems with uncertain coupling coefficients-Part II: Swapping design*. In 2016 Australian Control Conference (AuCC), pages 99–104. IEEE, 2016. (Cited on page 99.)
- [Anfinsen & Aamo 2017] H. Anfinsen and O.M. Aamo. *Adaptive output feedback stabilization of $n+m$ coupled linear hyperbolic PDEs with uncertain boundary conditions*. SIAM Journal on Control and Optimization, vol. 55, no. 6, pages 3928–3946, 2017. (Cited on page 99.)
- [Anfinsen & Aamo 2019] H. Anfinsen and O.M. Aamo. Adaptive control of hyperbolic PDEs. Springer, 2019. (Cited on pages 99 and 106.)
- [Anfinsen *et al.* 2016] H. Anfinsen, F. Di Meglio and O.M. Aamo. *Estimating the left boundary condition of coupled 1-D linear hyperbolic pdes from right boundary sensing*. In 2016 European Control Conference (ECC), pages 2179–2184. IEEE, 2016. (Cited on page 99.)
- [Annaswamy *et al.* 2000] A.M. Annaswamy, M. Fleifil, J.W. Rumsey, R. Prasanth, J.P. Hathout and A.F. Ghoniem. *Thermoacoustic instability: Model-based optimal control designs and experimental validation*. IEEE Transactions on Control Systems Technology, vol. 8, no. 6, pages 905–918, 2000. (Cited on pages 6 and 118.)

- [Artstein 1982] Z. Artstein. *Linear systems with delayed controls: A reduction*. IEEE Transactions on Automatic Control, vol. 27, no. 4, pages 869–879, 1982. (Cited on page 123.)
- [Auriol *et al.* 2018] J. Auriol, F. Bribiesca-Argomedo, D.B. Saba, M. Di Loreto and F. Di Meglio. *Delay-robust stabilization of a hyperbolic PDE-ODE system*. Automatica, vol. 95, pages 494–502, 2018. (Cited on pages 128 and 129.)
- [Auriol *et al.* 2020a] J. Auriol, U.J.F. Aarsnes, F. Di Meglio and R. Shor. *Robust control design of underactuated 2×2 PDE-ODE-PDE systems*. IEEE Control Systems Letters, vol. 5, no. 2, pages 469–474, 2020. (Cited on page 123.)
- [Auriol *et al.* 2020b] J. Auriol, G.A. de Andrade and R. Vazquez. *A differential-delay estimator for thermoacoustic oscillations in a Rijke tube using in-domain pressure measurements*. In 2020 59th IEEE Conference on Decision and Control (CDC), pages 4417–4422. IEEE, 2020. (Cited on page 48.)
- [Bakken *et al.* 2004] L.E. Bakken, K. Jordal, E. Syverud and T. Veer. *Centenary of the First Gas Turbine to Give Net Power Output: A Tribute to Ægidius Elling*. In Turbo Expo: Power for Land, Sea, and Air, volume 41677, pages 83–88, 2004. (Cited on page 3.)
- [Bale 2002] D.S. Bale. Wave propagation algorithms on curved manifolds with applications to relativistic hydrodynamics. University of Washington, 2002. (Cited on page 23.)
- [Barreau *et al.* 2018] M. Barreau, A. Seuret, F. Gouaisbaut and L. Baudouin. *Lya-punov stability analysis of a string equation coupled with an ordinary differential system*. IEEE Transactions on Automatic Control, vol. 63, no. 11, pages 3850–3857, 2018. (Cited on page 7.)
- [Baudouin *et al.* 2013] L. Baudouin, E. Cerpa, E. Crépeau and A. Mercado. *Lip-schitz stability in an inverse problem for the Kuramoto–Sivashinsky equation*. Applicable Analysis, vol. 92, no. 10, pages 2084–2102, 2013. (Cited on page 5.)
- [Baudouin *et al.* 2014] L. Baudouin, E. Cerpa, E. Crépeau and A. Mercado. *On the determination of the principal coefficient from boundary measurements in a KdV equation*. Journal of Inverse and Ill-posed Problems, vol. 22, no. 6, pages 819–845, 2014. (Cited on page 99.)
- [Bayly 1986] B.J. Bayly. *Onset and equilibration of oscillations in general Rijke devices*. The Journal of the Acoustical Society of America, vol. 79, no. 3, pages 846–851, 1986. (Cited on page 48.)
- [Beale *et al.* 2010] M.H. Beale, M.T. Hagan and H.B. Demuth. *Neural network toolbox. User’s Guide*, MathWorks, vol. 2, pages 77–81, 2010. (Cited on page 162.)

- [Bekiaris-Liberis & Krstić 2014] N. Bekiaris-Liberis and M. Krstić. *Compensation of wave actuator dynamics for nonlinear systems*. IEEE Transactions on Automatic Control, vol. 59, no. 6, pages 1555–1570, 2014. (Cited on page 129.)
- [Bernard & Andrieu 2018] P. Bernard and V. Andrieu. *Luenberger observers for nonautonomous nonlinear systems*. IEEE Transactions on Automatic Control, vol. 64, no. 1, pages 270–281, 2018. (Cited on pages 153 and 154.)
- [Bernard & Krstić 2014] P. Bernard and M. Krstić. *Adaptive output-feedback stabilization of non-local hyperbolic PDEs*. Automatica, vol. 50, no. 10, pages 2692–2699, 2014. (Cited on page 99.)
- [Betz *et al.* 2017] M. Betz, M. Wagner, M. Zahn, N.V. Stadlmair, M. Schulze, C. Hirsch and T. Sattelmayer. *Impact of damper parameters on the stability margin of an annular combustor test rig*. In Turbo Expo: Power for Land, Sea, and Air, volume 50855, page V04BT04A001. American Society of Mechanical Engineers, 2017. (Cited on page 6.)
- [Blackshear 1952] P.L. Blackshear. Driving standing waves by heat addition. National Advisory Committee for Aeronautics, 1952. (Cited on page 20.)
- [Blonbou *et al.* 2000] R. Blonbou, A. Laverdant, S. Zaleski and P. Kuentzmann. *Active control of combustion instabilities on a Rijke tube using neural networks*. Proceedings of the Combustion Institute, vol. 28, no. 1, pages 747–755, 2000. (Cited on page 118.)
- [Bloxsidge *et al.* 1987] G.J. Bloxsidge, A.P. Dowling, N. Hooper and P.J. Langhorne. *Active control of an acoustically driven combustion instability*. Journal de Mecanique Theorique et Appliquee Supplement, vol. 6, pages 161–175, 1987. (Cited on pages 7 and 119.)
- [Bonciolini *et al.* 2021] G. Bonciolini, A. Faure-Beaulieu, C. Bourquard and N. Noiray. *Low order modelling of thermoacoustic instabilities and intermittency: Flame response delay and nonlinearity*. Combustion and Flame, vol. 226, pages 396–411, 2021. (Cited on page 7.)
- [Bonnell *et al.* 1971] J. Bonnell, R. Marshall and G. Riecke. *Combustion instability in turbojet and turbofan augmentors*. In 7th Propulsion Joint Specialist Conference, page 698, 1971. (Cited on page 5.)
- [Bothien *et al.* 2007] M.R. Bothien, J.P. Moeck, A. Lacarelle and C.O. Paschereit. *Time domain modelling and stability analysis of complex thermoacoustic systems*. Proceedings of the Institution of Mechanical Engineers, Part A: Journal of Power and Energy, vol. 221, no. 5, pages 657–668, 2007. (Cited on page 13.)
- [Carrier 1955] G.F. Carrier. *The mechanics of the Rijke tube*. quarterly of Applied Mathematics, vol. 12, no. 4, pages 383–395, 1955. (Cited on page 48.)

- [Castillo *et al.* 2012] F. Castillo, E. Witrant, C. Prieur and L. Dugard. *Dynamic boundary stabilization of linear and quasi-linear hyperbolic systems*. In 2012 IEEE 51st IEEE Conference on Decision and Control (CDC), pages 2952–2957. IEEE, 2012. (Cited on page 123.)
- [Castillo *et al.* 2013] F. Castillo, E. Witrant, C. Prieur and L. Dugard. *Boundary observers for linear and quasi-linear hyperbolic systems with application to flow control*. *Automatica*, vol. 49, no. 11, pages 3180–3188, 2013. (Cited on page 123.)
- [Con 2016] Conrad Electronics SE. *Manual 1086556 Voltcraft DPPS-32-15 Bench PSU*, 2016. <https://asset.conrad.com/media10/add/160267/c1/-/gl/001086556ML04/manual-1086556-voltcraft-dpps-32-15-bench-psu-adjustable-voltage-1-32-v-dc-0-15-a-480-w-usb-programmable-no-of-outputs-1-x.pdf>. (Cited on page 41.)
- [Coron & Lü 2015] J.M. Coron and Q. Lü. *Fredholm transform and local rapid stabilization for a Kuramoto–Sivashinsky equation*. *Journal of Differential Equations*, vol. 259, no. 8, pages 3683–3729, 2015. (Cited on page 5.)
- [Coron *et al.* 1999] J.M. Coron, B. d’Andréa Novel and G. Bastia. *A Lyapunov approach to control irrigation canals modeled by Saint-Venant equations*. In 1999 European Control Conference (ECC), pages 3178–3183. IEEE, 1999. (Cited on page 99.)
- [Crocco & Cheng 1956] L. Crocco and S.I. Cheng. *Theory of combustion instability in liquid propellant rocket motors*. Technical report, Princeton University NJ, 1956. (Cited on page 20.)
- [Crocco 1965] L. Crocco. *Theoretical studies on liquid-propellant rocket instability*. In Symposium (International) on Combustion, volume 10, pages 1101–1128. Elsevier, 1965. (Cited on page 5.)
- [Culick 1988] F.E.C. Culick. *Combustion instabilities in liquid-fuelled propulsion systems*, 1988. (Cited on pages 6 and 118.)
- [Cuquel 2013] A. Cuquel. *Dynamics and nonlinear thermo-acoustic stability analysis of premixed conical flames*. PhD thesis, Châtenay-Malabry, Ecole centrale de Paris, 2013. (Cited on page 20.)
- [da Costa Ramos *et al.* 2020] L. da Costa Ramos, F. Di Meglio, V. Morgenthaler, L.F.F. da Silva and P. Bernard. *Numerical design of Luenberger observers for nonlinear systems*. In IEEE Conference on Decision and Control, 2020. (Cited on pages 151, 155 and 159.)
- [da Costa Ramos 2021] L. da Costa Ramos. *Numerical study of an unstable premixed laminar flame and numerical Luenberger observers*. PhD thesis, PSL Research University, 2021. (Cited on page 151.)

- [de Andrade & Vazquez 2020] G.A. de Andrade and R. Vazquez. *A backstepping-based observer for estimation of thermoacoustic oscillations in a Rijke tube with in-domain measurements*. IFAC-PapersOnLine, vol. 53, no. 2, pages 7521–7526, 2020. (Cited on page 48.)
- [de Andrade *et al.* 2016] G.A. de Andrade, R. Vazquez and D.J. Pagano. *Boundary feedback control of unstable thermoacoustic oscillations in the rijke tube*. IFAC-PapersOnLine, vol. 49, no. 8, pages 48–53, 2016. (Cited on page 44.)
- [de Andrade *et al.* 2017] G.A. de Andrade, R. Vazquez and D.J. Pagano. *Boundary control of a Rijke tube using irrational transfer functions with experimental validation*. IFAC-PapersOnLine, vol. 50, no. 1, pages 4528–4533, 2017. (Cited on page 44.)
- [de Andrade *et al.* 2018a] G.A. de Andrade, R. Vazquez and D.J. Pagano. *Backstepping-based linear boundary observer for estimation of thermoacoustic instabilities in a Rijke tube*. In 2018 IEEE Conference on Decision and Control (CDC), pages 2164–2169. IEEE, 2018. (Cited on pages 7, 48 and 119.)
- [de Andrade *et al.* 2018b] G.A. de Andrade, R. Vazquez and D.J. Pagano. *Backstepping stabilization of a linearized ODE–PDE Rijke tube model*. Automatica, vol. 96, pages 98–109, 2018. (Cited on pages 28, 48, 119 and 123.)
- [de Andrade *et al.* 2020] G.A. de Andrade, R. Vazquez and D.J. Pagano. *Backstepping-based estimation of thermoacoustic oscillations in a Rijke tube with experimental validation*. IEEE Transactions on Automatic Control, vol. 65, no. 12, pages 5336–5343, 2020. (Cited on pages 6 and 48.)
- [De Goey *et al.* 2011] L.P.H. De Goey, J.A. Van Oijen, V.N. Kornilov and J.H.M. ten Thijs Boonkamp. *Propagation, dynamics and control of laminar premixed flames*. Proceedings of the Combustion Institute, vol. 33, no. 1, pages 863–886, 2011. (Cited on page 15.)
- [Di Meglio & Aarsnes 2015] F. Di Meglio and U.J.F. Aarsnes. *A distributed parameter systems view of control problems in drilling*. IFAC-PapersOnLine, vol. 48, no. 6, pages 272–278, 2015. (Cited on page 99.)
- [Di Meglio *et al.* 2018] F. Di Meglio, F. Bribiesca-Argomedo, L. Hu and M. Krstić. *Stabilization of coupled linear heterodirectional hyperbolic PDE–ODE systems*. Automatica, vol. 87, pages 281–289, 2018. (Cited on page 123.)
- [Dines 1984] P.J. Dines. *Active control of flame noise*. PhD thesis, University of Cambridge, 1984. (Cited on pages 6 and 118.)
- [Docquier & Candel 2002] N. Docquier and S.M. Candel. *Combustion control and sensors: a review*. Progress in Energy and Combustion Science, vol. 28, no. 2, pages 107–150, 2002. (Cited on page 6.)

- [Dowling & Morgans 2005] A.P. Dowling and A.S. Morgans. *Feedback control of combustion oscillations*. Annual Review of Fluid Mechanics, vol. 37, pages 151–182, 2005. (Cited on pages 6, 118 and 179.)
- [Dowling 1995] A.P. Dowling. *The calculation of thermoacoustic oscillations*. Journal of Sound and Vibration, vol. 180, no. 4, pages 557–581, 1995. (Cited on page 13.)
- [Du *et al.* 2019] M.L. Du, F.Y. Li and L.J. Yang. *Effects of different heat source distribution on a Rijke tube*. Applied Acoustics, vol. 146, pages 66–75, 2019. (Cited on page 72.)
- [Ducruix *et al.* 2000] S. Ducruix, D. Durox and S.M. Candel. *Theoretical and experimental determinations of the transfer function of a laminar premixed flame*. Proceedings of the Combustion Institute, vol. 28, no. 1, pages 765–773, 2000. (Cited on pages 18, 19 and 20.)
- [Eldredge & Dowling 2003] J.D. Eldredge and A.P. Dowling. *The absorption of axial acoustic waves by a perforated liner with bias flow*. Journal of Fluid Mechanics, vol. 485, pages 307–335, 2003. (Cited on page 6.)
- [Emmert *et al.* 2014] T. Emmert, S. Jaensch, C. Sovardi and W. Polifke. *taX—A flexible tool for low-order duct acoustic simulation in time and frequency domain*. In Forum Acusticum, Krakow, Poland, Sept, pages 7–12, 2014. (Cited on page 135.)
- [Emmert 2016] T.M. Emmert. *State space modeling of thermoacoustic systems with application to intrinsic feedback*. PhD thesis, Technische Universität München, 2016. (Cited on page 12.)
- [Epperlein *et al.* 2015] J.P. Epperlein, B. Bamieh and K.J. Astrom. *Thermoacoustics and the Rijke tube: Experiments, identification, and modeling*. IEEE Control Systems Magazine, vol. 35, no. 2, pages 57–77, 2015. (Cited on pages 7, 13, 23, 25, 28, 44, 45, 49, 50 and 74.)
- [Epperlein 2014] J.P. Epperlein. *Topics in modeling and control of spatially distributed systems*. PhD thesis, UC Santa Barbara, 2014. (Cited on page 45.)
- [Freitag 2009] E. Freitag. *On the measurement and modelling of flame transfer functions at elevated pressure*. PhD thesis, Technische Universität München, 2009. (Cited on page 20.)
- [Gentemann *et al.* 2003] A. Gentemann, A. Fischer, S. Evesque and W. Polifke. *Acoustic transfer matrix reconstruction and analysis for ducts with sudden change of area*. In 9th AIAA/CEAS Aeroacoustics Conference and Exhibit, page 3142, 2003. (Cited on page 29.)

- [Ghousein & Witrant 2020] M. Ghousein and E. Witrant. *Adaptive boundary observer design for coupled ODEs-hyperbolic PDEs systems*. IFAC-PapersOnLine, vol. 53, no. 2, pages 7605–7610, 2020. (Cited on page 7.)
- [Ghousein *et al.* 2020] M. Ghousein, E. Witrant, V. Bhanot and P. Petagna. *Adaptive boundary observer design for linear hyperbolic systems; Application to estimation in heat exchangers*. Automatica, vol. 114, page 108824, 2020. (Cited on page 99.)
- [Goy *et al.* 2005] C.J. Goy, S.R. James and S. Rea. *Monitoring combustion instabilities: E.ON UK's experience*. Progress in Astronautics and Aeronautics, vol. 210, page 163, 2005. (Cited on page 4.)
- [Gulati & Mani 1992] A. Gulati and R. Mani. *Active control of unsteady combustion-induced oscillations*. Journal of Propulsion and Power, vol. 8, no. 5, pages 1109–1115, 1992. (Cited on pages 7 and 119.)
- [Gysling *et al.* 2000] D.L. Gysling, G.S. Copeland, D.C. McCormick and W.M. Proscia. *Combustion system damping augmentation with Helmholtz resonators*. Journal of Engineering for Gas Turbines and Power, vol. 122, no. 2, pages 269–274, 2000. (Cited on page 6.)
- [Han *et al.* 2015] X. Han, J. Li and A.S. Morgans. *Prediction of combustion instability limit cycle oscillations by combining flame describing function simulations with a thermoacoustic network model*. Combustion and Flame, vol. 162, no. 10, pages 3632–3647, 2015. (Cited on page 7.)
- [Heckl 1988] M.A. Heckl. *Active control of the noise from a Rijke tube*. Journal of Sound and Vibration, vol. 124, no. 1, pages 117–133, 1988. (Cited on pages 48 and 118.)
- [Higgins 1802] B. Higgins. *On the sound produced by a current of hydrogen gas passing through a tube*. Journal of Natural Philosophy, Chemistry and the Arts, vol. 1, no. 129-131, page 2, 1802. (Cited on page 5.)
- [Hong & Lin 2007] B.S. Hong and T.Y. Lin. *Robust observer design for thermoacoustic dynamics with distributed-delay heat input*. Asian Journal of Control, vol. 9, no. 3, pages 326–332, 2007. (Cited on page 6.)
- [Ioannou & Sun 2012] P.A. Ioannou and J. Sun. Robust adaptive control. Courier Corporation, 2012. (Cited on pages 78, 105 and 106.)
- [Irscheid *et al.* 2021] A. Irscheid, N. Gehring, J. Deutscher and J. Rudolph. *Observer design for 2×2 linear hyperbolic PDEs that are bidirectionally coupled with nonlinear ODEs*. In 2021 20th European Control Conference. IEEE, 2021. (In press). (Cited on pages 150, 151 and 152.)

- [Jaensch *et al.* 2017] S. Jaensch, M. Merk, E.A. Gopalakrishnan, S. Bomberg, T. Emmert, R.I. Sujith and W. Polifke. *Hybrid CFD/low-order modeling of nonlinear thermoacoustic oscillations*. Proceedings of the Combustion Institute, vol. 36, no. 3, pages 3827–3834, 2017. (Cited on page 151.)
- [Janny *et al.* 2021] S. Janny, V. Andrieu, M. Nadri and C. Wolf. *Deep KKL: Data-driven output prediction for non-linear systems*. arXiv preprint arXiv:2103.12443, 2021. (Cited on page 173.)
- [Johnson *et al.* 2001] C.E. Johnson, Y. Neumeier, M. Neumaier, B.T. Zinn, D.D. Darling and S.S. Sattinger. *Demonstration of active control of combustion instabilities on a full-scale gas turbine combustor*. In Turbo Expo: Power for Land, Sea, and Air, volume 78514, page V002T02A062. American Society of Mechanical Engineers, 2001. (Cited on page 118.)
- [Kathuriya & Munjal 1975] M.L. Kathuriya and M.L. Munjal. *An accurate method for the experimental evaluation of the acoustical impedance of a black box*. The Journal of the Acoustical Society of America, vol. 58, no. 2, pages 451–454, 1975. (Cited on page 74.)
- [Kazantzis & Kravaris 1998] N. Kazantzis and C. Kravaris. *Nonlinear observer design using Lyapunov’s auxiliary theorem*. Systems & Control Letters, vol. 34, no. 5, pages 241–247, 1998. (Cited on page 153.)
- [Kemal & Bowman 1996] A. Kemal and C.T. Bowman. *Real-time adaptive feedback control of combustion instability*. In Symposium (International) on Combustion, volume 26, pages 2803–2809. Elsevier, 1996. (Cited on page 118.)
- [Khalil & Grizzle 2002] H.K. Khalil and J.W. Grizzle. *Nonlinear systems*, volume 3. Prentice Hall, Inc., 2002. (Cited on pages 54 and 99.)
- [Kim 2010] Y.H. Kim. *Sound propagation: an impedance based approach*. John Wiley & Sons, 2010. (Cited on page 27.)
- [King 1914] L.V. King. *XII. On the convection of heat from small cylinders in a stream of fluid: Determination of the convection constants of small platinum wires with applications to hot-wire anemometry*. Philosophical Transactions of the Royal Society of London. Series A, containing papers of a mathematical or physical character, vol. 214, no. 509-522, pages 373–432, 1914. (Cited on pages 13 and 14.)
- [Kornilov *et al.* 2009] V.N. Kornilov, R. Rook, J.H.M. ten Thije Boonkamp and L.P.H. De Goeij. *Experimental and numerical investigation of the acoustic response of multi-slit Bunsen burners*. Combustion and Flame, vol. 156, no. 10, pages 1957–1970, 2009. (Cited on page 151.)
- [Krstić & Smyshlyaev 2008a] M. Krstić and A. Smyshlyaev. *Backstepping boundary control for first-order hyperbolic PDEs and application to systems with*

- actuator and sensor delays*. Systems & Control Letters, vol. 57, no. 9, pages 750–758, 2008. (Cited on page 99.)
- [Krstić & Smyshlyaev 2008b] M. Krstić and A. Smyshlyaev. Boundary control of PDEs: A course on backstepping designs. SIAM, 2008. (Cited on page 99.)
- [Krstić *et al.* 1995] M. Krstić, P.V. Kokotovic and I. Kanellakopoulos. Nonlinear and adaptive control design. John Wiley & Sons, Inc., 1995. (Cited on page 99.)
- [Krstić *et al.* 1999] M. Krstić, A. Krupadanam and C. Jacobson. *Self-tuning control of a nonlinear model of combustion instabilities*. IEEE Transactions on Control Systems Technology, vol. 7, no. 4, pages 424–436, 1999. (Cited on pages 6 and 118.)
- [Kuramoto 1978] Y. Kuramoto. *Diffusion-induced chaos in reaction systems*. Progress of Theoretical Physics Supplement, vol. 64, pages 346–367, 1978. (Cited on page 5.)
- [Kwon & Pearson 1980] W. Kwon and A. Pearson. *Feedback stabilization of linear systems with delayed control*. IEEE Transactions on Automatic Control, vol. 25, no. 2, pages 266–269, 1980. (Cited on page 123.)
- [Lang *et al.* 1987] W. Lang, T. Poinsot and S.M. Candel. *Active control of combustion instability*. Combustion and Flame, vol. 70, no. 3, pages 281–289, 1987. (Cited on page 118.)
- [Levine & Schwinger 1948] H. Levine and J. Schwinger. *On the radiation of sound from an unflanged circular pipe*. Physical review, vol. 73, no. 4, page 383, 1948. (Cited on pages 49, 72 and 91.)
- [Lieberman 2010] M.A. Lieberman. Introduction to physics and chemistry of combustion: explosion, flame, detonation. Springer Science & Business Media, 2010. (Cited on page 15.)
- [Lieuwen & Yang 2005] T.C. Lieuwen and V. Yang. Combustion instabilities in gas turbine engines: operational experience, fundamental mechanisms, and modeling. American Institute of Aeronautics and Astronautics, 2005. (Cited on pages 5, 12, 17 and 20.)
- [Lieuwen *et al.* 2001] T.C. Lieuwen, H. Torres, C. Johnson and B.T. Zinn. *A mechanism of combustion instability in lean premixed gas turbine combustors*. Journal of Engineering for Gas Turbines and Power, vol. 123, no. 1, pages 182–189, 2001. (Cited on page 4.)
- [Lieuwen 2005] T.C. Lieuwen. *Nonlinear kinematic response of premixed flames to harmonic velocity disturbances*. Proceedings of the Combustion Institute, vol. 30, no. 2, pages 1725–1732, 2005. (Cited on page 21.)

- [Lieuwen 2021] T.C. Lieuwen. *Unsteady combustor physics*. Cambridge University Press, 2021. (Cited on pages 12 and 15.)
- [Lighthill 1954] M.J. Lighthill. *The response of laminar skin friction and heat transfer to fluctuations in the stream velocity*. Proceedings of the Royal Society of London. Series A. Mathematical and Physical Sciences, vol. 224, no. 1156, pages 1–23, 1954. (Cited on pages 13 and 15.)
- [Liu & Krstić 2001] W.J. Liu and M. Krstić. *Stability enhancement by boundary control in the Kuramoto–Sivashinsky equation*. Nonlinear Analysis: Theory, Methods & Applications, vol. 43, no. 4, pages 485–507, 2001. (Cited on page 5.)
- [Liu 2003] W. Liu. *Boundary feedback stabilization of an unstable heat equation*. SIAM journal on control and optimization, vol. 42, no. 3, pages 1033–1043, 2003. (Cited on page 99.)
- [Ljung 1987] L. Ljung. *System identification: Theory for the user*. Prentice Hall, Inc., 1987. (Cited on page 110.)
- [Luenberger 1964] D.G. Luenberger. *Observing the state of a linear system*. IEEE Transactions on Military Electronics, vol. 8, no. 2, pages 74–80, 1964. (Cited on page 153.)
- [Magri & Juniper 2013] L. Magri and M.P. Juniper. *Sensitivity analysis of a time-delayed thermo-acoustic system via an adjoint-based approach*. Journal of Fluid Mechanics, vol. 719, pages 183–202, 2013. (Cited on page 6.)
- [Marchesin & Paes-Leme 1986] D. Marchesin and P.J. Paes-Leme. *A Riemann problem in gas dynamics with bifurcation*. In *Hyperbolic Partial Differential Equations*, pages 433–455. Elsevier, 1986. (Cited on page 99.)
- [Masson-Delmotte *et al.* 2021] V. Masson-Delmotte, P. Zhai, A. Pirani, S.L. Connors, C. Pean, S. Berger, N. Caud, Y. Chen, L. Goldfarb, M.I. Gomis *et al.* *Climate change 2021: The physical science basis contribution of working group I to the sixth assessment report of the intergovernmental panel on climate change*, 2021. (Cited on page 3.)
- [McManus *et al.* 1993] K.R. McManus, T. Poinsot and S.M. Candel. *A review of active control of combustion instabilities*. Progress in Energy and Combustion Science, vol. 19, no. 1, pages 1–29, 1993. (Cited on page 4.)
- [McPherson 2017] A. McPherson. *Bela: An embedded platform for low-latency feedback control of sound*. The Journal of the Acoustical Society of America, vol. 141, no. 5, pages 3618–3618, 2017. (Cited on page 41.)

- [Mechhoud *et al.* 2013] S. Mechhoud, E. Witrant, L. Dugard and D. Moreau. *Adaptive distributed parameter and input estimation in plasma tokamak heat transport*. IFAC Proceedings Volumes, vol. 46, no. 26, pages 209–214, 2013. (Cited on page 99.)
- [Merk 1957] H.J. Merk. *An analysis of unstable combustion of premixed gases*. In Symposium (International) on Combustion, volume 6, pages 500–512. Elsevier, 1957. (Cited on page 20.)
- [Met 2017] Metra Mess- und Frequenztechnik. *Instruction Manual IEPE Supply Module M29*, 2017. <https://www.mmf.de/manual/m29mane.pdf>. (Cited on page 41.)
- [Moeck 2010] J.P. Moeck. *Analysis, modeling, and control of thermoacoustic instabilities*. PhD thesis, Technische Universität Berlin, Berlin, Germany, 2010. (Cited on page 12.)
- [Morgans & Dowling 2007] A.S. Morgans and A.P. Dowling. *Model-based control of combustion instabilities*. Journal of Sound and Vibration, vol. 299, no. 1-2, pages 261–282, 2007. (Cited on page 6.)
- [Murugappan *et al.* 2003] S. Murugappan, S. Acharya, D.C. Allgood, S. Park, A.M. Annaswamy and A.F. Ghoniem. *Optimal control of a swirl-stabilized spray combustor using system identification approach*. Combustion Science and Technology, vol. 175, no. 1, pages 55–81, 2003. (Cited on page 118.)
- [Nasir *et al.* 2018] A. Nasir, A. Mohammed and J.Y. Jiya. *Gas turbine engine: design, application and performance analysis*. In The World Congress on Engineering, pages 115–126. Springer, 2018. (Cited on page 3.)
- [Neumeier *et al.* 1996] Y. Neumeier *et al.* *Experimental demonstration of active control of combustion instabilities using real-time modes observation and secondary fuel injection*. In Symposium (International) on Combustion, volume 26, pages 2811–2818. Elsevier, 1996. (Cited on page 118.)
- [Niculescu 2001] S.I. Niculescu. Delay effects on stability: a robust control approach, volume 269. Springer Science & Business Media, 2001. (Cited on page 55.)
- [Noiray *et al.* 2008] N. Noiray, D. Durox, T. Schuller and S.M. Candel. *A unified framework for nonlinear combustion instability analysis based on the flame describing function*. Journal of Fluid Mechanics, vol. 615, pages 139–167, 2008. (Cited on page 19.)
- [Oefelein & Yang 1993] J.C. Oefelein and V. Yang. *Comprehensive review of liquid-propellant combustion instabilities in F-1 engines*. Journal of Propulsion and Power, vol. 9, no. 5, pages 657–677, 1993. (Cited on page 118.)

- [Olgac *et al.* 2014] N. Olgac, U. Zalluhoglu and A.S. Kammer. *Predicting thermoacoustic instability: a novel analytical approach and its experimental validation*. Journal of Propulsion and Power, vol. 30, no. 4, pages 1005–1015, 2014. (Cited on page 7.)
- [Ome] Omega Engineering, Inc. *Resistance heating wire nickel-chromium alloy*. <https://www.omega.fr/temperature/pdf/NI60.pdf>. (Cited on pages 38, 44 and 45.)
- [Oran & Boris 2005] E.S. Oran and J.P. Boris. Numerical simulation of reactive flow. Cambridge University Press, 2005. (Cited on page 15.)
- [Pankiewitz & Sattelmayer 2003] C. Pankiewitz and T. Sattelmayer. *Time domain simulation of combustion instabilities in annular combustors*. Journal of Engineering for Gas Turbines and Power, vol. 125, no. 3, pages 677–685, 2003. (Cited on page 12.)
- [Poinsot & Veynante 2005] T. Poinsot and D. Veynante. Theoretical and numerical combustion. RT Edwards, Inc., 2005. (Cited on pages 15 and 16.)
- [Poinsot 2017] T. Poinsot. *Prediction and control of combustion instabilities in real engines*. Proceedings of the Combustion Institute, vol. 36, no. 1, pages 1–28, 2017. (Cited on pages 4, 7, 74, 95, 119 and 177.)
- [Polifke & Gentemann 2004] W. Polifke and A. Gentemann. *Order and realizability of impulse response filters for accurate identification of acoustic multi-ports from transient CFD*. International Journal of Acoustics and Vibration, vol. 9, no. 3, pages 139–148, 2004. (Cited on page 12.)
- [Polifke 2015] W. Polifke. *Six lectures on thermoacoustic combustion instability*. In 21st CISM-IUTAM International Summer School on Measurement, Analysis and Passive Control of Thermoacoustic Oscillations, pages 87–Seiten, 2015. (Cited on page 30.)
- [Price 1969] E.W. Price. *Recent advances in solid propellant combustion instability*. In Symposium (International) on Combustion, volume 12, pages 101–113. Elsevier, 1969. (Cited on page 5.)
- [Putnam & Dennis 1954] A.A. Putnam and W.R. Dennis. *Burner oscillations of the gauze-tone type*. The Journal of the Acoustical Society of America, vol. 26, no. 5, pages 716–725, 1954. (Cited on page 5.)
- [Putnam 1971] A.A. Putnam. Combustion-driven oscillations in industry. Elsevier Publishing Company, 1971. (Cited on pages 5 and 118.)
- [Rashwan *et al.* 2020] S.S. Rashwan, A. Mohany and I. Dincer. *Investigation of self-induced thermoacoustic instabilities in gas turbine combustors*. Energy, vol. 190, page 116362, 2020. (Cited on page 4.)

- [Raun *et al.* 1993] R.L. Raun, M.W. Beckstead, J.C. Finlinson and K.P. Brooks. *A review of Rijke tubes, Rijke burners and related devices*. Progress in Energy and Combustion Science, vol. 19, no. 4, pages 313–364, 1993. (Cited on page 36.)
- [Rayleigh 1878] Lord Rayleigh. *The explanation of certain acoustical phenomena*. Roy. Inst. Proc., vol. 8, pages 536–542, 1878. (Cited on page 5.)
- [Rienstra & Hirschberg 2004] S.W. Rienstra and A. Hirschberg. *An introduction to acoustics*. Eindhoven University of Technology, vol. 18, page 19, 2004. (Cited on pages 28 and 115.)
- [Rijke 1859] P.L. Rijke. *LXXI. Notice of a new method of causing a vibration of the air contained in a tube open at both ends*. The London, Edinburgh, and Dublin Philosophical Magazine and Journal of Science, vol. 17, no. 116, pages 419–422, 1859. (Cited on pages 5 and 36.)
- [ROG] ROGA-Instruments. *RG-50 1/4" ICP Microphone*. <https://sensores-de-medida.es/wp-content/uploads/2017/08/ROGA-RG-50.pdf>. (Cited on page 41.)
- [Rogers & Marble 1956] D.E. Rogers and F.E. Marble. *A mechanism for high-frequency oscillation in ramjet combustors and afterburners*. Journal of Jet Propulsion, vol. 26, no. 6, pages 456–462, 1956. (Cited on page 5.)
- [Safi *et al.* 2018] M. Safi, A. Seuret and L. Baudouin. *Lyapunov stability analysis of a system coupled to a hyperbolic PDE with potential*. In 2018 European Control Conference (ECC), pages 3007–3012. IEEE, 2018. (Cited on page 7.)
- [Schuermans *et al.* 2000] B.B.H. Schuermans, W. Polifke, C.O. Paschereit and J.H. van der Linden. *Prediction of acoustic pressure spectra in combustion systems using swirl stabilized gas turbine burners*. In Turbo Expo: Power for Land, Sea, and Air, volume 78552, page V002T02A025. American Society of Mechanical Engineers, 2000. (Cited on page 13.)
- [Schuermans *et al.* 2003] B. Schuermans, V. Bellucci and C.O. Paschereit. *Thermoacoustic modeling and control of multi burner combustion systems*. In Turbo Expo: Power for Land, Sea, and Air, volume 36851, pages 509–519, 2003. (Cited on page 13.)
- [Schuller *et al.* 2003] T. Schuller, D. Durox and S.M. Candel. *A unified model for the prediction of laminar flame transfer functions: comparisons between conical and V-flame dynamics*. Combustion and Flame, vol. 134, no. 1-2, pages 21–34, 2003. (Cited on page 19.)
- [Schultz *et al.* 2007] T. Schultz, M. Sheplak and L.N. Cattafesta III. *Uncertainty analysis of the two-microphone method*. Journal of Sound and Vibration, vol. 304, no. 1-2, pages 91–109, 2007. (Cited on page 75.)

- [Seo 2003] S. Seo. *Combustion instability mechanism of a lean premixed gas turbine combustor*. KSME International Journal, vol. 17, no. 6, pages 906–913, 2003. (Cited on pages 4 and 16.)
- [Seybert & Ross 1977] A.F. Seybert and D.F. Ross. *Experimental determination of acoustic properties using a two-microphone random-excitation technique*. the Journal of the Acoustical Society of America, vol. 61, no. 5, pages 1362–1370, 1977. (Cited on pages 74 and 115.)
- [Shoshitaishvili 1992] A. Shoshitaishvili. *On control branching systems with degenerate linearization*. In IFAC Symposium on Nonlinear Control Systems, pages 495–500, 1992. (Cited on page 153.)
- [Silva *et al.* 2017] C.F. Silva, M. Merk, T. Komarek and W. Polifke. *The contribution of intrinsic thermoacoustic feedback to combustion noise and resonances of a confined turbulent premixed flame*. Combustion and Flame, vol. 182, pages 269–278, 2017. (Cited on page 20.)
- [Sivashinsky 1977] G.I. Sivashinsky. *Nonlinear analysis of hydrodynamic instability in laminar flames—I. Derivation of basic equations*. Acta Astronautica, vol. 4, no. 11, pages 1177–1206, 1977. (Cited on page 5.)
- [Smyshlyaev & Krstić 2010] A. Smyshlyaev and M. Krstić. Adaptive control of parabolic PDEs. Princeton University Press, 2010. (Cited on page 99.)
- [Son 2018] Sony Corporation. *Sony SRS-XB01 wireless speaker reference guide*, 2018. <https://tinyurl.com/3h8mrera>. (Cited on page 43.)
- [Stow & Dowling 2009] S.R. Stow and A.P. Dowling. *A time-domain network model for nonlinear thermoacoustic oscillations*. Journal of Engineering for Gas Turbines and Power, vol. 131, no. 3, 2009. (Cited on page 12.)
- [Sugimoto & Matsui 1982] T. Sugimoto and Y. Matsui. *An experimental study on the dynamic behavior of premixed laminar flames*. In Symposium (International) on Combustion, volume 19, pages 245–250. Elsevier, 1982. (Cited on page 21.)
- [Sujith *et al.* 2016] R.I. Sujith, M.P. Juniper and P.J. Schmid. *Non-normality and nonlinearity in thermoacoustic instabilities*. International Journal of Spray and Combustion Dynamics, vol. 8, no. 2, pages 119–146, 2016. (Cited on page 5.)
- [Tang & Xie 2011] S. Tang and C. Xie. *State and output feedback boundary control for a coupled PDE-ODE system*. Systems & Control Letters, vol. 60, no. 8, pages 540–545, 2011. (Cited on page 123.)
- [Tsien 1952] H.S. Tsien. *Servo-stabilization of combustion in rocket motors*. Journal of the American Rocket Society, vol. 22, no. 5, pages 256–262, 1952. (Cited on pages 6 and 118.)

- [twi] *Ansys twin Builder: Create and Deploy Digital Twin Models*. <https://www.ansys.com/products/digital-twin/ansys-twin-builder>. Accessed: 2021-10-07. (Cited on page 151.)
- [Vazquez *et al.* 2011] R. Vazquez, J.M. Coron, M. Krstić and G. Bastin. *Local exponential H^2 stabilization of a 2×2 quasilinear hyperbolic system using backstepping*. In 2011 50th IEEE Conference on Decision and Control and European Control Conference, pages 1329–1334. IEEE, 2011. (Cited on pages 99, 100 and 123.)
- [wgn] *wgn: Generate white Gaussian noise samples*. <https://www.mathworks.com/help/comm/ref/wgn.html>. Accessed: 2020-03-31. (Cited on page 109.)
- [Wilhelmsen & Di Meglio 2020a] N.C.A. Wilhelmsen and F. Di Meglio. *Estimating both reflection coefficients of 2×2 linear hyperbolic systems with single boundary measurement*. In 2020 59th IEEE Conference on Decision and Control (CDC), pages 658–665. IEEE, 2020. (Cited on page 10.)
- [Wilhelmsen & Di Meglio 2020b] N.C.A. Wilhelmsen and F. Di Meglio. *An observer for the electrically heated vertical Rijke tube with nonlinear heat release*. IFAC-PapersOnLine, vol. 53, no. 2, pages 4181–4188, 2020. (Cited on page 9.)
- [Wilhelmsen & Di Meglio 2021] N.C.A. Wilhelmsen and F. Di Meglio. *Acoustic boundary output feedback stabilization of dynamic $n - \tau$ model flame via duct with variable cross section*. IEEE Transactions on Automatic Control, 2021. Submitted. (Cited on pages 9 and 10.)
- [Williams 1975] F.A. Williams. *Recent advances in theoretical descriptions of turbulent diffusion flames*. Turbulent Mixing in Nonreactive and Reactive Flows, pages 189–208, 1975. (Cited on page 16.)
- [Williams 1985] F.A. Williams. *Turbulent combustion*. In The Mathematics of Combustion, pages 97–131. SIAM, 1985. (Cited on page 17.)
- [Williams 2018] F.A. Williams. *Combustion theory*. CRC Press, 2018. (Cited on page 5.)
- [Yang *et al.* 1992] V. Yang, A. Sinha and Y.T. Fung. *State-feedback control of longitudinal combustion instabilities*. Journal of Propulsion and Power, vol. 8, no. 1, pages 66–73, 1992. (Cited on page 118.)
- [Zahn *et al.* 2015] M. Zahn, M. Schulze, C. Hirsch, M. Betz and T. Sattelmayer. *Frequency domain predictions of acoustic wave propagation and losses in a swirl burner with linearized Navier-Stokes equations*. In Turbo Expo: Power for Land, Sea, and Air, volume 56680, page V04AT04A055. American Society of Mechanical Engineers, 2015. (Cited on page 6.)

- [Zahn *et al.* 2016] M. Zahn, M. Schulze, C. Hirsch and T. Sattelmayer. *Impact of quarter wave tube arrangement on damping of azimuthal modes*. In Turbo Expo: Power for Land, Sea, and Air, volume 49750, page V04AT04A025. American Society of Mechanical Engineers, 2016. (Cited on page 6.)
- [Zumbahlen 2007] H. Zumbahlen. Basic linear design. Citeseer, 2007. (Cited on page 20.)

RÉSUMÉ

Les instabilités thermoacoustiques sont néfastes pour les systèmes de combustion dans lesquels elles apparaissent, tels que les chambres de combustion de turbines à gaz. Des systèmes de surveillance avancés sont nécessaires pour estimer et prévoir ce phénomène afin de le prévenir, et possiblement de le supprimer grâce à des méthodes de contrôle. Dans cette thèse, nous proposons d'utiliser une description sous forme de systèmes à paramètres distribués des phénomènes acoustiques couplés à des modèles de dégagement de chaleur. Les non-linéarités sont prises en compte chaque fois que possible, pour décrire les instabilités. Des algorithmes d'estimation d'état et de paramètres prenant en compte ces effets dynamiques sont proposés. Deux niveaux de complexité différents sont considérés. D'une part, on s'intéresse à une configuration de laboratoire et un modèle de modes thermoacoustiques longitudinaux dans une chambre de combustion. Pour ce système, un estimateur de l'état d'un tube de Rijke chauffé électriquement est synthétisé. Puis, un observateur globalement convergent, prenant en compte les non-linéarités du réchauffeur électrique et la dynamique distribuée, est proposé et analysé. Celui-ci est associé à un algorithme d'identification de paramètres pour estimer les impédances acoustiques aux frontières du domaine spatial. L'observateur d'état et l'identification de paramètres sont testés à la fois dans des simulations et expérimentalement. Ensuite, nous proposons un algorithme pour estimer les deux paramètres aux limites de systèmes hyperboliques linéaires 2X2 avec une seule mesure aux limites. En outre, un modèle dynamique de l'acoustique dans un conduit avec une section transversale variable dans l'espace est dérivé. En utilisant ces deux résultats ensemble, le schéma d'estimation des paramètres aux limites pour le tube de Rijke est étendu à des conduits plus généraux. Un bouclage de sortie, combinant une loi de commande par retour d'état et un observateur frontière colocalisé, pour les instabilités thermoacoustiques longitudinales dans un modèle d'une chambre de combustion avec acoustique distribuée et un modèle de flamme linéaire est ensuite proposé. Enfin, nous proposons un estimateur d'état pour un modèle de chambre de combustion avec une flamme non linéaire. Une méthode basée sur l'utilisation de réseaux de neurones est utilisée pour concevoir un observateur pour le sous-système de flamme, qui est ensuite vérifié sur les données CFD.

MOTS CLÉS

Thermoacoustique, observateur d'état, identificateur de paramètre, commande à bouclage de sortie, systèmes de paramètres distribués, systèmes non linéaires, backstepping, les réseaux de neurones

ABSTRACT

Unwanted thermoacoustic instabilities are harmful to combustion systems that suffer from them such as gas turbine combustors operating under lean premixed conditions. Advanced monitoring systems are needed to estimate and forecast the phenomenon to assist in decision making and automatic stabilization. In this Thesis we propose using a distributed description of acoustics interfaced to heat release models, with nonlinearities whenever possible, to describe the instabilities. State and parameter estimation algorithms taking these dynamic effects into account are explored. Two different levels of complexity are considered: we start with a laboratory setup and move towards a model of longitudinal thermoacoustic modes in a can combustor. First, state estimation for the electrically heated Rijke tube is considered. A globally convergent observer, taking into account nonlinearities from the electrical heater and distributed dynamics, is proposed and analysed. This is paired with a parameter identifier for estimating boundary acoustic impedances. The state observer and parameter identifier are tested both in simulations and experimentally. Next, a parameter identifier to estimate both boundary parameters of 2X2 linear hyperbolic systems with a single boundary measurement is proposed. Also, a transient model of acoustics in a duct with spatially varying cross-sectional area is derived. Using these two results together the boundary parameter estimation scheme for the Rijke tube is extended to more general ducts. An output feedback controller, combining a full-state feedback control law and collocated boundary observer, for longitudinal thermoacoustic instabilities in a model of a can combustor with distributed acoustics and a linear flame model is proposed next. Convergence is proven and it is tested in simulations. Lastly, the state estimation problem for a can combustor model with a nonlinear flame is considered. Neural networks are used to design an observer for the flame subsystem, which is subsequently verified on CFD data.

KEYWORDS

Thermoacoustics, state observer, parameter identifier, output feedback control, distributed parameter systems, nonlinear systems, backstepping, neural networks